UNIVERSITÀ
DEGLI STUDI
FIRENZE

PhD in
Energetica e Tecnologie Industriali ed Ambientali Innovative

CYCLE XXXIII

COORDINATOR Prof. Giampaolo Manfrida

CFD analysis of the combustion process in a 4-stroke engine equipped with different passive prechambers using a detailed chemistry solver

Academic Discipline (SSD) ING-IND/08

Doctoral Candidate
Dr. Bigalli Simone

_____
(signature)

Supervisor
Prof. Ferrara Giovanni

_____
(signature)

Coordinator
Prof. Manfrida Giampaolo

_____
(signature)

Years 2017/2021

Ai miei genitori, che non mi hanno mai fatto mancare niente

A Primo e Dino Bigalli... sono sicuro che sarebbero fieri di me

"... non c'è niente di male a cadere. È sbagliato rimanere a terra."

Ringraziamenti

Per prima cosa desidero ringraziare tutti i miei parenti per l'affetto ricevuto in questi anni, a partire dai nonni, per passare agli zii ed arrivare ai cugini: grazie di tutto. Desidero ringraziare il Prof. Giovanni Ferrara: il Dottorato di Ricerca ha rappresentato per me un percorso di crescita non solo professionale, ma soprattutto umano. Un ringraziamento speciale a Francesco Balduzzi, che mi ha seguito durante tutto il mio Dottorato ed ha saputo farmi da guida nel mio percorso accademico: in lui ho trovato non solo un mentore, ma anche un modello da seguire e, soprattutto, un amico. Grazie per tutto quello che mi hai insegnato e quello che hai tentato di insegnarmi. Un ringraziamento enorme a tutti i membri del gruppo di ricerca REASE dell'Università degli Studi di Firenze, quelli che ci sono e quelli che ci sono stati. Quindi… Un grazie ad Alessandro Bianchini, che mi ha trasmesso la passione per le fonti rinnovabili: grazie per aver avuto fiducia e avermi portato con te al mio primo congresso. Grazie ad Andrea Tanganelli, mio ex-compagno di ufficio, con il quale ho condiviso gioie e dolori della CFD: a lui il merito di aver riscritto la storia delle freccette. Grazie a Michele Becciani, che mi ha sempre dato buoni consigli, sia fuori che dentro l'Università. Grazie a Marco Ciampolini, mio compagno di studi prima, mio primo tesista poi e, infine, mio collega di Dottorato: ne abbiamo passate tante insieme… Grazie a Iacopo Catalani, il mio CAD master e secondo tesista: con lui ho simulato la prima vera fiamma CFD del gruppo di ricerca… e certo che siamo proprio nati con la camicia, eh! Grazie a Francesco Papi, l'anima messicana del gruppo: OH, non dimenticare di chiamare tu sai chi. Grazie a Pier Francesco Melani, il tusseiungrande del gruppo: ho ancora impressa nella mente la telefonata di protesta contro un noto operatore di telefonia mobile. Un sentito e profondo ringraziamento a Niccolò Fiorini, il Maestro. Ho avuto la fortuna di trascorrere gli ultimi 6 mesi in ufficio con lui e mi sono sentito bene come non mi accadeva da tempo: condividere la stanza con il maestro è stato un onore che in pochi possono vantare. E come dimenticare la sua maestria… essa ha alleviato la mia mente dalle sofferenze numeriche e mi ha regalato perle di saggezza da custodire e tramandare… rimane un'ultima questione aperta: was the juice worth the squeeze? Un grazie a tutto il comparto sperimentale del gruppo di ricerca, Luca Romani, Lorenzo Bosi, Alberto Baroni e Sandro Raspanti: forse un giorno riuscirò a battervi su un go-kart. Un doveroso ringraziamento al Prof. Bruno Facchini: grazie per avermi chiesto come stavo ogni volta che ci incontravamo. Un grazie ad Antonio Andreini per i tutti i consigli che mi ha dato durante il mio dottorato. Gli anni universitari sono stati tanti e, per fortuna, non mi hanno lasciato solo diplomi e lauree… Quindi… Un grazie speciale alla mia amica Giulia Andreini, nonché compagna di studi e collega di dottorato: sei la sorella che non ho avuto… grazie per il tuo supporto, per i consigli che mi hai dato e per le risate che mi hai regalato… sono sicuro che ce ne saranno tante altre ancora. Un grazie enorme al mio amico Giovanni Peruzzi, detto Giova, con il quale ho fatto parte del Gruppo dei Guardiani: una persona speciale e un amico vero che si è sempre preoccupato per me… Insieme abbiamo studiato tanto, ma ci siamo divertiti altrettanto. Un sentito ringraziamento al mio amico Gabriele Grazzini, forse il fratello che non ho mai avuto, con il quale ho affrontato quasi per intero il mio percorso accademico: è vero, abbiamo sofferto, ma ogni volta che ripenso agli anni di studio sorrido sempre. E adesso che stanno per arrivare novità importanti nella sua vita, gli auguro il meglio per gli anni a venire. Un enorme grazie a Matteo Bianchi, amico, compagno di sommelier, collega e rivale di tennis: grazie per i consigli, grazie per il supporto e grazie per le risate. Un grazie speciale

a Pierpaolo Emili, il Capitano e unico vero scopritori di talenti calcistici: raramente ho visto una tale abilità nel fare talent scout. E come dimenticare quella cena in cui… no, la mia memoria non è un granché, forse 10 dollari potrebbero rinfrescarla… Un grazie enorme a Elena Serrano, la dottoressa nonché mia compagna di allenamenti in palestra: grazie per le risate, grazie per le esclamazioni (quelle che si possono dire e quelle che non si possono dire), grazie per avermi spronato (poco) negli allenamenti in palestra, grazie per tutto… sono sicuro che farai ridere tutti noi ancora a lungo (per fortuna) … Un grazie particolare ad Arianna Idini, il mio procuratore personale nella vita: non prenderò mai più una decisione senza essermi prima consultato con lei. Un enorme grazie a Giulia Stefanini, che con la sua spontaneità e la sua sincerità mi ha sempre fatto sentire come uno di famiglia. E grazie per aver portato alla ribalta l'onestà intellettuale. E come dimenticare il cappotto… senza maniche… Un enorme grazie a tutte le persone conosciute durante questi anni passati all'Università. Grazie a tutti quelli che mi hanno aiutato, grazie a quelli che mi hanno spronato, grazie a quelli che mi hanno chiesto aiuto, grazie a quelli che hanno avuto fiducia in me, grazie a quelli che si sono preoccupati per me… grazie a tutti voi. Non mi sono certo dimenticato di tutti gli amici che ho conosciuto al di fuori dell'Università, né di quelli che già conoscevo. Purtroppo la lista qui si fa davvero troppo lunga e per ovvie ragione non posso elencarvi tutti. Vi dedico quindi un enorme grazie collettivo per avermi supportato e sopportato. Un grazie enorme a Marco Pacetti, detto la bestia, amico e fratello, e a Elena Pacini e al piccolo Enea: grazie per le risate, grazie per i pranzi, grazie per le cene… grazie di tutto. Un sincero grazie a Matteo Milicia, il Doc, e a Filippo Fontani, il biologo: quando siamo insieme mi sento come a casa. Un grazie ai bomber(s) del gruppo, Lorenzo Cianfrone e Lorenzo Ciappi, amici e compagni di tante battaglie. Voglio ringraziare tutti partecipanti del Corso Uefa D di Prato: durante i mesi passati insieme mi sono sentito di nuovo dentro uno spogliatoio di calcio ed è stato bellissimo… è stato come tornare a casa dopo un lungo viaggio. Grazie ai miei compagni e maestri del corso di nuoto e del corso di Cross&Swim: ci siamo allenati tanto, ma abbiamo riso e scherzato di più. Grazie a tutti… quelli che ho nominato e quelli che ho dimenticato.

Un ringraziamento speciale al Dott. Nicola Limbucci: sono passati più di sette anni e ancora ricordo benissimo la professionalità e l'umanità che lo contraddistinguono. Grazie davvero dal profondo del cuore. Se è vero che la medicina cura la malattia e la parola cura il malato… lei è riuscito a fare entrambe le cose!

Un ultimo e doveroso ringraziamento va a me stesso, che ho affrontato molte difficoltà da solo… un grazie a me stesso perché non ho mai mollato… un grazie a me stesso perché, nonostante tutto, non ho mai perso il sorriso. Termino quindi questa mia avventura sapendo di dover lavorare tanto per emergere, ma con la consapevolezza di non essere così mediocre come alcuni credono.

Abstract

The prechamber jet ignition combustion system is one of the most promising technique to improve the thermal efficiency of spark ignition engines and to reduce the pollutant emissions. This technology allows to enhance the ignition of the air-fuel mixture in the main combustion chamber through several hot turbulent jets exiting from the small prechamber volume, thus leading to a shortening of the combustion duration. In the present study, the combustion process of a 4-stroke PFI gasoline engine equipped with a passive prechamber has been investigated through three dimensional CFD analysis. The goal was to analyse the behaviour of the flame front during the entire combustion process and to evaluate the improvements in terms of both combustion speed and ignitability of lean mixtures. The trade-off between the accuracy and complexity of the numerical approach and computational costs was assessed by adopting two different combustion models, with different detail level, for the simulation of the engine cycle: a detailed chemistry model and a flame surface density model. Both combustion models were first calibrated against experimental data of the engine in the baseline configuration without prechamber. The validated numerical models were exploited to perform predictive simulations of the engine equipped with the prechamber. The results on a preliminary geometry of the prechamber allowed assessing the reliability and the physical response of both combustion models, confirming the necessity of a detailed chemistry solver over the more simplified flame surface density approach, despite the high computational burden. The analysis of the combustion process with the detailed chemistry solver allowed to analyse the properties of the hot flame jets flowing through the narrow orifices and igniting the mixture inside the main combustion chamber. Different sensitivity analyses were carried out, by varying the wall temperature of the prechamber, the shape of the prechamber body and the size of prechamber holes. The influence of the geometrical features on the efficiency of the combustion process, the heat release rate and pressure trends inside both the prechamber and the main chamber was assessed and discussed. Since the prechamber allows to extend the flammable limit, an additional sensitivity to the air-fuel ratio was carried out in order to investigate the performance in case of lean mixtures.

Contents

List of Figures

List of Tables

Introduction

The continuous development of the legislation concerning the pollutant emissions and the introduction of new protocols for the type-approval procedure of new vehicles have pushed manufacturers and research towards new engine concept. It is well known that the combustion of fossil fuels produces emissions of carbon dioxides (CO_2) and pollutants such as nitrogen oxides (NO_x), soot, unburnt hydrocarbons (UHC) and carbon monoxides (CO) [1, 2]. The Low Temperature Combustion (LTC) seems to have the potential to overcome the issues of Internal Combustion Engines related to the pollutant emissions. LTC blends the best characteristic of Diesel and spark ignition combustion by igniting a homogeneous, lean air/fuel mixture, resulting in a high efficiency process with low emissions. Nevertheless, the operational instabilities of the engine, like the cycle-to-cycle variation, have limited the development of this new concept. The prechamber combustion seems to be the most promising technique to overcome this issue. A small volume, with the spark plug inside, is placed above the engine head. The ignition phase occurs inside the prechamber: the flame front propagates towards the orifices and enters into the main chamber through the narrow passages, generating hot turbulent jets, which are able to ignite the mixture in the cylinder. The combustion process with prechamber is a very complex phenomenon and it depends on several parameters, such as the mixture composition, the prechamber geometrical characteristics, and the flow field inside the cylinder. Considering the limitations of currently available experimental techniques to study combustion, theory and Computational Fluid Dynamics (CFD) are becoming very important tools, allowing to perform fluid dynamics studies without the necessity of expensive experimental tests and avoiding the costs of equipment with optical access and measurement devices [3]. Still, it should be reminded that the numerical analysis of combustion processes is an extremely challenging task, as it adds the complexity of the chemical reaction mechanisms to the difficult modelling of a non-reacting turbulent flow [4].

Within this scenario, the main aims of the present thesis project are:

- The development of a predictive and accurate numerical setup for the three-dimensional simulation of the combustion process in SI engines;
- The design of different prechambers to apply on a 4-stroke SI engine;
- The analysis of different numerical approaches for studying the combustion process in engine equipped with prechamber;
- The analysis of the advantages and potential of the prechambers in terms of increasing the combustion speed, enhancing the combustion quality and extending the flammable limit;
- The analysis of the effect of geometrical features of prechamber on the combustion process, giving advice on design criteria.

The activity starts with an extensive literature search, focusing on the LTC concept, on the prechamber operating principle and design criteria and, finally, on CFD numerical models of the combustion process, with particular focus on prechamber applications. When the prechamber is applied to the engine, the spark plug is located inside the prechamber as well. At the spark time, the mixture between the electrodes is

ionized, the local temperature of the fluid arises, the energy activation is overcome and the chemical reactions start. The flame kernel grows generating at first a laminar flame, which propagates inside the prechamber. High temperature gradient are generated across the flame front, together with strong density gradient. These add additional turbulence in the flow field, where the flame is growing. Turbulent structures interact with the flame front and chemical kinetics, enhancing the mixing and accelerating the flame front propagation: the combustion becomes a turbulent one and it is characterized by wrinkled flame front and high flame speed propagation. The flame flows through the narrow passages and enters into the main chamber. As the flame exits out from the orifices, several hot jets are generated. The thermodynamic properties of the jets strongly depend on the prechamber geometrical parameters and the flow field inside the engine. The hot jets enter in the combustion chamber and propagate into a low temperature mixture. This temperature gradient interacts with the chemical kinetics of the flame jets, as the flame jets affect the flow field generating additional turbulence.

Concerning the CFD approach of Internal Combustion Engine, since the test case is a PFI engine, the air/fuel mixture can be considered homogeneous with good approximation: therefore, the fuel injection is not simulated and the combustion can be treated as premixed one. One of the most combustion model used in these applications is the ECFM [5-12], or its extension ECFM-3Z for partially premixed flame and diffusion flame: it is a flame surface density model based on the definition of the progress variable (and eventually a mixture fraction for ECFM-3Z) to identify the fresh mixture from the burnt gases. This model may represent a good compromise between calculation efficiency and accuracy of the solution. Perhaps, it is still a simplified approach and it does not take into account for chemical reactions, computing the flame speed through empirical correlations. When simulating the combustion in prechamber applications, the lack of a chemical reaction mechanism may lead to neglect some features of the coupling between turbulence and kinetic reactions, resulting in wrong conclusions. A strong two way coupling, between turbulent and chemical kinetics, is established, leading to very complex phenomena to study and to simulate through CFD approach. Since the hard topic, which involves chemical kinetics, turbulence modelling, aerodynamic and mixing processes, it is obvious that a simplified approach based on the progress variable and the flame surface density model may be not appropriate for studying such a complex application. Thus, a more in-depth analysis of the problem is necessary in order to analyse properly the combustion process with prechamber and in order to evaluate how the prechamber parameters affect the flame front propagation and the combustion performance. Thus, the detailed chemistry solver seems to represent the right way for studying this particular topic. A chemical kinetic mechanism is required for taking into account the species and reactions implied in the combustion process, together with the thermodynamic properties of the elements involved. When a detailed chemistry model is used for combustion modelling, the reaction rates of the species are computed based on local temperature and pressure of the flow and on the mixture composition, using the Arrhenius formulation. Thus, the growth of the flame kernel and the flame propagation result from the calculation of the chemical kinetics parameters and not by using empirical correlations. This more level of detail is combined with a more complex numerical set-up and a higher computational effort. Nevertheless, it is necessary to take into account the chemical effects, since their interaction with flow field and turbulence structures can strongly affect the behaviour of the flame front and the engine performance.

In this thesis, two different combustion models are used to analyse the combustion process with prechamber: the ECFM-3Z, using a commercial software, and a detailed chemistry solver, the SAGE combustion model, implemented in CONVERGE CFD. The goal was the best trade-off between the accuracy and complexity of the numerical approach and computational. The test case investigated in this study is a Betamotor 430 cm^3 4-stroke, four valves, PFI spark ignition engine. The activity started with building a 1D model of the engine using GT-Power. The model was calibrated against the experimental data and it was used for extracting the boundary conditions for the 3D CFD simulation. At first, RANS simulations are carried out of the engine without prechamber in order to calibrate the two different combustion models against the experimental data. Since one of the aim of this project is to build a predictive numerical model for analysing the engine performance, an in-depth analysis of the effects of settings is carried out for the detailed chemistry model, which is calibrated for the maximum power condition and, then, validated for another engine operating point. After CFD simulations on the engine in baseline configuration, four different prechambers are designed, by varying the shape, the aspect ratio and the dimensions of the orifices. Basing on the literature review, the aspect ratio and the orifices diameters were found to be the crucial aspect in design prechambers. Especially the dimensions of the narrow passages may affect both the scavenging process, the flame propagation and the ignition of the mixture inside the main chamber: larger diameters lead to easier scavenging of the prechamber but, conversely, produce lower pressure drop between the prechamber and the main chamber, generating low momentum jets. Thus, the ignition of the mixture inside the main chamber may be slower than the one occurred with smaller diameters. A comparison between the two combustion models on the first geometry generated shows the capability and reliability of the detailed chemistry model against the flame surface density model. Thus, the former is used for further analysis of the phenomenon. A sensitivity to the wall temperature of the prechamber, to the geometrical features of the prechamber and to the spark advance is carried out, comparing the duration of combustion with prechamber against the baseline curve and analysing the pressure curves and flame front behaviour. Since the lack of information on the wall temperature of the prechamber, it was necessary to carry out a sensitivity on this parameter in order to evaluate the effect on the reaction rate, and thus on the whole combustion process. Since the use of prechamber allows to ignite a lean mixture, a further sensitivity to the air-to-fuel ratio of the fresh gases is carried out, in order to evaluate the advantages and capability of prechamber system. In fact, the use of the prechamber avoid the ignition instability typical of the 4-stroke engine with high air-to-fuel ratio. Furthermore, the hot flame jets generated by the prechamber allow to ignite the fresh gases inside the main chamber even if the amount of fuel is very low, extending the flammable limit of the mixture. The performance of the engine is finally compared with the baseline ones.

Based on CFD results, two prechambers simulated are manufactured. At the time of writing this thesis, the bench for testing the engine equipped with prechamber is under construction at LInEA (Laboratory for Innovation in Engines and Advanced systems for energy) laboratory of University of Florence. Thus, no experimental data of the engine with prechamber are available.

The present thesis is structured as follows:

- Chapter 1: the literature review is presented, together with the concepts and basic ideas of Low Temperature Combustion technology and prechamber combustion.
- Chapter 2: the main concepts related to Navier-Stokes equations and RANS approach in the context of turbulence modelling are presented, focusing on the turbulence models used in this work, the standard $k-\varepsilon$, Realizable $k-\varepsilon$ and RNG $k-\varepsilon$.
- Chapter 3: the main features of combustion in spark ignition engines and combustion modelling are introduced. The Navier-Stokes equations for reacting flows are presented, together with the phenomenology of turbulent premixed combustion. Finally, the combustion numerical closures are presented, explaining the models used in this thesis: a detailed chemistry model and a flame surface density model.
- Chapter 4: the numerical setup of the engine without prechamber (i.e. baseline configuration) is presented, for both cold-flow and reacting-flow simulations. The mesh and time-step sensitivity are analysed, together with the parameters for calibrating the combustion models and their effect on the flame front propagation. Lastly, the results of the calibration of the combustion models against the experimental data are shown. In addition, the validation of the detailed chemistry solver is presented.
- Chapter 5: this chapter includes the results of the simulations of the engine with prechamber. Different geometries are designed in this thesis. At first, the comparison between the results of two combustion models are shown on the first test case. Then, the effect of wall temperature of prechamber, the effect of geometrical parameters (such as aspect ratio and orifices diameters), the effect of the spark advance and the effect of the air-to-fuel ratio of the mixture are evaluated, considering the detailed chemistry model only. An in-depth analysis of the combustion process was carried out, comparing the whole test cases and analysing the pressure curves, burned mass fraction and views of flame front.

1 - Low Temperature Combustion (LTC)

Through the combustion process, the chemical energy of the fuel is converted to heat, which can be converted to work through a heat engine. The success of the combustion technology is linked to the availability of fossil fuels and the controllability of combustion processes. However, some issues have arisen: first, the limited availability of fossil fuels; second, the greater attention dealt to the health effects and environmental implications of combustion products. The continuous development of the legislation concerning pollutant emissions have been creating difficulties for vehicle manufacturers in the last few years and the ongoing update of the European directive on vehicle emissions pushed manufacturers to develop less polluting and more efficient powertrains. In order to improve SI engines efficiency, it is possible to replace throttling at partial loads with lean or diluted mixtures (with exhaust gas recirculation), or to exploit the capability of direct injection to create a stratified mixture which grants stoichiometric conditions near the spark but a globally lean combustion. While these strategies grant a reduced fuel consumption, some issues related to pollutant emissions still remain. The Low Temperature Combustion (LTC) seems to have a great potential to solve Internal Combustion Engines (ICE) issues. The LTC blends the best characteristics of Diesel and Spark Ignition (SI) combustion (i.e. high efficiency with low emissions) by igniting a homogeneous, lean air/fuel mixture through compression, like Diesel engines. This implies the use of a lean and homogeneous (or premixed) mixture in order to reduce the specific fuel consumption and the emissions of nitric oxides (NO_x) and particulate matter (PM) both. However, the LTC technologies suffer from the ignition instability, cycle-to-cycle variation and, sometimes, higher carbon monoxide (CO) and unburned hydrocarbons (UHC) emissions. It is clear that the study of combustion is the main focus in the development of innovative SI engines. Combustion is a complex process of chemical reactions,

1.1 - Issues of standard combustion

In the premixed combustion engines, the mixture is partially premixed before reaching the intake valve, for both carburettor and PFI (Port Fuel Injection) systems. Thus, the mixture inside the combustion chamber is almost homogeneous and stoichiometric to ensure its ignition by the spark plug (hence the name SI "Spark Ignition" engines). A semi-spherical flame front will develop from the gap location to the chamber volume sides. The engine load regulation is acquired by quantity through to the throttle, which introduces unavoidable losses on pumping efficiency. SI engines are inexpensive, compact and easy to design. The mixture homogeneity makes SI engines almost PM free. However, the combustion through the development of a flame front leads to the development of incomplete combustion products, i.e. CO and HC. Moreover, the high temperature peak of the stoichiometric combustion leads to thermal NO_x formation. Furthermore, SI engines suffer detonation of gasoline, which limits the volumetric compression ratio, thus limiting the Indicated Mean Effective Pressure (IMEP) inside the cylinder. The detonation limits can be solved using methane instead of gasoline, however up to now only dual-fuel powertrains are available on the market. On the other hand, in the diffusive combustion engines the combustion takes place at the same time as the mixing process. The engine intakes only air, then the fuel enters the combustion chamber through a high-

pressure injector in the cylinder head. The fuel is mixed with the air and, thanks to high pressure and temperature conditions, it ignites spontaneously. The main advantage of the diffusive combustion is the combustion process speed, which together with the use of a globally lean mixture, leads to higher thermal and thermodynamic efficiencies compared to SI engines, as well as low CO and UHC emissions. In fact, the equivalence ratio is generally limited below 0.8 to reduce mechanical stresses and NO_x emissions. The engine load adjustment is made by quality through the variation of the equivalence ratio, e.g. introducing less fuel but the same amount of air, thus pumping efficiency is less affected. Unfortunately, high pressure and temperature levels, in addition to the high amount of oxygen, leads to a NO_x formation that is much higher than the gasoline engines. Another problem is the PM formation, which originates from the quenching of pyrolysis products in the spray axis. Finally, the system complexity leads to high manufacturing costs.

1.2 - The prechamber combustion

In light of the evolution of emission limits regulation, in the new millennium researchers have developed the LTC technology [14-19]. The Low Temperature Combustion was originally born to avoid thermal NO_x formation, but it has been extended also to the improvement of engine efficiency and to the reduction of other pollutant emissions. The key idea is to develop a low-temperature combustion process to avoid thermal NO_x formation and fuel-rich zones to eliminate PM production (Figure 1-1). In order to do that, it is necessary to operate with a lean and almost homogenous mixture. Fuel rich zones should theoretically be avoided as much as possible, even if that causes a more difficult ignition.

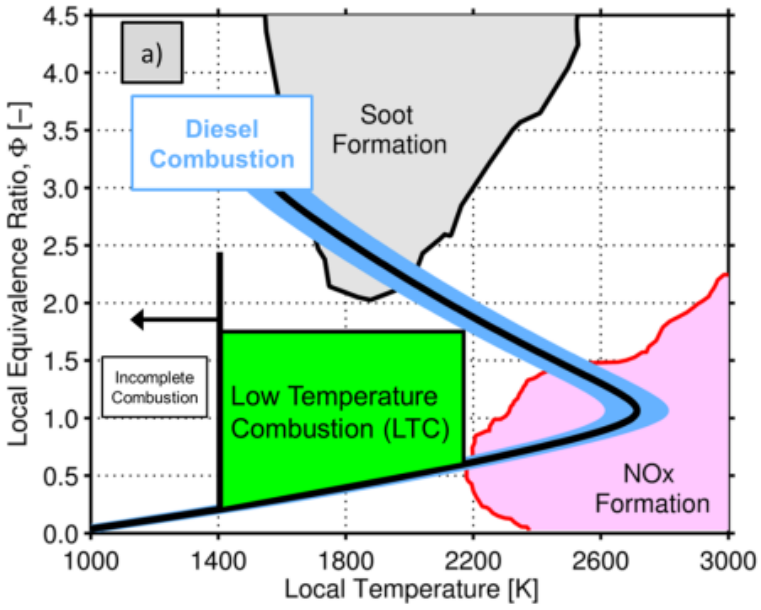

Figure 1-1. Pollutant emissions formation in ICEs depending on temperature and equivalence ratio.

A low-temperature combustion process must be almost instantaneous since it is not possible to burn via flame front propagation a fuel-lean mixture without encountering flame quenching. Thus, combustion must

have a knocking-like process. Compared to the standard SI combustion, the increase in burning speed leads to:

- a higher combustion efficiency;
- a higher indicated efficiency;
- an almost CO and UHC free combustion.

Furthermore, LTC engines can be regulated varying the amount of fuel thus increasing pumping efficiency. Thus, LTC merges together the best characteristics of gasoline and diesel engines (on one side, the high efficiency and the low UHC and CO emissions of diesel engines, on the other, the low PM emissions of SI engines) adding the concept of a low-temperature chemical process to solve NO_x production issue.

The prechamber-aided combustion is a single-fuel strategy in which a small prechamber is used to generate hot turbulent jets capable of igniting a fuel-lean mixture inside the main combustion chamber [20]. The combustion chamber is split into two different communicating volumes: a small volume prechamber and the main combustion chamber. The two volumes are connected through a small diameter duct or through small orifices. The sparkplug overlooks over the prechamber head (Figure 1-2).

Figure 1-2. Example of prechamber combustion: Mahle TJI active prechamber.

The combustion starts in the prechamber via spark ignition and develops via flame front propagation trough an almost stoichiometric mixture. Then, the flame front enters the duct or the orifices and accelerates itself, with or without or partially quenching. The hot turbulent jets enter the main combustion chamber through the orifices, generating turbulent phenomena of heat and mass exchange capable of igniting the fuel-lean fresh mixture. The use of the prechamber reduces the ignition delay and highly accelerates the combustion process, thanks to the increase in turbulent transport phenomena, which involves a higher amount of fresh mixture. This makes possible the ignition of an ultra-lean premixed mixture [20]: it can be considered a method to increase the reactivity of a lean mixture without the use of in-cylinder stratification or dual-fuel systems. The prechamber-aided combustion shows the same advantages of LTC systems: the ignition of a fuel-lean premixed mixture leads to lower NO_x and PM emissions, the increase in burning velocity leads to

higher combustion and indicated efficiencies, furthermore the engine can be regulated varying the amount of fuel, thus increasing pumping efficiency.

The main challenge is preparing an almost stoichiometric mixture inside the prechamber when a fuel-lean mixture is used inside the main chamber. Two different macro-classes of prechamber have been developed, depending on the fueling system:

- active (or stratified) prechamber: the prechamber is provided with a dedicated injector in addition to the main one/s. This guarantees stoichiometric conditions inside the prechamber at each engine operation, but at the same time it increases system complexity;
- passive (or un-stratified) prechamber: the prechamber is fueled during the compression stroke by the mixture coming from the cylinder. Passive prechambers are simple to install: commonly they can be screwed in the spark plug filleting without changing the cylinder head. However, they need of an accurate set-up of the injection system (in case of direct injection) or the use of a not too fuel-lean mixture (in case of indirect injection).

Mixture ignitability, e.g. stoichiometric conditions, inside passive prechambers is generally carried out through direct injection phasing. Generally, spray-guided direct injectors are used, in such a way to directly fill the prechamber with fuel. However, passive prechambers have been applied to fuel-lean natural gas power-generation engines fueled via PFI. In this case, the ignition a fuel-lean mixture inside the prechamber is made possible by the high turbulence and the slow flow field, which form in the spark gap zone. The passive prechamber will be the subject of this thesis work. First, a literature search will be made to understand the design criteria and the influence of geometric parameters on prechamber filling and combustion processes.

1.2.1 - Literature review

In this chapter, the results of the most significant works available in literature concerning passive prechambers will be resumed. This literature review aims at establishing the main parameters which influence prechamber scavenging, fuel filling and combustion processes. At first, the review shows a brief argumentation on the ignition process inside the combustion chamber, which depends on prechamber geometry and engine operating conditions. Several geometric parameters have been selected as main actors to design passive prechambers:

- prechamber shape;
- orifice/s shape;
- prechamber volume (V_p);
- overall flow passage (A_t);
- number of orifices;
- inclination of orifices;

- prechamber position.

1.2.2 - Ignition process inside the prechamber

The combustion process inside the prechamber is similar to the flame front propagation in standard SI (Spark Ignition) engines. Thus, the mixture in the gap zone must be stoichiometric or at least slightly fuel-lean. In the second case, the ignition zone must be provided by a high turbulence level and a slow flow field, as it happens in passive prechambers applied in premixed lean-burn engines. When the flame front reaches prechamber orifice/s, it accelerates with or without quenching itself [21]. If the flame front quenches passing through orifices, the ignition process may be called TJI (Turbulent Jet Ignition); otherwise, if the flame front survives, it may be called TI (Torch Ignition). Main differences between TJI and TI lie in penetration, momentum and turbulence of the hot jets when they enter the combustion chamber, which lead to different combustion processes:

- in TJI combustion, turbulent high-momentum jets composed of active radicals and partially burnt gases reach the centre of the combustion chamber, generating a high-turbulence spheroidal-like flame front which quickly leads to the detonation of the surrounding fresh mixture;
- in TI combustion, hot low-momentum jets composed of wrinkled flames and burnt gases penetrate less the cylinder charge, compared to TJI, but increase the local heat exchange since the flame is still alive, acting as multiple flashpoints on the upper zone of the cylinder. It results in a 2D-like turbulent flame front which may cause (or not) the detonation of the surrounding fresh mixture, depending on the engine operating conditions.

TJI combustion process seems to be more effective compared to TI, thus for an equal equivalence ratio inside the prechamber and equal engine operating conditions, it leads to the ignition of a leaner mixture inside the combustion chamber [21]. Indeed, the separation between these two classes is not so marked. It is possible that the flame partially quenches only inside the orifice/s. Yamaguchi et al. [22] have categorized in detail the ignition process into four different classes, depending on the predominance of the chemical processes between active radicals and fresh mixture rather than thermodynamic processes between flame and fresh mixture:

- chemical chain ignition and well-dispersed burning;
- composite ignition and well-dispersed burning followed by wrinkled laminar burning;
- flame kernel torch ignition and wrinkled laminar burning;
- flame front torch ignition and wrinkled laminar burning.

Even if all the four classes were able to ignite the in-chamber mixture, the second one, in which chemical and thermodynamic processes coexist, is found to be the best choice. The same prechamber can perform both TJI combustion and TI combustion, depending on the engine operating conditions. Big prechamber volumes V_p and small flow passage areas A_t lead to high pressure differences between the prechamber and the main chamber, which promote TJI combustion [21]. Furthermore, TJI combustion is promoted by low

pressure and fuel-lean in-cylinder mixtures, while high temperatures and stoichiometric mixtures support TI combustion [22, 23]. An expression to evaluate the critical orifice diameter, which separates the TJI from the TI combustion, as a function of the engine operating conditions is given by Adams [24]. The critical diameter only refers to prechambers characterized by an opened duct, but it can be extended to the overall flow passage area A_t in multi-orifice prechambers, on condition that the increase in the wetted perimeter will be considered.

1.2.3 - Geometrical parameters

The prechamber can be characterized by:

- a lengthened shape: the prechamber is characterized by a big volume on top, which can take a cylindrical or conical shape, and a cylindrical lengthened channel. The channel bottom can be opened or closed to the combustion chamber. In the second case, duct and combustion chamber communicate through one or more small orifices.
- a stumpy shape: the prechamber is large and flattened, characterized by a height-to-width ratio typically lower than 1.5, without a connection duct which separates the prechamber head from the main combustion chamber. Prechamber and combustion chamber communicate through one or more small orifices.

Lengthened-shape prechambers, as said, are characterized by two different volumes: the head and the duct. The channel length is frequently tantamount to the cylinder head thickness. The external diameter is the same as standard sparkplugs to not adjust the cylinder head, thus the filleting pitch of the external wall of the duct is 1.25 mm. The internal wall of the prechamber head is filleted to hold the sparkplug (pitch 1.25 mm), for small volume prechambers, or the sparkplug adaptor, for big volume ones. These typologies of prechambers can be both passive or active, even if they are more suitable for the second use. It seems that there are no passive lengthened prechambers available on the market, while active ones have been recently introduced by Mahle. Stumpy-shape prechambers frequently consist in a sort of small-volume cylindrical (or semi-spherical) capsule, which covers the sparkplug electrodes. In this case, the prechamber is integrated into the sparkplug itself. That system is usually called "Prechamber Spark Plug". These prechambers are frequently used in natural gas power-generation engines and have been available on the market for years.

Stumpy-shape prechambers can also be independent from the sparkplug. In that case, the internal wall is filleted to hold the sparkplug itself (pitch 1.25), for small-volume prechambers, or the sparkplug adaptor, for big-volume ones; the external wall instead is filleted to be screwed on the cylinder head (pitch 1.25). Obviously, the use of big-volume stumpy prechambers could require the enlargement of the pre-existing hole on the cylinder head.

Figure 1-3. From the left: the Mahle active lengthened prechamber, two examples of passive lengthened prechambers [25, 26], two passive stumpy prechambers available on market (Guascor 7664604 Spark Plug and Altronic Prechamber Spark Plug).

Once defined the two typical prechamber shapes, it is now possible to show the main differences in their behaviour. In general, it can be claimed that in four-stroke engines, the scavenging process inside the prechamber is much better when using stumpy prechambers instead of lengthened ones. That can be seen, for example, comparing the in-prechamber flow fields reported by Radicchi et al. [25], in a lengthened prechamber, and Fu et al. [27], in a stumpy one. The better scavenging of stumpy-shape prechambers can be attributed to the fact that, when using more than one orifice, they are better able to exploit the flow field inside the cylinder, primarily the tumble motion.

1.2.4 - Influence on the fuel filling process and the mixture homogeneity

In PFI engines, the equivalence ratio of the mixture inside the prechamber is almost the same as that inside the cylinder. It can be stated that, when using lean-burn engines, the use of the prechamber may lead to the ignition of a slightly leaner mixture because of the higher turbulence level and the lower flow field intensity, which can form in the head zone of the prechamber. Wolff et al. [28] have investigated the mixture formation inside a passive prechamber applied to a lean-burn natural gas PFI engine through the LIF (Laser-Induced Fluorescence) analysis of acetone. Cylindrical and conical shapes have been investigated on equal prechamber height and head diameter. Experimental results have shown that the use of a cylindrical prechamber leads to a higher mixture homogeneity, thus to a lower cycle-to-cycle variation. On the contrary, when using DI engines, the mixture formation inside the prechamber strictly depends on injector pressure and timing, while the prechamber effectiveness strictly depends on the ignition point [21].

Fu et al. [27] have investigated the mixture formation inside a passive prechamber applied to a four-stroke GDI engine. The prechamber is characterized by a diameter of 12 mm and three holes of 4 mm (one facing the intake manifold). The injection has been split into two separate phases: the main injection, during the intake stroke, used to adjust the engine power output, and the pilot injection, during the compression stroke,

used to control the equivalence ratio inside the prechamber. The spray was directed toward the orifice facing the intake valves. Results have shown that it is possible to successfully fill the prechamber with gasoline without allowing the fuel to escape from the other two orifices before the ignition phase takes place. Furthermore, the mixture inside the upper volume of the prechamber was found to be almost stoichiometric, thus highly ignitable.

1.2.5 - Influence on combustion and performance

As for premixed engines, Gomes et al. [29] have investigated three different prechamber shapes to be used in a Fiat's 1.6 liters PFI gasoline engine under stoichiometric conditions. All the prechambers have a lengthened shape and are characterized by: V_p of 1.97 cc, V_p/V_c of 0.5%, V_p/V_{cc} of 4.14%. Geometric parameters of the three prechambers are:

- four 3 mm diameter orifices on the prechamber bottom, each with a dedicated channel of the same diameter. A_t of 28.27 mm^2, equivalent to A_t/V_p of 14.35*10-3 mm^{-1};
- four 1.5 mm diameter orifices on the prechamber bottom. One only central channel connects orifices to the prechamber head. A_t of 7.07 mm^2, equivalent to A_t/V_p of 3.59*10^{-3} mm^{-1};
- one only 6 mm diameter channel, fully opened to the combustion chamber. A_t of 28.27 mm^2, equivalent to A_t/V_p of 14.35*10^{-3} mm^{-1}.

Experimental results have shown, in all cases, a reduction in torque when using the prechambers. That behaviour has been attributed to the higher thermal losses, due to the increase in the external surface of the engine, and to the lower volumetric compression ratio, due to the addition of the prechamber volume. Furthermore, in all cases, the prechamber has led to an increase in the NO_x formation due to the higher temperature peak, which is due to the faster combustion process.

Mavinahally et al. [30] have investigated four different prechamber shapes to be used in a single-cylinder 661cc PFI engine. The engine, originally made to be fueled with mineral diesel, has been arranged to be ran as a lean-burn premixed gasoline engine. Prechambers have been positioned in lieu of the diesel injector. Geometric parameters of the four prechambers are:

- V_p of 0.926cc, equal to V_p/V_c of 0.14%. Duct with a 6mm diameter directly opened to the combustion chamber. A_t of 28.27mm^2, equal to A_t/V_p of 30.53*10^{-3} mm^{-1};
- V_p of 0.926cc, equal to V_p/V_c of 0.14%. Duct with a 6mm diameter directly opened to the combustion chamber. Four lateral orifices of 3mm diameter. A_t of 65.96 mm^2, equal to A_t/V_p of 71.23*10^{-3} mm^{-1};
- V_p of 1.462cc, equal to V_p/V_c of 0.22%. Duct with a 9 mm diameter directly opened to the combustion chamber. Four lateral orifices of 3 mm diameter and eight lateral orifices of 2 mm diameter. A_t of 117mm^2, equivalent to A_t/V_p of 80.03*10^{-3} mm^{-1};
- V_p of 1.462cc, equal to V_p/V_c of 0.22%. Closed duct with a single orifice of 2.5 mm diameter on the bottom and four lateral orifices of 3 mm diameter. A_t of 33.18 mm^2, A_t/V_p of 22.69*10^{-3} mm^{-1}.

The authors suggest adopting prechambers characterized by a closed channel and a consistent number of orifices, with which they have obtained a higher brake thermal efficiency, a lower cycle-to-cycle variation and an extension of the operative range toward leaner premixed mixtures. Mavinahally et al.'s results seem to contrast with Gomes et al.'s ones. The authors have also investigated the influence of the distance between sparkplug and orifices on the brake thermal efficiency and flammability limits using the same prechamber volume and geometry. Experimental results have shown that by decreasing the distance between sparkplug and orifices it is possible to increase both lean and rich flammability limits and to enhance the BTE, thanks to the faster combustion process. Authors have noted that the increase in the combustion speed allows the ignition advance timing to be reduced, which leads to lower NO_x formation, as stated by Kataoka e Hirako [31].

Moreira [32] have applied a lengthened prechamber of 3.66cc (V_p/V_c of 0.92%), with a 6 mm diameter opened duct (A_t of 28.27 mm^2) to a Fiat 1.6 litre PFI engine. Investigating the engine performance up to 50% of the torque and operating it at λ 1.2, experimental results have shown a reduction in BFSC up to 9.74%, a reduction in HC emissions up to 52.4%, a reduction in CO emissions up to 91.21% and a reduction of CO_2 emissions up to 8.82%. Even if the PFI engine has shown great performances at λ 1.3, it has also shown a too high cycle-to-cycle variation, thus it was stated that it is not possible to operate the engine at λ higher than 1.2. It should be noted that the improvements in performance obtained by Moreira, compared to Gomes's [29] and Baptista's [26] results, is probably due mainly to the reduction of the cylinder height in such a way to keep the original compression ratio constant, instead of the prechamber itself.

Another important issue of lengthened prechambers seems to be the overheating. Since the prechamber head comes out from the cylinder head, the cooling liquid, which passes through the cylinder head channels, can not cool the prechamber adequately. This problem has been seen by Sa [33].

Regarding the direct-injection engines, stable operating conditions have been obtained using very fuel-lean mixtures at low-loads (up to λ 1.7 compared to λ 1.35 without prechamber), by Chiodi et al. [21], applying a 0.3cc eight-orifices stumpy prechamber to a 400cc GDI engine, both numerically and experimentally. Chiodi et al. in the same work have also numerically compared the engine performance with and without the prechamber at full load. Authors have stated that when using the prechamber, the faster combustion process leads to a too-high in-cylinder pressure when using a stoichiometric mixture, thus fuel-lean mixtures must be adopted even at full load. In fact, the SI engine was operated at λ 0.85, like standard PFI engines at full load, while the TJI engine was operated at λ 1.4.

Results have shown, as expected, a reduction of 15% in IMEP due to the lower fuel mass burned per cycle. However, the indicated efficiency has been increased by 25% and the temperature peak has been reduced by 500 K, achieving LTC goals.

1.2.6 - Prechamber volume

The amount of fuel inside the prechamber does not directly contribute to the production of work as it is used to accelerate the combustion process inside the main chamber. Since the amount of fuel inside the prechamber is strictly related to its volume, it should be as little as possible to reduce the fuel consumption. On the other hand, the higher the amount of fuel inside the prechamber, the higher the effectiveness of the ignition process inside the main chamber, since the hot jets increase their velocity, turbulence and heating capacity. This is a very important aspect, especially when very fuel-lean mixtures are used. Furthermore, the prechamber volume is useless if not compared to the displacement of the engine, since it must be chosen depending on the amount of fuel and air inside the cylinder. For this reason, we always refer to the ratio between the prechamber volume and the displacement V_p/V_c. Prechamber volumes used in premixed engines lie in a very wide range, for example:

- Baptista [33]: V_p of 3.816cc and V_p/V_c of 0.85% in a gasoline PFI engine;
- Gomes [36]: V_p of 1.97cc and V_p/V_c of 0.5% in a gasoline PFI engine;
- Mavinahally et al. [37]: V_p of 1.462cc and V_p/V_c of 0.22% in a gasoline PFI engine;
- Moreira [39]: V_p 3.66cc and V_p/V_c of 0.92% in a gasoline PFI engine;
- Roethlisberger and Favrat [41]: V_p of 4.54cc and V_p/V_c of 0.28% in a natural gas PFI engine.

Chiodi et al. [21] have investigated two stumpy-shape prechambers of 0.15cc and 0.3cc in a 400cc single-cylinder GDI engine, equal to V_p/V_c of 0.0375% and 0.075% respectively. Both prechambers are characterized by eight holes (the authors have not specified the diameter). Comparing the two prechambers, the bigger one has shown first a 5% lower scavenging, in terms of trapped residual gases, thus slightly higher cycle-to-cycle variation and misfiring risk. The flame front inside the bigger prechamber was found to be slower, leading to a reduced mass flow coming out of the prechamber. However, a higher pressure difference between the chambers was observed. The delay between the sparkplug signal and the ignition of the main chamber was found to be almost the same. However, the greater ignition capacity of the bigger prechamber hot jets due to the higher pressure difference, has resulted in a reduction in time of 40% from ignition point to 5% MFB (Mass of Fuel Burnt). In the same manner, the total combustion duration was decreased, increasing the maximum pressure and the indicated mean effective pressure. Authors have noted that the combination of a slower flame front propagation speed with a higher pressure difference increases the amount of unburnt mass ejected (with a high concentration of radicals), which positively affects the TJI combustion inside the main chamber.

In PFI engines, the prechamber volume seems to affect the combustion in the same way as in DI ones. Higher volumes, for a given A_t, have led to greater pressure differences between prechamber and main chamber, which promote the TJI combustion, thus a lower combustion duration [22, 35]. On the contrary, higher volumes, for a given A_t/V_c, have led to lower pressure differences between prechamber and main chamber, slowing down the combustion process [34, 35].

1.2.7 - Overall flow passage area

Gentz et al. [20] have experimentally investigated the prechamber-aided combustion process in a rapid compression machine fueled by hydrogen/air mixture. Experiments aimed at reproducing the PFI engine conditions, thus with the same equivalence ratio both in prechamber and chamber. The prechamber is characterized by V_p of 1cc, equal to V_p/V_c of 0.22%, and one single orifice. Four different orifices have been investigated:

- diameter of 1.0 mm, equal to A_t of 0.79 mm^2 and A_t/V_p of 0.79*10-3 mm^{-1};
- diameter of 1.5 mm, equal to A_t of 1.77 mm^2 and A_t/V_p of 1.77*10-3 mm^{-1};
- diameter of 2.0 mm, equal to A_t of 3.14 mm^2 and A_t/V_p of 3.14*10-3 mm^{-1};
- diameter of 3.0 mm, equal to A_t of 7.07 mm^2 and A_t/V_p of 7.07*10-3 mm^{-1}.

Results have shown that using too small orifices, the hot jet bumps into the piston bowl and the ignition inside the combustion chamber starts from the bottom and then develops to the top. In the main chamber, fuel-lean ignitability difficulties have been found with flow passages too big and too small. With the diameter of 3 mm, it was not possible to operate above λ 1.65 due to a too low jet penetration, while with the diameter of 1 mm, it was not possible to operate over λ 1.25 due to a too high jet velocity which leads to excessive shearing stresses. With diameters of 1.5 mm and 2 mm, the lean ignitability limit has been respectively extended up to λ 1.85 and 1.81. Diameters of 1.5 mm and 2 mm have led to the lowest 0-10% and 10-90% MFB duration when using fuel-lean mixture, more than the 1/3 lower compared to the standard SI engine. Vice versa, when using a stoichiometric mixture, there were no significant differences between the four diameters. Thus, it can be stated that the overall flow passage plays a key role both on the combustion duration and lean flammability limits.

1.2.8 - Number of orifices

Before reporting the studies that deal with the influence of the number of orifices on the combustion, it should be noted that for an equal geometric total flow passage area, an increase in the number of orifices leads to an increase of the overall wetted perimeter, thus to higher pressure losses during compression. That may lead to a lower amount of mixture mass entering the prechamber. Thus, the increase in the number of orifices leads to a reduction in the effective flow passage area. Hence, increasing the number of orifices, a higher pressure difference can be expected between prechamber and main chamber and an increase in the critical area, i.e. the geometric overall flow passage area which separates TJI combustion from TI one.

Roethlisberger and Favrat [34] have experimentally studied the influence of the number of orifices on the combustion process in a lean-burn single-cylinder 1.8 liters PFI engine with a passive prechamber. It is characterized by V_p of 4.54 cc, equal to V_p/V_c of 0.28% and V_p/V_{cc} of 2.99%. Two numbers of orifices are tested, keeping constant A_t of 14.10 mm^2 and A_t/V_p of 3.11*10^{-3} mm^{-1}: four orifices with diameters of 2.12 mm and six orifices with diameters of 1.73 mm. For the same A_t, reducing the number of orifices the combustion process is faster, a higher efficiency is achieved and lower CO and UHC emissions are produced. The variation

in the number of orifices has not influenced significantly the pressure difference between prechamber and chamber.

Gentz et al. [20] have experimentally investigated the prechamber-aided combustion process in a rapid compression machine fueled by hydrogen/air mixture. Experiments aimed at reproducing PFI engine conditions, thus with the same equivalence ratio both in prechamber and chamber. The prechamber is characterized by V_p of 1cc, equal to V_p/V_c of 0.22%. Three different numbers of orifices have been investigated:

- single orifice with diameter of 3 mm, equal to A_t of 7.07 mm^2 and A_t/V_p of 7.07*10-3 mm^{-1};
- two orifices with diameter of 2.165 mm, equal to A_t of 7.36 mm^2 and A_t/V_p of 7.36*10-3 mm^{-1};
- three orifices with diameter of 1.707 mm, equal to A_t of 6.8 mm^2 A_t/V_p of 6.873 mm^{-1}.

During stoichiometric operations, results show lower 0-10% and 10-90% MFB durations when using all the three prechambers compared to the standard combustion. Increasing the air-to-fuel equivalence ratio i.e. moving toward fuel-lean conditions, one- and three- orifices configurations have progressively deteriorated their combustion performances, making the combustion duration worse than standard combustion for λ higher than 1.5. On the contrary, when using the two-orifice prechamber, results have shown much lower 0-10% and 10-90% MFB duration even at very fuel-lean conditions. The higher combustion rate of the two-orifice prechamber has been explained in the more homogenous combustion, which takes place on the whole volume of hot jets. In the two-orifice configuration, the hot jets have lower shear and thermal losses compared to the three-orifice one. In fact, in the three-orifice prechamber, combustion has started first on the central jet head due to the compression carried out by lateral jets. Furthermore, the better distribution of hot jets inside the combustion chamber reduces the interaction with cylinder walls and leads to a much volumetric combustion compared to the single orifice configuration, in which combustion has started on the piston head during the jet impingement and then has propagated toward the cylinder head.

Roethlisberger and Favrat [35] have numerically studied the addition of a coaxial orifice on prechamber filling and combustion process in a single-cylinder PFI engine of 1.8 liters equipped with a passive prechamber, working with premixed slightly lean natural gas/air mixture. The prechamber is characterized by V_p of 4.54cc, equal to V_p/V_c of 0.28% and V_p/V_{cc} of 2.99%. A_t was kept constant and equal to 18.85 mm^2 for A_t/V_p of 4,15*10^{-3} mm^{-1}. Two configurations of orifices have been investigated: six lateral 2 mm diameter orifices and six lateral orifices plus a coaxial orifice, all with a 1.85 mm diameter. For the same overall flow passage area, the addition of a coaxial orifice has resulted in an increase in axial velocity during prechamber filling, which prepares the way for the fresh mixture to reach the sparkplug zone, and a higher turbulence intensity in the spark zone, which improves mixture ignitability. The addition of a coaxial orifice has not significantly influenced on the pressure difference between prechamber and main chamber.

Even if the aforementioned works clearly explain the influence of orifices on the combustion process, it is not possible to establish a general selection criterion, since it depends firstly on the injection system (indirect or direct injection), on the equivalence ratio at which the engine is operated (stoichiometric or lean-burn) and on the prechamber volume. Great results have been obtained both by Moreira [39] using a lengthened-

shape opened-channel prechamber in a slightly fuel-lean PFI gasoline engine and by Chiodi et al. [21] using a stumpy-shape prechamber with eight orifices in a GDI gasoline engine. Surely, when using a GDI engine, the process with which the prechamber is filled with fuel become crucial and the best choice seems to be the adoption of small stumpy-shape multi-orifice prechambers, in such a way as to not let the fuel escape once entered the prechamber. In premixed engines, the design will be based on the achievement of an adequate scavenging process (simpler in stumpy-shape prechambers), and on the achievement of the most effective combustion process, in such a way to improve the leanness of the mixture.

1.2.9 - Inclination of orifices

Adams [36] has investigated two different orientations of hot jets in a passive prechamber with a single opened channel. The author has stated that orienting the prechamber duct toward the exhaust valve leads to a better scavenging of the prechamber, thus a lower cycle-to-cycle variation, and to lower NO_x and UHC emissions. Vice versa, when the duct has been pointed toward the cylinder axis the author has observed a higher in-cylinder pressure, thus a higher engine torque.

Roethlisberger and Favrat [35] have numerically investigated the use of a passive prechamber in a single-cylinder PFI engine of 1.8 liters working with premixed slightly lean natural gas/air mixture. The lengthened-shape prechamber was characterized by V_p of 4.54cc, equal to V_p/V_c of 0.28% and V_p/V_{cc} of 2.99%, and six 2 mm diameter orifices, equal to A_t of 18.85 mm^2 and A_t/V_p of 4.15*10^{-3} mm^{-1}. Three inclinations of orifices towards the cylinder axis have been investigated: 45°, 60° and 75°. The increase in the inclination of orifices has led to the following considerations:

- a higher pressure difference between the two chambers, due to the lower mass flow which passes through orifices;
- a higher turbulence at the orifice outlet;
- a higher dissipation of turbulence in the prechamber bottom zone;
- a higher axial velocity inside the prechamber during compression, which leads to a higher flow field in the sparkplug gap zone.

Varying the orifice inclination has not influenced the equivalence ratio in the sparkplug gap zone during the ignition window, since the increase in the axial velocity balances the lower mass flow. The authors have also numerically examined the use of a 15° swirl angle applied on the prechamber orifices. The resulting swirl motion both inside the prechamber, during the compression phase, and inside the combustion chamber, during the combustion and expansion phases, have led to a higher pressure difference between prechamber and main chamber, thus to a better combustion process. However, it has reduced the quality of the prechamber scavenging process since exhaust gases on the prechamber axis tend to be stagnant, delaying the incoming of fresh mixture in the sparkplug gap zone, thus increasing the probability of misfiring.

1.2.10 - Prechamber position

Ryu and Asanuma [37] have investigated a passive lengthened-shape prechamber of 21cc, equal to V_p/V_c of 7%, in a single-cylinder four-stroke side-vale PFI gasoline engine of 297cc, varying the prechamber position on the cylinder head. The prechamber is connected to the main chamber through a single duct of 17 mm in length. Four different positions towards the cylinder axis have been investigated. Experimental results have shown that using a central prechamber with the duct aligned with the cylinder axis leads to:

- a higher turbulence in the main chamber;
- a higher pressure and temperature peak;
- a lower combustion duration;
- a lower fuel specific consumption;
- an increase of NOx emissions.

2 - CFD modelling for non-reacting flows

Computational Fluid Dynamic codes are based on conservation laws, which can be obtained by considering a given quantity of matter or control mass and its extensive properties, such as mass, momentum and energy. In fluid dynamic, it is more convenient to define a control volume and to study the evolution of the flow that spatial region. The conservation equations required are:

- continuity equation;
- momentum equation;
- energy equation.

This set of equations, when applied to a viscous flow, is known as Navier-Stokes equations. In 3D problems, this is a 5 equations system, since the momentum equation is a vectorial quantity. Furthermore, the equation of the state is required to determine the state of the fluid and to link the thermodynamic variables, pressure, temperature, energy and density.

A conservation equation for a generic scalar quantity ϕ:

$$\frac{\partial}{\partial t}\int_{\Omega} \phi d\Omega = -\oint_{S} \vec{F}\cdot d\vec{S} + \int_{\Omega} \vec{Q}_v d\Omega + \oint_{S} \vec{Q}_s \cdot d\vec{S}$$

where:

- Ω is the control volume domain;
- S is the surface of the volume domain;
- $\vec{F}$ is the flux;
- $\vec{Q}_v$ and $\vec{Q}_S$ are volume and surface source terms respectively.

From this general formulation, the conservation equations for a fluid flow can be derived. Considering ρ as the scalar quantity, the continuity equation can be written:

$$\frac{\partial \rho}{\partial t} + \nabla \cdot (\rho \vec{u}) = 0$$

The momentum equation can be derived from the conservation equation, considering $\phi = \rho\vec{u}$:

$$\frac{\partial (\rho \vec{u})}{\partial t} + \nabla \cdot \left(\rho \vec{u}\vec{u} + p\bar{\bar{\delta}} - \bar{\bar{\tau}}\right) = \rho\overrightarrow{f_e}$$

Where:

- $p\bar{\bar{\delta}}$ is the isotropic pressure component;

- $\bar{\bar{\tau}}$ is the viscous shear stress tensor, representing the internal friction forces of fluid layers against each other; according to the Newton's constitutive law, the shear stress can be written as follows:

$$\overline{\overline{\tau_{ij}}} = \mu\left[\left(\frac{\partial u_j}{\partial x_i} + \frac{\partial u_i}{\partial x_j}\right) - \frac{2}{3}(\nabla \cdot \vec{u})\delta_{ij}\right]$$

To obtain the energy equation, the conserved quantity is the total energy E, defines as the sum of fluid internal energy plus its kinetic energy per unit mass ($E = e + {}^{1}/_{2}\, u^2$):

$$\frac{\partial(\rho E)}{\partial t} + \nabla \cdot (\rho E \vec{u}) = \nabla \cdot (\lambda \nabla T) + \nabla \cdot (\bar{\bar{\sigma}} \cdot \vec{u}) + \rho\overrightarrow{f_e} \cdot \vec{u} + q_H$$

Where:

- λ is the thermal conductivity of the fluid;
- $(\bar{\bar{\sigma}} \cdot \vec{u})$ represents the work done on the fluid by pressure and internal shear stress acting on the control volume;
- $(\rho\overrightarrow{f_e} \cdot \vec{u} + q_H)$ represents the work of the volume forces and heat sources.

These conservation equations are sufficient to study the non-reacting flows. Nevertheless, turbulence must be modelled in order to take into account the effect of turbulent eddies on the fluid motion.

2.1 - Turbulent flows

Turbulence is the natural state of a fluid flow and it occurs when the Reynolds number ($Re = {}^{\rho L}/_{\nu}$) exceeds a critical value: inertia of the flow is higher than viscous forces and flow becomes irregular and chaotic. In such conditions, measurements of flow velocity reveal the appearance of stochastic velocity fluctuations $u_i'(t)$ generated by small vortices. The characteristic size of the smallest vortices strongly depends on the Reynolds number (Figure 2-1) and the phenomenon is intrinsically three-dimensional, since turbulent eddies evolve in all directions. Turbulent flows show some typical features. Turbulent flows contain fluctuations in the dependent-field quantities, such as velocity, pressure and temperature, even when the flow's boundary conditions are steady. Turbulent fluctuations appear to be irregular, chaotic and unpredictable. Turbulence involves a range of eddy sizes, which increase as the Reynolds number increases. Turbulent eddies lead to transfer energy to smaller scales, via nonlinear interactions, until velocity gradients become so large that the energy is dissipated into heat by the action of viscosity and motion of the smallest eddies. Therefore, persistent turbulence requires a continuous supply of energy in order to make up for this energy losses. Furthermore, turbulent flows are characterized by a rapid rate of mixing and diffusion process due to the effect of fluctuations.

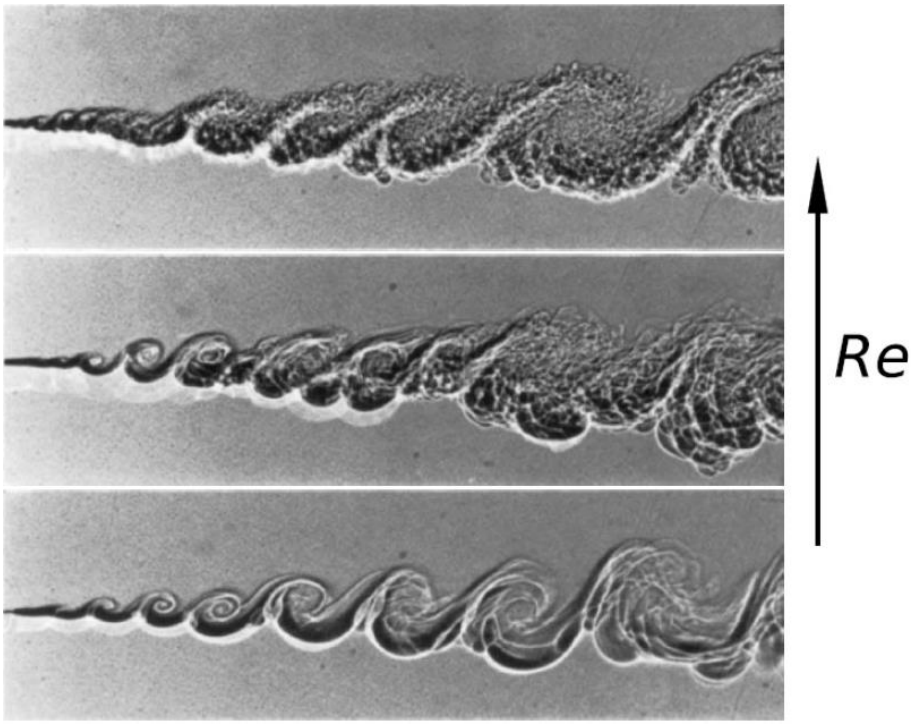

Figure 2-1. Effect of Reynolds number on turbulent structures.

Turbulence can be represented with the so-called Reynolds decomposition:

$$u_i(x,t) = \bar{u}_i(x) + u_i'(x,t)$$

Where $\bar{u}_i$ is the mean value and u_i' is the fluctuating component. In order to predict turbulent flows, both physical and statistical considerations are required. From measurements of $u_i(t)$, its standard deviation $u_{i,rms}$ can be computed, which is related to some important characteristic such as turbulent intensity I:

$$I = \frac{u_{rms}}{\bar{u}} = \frac{\sqrt{u_{x,rms}^2 + u_{y,rms}^2 + u_{z,rms}^2}}{\sqrt{\bar{u}_x^2 + \bar{u}_y^2 + \bar{u}_z^2}}$$

And turbulent kinetic energy (TKE) k, which reflects the level of unsteadiness:

$$k = \frac{1}{2}\left(u_{x,rms}^2 + u_{y,rms}^2 + u_{z,rms}^2\right) = \frac{3}{2}(I\bar{u})^2$$

In a turbulent flow, eddies can be found in a wide range of spatial, temporal and velocity scales. Each one has a specific role in the so-called Energy Cascade process, which explains how the flow dissipates the turbulent kinetic energy (Figure 2-2). Biggest anisotropic scales (energy containing range) introduce the energy in the cascade process whereas the smallest isotropic ones dissipate it (dissipation range). Between these scales, there is the inertial sub-range that transports the turbulent kinetic energy towards the smaller scales. This transfer process occurs because eddies break down and become ever smaller and more isotropic. The energy distribution between eddies of different scales is represented by the energy spectrum $E(\kappa)$:

$$E(\kappa)d\kappa = dk$$

Where $\kappa = {2\pi}/{l}$ is the wave number related to the eddies of size l.

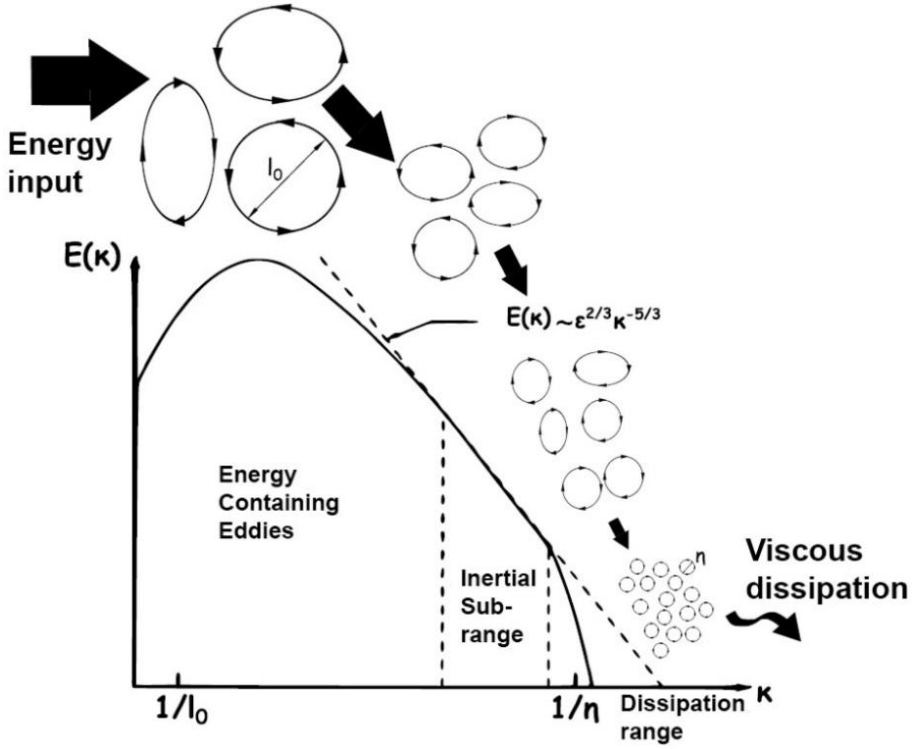

Figure 2-2. Energy cascade process.

The largest eddies have scales called integral scales (l_0, u_0, τ_0) and they are related to the studied problem. The dimension of these scales has the same order of the characteristic scales of the flow: therefore, they are influenced by boundary conditions. As a consequence, the turbulent structures do not show universal features and they represent the main source of energy and anisotropic of the flow. On the other hand, the smallest scales, called Kolmogorov scales (η), are responsible for the dissipation process: thus, viscous forces are comparable to the inertial ones ($Re_\eta = \frac{u_\eta \eta}{\nu} \approx 1$). Since in equilibrium condition the energy transfer equals the energy dissipation, this last term depends only on the integral scales. Through dimensional analysis, it is possible to define the turbulent dissipation rate ε:

$$\varepsilon \approx \frac{u_0^3}{l_0} \approx \frac{u_0^2}{\tau_0}$$

It can be noted that the turbulent dissipation rate is independent from cinematic viscosity. Assuming $k \approx u_0^2$, the turbulent length scale can be written as:

$$l_0 \propto \frac{k^{1.5}}{\varepsilon}$$

The remaining scales can be calculated for high Reynolds flows, considering the three Kolmogorov hypothesis:

- In turbulent flows exist a length scale $l_{E1} \ll l_0$ below which the turbulent scales are statistically isotropic. These are the Kolmogorov scales.
- These isotropic scales and their statistics have universal shape only determined by ν and ε. Thus, by means of dimensional analysis, those quantities can be estimated as:

$$\eta = \left(\frac{\nu^3}{\varepsilon}\right)^{0.25}, u_\eta = (\varepsilon\nu)^{0.25}, \tau_\eta = \left(\frac{\nu}{\varepsilon}\right)^{0.5}$$

- Statistics quantities of intermediate scales l ($\eta \ll l \ll l_0$) have a universal shape which depends only on ε. In this range, for a given length scale l, velocity and time scales are estimated as:

$$u(l) \approx (\varepsilon l)^{1/3} \approx u_0 \left(\frac{l}{l_0}\right)^{1/3}, \tau(l) \approx \left(\frac{l^2}{\varepsilon}\right)^{1/3} \approx \tau_0 \left(\frac{l}{l_0}\right)^{2/3}$$

2.2 - Turbulence modelling

Turbulence modelling is one of the key elements in CFD and a considerable modelling effort is required. There are several methods to obtain a solution of the Navier-Stokes equations [38-41]. These methods differ by which information are solved compared to those which are modelled. Three different levels of approximation for turbulence are available:

- Direct Numerical Simulation (DNS): simulates the whole range of the turbulent fluctuations at all relevant scales. This technique requires a notable computational effort, since to solve even the smallest turbulent velocity fluctuations, the spatial grid needs to be extremely fine and time steps small enough to resolve the fastest perturbations. Thus, this technique can not be used for industrial applications.
- Large Eddy Simulation (LES): it computes directly the turbulent fluctuations in space and time above a certain length scale, below which turbulence is modelled by semi empirical laws.
- Reynolds-averaged Navier-Stokes (RANS) equations: this method involves time averaging of the Navier-Stokes equations. It is so far the most common approach used in CFD applications.

Since the RANS approach was used in this thesis, only this numerical method will be presented in the next paragraph.

2.2.1 - RANS approach

In RANS approach, a time average operation is applied to the Navier-Stokes equations. A generic quantity $\phi(x,t)$ is decomposed as a mean value plus a fluctuating component:

$$\phi(x,t) = \bar{\phi}(x) + \phi'(x,t)$$

Then, the time average operator is applied to the whole system, considering that:

- The average of the mean term is equal to itself:

$$\bar{\bar{\phi}} = \bar{\phi}$$

- The average of the fluctuating term is equal to zero:

$$\overline{\phi'} = 0$$

- The average is a linear operator:

$$\overline{(a + b)} = \bar{a} + \bar{b}$$

By performing this mathematical operation, a new tensor, called Reynolds stress tensor, appears in the non-linear convective term of the momentum equations:

$$\tau'_{ij} = \rho\overline{u'_i u'_j}$$

This tensor represents the turbulence fluctuations effects on the mean flow. Since $\rho\overline{u'_i h'_0} \neq 0$, an additional term compares in the energy equation too. This vector describes the increase in heat flux due to the turbulence. All these terms are unknown and they must be modelled with the turbulence closure problem. Most common turbulence models use the Boussinesq hypothesis, which assumes an analogy between the microscopic behaviour of molecules and the macroscopic behaviour of vortices. Thus, introducing the turbulent viscosity μ_t, the Reynolds stress tensor is modelled as proportional to the gradient of the mean velocity:

$$\tau'_{ij} = \rho\overline{u'_i u'_j} = \mu_t \left(\frac{\partial \overline{u}_i}{\partial x_j} + \frac{\partial \overline{u}_j}{\partial x_i} \right)$$

Turbulent viscosity is not a physical property of the fluid, but it is a result of modelling the effects of turbulence on the mean flow field. Several RANS models are available in literature. The two-equation models represent a good compromise between the computational efforts and accuracy. In these models, the turbulent viscosity is calculated as function of two scalars, that are k and either ε or the specific turbulence dissipation rate $\omega = {\varepsilon}/{k}$. Thus, two transport equations are solved in order to evaluate these scalars.

In this thesis, two different versions of the $k - \varepsilon$ turbulence closure model were adopted: Realizable $k - \varepsilon$ model for flushing simulations and $k - \varepsilon$ RNG for the engine simulations. These models will be presented in next paragraphs.

2.2.2 - The standard $k - \varepsilon$ model

The $k - \varepsilon$ model is a two equations model, in which a transport equation is solved for k and another for ε, in order to evaluate the turbulent viscosity, using the following closure equation:

$$\mu_t = \rho C_\mu \frac{k^2}{\varepsilon}$$

Where C_μ is a dimensionless constant, k is the turbulent kinetic energy and ε is the dissipation rate of turbulent kinetic energy. The transport equations for k and ε are:

$$\frac{\partial \rho k}{\partial t} + \frac{\partial \rho k u_i}{\partial x_i} = \tau_{ij}\frac{\partial u_i}{\partial x_j} + \frac{\partial}{\partial x_j}\left[\left(\frac{\mu + \mu_t}{\sigma_k}\right)\frac{\partial k}{\partial x_j}\right] + P_k - \rho\varepsilon$$

$$\frac{\partial \rho \varepsilon}{\partial t} + \frac{\partial \rho \varepsilon u_i}{\partial x_i} = \frac{\partial}{\partial x_j}\left[\left(\mu + \frac{\mu_t}{\sigma_\varepsilon}\right)\frac{\partial \varepsilon}{\partial x_j}\right] + C_{\varepsilon 1}P_k\frac{\varepsilon}{k} - \rho C_{\varepsilon 2}\frac{\varepsilon^2}{k}$$

Where $\sigma_k, \sigma_\varepsilon, C_{\varepsilon 1}, C_{\varepsilon 2}$ are the model constants and P_k is the production term of turbulent kinetic energy. The typical values of the model constant parameters are summarized in Table 2-1.

Parameter	Value [-]
C_μ	0.09
σ_k	1.00
σ_ε	1.30
$C_{\varepsilon 1}$	1.44
$C_{\varepsilon 2}$	1.92

Table 2-1. Standard $k-\varepsilon$ model constants.

2.2.3 - The Realizable $k-\varepsilon$ model

In some simulations with high strain rate, standard $k-\varepsilon$ model can produce negative values for turbulent kinetic energy. The Realizable $k-\varepsilon$ model ensure the non-negativity of turbulent normal stresses. Thus, the transport equation for turbulence dissipation is derived from an exact equation for the transport of the mean-square vorticity fluctuation, resulting as follows:

$$\frac{\partial \rho \varepsilon}{\partial t} + \frac{\partial \rho \varepsilon u_j}{\partial x_j} = \frac{\partial}{\partial x_j}\left[\left(\mu + \frac{\mu_t}{\sigma_\varepsilon}\right)\frac{\partial \varepsilon}{\partial x_j}\right] + \rho C_1 S\varepsilon - \rho C_2\frac{\varepsilon^2}{k + \sqrt{\upsilon\varepsilon}} + C_{1\varepsilon}\frac{\varepsilon}{k}C_{3\varepsilon}P_b + S_\varepsilon$$

Where:

$$C_1 = \max\left[0.43, \frac{\eta}{\eta + 5}\right]$$

$$\eta = S\frac{k}{\varepsilon}$$

And S is the main strain rate. Furthermore, the model constant C_μ for the Realizable model varies as a function of turbulent kinetic energy, dissipation of turbulent kinetic energy and friction velocity:

$$C_\mu = \frac{1}{A_0 + A_s \frac{kU^*}{\varepsilon}}$$

Where A_0 and A_s are model constants and U^* is the friction velocity.

2.2.4 - The RNG $k-\varepsilon$ model

The RNG $k-\varepsilon$ model was developed by Yakhot et al. [42] to renormalize the Navier-Stokes equations and to take into account for the effects of smaller scales of motion. The turbulent viscosity is calculated in the same manner as with the standard $k-\varepsilon$ model. The transport equation for turbulent kinetic energy is unchanged too. The transport equation for the dissipation of turbulent kinetic energy is given by:

$$\frac{\partial \rho \varepsilon}{\partial t} + \frac{\partial \rho \varepsilon u_i}{\partial x_i} = \frac{\partial}{\partial x_j}\left[\left(\mu + \frac{\mu_t}{\sigma_\varepsilon}\right)\frac{\partial \varepsilon}{\partial x_j}\right] + C_{\varepsilon 1} P_k \frac{\varepsilon}{k} - \rho C_{\varepsilon 2}^* \frac{\varepsilon^2}{k}$$

Where:

$$C_{\varepsilon 2}^* = C_{\varepsilon 2} + \frac{C_\mu \eta^3 \left(1 - {}^{\eta}/_{\eta_0}\right)}{1 + \beta \eta^3}$$

$$\eta = S\frac{k}{\varepsilon}$$

And S is the mean strain rate tensor. Table 2-2 shows the typical values of the model constant parameters.

Parameter	Value [-]
C_μ	0.0845
σ_k	0.7194
σ_ε	0.7194
$C_{\varepsilon 1}$	1.42
$C_{\varepsilon 2}$	1.68
η_0	4.38
β	0.012

Table 2-2. RNG $k-\varepsilon$ model constants.

3 - Combustion

Combustion is a thermo-chemical process in which fuel and oxidizer react to generate heat, which can be converted into power. Combustion also produces pollutants such as oxides of nitrogen (NO_x), soot and unburnt hydrocarbons (HC). This process is affected by several variable:

- reactant's physical properties;
- reactant's chemical properties;
- flow conditions.

The combustion process can be divided in terms of mixing:

- premixed combustion: the mixing between fuel and oxidizer is performed before combustion. This generates a flame front that propagates in a mixture of fresh reactants. This is typical of spark ignition engine;
- non-premixed (or diffusion) combustion: fuel and oxidizer are not mixed before they enter the combustion chamber. Fuel and oxidizer diffuse towards the reaction zone where they burn. A diffusion flame does not exhibit a reference speed because the flame is unable to propagate towards fuel due to the lack of oxidizer. On the contrary, the flame cannot propagate towards the oxidizer due to the lack of fuel.

Furthermore, depending on the flow conditions, two different types of combustion can be observed:

- laminar combustion: flame propagation requires thermal conduction and thermal diffusion of species; this application is almost limited to candles, lighters and domestic furnaces;
- turbulent combustion: turbulent mixing enhances molecular processes; this particular combustion is encountered in most of practical combustion systems, such as internal combustion or aircraft engines.

Turbulence plays a crucial role in combustion process, modifying the flame front, the burning rate and, thus, the heat release and pollutant emissions. Turbulent combustion is a consequence of a two-way interaction between turbulence and chemistry:

- Turbulence is modified by combustion due to the strong accelerations through the flame front induced by heat release;
- Turbulence modifies the flame structure, which can increase the chemical reaction or inhibit it, leading to the flame quenching.

Thus, numerical simulations of turbulent combustion process are difficult to handle and they remain a complex topic. In a SI engine, the combustion process depends on the flow field characteristics at the spark time. Studying the combustion phenomena means studying the equivalence ratio, turbulence intensity, mixing process and mean flow velocity inside the cylinder. Thus, a deep understanding of ignition process

and flame propagation is required. Considering the limitations of currently available experimental techniques, the computational fluid dynamics (CFD) is becoming a very important tool in order to obtain a deep understanding of combustion phenomena. Since the engine studied in this work is a PFI, fuel and oxidizer entering in the cylinder are considered well mixed. Thus, only the premixed combustion flame will be discussed in next chapters. At first, the combustion process in a spark ignition engine is presented. Later, the fundamentals of combustion are discussed, presenting the combustion regimes for premixed flames and the numerical models adopted to simulate the combustion process in this thesis.

3.1 - Spark Ignition (SI) combustion engine

In internal combustion engines, the flow is always turbulent inside the cylinder. In conventional spark ignition engines, fuel and oxidizer are well mixed by turbulence for a sufficiently long period before the spark plug. The electrical energy from ionizes the mixture increasing its temperature. The heat released from spark to the gas allows the chemical reactions to initiate, generating a flame kernel that grows at first by laminar (flame incubation phase) and, after a short time, by turbulent flame propagation (turbulent combustion phase). During the first phase, the combustion process is mainly affected by the physical and chemical properties of the mixture, since the process is just started. The main phase is the second one. A turbulent flame front is established and it propagates through the combustion chamber, leading to a rapid mixture burning. Finally, the flame front reaches the wall of the combustion chamber and stops (burnout phase). The heat released by mixture burning, together with the volume variations caused by piston motion, causes the in-cylinder pressure variations shown in Figure 3-1.

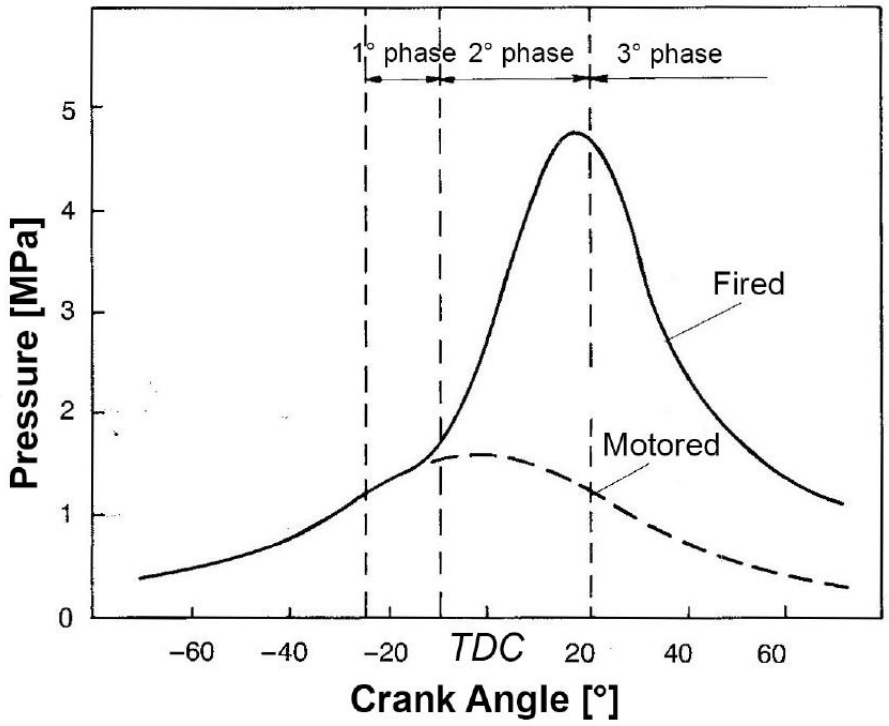

Figure 3-1. Evolution of the in-cylinder pressure in a SI engine during combustion.

3.2 - Governing equations for reacting flows

When the reacting flows are considered, some differences must be taken into account respect to the non-reacting flow [43-46]. A reacting gas is a non-isothermal mixture of multiple species, each with their own thermodynamic properties, which must be tracked individually. Furthermore, heat capacities change significantly since the temperature and composition of the mixture varying during combustion. Moreover, combustion phenomena imply multiple species reacting through multiple chemical reactions. Each species is characterized by their own mass fractions. The mass fraction Y_k of the species k is defined by:

$$Y_k = \frac{m_k}{m}$$

Where m_k is the mass of species k. The mass fractions Y_k of the N reacting species must be considering together with the continuity equation, the momentum equation and the energy equation. Thus, reacting cases require solving for $(N-1)+5$ variables, since the closure for the last reacting species is obtained as the complement to unity of the other species. Total mass conservation equation is unchanged compared to non-reacting case, since combustion does not generate mass:

$$\frac{\partial \rho}{\partial t} + \frac{\partial \rho u_i}{\partial x_i} = 0$$

The mass conservation equation for species k is written as follow:

$$\frac{\partial \rho Y_k}{\partial t} + \frac{\partial}{\partial x_i}\left[\rho\left(u_i + V_{k,i}\right)Y_k\right] = \dot{\omega}_k \, , for \; k = 1, N$$

$V_{k,i}$ is the i-component of the diffusion velocity of species k and $\dot{\omega}_k$ is the reaction rate of species k.

The momentum equation is the same in reacting and non-reacting flows:

$$\frac{\partial \rho u_i}{\partial t} + \frac{\partial \rho u_i u_j}{\partial x_i} = -\frac{\partial p}{\partial x_i} + \frac{\partial \tau_{ij}}{\partial x_i} + \rho \sum_{k=1}^{N} Y_k f_{k,j}$$

Where $f_{k,j}$ is the volume force acting on species k in direction j. Notwithstanding the momentum equations are the same with or without combustion, the flow behaviour is very different. In fact, in reacting flows, temperature varies in a ratio from 1:8 to 1:10, causing strongly variation in density and dynamic viscosity.

Multiple forms exist for the energy conservation equation. Starting from the conservation equation for total energy and introducing the relation between total enthalpy and total energy ($h_t = e_t + {}^{p}/_{\rho}$), the energy conservation equation can be written as follows:

$$\frac{\partial \rho h_t}{\partial t} + \frac{\partial \rho u_i h_t}{\partial x_i} = \frac{\partial p}{\partial t} - \frac{\partial q_i}{\partial t} + \frac{\partial \tau_{ij} u_i}{\partial x_j} + \dot{Q} + \rho \sum_{k=1}^{N} Y_k f_{k,j}\left(u_i + V_{k,i}\right)$$

Where:

- q_i is the energy flux, which consists of heat diffusion term expressed by Fourier's law and a diffusion term related to the diffusion of species with different enthalpies;
- $\dot{Q}$ is a heat source term (for example an electric spark);
- $\rho \sum_{k=1}^{N} Y_k f_{k,j}\left(u_i + V_{k,i}\right)$ is the power produces by volume force f_k on species k.

3.3 - Turbulent premixed flames

In premixed combustion, fuel and oxidizer are mixed before entering in the combustion chamber. Once a heat source is applied, the flame front propagates through the mixture. The most important quantity in premixed combustion is the velocity at which the flame front propagates. This velocity is called the laminar burning velocity and it depends on the fuel-to-air ratio, the temperature of the fresh mixture and pressure. The main effect of turbulence on combustion is to increase the combustion rate. In a turbulent premixed flames, the flame front interacts with turbulent eddies leading to an increase of the mass consumption rate [47-51]. The turbulence effects occur at different scales ranging from the smallest, the Kolmogorov length scale η_k, to the largest one, the integral length scale l_t. In order to evaluate which turbulent eddies are the most relevant in controlling the flame structure, some parameters must be introduced. The Damköhler number compares the integral time scale τ_t, which depends on the turbulent flow field, and a chemical time scale τ_c, which depends on the flame type:

$$Da = \frac{\tau_t}{\tau_c}$$

For a premixed flame, τ_c corresponds to the time required by the flame front to propagate over a distance δ_l and it can be defined as follow:

$$\tau_c = \frac{\delta_l}{s_l}$$

Where δ_l is the flame front thickness and s_l is the velocity of the flame front. Thus, it can be written:

$$Da = \frac{{l_t}/{u'}}{{\delta_l}/{s_l}}$$

The Karlovitz number compares the chemical time scale and the Kolmogorov time:

$$Ka = \frac{\tau_c}{\tau_k} = \frac{{\delta_l}/{s_l}}{{\eta_k}/{u'(\eta_k)}}$$

The turbulence Reynolds number based on the integral length scale is defined as:

$$Re_t = \frac{u' l_t}{\nu} = \frac{u' l_t}{s_l \delta_l}$$

Thus, the following relationship can be written:

$$Re_t = Da^2 Ka^2$$

Different extreme cases can be introduced:

- for large values of Damköhler number ($Da \gg 1$), the integral time scale is greater than chemical time scale; the turbulent mixing is slower than chemical reactions and the length scales of turbulent eddies are greater than the flame front thickness; as a consequence, turbulence generates a wrinkled flame, which maintains a laminar structure;
- for small values of Damköhler number ($Da \ll 1$), the integral time scale is shorter than the chemical time scale; this is the so-called "Perfectly Stirred Reactor" (PSR), in which reactants and products are mixed in a time shorter than the chemical time; turbulent eddies are smaller than the flame front thickness, causing a thickening of the flame front.

All the turbulent premixed flame regimes can be represented in the Borghi-Peters diagram. Figure 3-2 reports the modified combustion regimes proposed by Peters, for turbulent premixed flame. When $Ka < 1$ (flamelet regime), turbulent time scales are greater than chemical time scale, the flame front is thin and there is a clear separation between fresh and burnt gases. Internal combustion engines typically works with Ka close to unity. When $1 < Ka < 100$ (thickened-wrinkled flame), the turbulent eddies are able to modify the flame structure, since their length scales are similar to the flame front thickness. When $Ka > 100$, the

characteristic time scales are smaller than the chemical reaction times. Here, laminar structures can no longer be observed.

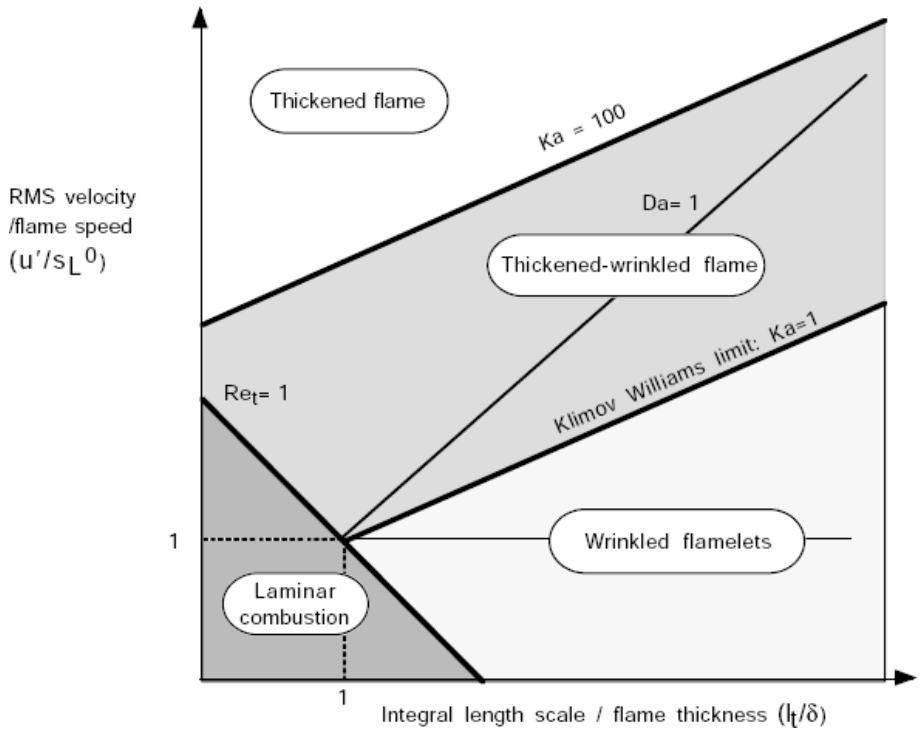

Figure 3-2. Modified combustion diagram proposed by Peters: combustion regimes are identified in terms of length and velocity ratios (log-log scale).

3.4 - RANS approach for turbulent premixed flames

Starting from balance equations for mass, species, momentum and enthalpy, balance equations for the mean quantities in RANS approach can be obtained:

$$\frac{\partial \rho}{\partial t} + \frac{\partial (\rho u_i)}{\partial x_i} = 0$$

$$\frac{\partial (\rho Y_k)}{\partial t} + \frac{\partial (\rho u_i Y_k)}{\partial x_i} = -\frac{\partial \left(V_{k,i} Y_k\right)}{\partial x_i} + \dot{\omega}_k$$

$$\frac{\partial \rho u_i}{\partial t} + \frac{\partial \left(\rho u_i u_j\right)}{\partial x_i} = -\frac{\partial p}{\partial x_j} + \frac{\partial \tau_{ij}}{\partial x_i}$$

$$\frac{\partial (\rho h_s)}{\partial t} + \frac{\partial (\rho u_i h_s)}{\partial x_i} = \dot{\omega}_T + \frac{Dp}{Dt} + \frac{\partial}{\partial x_i}\left(\lambda \frac{\partial T}{\partial x_i}\right) - \frac{\partial}{\partial x_i}\left(\rho \sum_{k=1}^{N} V_{k,i} Y_k h_{s,k}\right) + \tau_{ij} \frac{\partial u_i}{\partial x_j}$$

Averaging the instantaneous balance equations introduces unclosed quantities that have to be modelled. Splitting the quantity f into mean and fluctuating components and applying the Reynolds average, the balance equations become:

$$\frac{\partial \bar{\rho}}{\partial t} + \frac{\partial (\bar{\rho}\widetilde{u_\iota})}{\partial x_i} = 0$$

$$\frac{\partial (\bar{\rho}\widetilde{Y_k})}{\partial t} + \frac{\partial (\bar{\rho}\widetilde{u_\iota}\widetilde{Y_k})}{\partial x_i} = -\frac{\partial (\overline{V_{k,\iota} Y_k} + \bar{\rho}\widetilde{u_\iota'' Y_k''})}{\partial x_i} + \overline{\dot{\omega}_k}$$

$$\frac{\partial \bar{\rho}\widetilde{u_\iota}}{\partial t} + \frac{\partial (\bar{\rho}\widetilde{u_\iota}\widetilde{u_\jmath})}{\partial x_i} = -\frac{\partial \bar{p}}{\partial x_j} + \frac{\partial (\overline{\tau_{\iota\jmath}} - \bar{\rho}\widetilde{u_\iota'' u_\jmath''})}{\partial x_i}$$

$$\frac{\partial (\bar{\rho}\widetilde{h_s})}{\partial t} + \frac{\partial (\bar{\rho}\widetilde{u_\iota}\widetilde{h_s})}{\partial x_i} = \overline{\dot{\omega}_T} + \frac{D\bar{p}}{Dt} + \frac{\partial}{\partial x_i}\left(\overline{\lambda \frac{\partial T}{\partial x_\iota}} - \bar{\rho}\widetilde{u_\iota'' h_s''}\right) - \frac{\partial}{\partial x_i}\left(\overline{\rho \sum_{k=1}^{N} V_{k,\iota} Y_k h_{s,k}}\right) + \overline{\tau_{\iota\jmath} \frac{\partial u_\iota}{\partial x_\jmath}}$$

Where:

$$\frac{D\bar{p}}{Dt} = \frac{\partial \bar{p}}{\partial t} + \widetilde{u_\iota}\frac{\partial \bar{p}}{\partial x_i} + \overline{u_\iota'' \frac{\partial p}{\partial x_\iota}}$$

From averaging operations, some unclosed terms arise:

- Reynolds stresses ($\bar{\rho}\widetilde{u_\iota'' u_\jmath''}$): these terms are closed by a turbulence model;
- Species turbulent flux ($\bar{\rho}\widetilde{u_\iota'' Y_k''}$): these terms are generally closed using the gradient assumption, so the species turbulent flux is proportional to the gradient of itself:

$$\bar{\rho}\widetilde{u_\iota'' Y_k''} = -\frac{\mu_t}{Sc_{kt}}\frac{\partial \widetilde{Y_k}}{\partial x_i}$$

  Where μ_t is the turbulent viscosity and Sc_{kt} is the turbulent Schmidt number for species k;

- Enthalpy turbulent fluxes ($\bar{\rho}\widetilde{u_\iota'' h_s''}$): these terms are closed using the gradient assumption; in turbulent premixed flames, this assumption may lead to some inconsistency, depending on turbulence levels. For low turbulence levels, the flow field is strongly affected by the acceleration of the flame front, which is able to impose its own dynamic on the flow field. In this case, the turbulent transport may become counter-gradient:

$$\frac{\overline{\rho u_\iota'' h_s''}}{\left(\partial \widetilde{h_s} / \partial x_i\right)} > 0$$

  The counter-gradient diffusion condition does not occur in non-premixed turbulent flames. In fact, non-premixed flame does not propagate through the fresh mixture, thus, the flow field near the flame is dominated by the turbulent motions;

- Species chemical mean reaction rates ($\overline{\dot{\omega}_k}$). This term is the main focus of combustion modelling.

Two different combustion models are used in this thesis. Since it is crucial to take into account the chemical effects in prechamber applications, a detailed chemistry model (SAGE combustion model) is used to analyse

the combustion process of the engine, in both baseline and prechamber configurations. In fact, in an engine equipped with a prechamber, the combustion is activated by the spark plug inside the prechamber. The flame kernel grows and the flame front enters the cylinder through the orifices. Since the flame passage through the orifices is a hard topic in which there is a two-way coupling between turbulent structures and chemical reactions, a detailed chemistry solver is necessary in order to evaluate properly the evolution of the flame front and the main benefits and drawbacks that occur with prechamber. The high fidelity details of the CFD simulations using a detailed chemistry solver is paid with a higher computational effort. In order to verify the capability of a simplified approach in CFD combustion modelling, a simplified model based on the progress variable and the flame surface density (ECFM-3Z combustion model) is also used to perform the combustion process of the engine, in the baseline configuration and with the prechamber. Since this model does not use a reaction mechanism and since the reaction rate is modelled through semi-empirical correlations, the simplified combustion model may not be able to model the flame propagation properly, and may not be able to capture the behaviour of the flame front inside the narrows passages. The aforementioned models used in this thesis will be presented in the next paragraphs.

3.4.1 - SAGE combustion model

Combustion is one of the most important process in internal combustion engines. During this process turbulence, heat transfer and chemical process interact with each other. Thus, it is fundamental to be able to predict the flow field inside the cylinder, the pressure and temperature fields, the species concentrations and pollutant emissions, in order to improve the combustion process and give suggestions at the design stage. It is essentials to predict the chemical processes during combustion since chemical reaction rates control the ignition flame, the heat release, pollutant formations and flame extinction. The SAGE model is a detailed chemistry combustion model available in CONVERGE CFD [52, 53]. It is the most predictive way to model the combustion process. Since this model takes into account the different species that participate to the mixture oxidation, it can be applied to premixed flames, non-premixed flames and fuel blend composition. In this model, the local values of pressure, temperature and mixture composition are used to compute the reaction rates of the chemical kinetics. Considering the oxidation of a generic fuel F with an oxidizing O, which form the combustion products P:

$$F + O \rightarrow P$$

The rate at which the fuel is consumed can be defined by considering the rate variation in its molar concentration in time:

$$\omega_f = \frac{d[X_f]}{dt} = k(T)[X_f]^n [X_o]^m$$

Where the exponents m and n define the order of the reaction and can be determined experimentally. The constant $k(T)$ is the global rate constant; it is typical of the reaction and, according to the Arrhenius law, it strongly depends on temperature:

$$k(T) = Ae^{-E_a/RT}$$

Where A is pre-exponential factor and E_a is the activation energy. Actually, the fuel oxidation takes place in more steps, i.e. in more elementary reactions, which involve radicals and intermediate species highly reactive. A chemical reaction mechanism is a set of elementary reactions that describe the overall chemical reaction. A multi-step chemical reaction mechanism can be written as follows:

$$\sum_{m=1}^{M} \nu'_{m,i}\chi_m \leftrightharpoons \sum_{m=1}^{M} \nu''_{m,i}\chi_m \ for\ i = 1, \dots, N$$

Where $\nu'_{m,i}$ and $\nu''_{m,i}$ are the stoichiometric coefficients for the reactants and products respectively, for species m and reaction i and M and N are the total number of species and reactions respectively; χ_m is the chemical symbol for species m. The net production rate of species m can be written in the following form:

$$\dot{\omega}_m = \sum_{m=1}^{M} \nu_{m,i} q_i$$

Where:

$$\nu_{m,i} = \nu''_{m,i} - \nu'_{m,i}$$

And q_i is the rate-progress parameter of the i^{th} reaction:

$$q_i = k_{f,i} \prod_{m=1}^{M} [X_m]^{\nu'_{m,i}} - k_{r,i} \prod_{m=1}^{M} [X_m]^{\nu''_{m,i}}$$

Where $[X_m]$ is the molar concentration of species m, and $k_{f,i}$ and $k_{r,i}$ are the forward and reverse rate coefficients for the reaction i. The forward rate coefficient is expressed by the Arrhenius form:

$$k_{f,i} = A_i T^{\beta_i} e^{-E_{a,i}/RT}$$

The reverse rate coefficient is computed from the equilibrium $K_{c,i}$, which is determined from thermodynamic properties:

$$K_{c,i} = K_{p,i} \left(\frac{p_{atm}}{RT}\right)^{\sum_{m=1}^{M} \upsilon_{m,i}}$$

$$K_{p,i} = e^{\left(\frac{\Delta S_i^0}{R} - \frac{\Delta H_i^0}{RT}\right)}$$

Where p_{atm} is the atmospheric pressure and S and H are entropy and enthalpy respectively. Δ refers to a change that occurs in passing completely from reactants to products in the i^{th} reaction:

$$\frac{\Delta S_i^0}{R} = \sum_{j}^{N} \nu_{ji} \frac{S_j^0}{R}$$

$$\frac{\Delta H_i^0}{RT} = \sum_j^N \nu_{ji} \frac{H_j^0}{RT}$$

Thus, the governing equations for mass and energy can be solved for each computational cell. The governing equation for mass results:

$$\frac{d[X_m]}{dt} = \dot{\omega}_m$$

And the governing equation for energy results:

$$\frac{dT}{dt} = \frac{V\frac{dp}{dt} - \sum_m^M(\bar{h}_m\dot{\omega}_m)}{\sum_m^M([X_m]\bar{c}_{pm})}$$

For a constant-volume combustion, while:

$$\frac{dT}{dt} = \frac{\left(\frac{\dot{Q}}{V}\right) - \sum_m^M(\bar{h}_m\dot{\omega}_m)}{\sum_m^M([X_m]\bar{c}_{pm})}$$

For a constant-pressure combustion, where $\dot{Q}$ is the heat release rate and $\bar{h}_m$ and $\bar{c}_{pm}$ are the molar specific enthalpy and the molar constant-pressure specific heat of species m, respectively. The above equations are solved for each computational cells in the domain, at each computational time-step. It is worth noting that temperature computed from the above equations is used only to update the rate coefficients, while the temperature cell is updated after the detailed chemistry calculation has converged using the computed species. In order to use the SAGE combustion model, a reaction mechanism file, a species-specific thermodynamic properties file and a molecular transport properties file are required. The mechanism used in this thesis for combustion modelling with SAGE consists of 41 species and 124 reactions. It is a skeletal kinetic mechanism for iso-octane oxidation developed for HCCI combustion [61].

3.4.2 - ECFM-3Z combustion model

The 3-Zones Extended Coherent Flame Model (ECFM-3Z) is a combustion model for both premixed and non-premixed flames [55]. This is a simplified model, since the mean chemical source term is evaluated as function of two typical parameters of turbulent combustion: the progress variable and the flame surface density, which are computed using two different transport equations. The state of the mixture in the combustion chamber is represented by two variables:

- the progress variable c, which identified the fresh gas ($c = 0$) or fully burnt gas ($c = 1$);
- the mixture fraction z, which measure the local fuel/oxidizer ratio.

In this model, each computational cells of the domain is divided into three different regions (Figure 3-3):

- the unmixed fuel zone (zone F);
- the mixed zone, containing fuel (zone M);
- the unmixed air plus possible residual gases (EGR) zone (zone A).

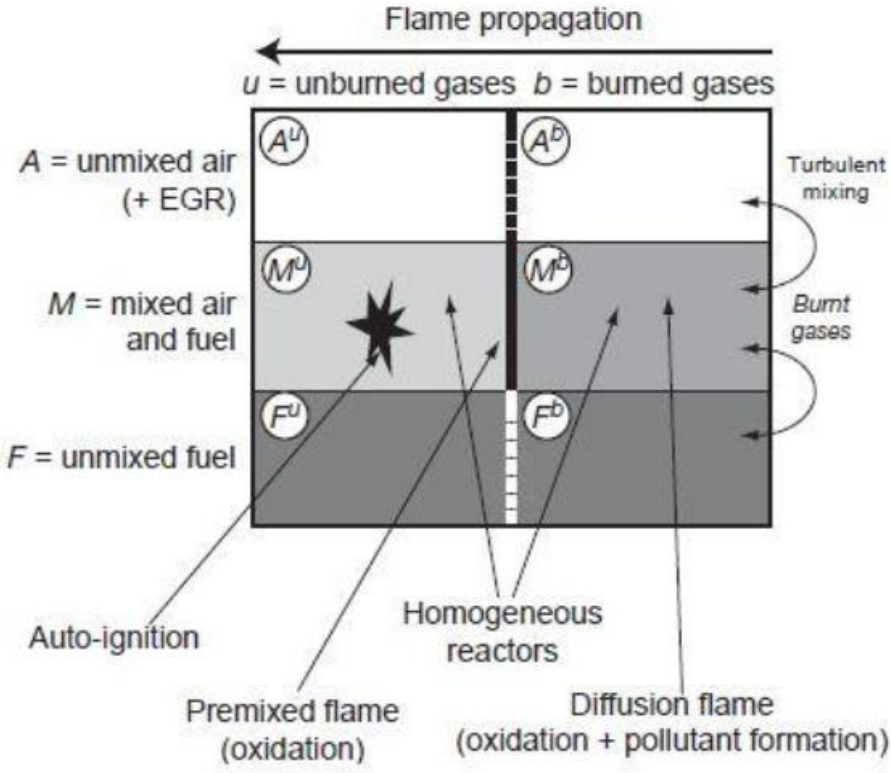

Figure 3-3. Schematic of the ECFM-3Z model computational cell.

Since the combustion process can not take place in regions A and F, it is only considered possible in region M. Therefore, the combustion process is modelled in this zone considering a transport equation for the progress variable, according to the ECFM model. Only two different states for gases are considered, the unburnt gas ($c = 0$) and the burnt gas zone ($c = 1$), depending on the value of the progress variable:

$$c = 1 - \frac{Y_{f,u}}{Y_{T,u}}$$

Where:

- $Y_{f,u}$ is the fuel mass fraction present in the unburnt gas;
- $Y_{T,u}$ is the fuel mass fraction before the combustion occurs.

The progress variable is evaluated using a transport equation that can be expressed, after the Reynolds averaging, as follows:

$$\frac{\partial \bar{\rho}\tilde{c}}{\partial t} + \frac{\partial (\bar{\rho}\tilde{u}_i\tilde{c})}{\partial x_i} = -\frac{\partial \left(\bar{\rho}\widetilde{u_i''c''}\right)}{\partial x_i} + \widetilde{\Omega}_c$$

Where $\widetilde{\Omega}_c$ is the source term that needs to be closed. In this model, this term is expressed as a function of the flame surface density Σ, which measures the flame front convolutions:

$$\widetilde{\Omega}_c = \bar{\rho}_u \omega_l \Sigma$$

Where $\bar{\rho}_u$ is the unburnt density mixture and ω_l is the laminar velocity of the flame front. The flame surface density Σ is then evaluated using a transport equation:

$$\frac{\partial \Sigma}{\partial t} + \nabla \cdot (\vec{u}\Sigma) - \nabla \cdot \left[\left(D + \frac{\mu_t}{Sc_t}\right)\nabla\left(\frac{\Sigma}{\rho}\right)\right] = \Sigma\left[C_{divu}\frac{2}{3}\nabla \cdot \vec{u} + C\alpha\Gamma\frac{\varepsilon}{k} + C\frac{2}{3}\frac{\rho_u}{\rho_b}U_l\Sigma\frac{1-c}{c} - \beta\omega_l\frac{\Sigma}{1-\bar{c}} - \frac{2}{3}\frac{1}{(\gamma p)}\frac{\partial p}{\partial t}\right] + S_{conv}$$

Where:

- D is the molecular diffusivity;
- ρ_b, ρ_u are the density of burnt gases and unburnt gases respectively;
- C, C_{divu} are empirical constant to take into account the interaction between flame and wall;
- γ is the ratio between the specific heat at constant pressure and constant volume;
- μ_t, Sc_t are the turbulent viscosity and turbulent Schmidt number respectively;
- p is the pressure field;
- $\bar{c}$ is the mean progress variable;
- α, β are empirical coefficients for production and consumption of the flame surface due to its interaction with turbulent eddies;
- ω_l is the laminar flame speed.

In this model, the laminar flame speed is calculated based on the theoretical laminar flame speed, which depends on pressure, temperature and mixture composition, multiplied by a corrective factor to take into account the heat loss through the walls.

4 - Numerical setup

The numerical setup of CFD simulations is described in this chapter. At first, the engine is presented, together with the CAD model and the fluid domain. Later, the numerical setup will be presented. In this chapter, the following activities will be presented: at first, the test case is presented; later the flushing simulations results are shown, with the boundary conditions extracted from the 1D model, and eventually, the numerical set-up of the combustion models for the baseline configuration are presented, together with the comparison CFD results against the experimental data. As explained in previous chapter, two different combustion models are used in this thesis. Since the goal of this work is to evaluate and analyse the performance of a 4-stroke engine with prechamber, a detailed chemistry solver is necessary in order to give an in-depth analysis of the phenomena. The combustion process involves several topics, from the aerodynamics up to chemical aspects, passing through the turbulent flow. These features are all coupled with each other: the flow field can affect combustion stretching and corrugating the flame front; turbulence can affect the combustion process enhancing the mixing between species or extinguishing the reactions; combustion can generate and modify the flow field due to the high temperature gradient across the flame front. Therefore, the use of simplified approaches may neglect some features, leading to erroneous conclusions. For this reason, the detailed chemistry solver is deemed to be more suitable for investigating the behaviour of the flame front during the ignition phase inside the prechamber, of the propagation through the orifices and of the flame jets affecting the combustion process inside the main chamber. The combustion model based on chemical reactions (SAGE model) was first calibrated with experimental data on the baseline engine at maximum power, and the numerical set-up was then validated at a different rotational speed. In order to verify the limits of using a simplified approach, the ECFM-3Z combustion model was also tuned against the experimental results at maximum power. Then, both calibrated models will be used to perform predictive simulations of the engine equipped with the prechamber, as will be shown in in chapter 5.

4.1 - Test case

The engine studied in this thesis is manufactured by Betamotor S.p.A. It is a 4-stroke engine for motorcycle application. It is a single cylinder engine, with four valves (two intake valves and two exhaust valves). The main engine data are summarized in table 4.1.

Engine	4-stroke
Fuel supply	Port Fuel Injection (PFI)
Fuel type	Gasoline
Number of valves	4
Displacement	430.90 cm^3
Bore	95 mm
Stroke	60.80 mm

Compression ratio	12.33 : 1

Table 4-1 Specifications of studied engine.

The calibration of the numerical setup and the analysis of the combustion process are performed for the maximum power speed at full load, since it is a critical operation point for the engine performance due to the high rotational speed. Figure 4.1 shows the 3D CAD model of the engine.

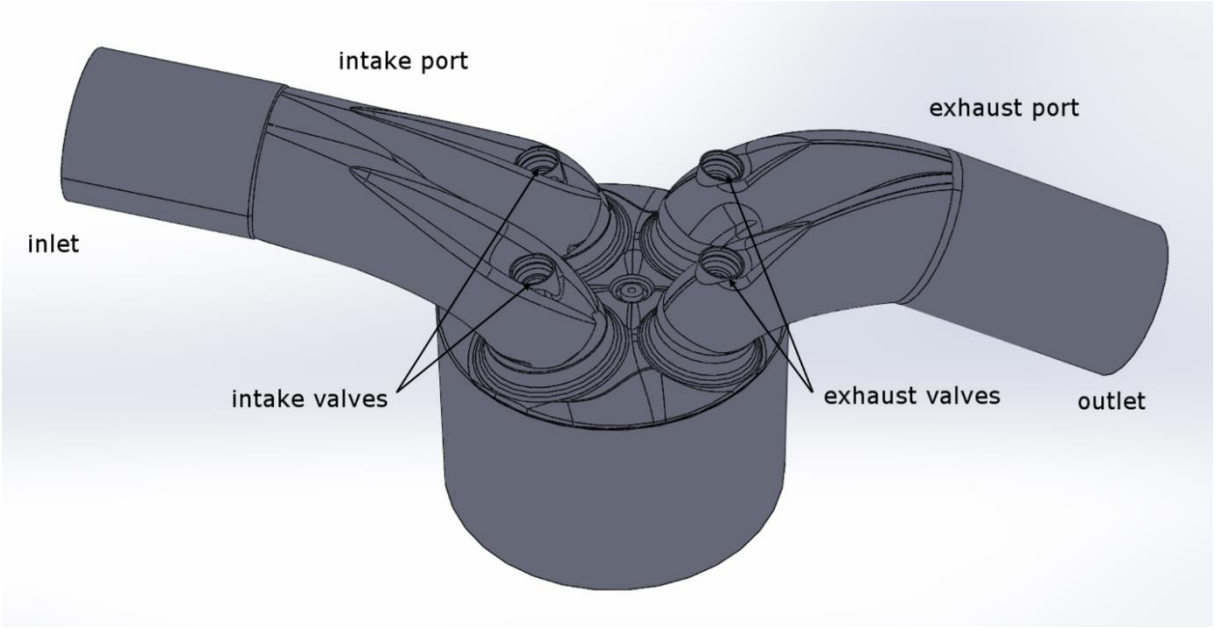

Figure 4-1. 3D CAD model of the studied engine.

4.2 - Flushing simulations

The flushing simulations for intake and exhaust valves are carry out for validating the numerical setup in steady conditions against the experimental data. A commercial solver is used for flushing simulation, with a RANS approach with Realizable k-ε model for turbulence modelling. Figure 4-2 shows the valve lift for both intake and exhaust valves. The lift values are scaled respect to the maximum lift.

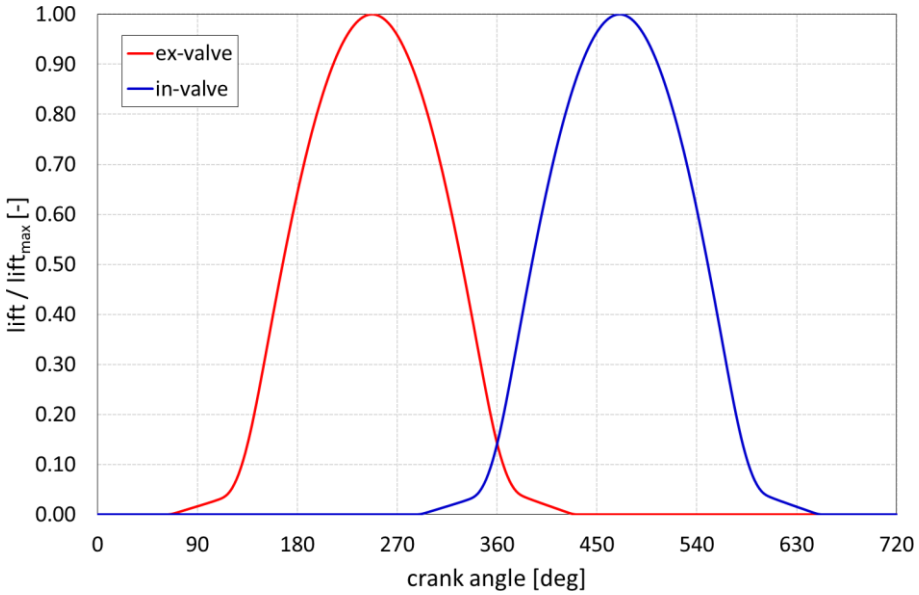

Figure 4-2. Valves lift.

The fluid domain of the engine is modified in order to model the plenum. In particular, a hemisphere was adding at the inlet and a cylindrical control volume is added at the outlet for intake valves (Figure 4-3), while a hemisphere is appended at the end of the intake port for the exhaust valves simulations. The liner of the cylinder engine is extended in both flushing valves (Figure 4-4).

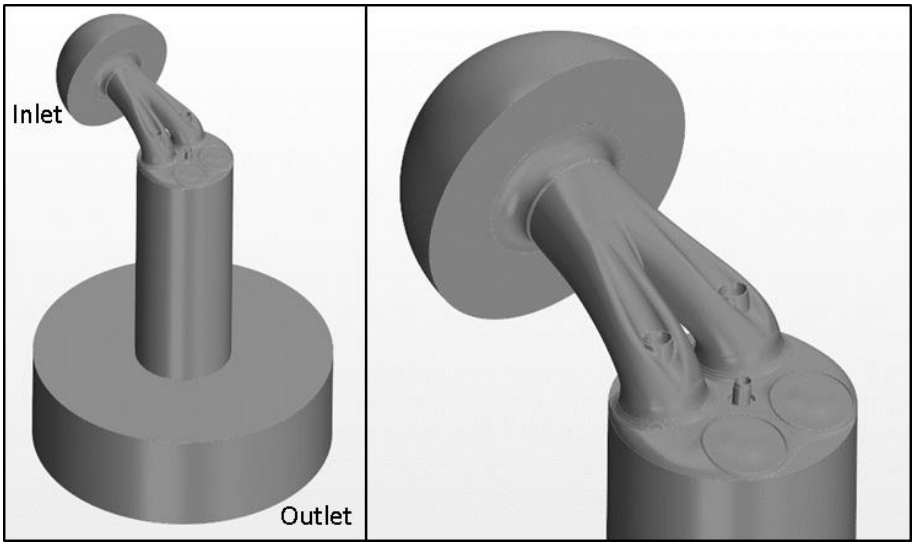

Figure 4-3. Fluid domain for intake flushing simulation.

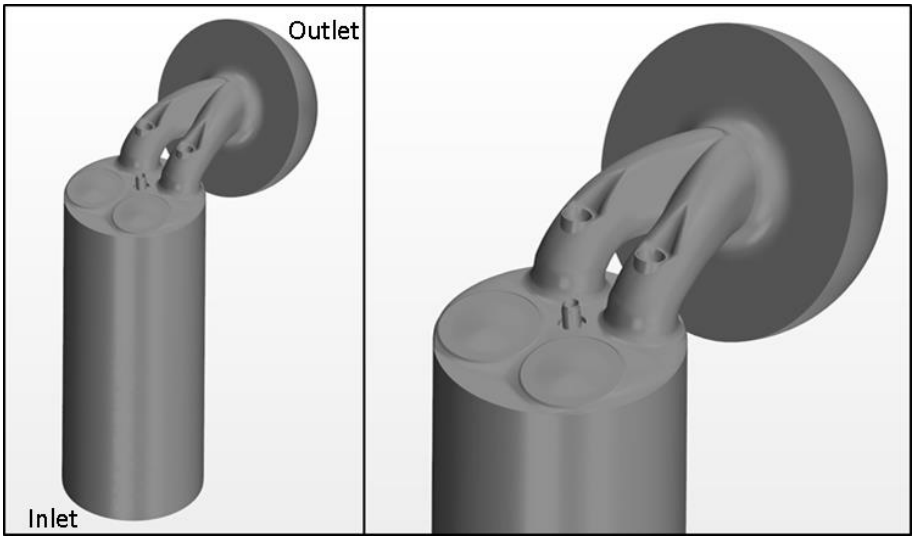

Figure 4-4. Fluid domain for exhaust flushing simulation.

The mesh for flushing simulations is generated automatically generated by the solver. It is a non-structured mesh, with a base grid size of 5 mm for both intake and exhaust simulations. In order to resolve properly the flow field through the valves, a mesh refinement up to 2 mm is used inside the ports, head and cylinder, while a refinement up to 0.5 mm is used in the valves seat zones (Figure 4-5 a and Figure 4-6 a). Since the discharge coefficient may be affected by shear wall stresses, 10 prismatic layers are added near the wall. The first layer height is 0.015 mm for intake valves simulation (Figure 4-5 b) and 0.010 mm for exhaust valves simulation (Figure 4-6 b). The growth rate of prismatic layer is set to 1.3 for both flushing simulations.

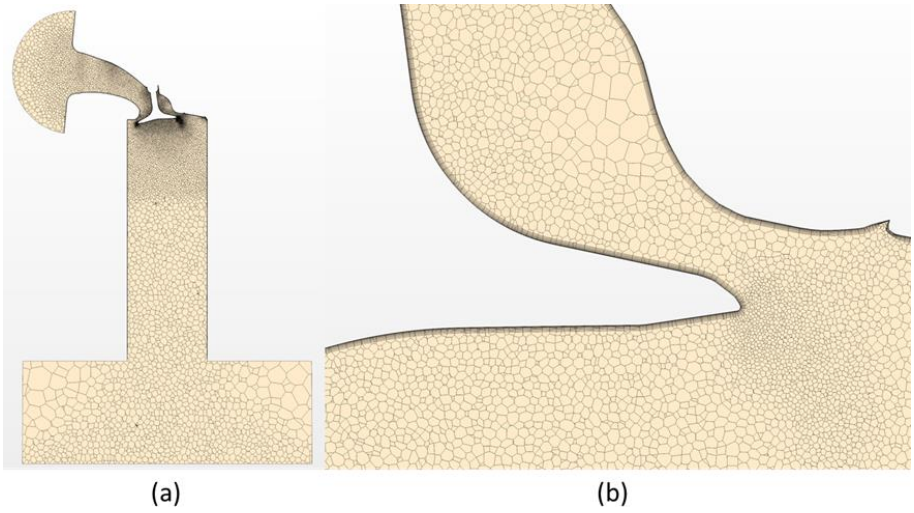

Figure 4-5. Mesh used during intake flushing.

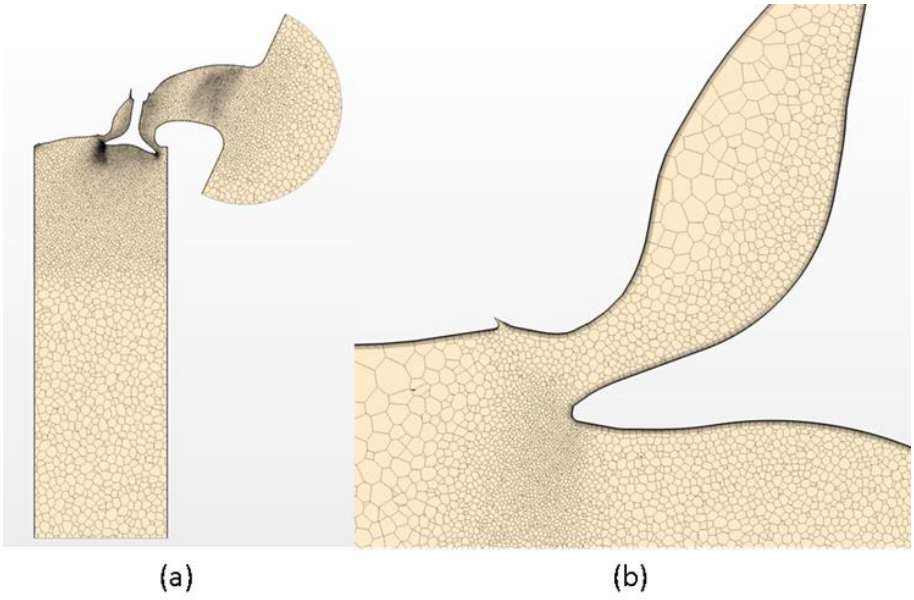

Figure 4-6. Mesh used during exhaust flushing.

Table 4-2 summarizes the number of elements of the mesh during the flushing simulations.

Lift / $Lift_{max}$ [-]	Number of elements – intake flushing	Number of elements – exhaust flushing
0.05	2736402	2453254
0.10	2534584	2336926
0.20	2600340	2422925
0.30	2747301	2544096
0.40	2886835	2659052
0.50	3048811	2787463
0.60	3313164	2993084
0.70	3797535	3139588

0.80	3954148	3855505
0.90	4102395	4007781
1.00	4160454	4172852

Table 4-2. Number of elements during flushing simulations.

Table 4-3 reports the boundary conditions used during the simulations.

	Intake flushing	Exhaust flushing
$\lvert\Delta P_{inlet/outlet}\rvert$ [Pa]	15000	55000
Fluid temperature [K]	300	300
Wall temperature	Adiabatic condition	Adiabatic condition

Table 4-3. Boundary conditions for flushing simulations.

Air is set as fluid with ideal gas assumption. Table 4-4 summarizes the air properties used for flushing simulations.

Dynamic viscosity [Pa*s]	$1.85508*10^{-5}$
Molecular weight [kg/kmol]	28.9664
Specific heat [J/kg/K]	1003.62
Thermal conductivity [W/m/K]	0.0260305
Turbulent Prandtl [-]	0.9

Table 4-4. Fluid properties for flushing simulations.

A constant reference area was used for each lift position of the valve, considering the minimum diameter of the valve seat. Figure 4-7 and Figure 4-8 report the comparison of the flow coefficient between CFD and experimental results. It can be noted that a good agreement is obtained for both flushing valves, especially for exhaust valves. The main differences are notable in the intake valves results. In fact, the intake port is not symmetric and this geometrical feature creates a flow field and turbulent eddies hard to reproduce via CFD. Nevertheless, the CFD flow coefficients are in accord with the experimental ones and a good agreement is achieved during the steady state simulations. Thus, the experimental flow coefficients are used for developing the 1D model. The 1D model is then calibrated against the experimental results of the manufacturer.

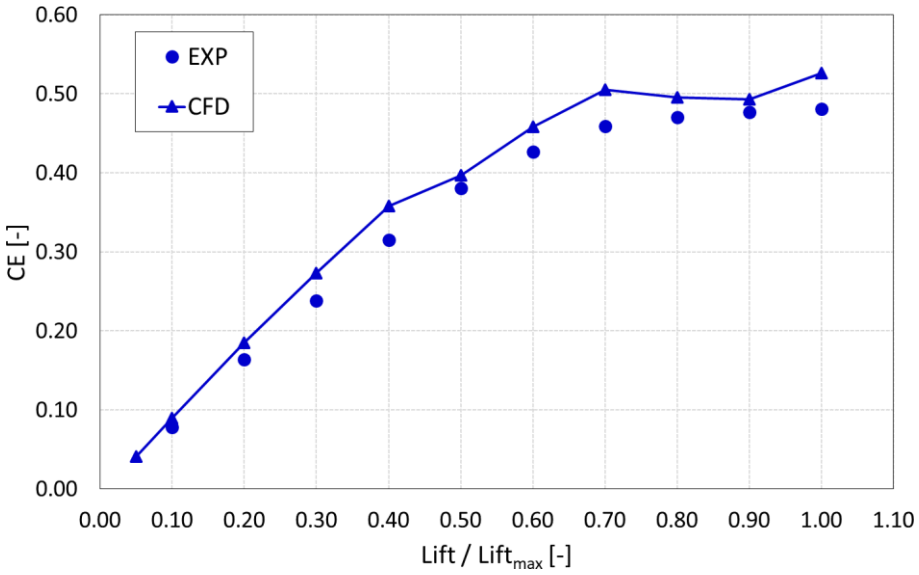

Figure 4-7. Flow coefficient of intake valves.

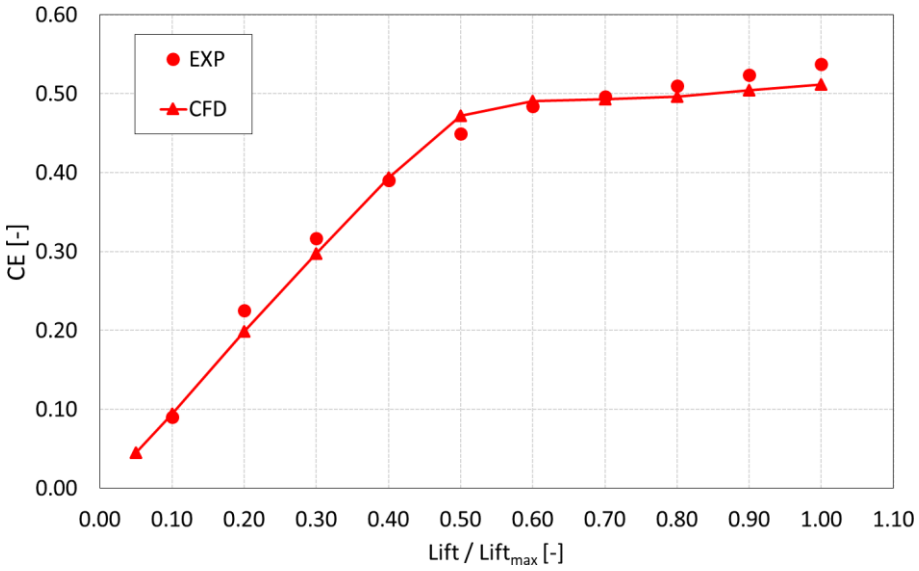

Figure 4-8. Flow coefficient of exhaust valves.

4.3 - Boundary conditions

As explained before, the experimental flow coefficients are used for developing the 1D model in GT-POWER. The 1D model is necessary in order to extract the boundary conditions for running the 3D CFD simulations. The boundary conditions are the set of constraints to boundary value problems in computational fluid dynamics. They include inlet and outlet boundary conditions for pressure, temperature and species, and wall boundary conditions for temperatures of solid parts. The boundary conditions are set according to the 1D model built in GT-POWER. The 1D model is tuned with the experimental data. Figure 4-9 shows the comparison of the in-cylinder pressure between the GT-POWER model and the experimental results for the

revolution at maximum power. It can be noted that a very good agreement is achieved in terms of cylinder pressure.

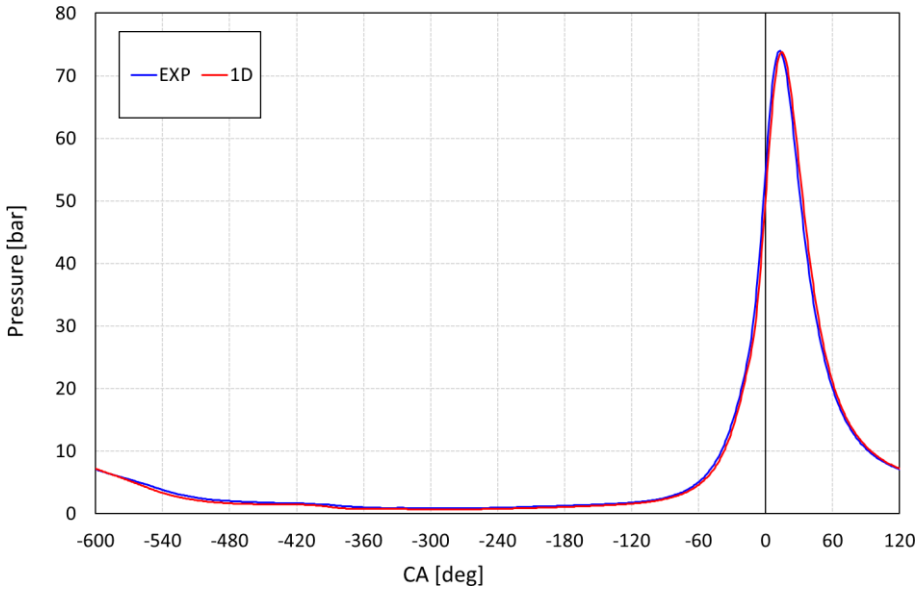

Figure 4-9. Comparison of in-cylinder pressure between experimental results (blue line) and 1D model results (red line) at maximum power.

Figure 4-10, Figure 4-11 and Figure 4-12 report pressure and temperature at inlet and outlet extracted from the 1D solver and used for setting the 3D CFD simulations.

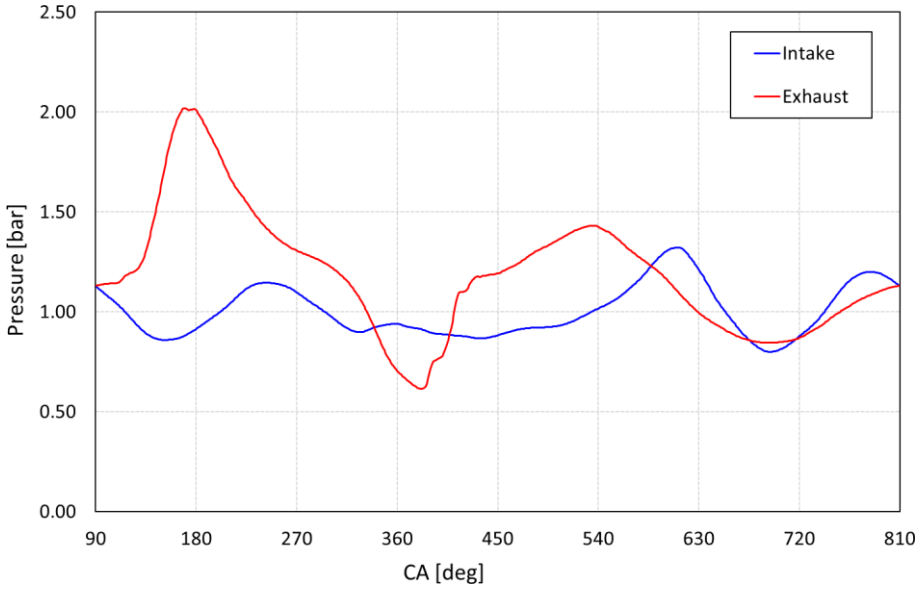

Figure 4-10. Inlet pressure (blue line) and outlet pressure (red line) boundary conditions.

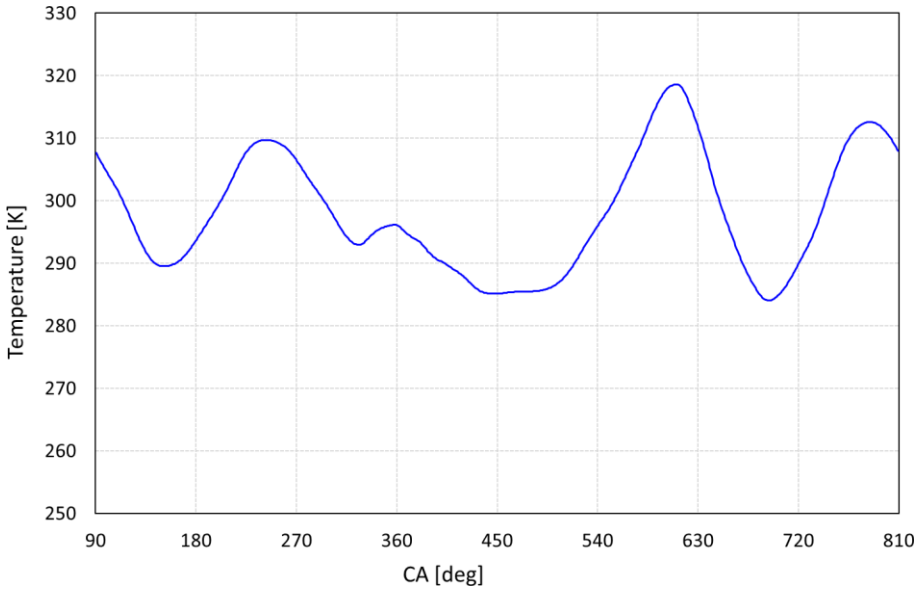

Figure 4-11. Inlet temperature boundary condition.

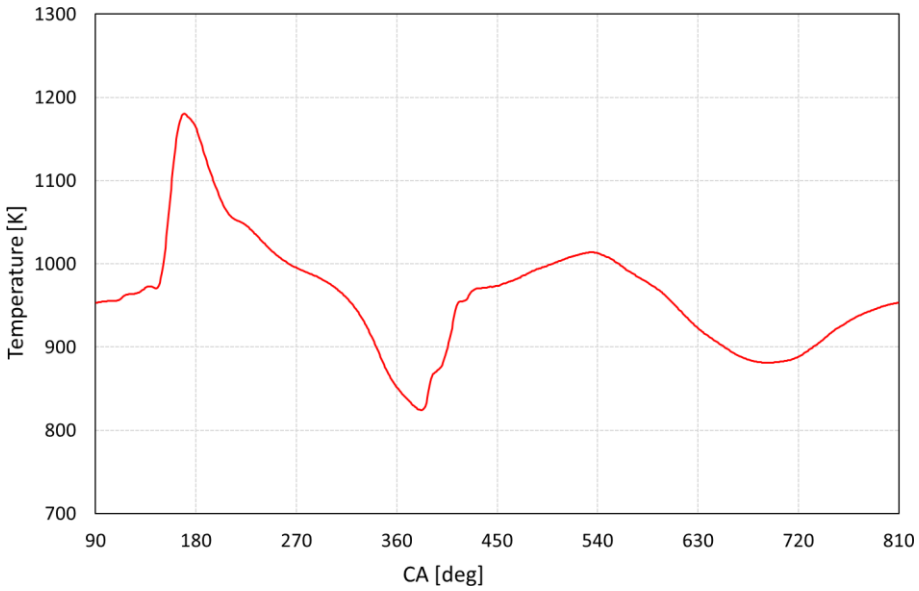

Figure 4-12. Outlet temperature boundary condition.

Wall temperature values are set according to the 1D model too and they are summarized in Table 4-5.

Wall region	Temperature [K]
Cylinder	398
Piston	562
Head	446
Intake port	357
Exhaust port	384
Intake steam valves	522
Exhaust steam valves	644

Intake valves plate	564
Exhaust valves plate	652

Table 4-5. Wall temperatures boundary conditions for 3D CFD simulations.

4.4 - CFD combustion results: baseline configuration

In this paragraph, the numerical set-up for 3D CFD simulations on the baseline configuration is presented. The fluid domain and the mesh construction will be presented, together with the calibration of the combustion model and the comparison with the experimental data. As explained in previous chapter, two different software are used in this thesis, with two different combustion model. Since the prechamber involves a strong interaction between turbulence and chemistry, especially while the flame front passes through the orifices, a detailed chemistry solver is used. Therefore, the SAGE combustion model in CONVERGE CFD is calibrated with the experimental data for the baseline configuration and it is used to analyse the engine performance with different prechamber geometries. In order to verify the predictability of the numerical set-up, the combustion model is then validated, comparing the CFD results at a different engine operational point with the experimental data. Using a detailed chemistry model to analyse the combustion process means a high fidelity details, but a more complexity and computational cost too. Thus, a simplified combustion model based on the progress variable and flame surface density is calibrated to evaluate the capability of a low fidelity approach in modelling the engine performance. In this chapter, only the results of CFD analysis of the two combustion models of the engine without prechamber, i.e. of the engine in the baseline configurations, are presented. The results of the engine equipped with prechamber will be presented in the next paragraph, together with the different geometries tested.

4.4.1 - Detailed chemistry model: numerical set-up

The modelling of non-conventional combustion process is a hard topic to study, since several thermodynamics phenomena are involved. In prechamber applications, after the flame kernel grown, the flame front develops and propagates inside a small volume, flows across different orifices and enters the main combustion chamber in the form of turbulent hot jets, which ignite the air/fuel mixture in the cylinder. The passage of hot flame into the narrow holes represents a challenge in CFD combustion modelling, since chemical kinetics interact with small turbulent eddies, which may lead to a quenching of the flame as well as an increase of the momentum of the jets, enhancing the transport phenomena. All of these aspects play a crucial role in the engine performance and the simplified combustion models, such as the models based on progress variable, introduce some simplifying assumptions which may lead to an under estimate of the engine performance and a non-correct evaluation of the real potential of this technology. Thus, considering and modelling the chemical effects in prechamber applications seems to be necessary in order to examine in depth the phenomenon and to provide useful recommendations for the manufactures. Hence, a detailed chemistry solver is adopted to better investigate benefits and drawbacks of the prechamber. The solver used for detailed chemistry combustion model is CONVERGE CFD. It is developed by engine simulations experts

and it can be used for both ICE and non-ICE applications. CONVERGE CFD allows to simulate three dimensional problems, incompressible or compressible flow and transient or steady state case, as well as reacting and non-reacting flows, together with stationary or moving boundaries. This software automatically generates a Cartesian grid at run-time during simulation, according to user-defined grid control parameters, removing the need of a manually grid generation. A Stereo Lithography (STL) file of the geometry is required in order to setting up the test case. Figure 4-13 shows the fluid domain of the engine used for CFD simulations in CONVERGE CFD.

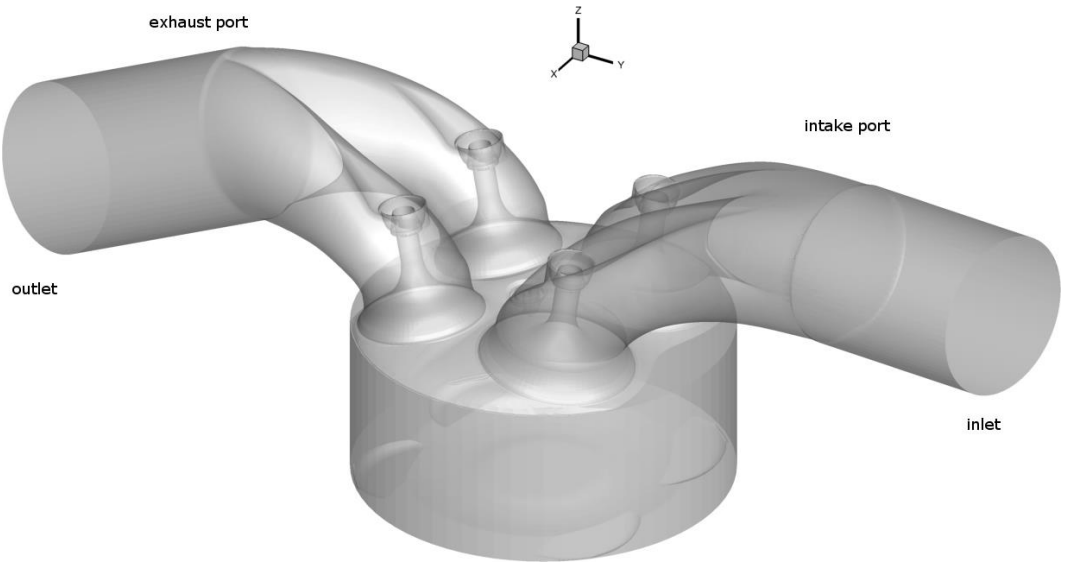

Figure 4-13. Fluid domain for simulations in CONVERGE CFD.

As explained in previous chapter, CONVERGE allows to simulate reacting flows using a detailed chemistry combustion model, namely SAGE, which is used in this thesis in order to study the performance of the engine with different prechamber configurations. SAGE is the most predictive and accurate way to model combustion process in internal combustion engines, since it accounts for the chemical kinetics, which allows to model the ignition phase and flame propagation properly. Furthermore, this combustion model can be used to model premixed flame as well as non-premixed one. Since the SAGE model considers the chemical reactions involved in the chemical mechanism, it is more expensive than simplified combustion model, such as ECFM-3Z, but it may provide more in-depth analysis of the phenomenon. In this paragraph, the numerical set-up adopted for CFD simulations with CONVERGE CFD will be explained, together with the calibration and validation of the SAGE model on the baseline configuration engine.

Meshing

CONVERGE includes several options for controlling the element size during simulation:

- Grid scaling: this allows to change the base grid size during simulation at a specified time by defining the grid scale parameter n:

$$dx_{scaled} = \frac{dx_{base}}{2^n}$$

Where dx_{base} is the base grid size and dx_{scaled} is the grid size after applying the scale factor. A negative value of the grid scale coarsen the grid, while a positive value refine the grid; the grid is unchanged if a value of 0 is defined.

- Fixed embedding: it allows to refine the grid in specific locations of the domain, or in an entire region flow, by specifying an embedding scale s:

$$dx_{embedding} = \frac{dx_{base}}{2^s}$$

The grid size in the rest of the domain remains unchanged.

- Adaptive Mesh Refinement (AMR): this technique automatically refines the grid based on fluctuating and moving variables, such as temperature, velocity and species. This option is very useful for using a refine grid without increasing the computational cost of the simulation. The AMR estimates the magnitude of the sub-grid field to determine where the grid is necessary to be refined. For a scalar, the sub-grid field is defined as the difference between the actual field and the resolved field:

$$\varphi' = \varphi - \bar{\varphi}$$

Where φ is the actual scalar field, $\bar{\varphi}$ is the resolved scalar field and φ' is the sub-grid scalar field. The sub-grid for any scalar can be expressed as an infinite series [56, 57]:

$$\varphi' = -\alpha_k \frac{\partial^2 \bar{\varphi}}{\partial x_k \partial x_k} + \frac{1}{2!}\alpha_k \alpha_l \frac{\partial^4 \bar{\varphi}}{\partial x_k \partial x_k \partial x_l \partial x_l} - \frac{1}{3!}\alpha_k \alpha_l \alpha_m \frac{\partial^6 \bar{\varphi}}{\partial x_k \partial x_k \partial x_l \partial x_l \partial x_m \partial x_m} + \cdots$$

Where α_k is $dx_k^2/24$ for a rectangular cell. Since it is not possible to handle the entire series, only the second-order term is used. Hence, it results:

$$\varphi' \cong -\alpha_k \frac{\partial^2 \bar{\varphi}}{\partial x_k \partial x_k}$$

A cell is refined if the absolute value of the sub-grid field is above a user-specified value. Conversely, a cell is released if the absolute value of the sub-grid is below the 1/5th of the user-specified value. Note that the above equations can be generalized for a vector field too, such as velocity. Furthermore, the maximum number of cells can be specified in order to limit the computational effort.

In this thesis, in order to identify the best numerical set-up for combustion analysis, three different meshes are considered for the cold-flow simulations, each one characterized by different properties. Table 4-6 reports the main properties of the three different meshes tested for the scavenging process.

Mesh type	Coarse	Fine	Finest
Base grid size [m]	$5*10^{-3}$	$4*10^{-3}$	$4*10^{-3}$

AMR scale based on velocity	2	2	3
AMR scale based on temperature	4	4	4
Embedding scale cylinder	2	2	2
Embedding scale intake valves	4	4	4
Embedding scale exhaust valves	4	4	4
Wall embedding scale	2	2	2

Table 4-6. Mesh properties for cold-flow simulations with CONVEGRE CFD.

The results show that there are not any major differences between the meshes, in terms of in-cylinder pressure and temperature, as shown in Figure 4-14 and Figure 4-15.

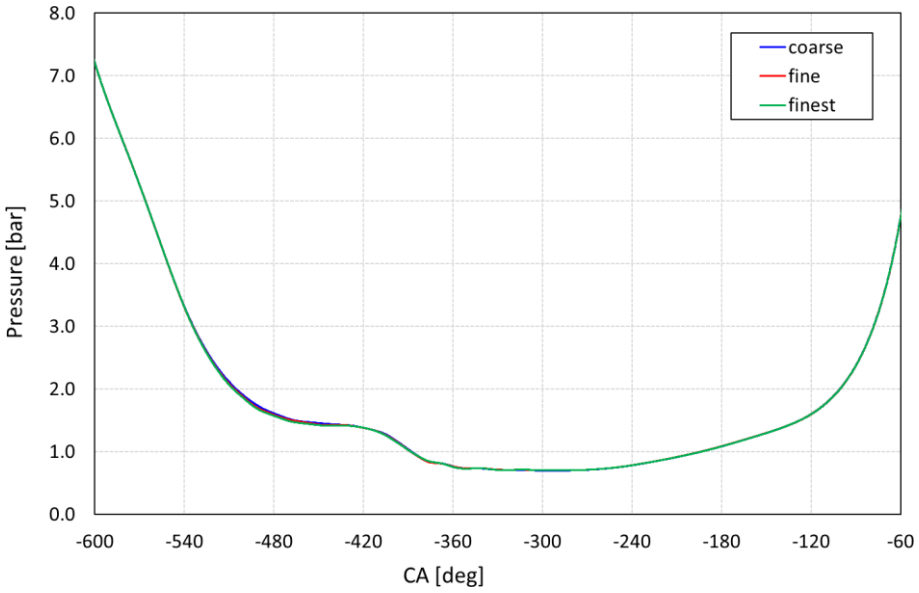

Figure 4-14. In-cylinder pressure during the cold-flow simulation with CONVERGE CFD.

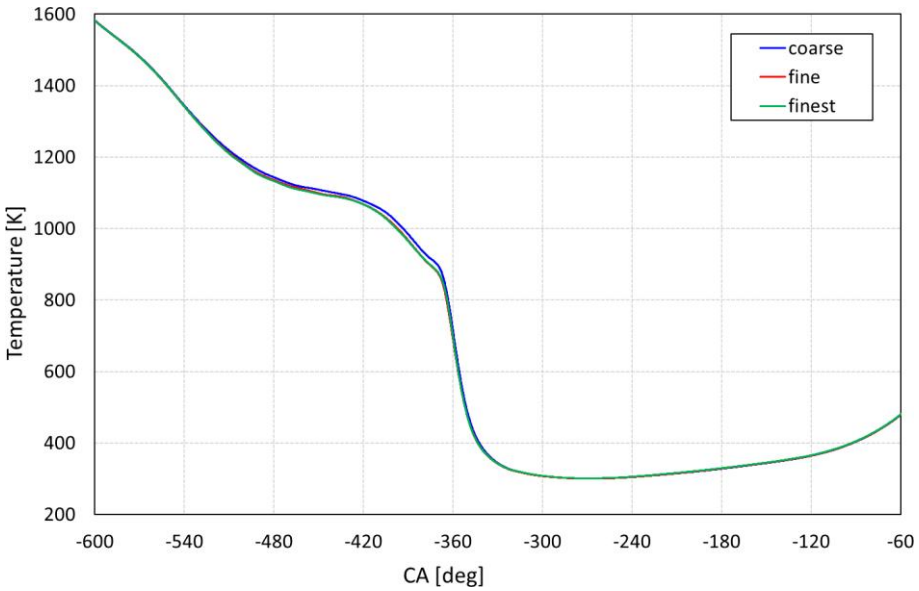

Figure 4-15. In-cylinder temperature during the cold-flow simulation with CONVERGE CFD.

Conversely, some differences arise in terms of Turbulent Kinetic Energy and tumble ratio. As shown in Figure 4-16 and Figure 4-17, TKE and tumble ratio are similar between the three meshes during the exhaust and overlap phases. As the intake valves open, some differences arise and the finest mesh computes greater TKE and tumble ratio than the others do, since the finest mesh allows to take into account smaller scale phenomena, reducing the filtering of the grid size.

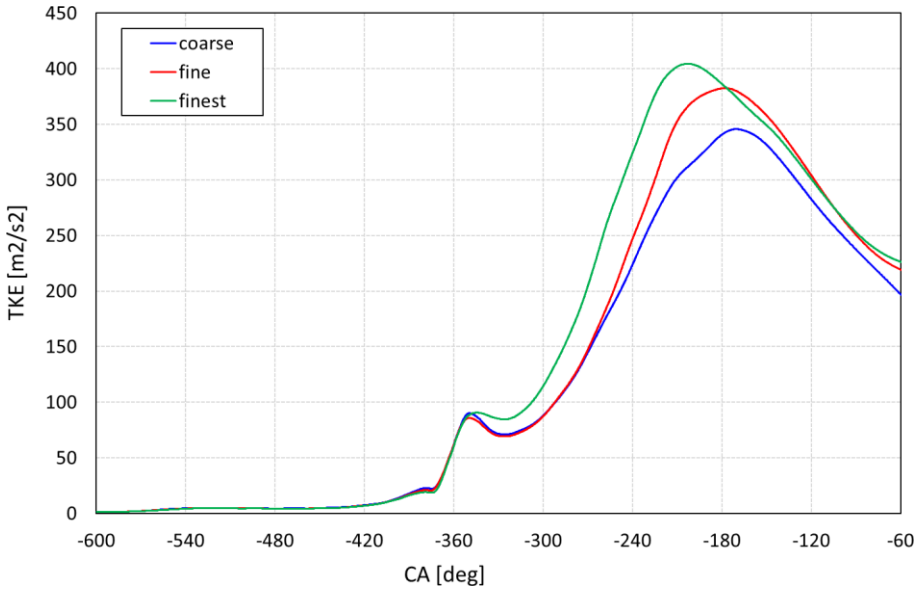

Figure 4-16. In-cylinder TKE during cold-flow simulation with CONVERGE CFD.

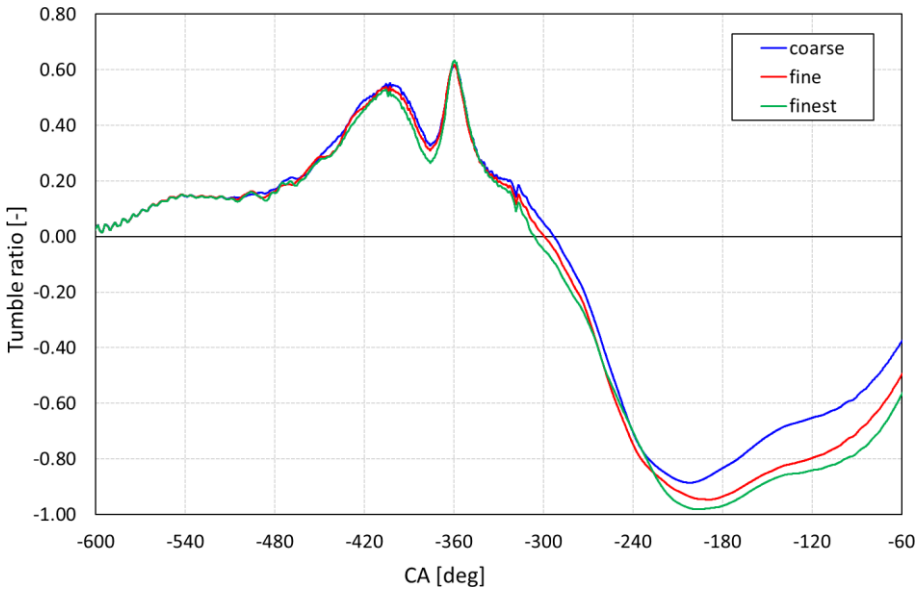

Figure 4-17. In-cylinder tumble ratio during cold-flow simulation with CONVERGE CFD.

Since the differences in terms of TKE and tumble ratio, the finest mesh is used to carry out the CFD analysis. It is worth noting that, even if the refinement in the cylinder region allows to have a mesh size of 1 mm, the AMR based on the velocity fluctuations grants to reach a minimum cell size of 0.5 mm inside the cylinder. In addition, during the combustion process, the finest mesh is further refined, in order to ensure a correct modelling. In particular, the cylinder zone is refinement with a scale by 3 and two additional embedding are added in the spark-plug zone, with scale of 4 and 5 respectively, in order to model properly the ignition phase. Table 4-9 reports the mesh characteristics used for the non-reacting and reacting CFD analysis with CONVERGE CFD.

Operation point	Maximum power

Mesh	finest
Base grid size [m]	$4.0*10^{-3}$
Cylinder element size [m]	$1.0*10^{-3}$
Cylinder element size [m]	$0.5*10^{-3}$
Spark-plug 1 element size [m]	$0.250*10^{-3}$
Spark-plug 2 element size [m]	$0.125*10^{-3}$
AMR based on velocity element size [m]	$0.5*10^{-3}$
AMR based on temperature element size [m]	$0.125*10^{-3}$
Number of elements @TDC	4047277
Maximum number of elements in the combustion chamber (@14°CA)	5001504

Table 4-7. Properties of the mesh used for CFD simulation in CONVERGE CFD at maximum power.

It is worth remembering that the adaptive mesh refinement based on the temperature fluctuations allows to add a higher grid resolution in the whole cylinder region, with an element size of $0.125*10^{-3}$ m, and capturing the flame front propagation. Figure 4-18 shows the mesh on a section near the spark plug during a combustion simulation. It can be noted the refinement of the grid in the cylinder zone, the two spheres of embedding around the spark plug and the refinement due to the AMR.

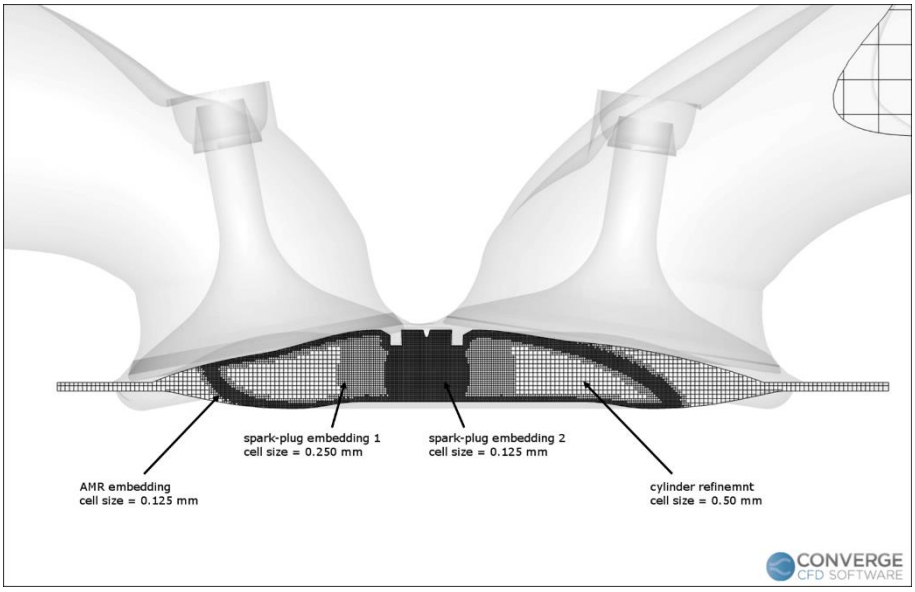

Figure 4-18. Example of mesh generated during combustion simulation with CONVERGE CFD.

A variable time-step is used for CFD simulations in CONVERGE CFD. The solver performs a number of check in order to determine the size of the next time-step and takes the largest value that satisfies all the limits imposed by the user. Since the flow field inside the combustion chamber has a strong influence on the combustion process, in addition to the mesh sensitivity, a time-step sensitivity analysis is carried out. In order to verify the goodness of numerical set-up, two different configurations are tested, changing the minimum

time-step adopted during the simulation. Table 4-8 reports the properties of the simulations carried out for the time-step analysis.

Simulation	T1	T2
Mesh	finest	finest
Minimum time-step [s]	10^{-6}	10^{-8}

Table 4-8. Simulations for the time-step sensitivity with CONVERGE CFD.

Figure 4-19 and Figure 4-20 show the evolution of in-cylinder pressure and in-cylinder temperature, respectively, during the intake phase and compression phase. The differences between the two simulations are very small, with a difference of 1.44% in term of in-cylinder temperature at the end of the compression phase.

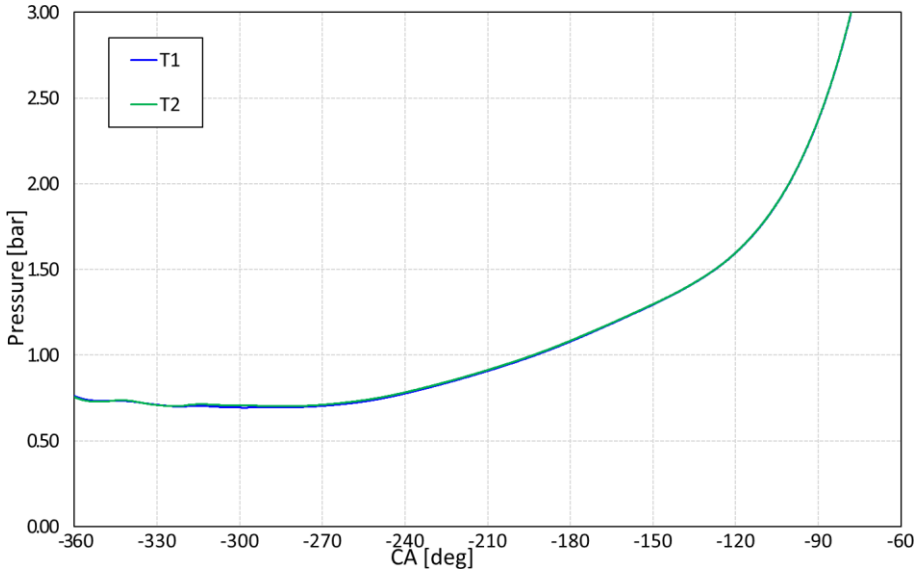

Figure 4-19. Evolution of the in-cylinder pressure for different time-steps, during the intake and compression phases (CONVERGE CFD).

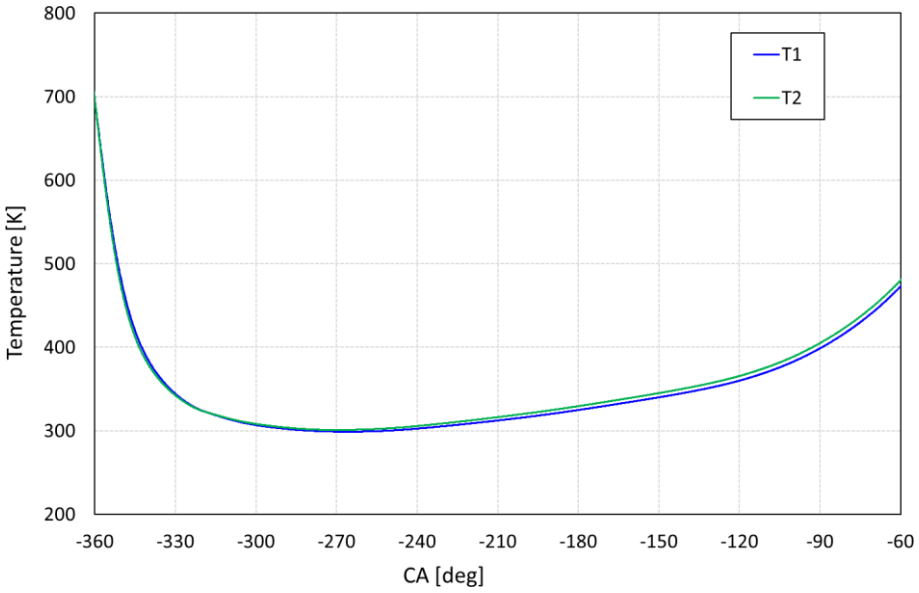

Figure 4-20. Evolution of in-cylinder temperature for different time-steps, during the intake and compression phases (CONVERGE CFD).

Even if the differences are very small, the minimum time-step of 10^{-8} is used for the CFD analysis with CONVERGE, since it is more suitable for modelling the combustion process, during which the strong interaction between turbulence and chemistry requires more strictly numerical settings. Table 4-9 reports the properties in terms of mesh and time-step adopted for CFD simulations with CONVERGE CFD.

Mesh	finest
Minimum time-step [s]	10^{-8}
Maximum time-step [s]	10^{-6}
Maximum CFL number [-]	1

Table 4-9. Mesh and time-step properties for CFD simulations with CONVERGE.

Numerical models

For the numerical simulation with the commercial code CONVERGE CFD, the turbulent flow is described by the time-dependent unsteady RANS equations and the RNG $k-\varepsilon$ model is used for turbulence modelling, since it is more appropriate for studying the Internal Combustion Engine [58-60]. The pressure velocity coupling is handled by PISO algorithm, with pressure-based solver. The second-order upwind numerical scheme is used for the spatial discretization of the governing equations and the convergence residuals are set to 10^{-5} for all the solved quantities. As explained before, SAGE detailed chemistry model is used for combustion modelling, with a chemical file, which consists of 41 species and 124 reactions [61]. Since the detailed chemistry solver takes into account the chemical kinetics, the ignition model has a key role in modelling the combustion process. In a typical spark discharge, voltage rises between the two electrodes until the electrical breakdown between the spark gap. In this first stage (breakdown phase), the mixture between the electrodes is ionized into plasma. This phase is followed by the arc phase, in which the plasma

expands due to heat conduction and diffusion. After the arc phase, the energy storage device will dump its energy into the discharge circuit (glow discharge phase). In CONVERGE, the engine ignition has been modelled like two energy sources. Since time scales in the breakdown phase are significantly smaller than the arc and glow phases, the source 1, which represents this first phase, acts for very few crank angle degrees. Furthermore, since the discharge times of arc and glow phases are similar, the source 2 represents the combined energy supplied during the arc and glow phases (Figure 4-21).

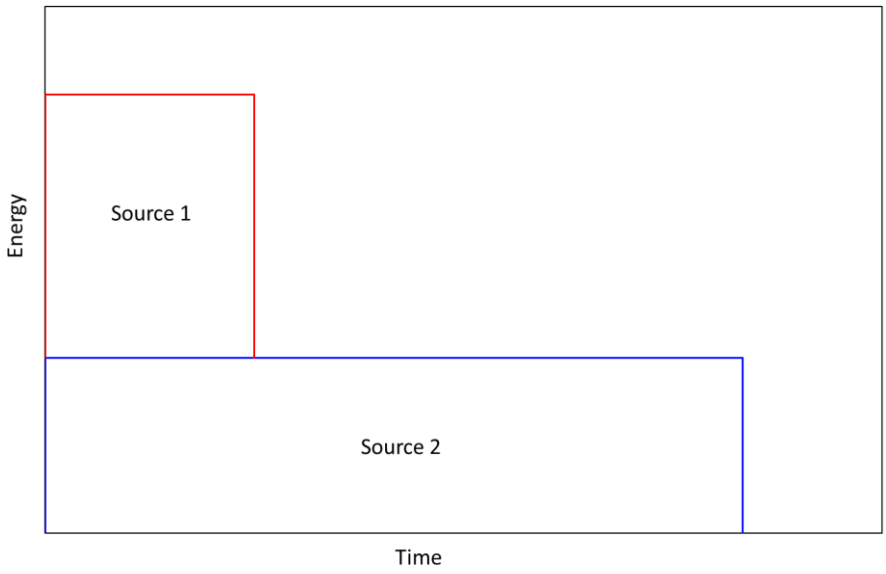

Figure 4-21. Ignition modelling in CONVERGE CFD.

The model requires the definition of some parameters that have to be adjust in order to calibrate the combustion model:

- Radius sources: the radius of the energy sources are set according to the CAD model of the spark;
- Shape of the sources: assuming that during the spark discharge the flame kernel grows ideally, two spherical energy sources are considered for modelling the ignition phase, with a diameters equal to the gap between the electrodes;
- Energy sources: the energy provided by the sources must be specified;
- Duration: the period of time in which the sources provide energy must be specified.

Several CFD tests are carried out varying the spark energy and duration, in order to identify how they affect the combustion process and to find the best configuration to reproduce the experimental data. The results of CFD combustion model calibration will be shown in the next paragraph.

Materials

CONVERGE CFD, when using the detailed chemistry model, requires a thermodynamic file and a gas file in which the species-specific thermodynamic properties and molecular transport properties are reported,

respectively. As explained before, the file species properties refer to the ones contained in the mechanism file. Thus, thermodynamic properties are already storage in the input files. Some differences with the actual mixture composition may be arise. In fact, the fuel considered in the mechanism file is iso-octane (IC_8H_{18}), which involves 124 reactions for its oxidation. These simplified assumptions imply different thermodynamic properties between the two mixtures, such as diffusion coefficients, molecular weight and LHV. Since the lack of information about the actual mixture composition used in the test bench, the LHV value computed by the solver is used for calibration the SAGE combustion model, even if its value may be not the real one. The equivalence ratio of the mixture is set according to the experimental data. For compressible flows, an equation of state is required to couple density, pressure and temperature. In CONVERGE simulation, the Redlich-Kwong equation of state is used to take into account variations due to the non-ideal gas behaviour. Table 4-10 reports the main mixture properties.

Fuel chemical composition	Iso-octane (IC_8H_{18})
Fuel LHV [kJ/kg]	44658.37
Air-to-fuel ratio [-]	0.82
Equation of state	Redlich-Kwong equation
Specific heat at constant pressure [J/kg/K]	from file
Thermal conductivity [W/m/K]	from file
Molecular viscosity [Pa*s]	from file

Table 4-10. Species properties for CFD simulations in CONVERGE CFD.

4.4.2 - Detailed chemistry model: combustion model calibration

With the presented numerical set-up, the 3D CFD analysis of the engine is carried out using CONVERGE CFD. At first, the results of the cold-flow are presented, together with the contours of velocity during the scavenging process. Finally, the reacting-flow simulations results are presented, together with the combustion model calibration. In order to verify the predictivity of the model, the numerical same numerical set-up is used for CFD simulations at different engine operational point. The results with the calibrated combustion model at a different rotational speed will be shown and compared with the experimental one.

Non-reacting flow results

Since the combustion model adopted with this software is a detailed chemistry solver, it is very important the modelling of the scavenging process, in order to resolve properly the flow field and turbulent structures, which will interact with the chemical reactions and will determine the flame front propagation. In order to wash out the test case from the initial conditions, two revolutions of the scavenging process are necessary. A user-defined function (UDF) is applied during these first two revs to simulate the combustion process and to reduce the computational cost of the simulations and speed-up the simulations. Thus, during the first two cold flow simulations, the in-cylinder pressure data from experimental test bench is applied as source during

combustion process and the UDF allows to turn the species of fresh mixture (i.e. fuel, nitrogen and oxygen) into combustion products (i.e. nitrogen, water and carbon dioxide). After these two revolutions, the flow field is then used to initialize the third rev. Thus, the following results refer to the third CFD engine revolution, which is used to calibrate the combustion model. Figure 4-22 shows the evolution of the pressure inside the cylinder during the scavenging process and compression phase. The CFD results are quite accurate, especially during the intake phase and compression phase of the mixture. Comparing the numerical results with the experimental data, some differences can be noted. The CFD computes a lower in-cylinder pressure during the exhaust phase. The gap between the numerical and experimental results tend to decrease during the overlap, intake and compression phases, at the end of which an underestimate of 6% still remain. These differences may be caused by several factors, such as the mixture composition, which is different from the actual one since it is represented by a reduced chemical mechanism, and defeaturing of the CAD model, that is necessary in order to build a stable numerical set-up.

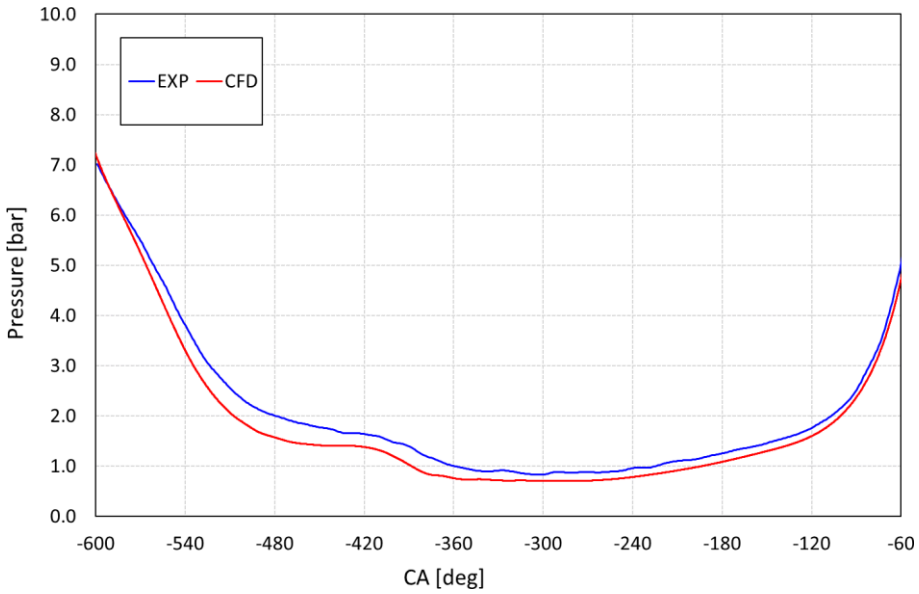

Figure 4-22. Evolution of in-cylinder pressure during the cold flow simulation in CONVERGE CFD.

Figure 4-23 shows the contours of fuel mass fraction during the overlap phase in CONVERGE CFD simulation, on a section passing through the intake valves. As soon as the intake valves open, the difference pressure between the cylinder and intake ports lead to a recirculation of the burnt gas from the combustion chamber towards the inlet (340°CA). While the exhaust valves are closing, the not perfect tuning of the dynamic effects ensures an amount of fuel mass to exit from the combustion chamber towards the exhaust port. Nevertheless, the short-circuit of the fuel is less than 2%. Figure 4-24 reports the comparison between the CONVERGE CFD simulation and 1D model results in term of fuel mass trapped at the end of the intake phase. It can be noted that the CFD results are in accord with the GT model, with a difference of roughly 0.7%, confirming the goodness of the CFD results.

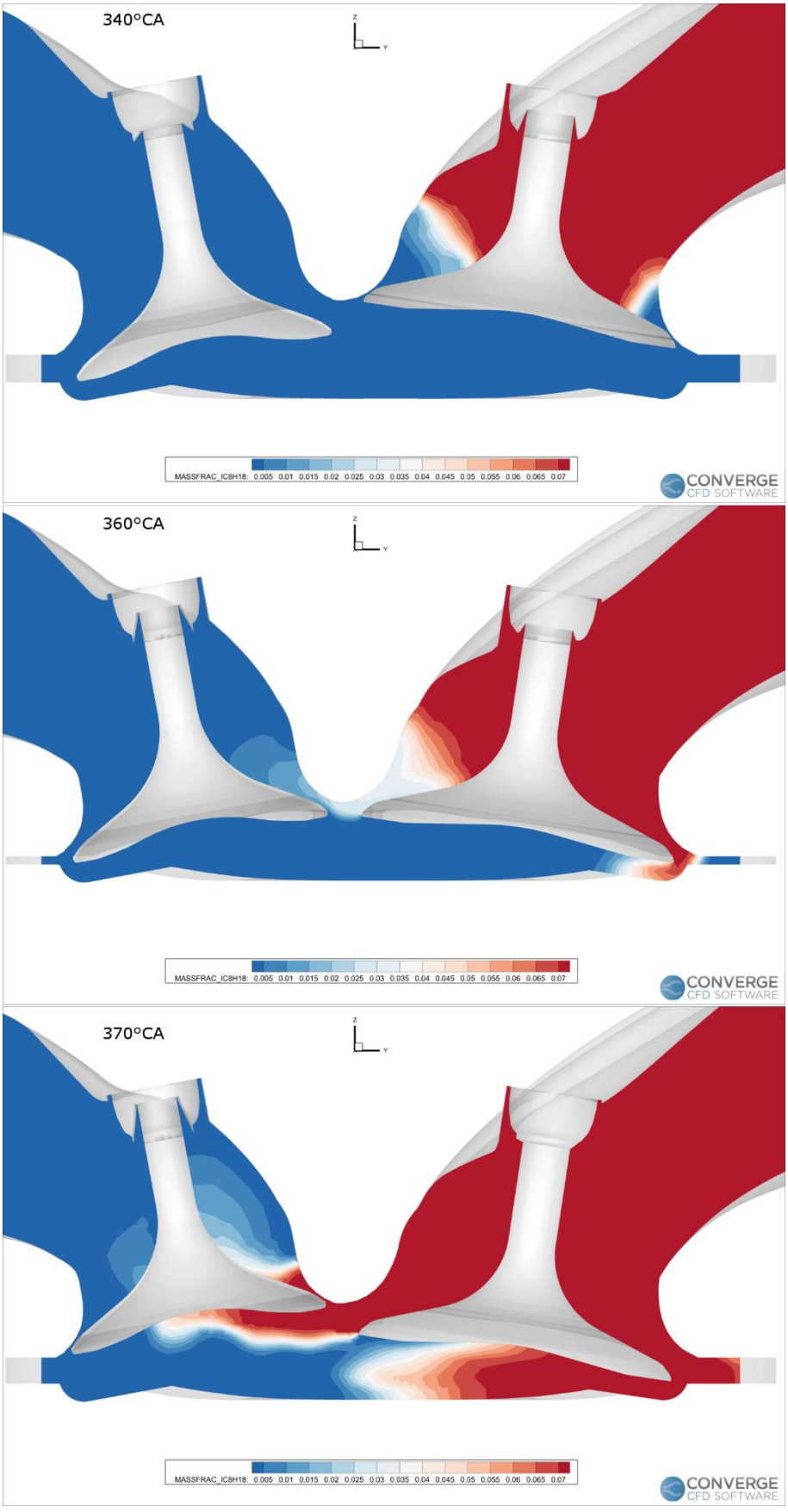

Figure 4-23. Contours of fuel mass fraction during the overlap phase in CONVERGE CFD.

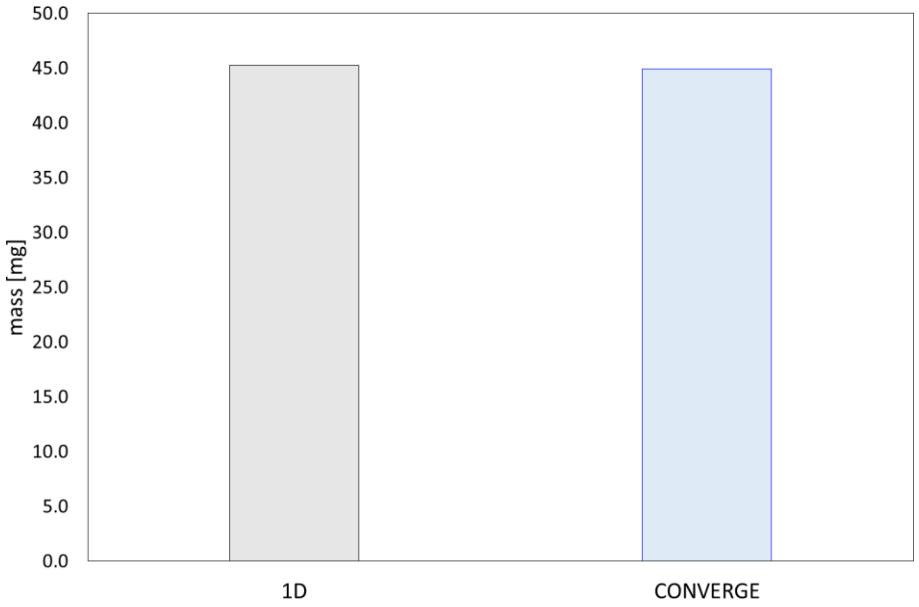

Figure 4-24. Fuel mass trapped: comparison between CONVERGE and 1D model results.

Figure 4-25 shows the evolution of the tumble ratio inside the cylinder during the cold flow simulation. Two different peaks can be noted: the first, during the overlap phase, during which the intake and exhaust valves are both opened and the fresh mixture starts to enter the cylinder; the second, where the piston is almost at the BDC, due to the wave coming from the intake port. As the piston moves upwards to the TDC, the tumble motion gradually decays.

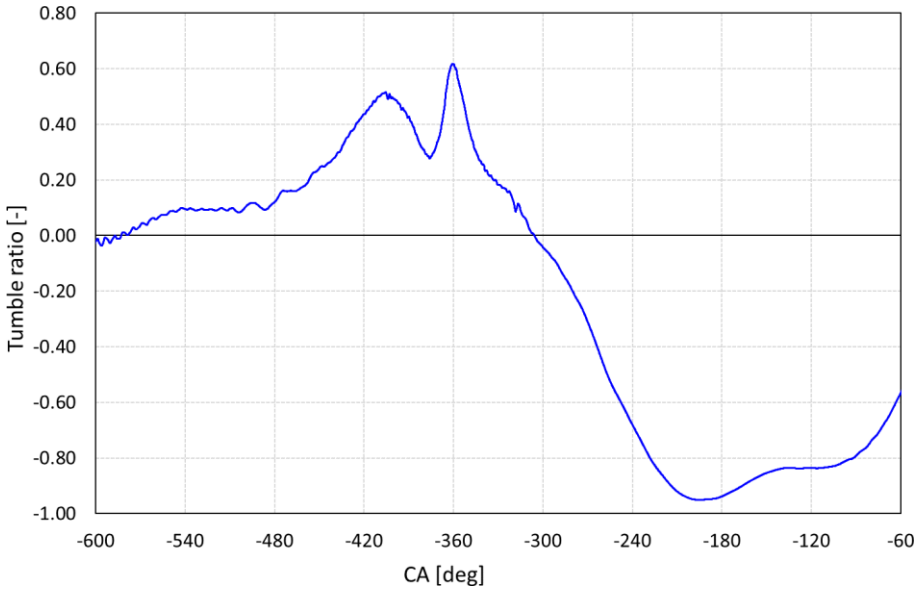

Figure 4-25. Evolution of tumble ratio inside the cylinder during the cold flow simulation in CONVERGE CFD.

Figure 4-26 shows the contours of velocity and turbulent kinetic energy inside the cylinder at the end of the intake phase, on a section passing through the spark plug. Observing the vector lines, the tumble motion, generating after the intake phase, is clearly noticeable. The highest values of turbulent kinetic energy are

observed where the flow coming down from the intake valves run into the recirculating flow, generating high levels of shear stresses.

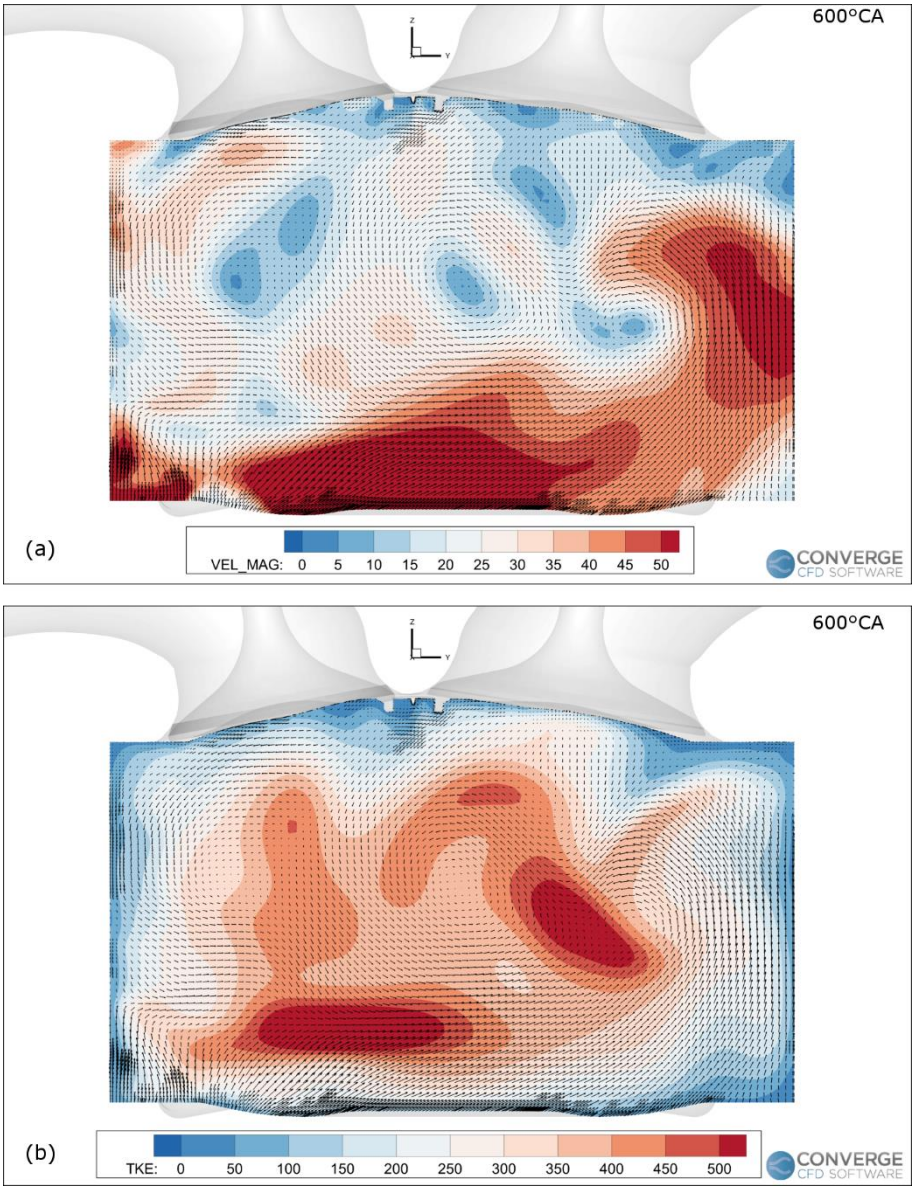

Figure 4-26. Contours of velocity (a) and TKE (b) inside the cylinder at 600°CA (CONVERGE CFD).

It is fundamental to analyse the flow field inside the cylinder before the combustion starts, since the charge motions, velocity flow and turbulence structures may affect the flame front propagation. Another interesting view of the flow field inside the cylinder is during the compression phase, when the piston is moving towards the TDC (Figure 4-27). It is still present a tumble motion which evolves counter clockwise, from the intake valves (on the right) to the exhaust valves (on the left) and it is clearly noticeable a high TKE zone near the intake valves.

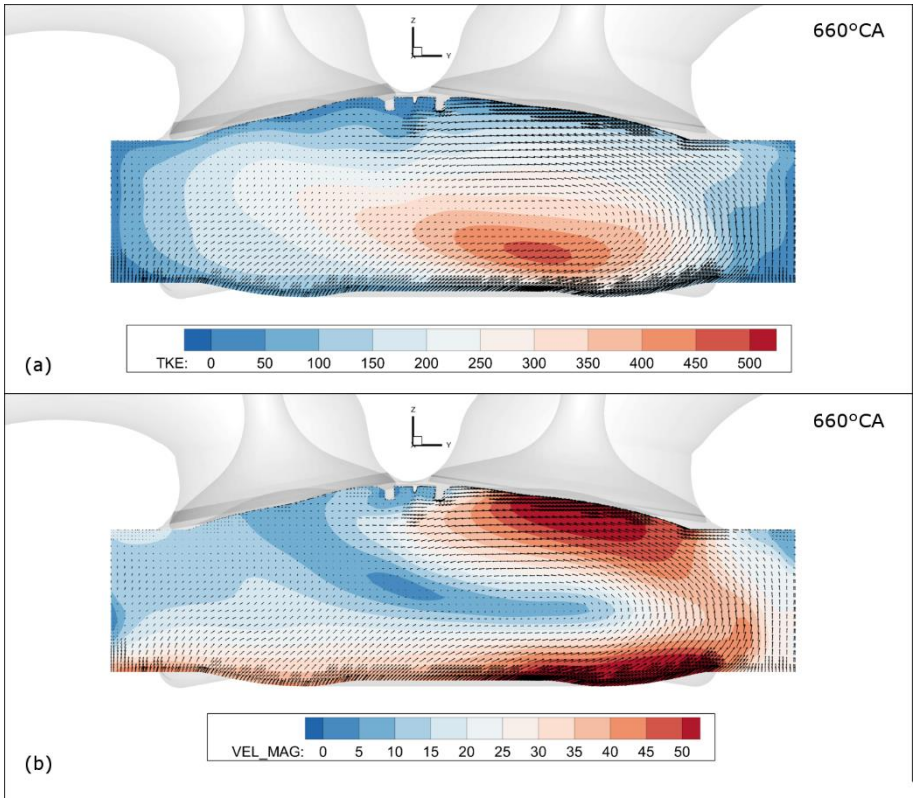

Figure 4-27. Contours of velocity (a) and TKE (b) inside the cylinder at 660°CA (CONVERGE CFD).

Reacting flow results

After the cold flow analysis, the combustion results are here presented. The SAGE combustion model is used for analysing the combustion process of the engine. As explained before, during the combustion process, a refinement of the mesh is done inside the cylinder and the AMR based on temperature fluctuations is used with a scale factor equal to 5, which allows to obtain a minimum cell size equal to 0.125 mm (see Table 4-7 and Figure 4-18). When a detailed chemistry solver is used for combustion simulations the complexity and the computational effort of the topic raise (see 3.4 -). In fact, when the chemical reactions are considered, the reaction rates of the species are computed to simulate the ignition phase and flame front propagation. Conversely, when a simplified approach is used, the turbulent flame speed is modelled through semi-empirical correlations. The increase in the computational cost due to the higher number of equations to be solved is balanced by the major high fidelity of the results and by the more in-depth analysis of the combustion process. Furthermore, when considering a chemical reaction mechanism, the mixture composition may be different respect to the actual air/fuel mixture used during the experiment, which may lead to differences in thermodynamic properties and, thus, in different combustion behaviour. Since the lack of information about the actual composition of the mixture, a fine tuning of turbulent combustion parameters is necessary in order to calibrate the combustion model according to the experimental results. Thus, the calibration of the model is carried out by varying the spark ignition model parameters, energy and duration of the sources, and a combustion model parameter, called reaction multiplier (R_m), which is a scale factor for reaction rates. In addition, the effect of turbulent Schmidt number (Sc_t) on combustion process is

evaluated to determine the correct numerical set-up for combustion modelling. The spark time is kept equal to the experimental data. A spherical shape is imposed for the energy sources and the radius is set according to the gap between the spark electrodes. As explained in previous paragraph, two energy sources are considered for ignition modelling: the first (S1) for modelling the breakdown phase, the second (S2) for modelling the arc/glow phase. An in-depth analysis is carried out in order to tune the combustion model and reproduce the flame propagation inside the engine during the whole process, starting from the ignition phase, passing through the turbulent combustion phase and up to the ending laminar phase, in which the flame front reach the walls and extinguishes. Several simulations are run in order to investigate the effect of these parameters on the process. Table 4-11 reports the characteristics that are kept constant during the calibration and for the whole CFD simulations carried out.

Spark advance	-33°CA
Shape S1	sphere
Shape S2	sphere
Radius S1	$0.6*10^{-3}$ m
Radius S2	$0.6*10^{-3}$ m

Table 4-11. Simulation set-up for the combustion model in CONVERGE CFD.

At first, the effects of turbulent Schmidt number on the combustion process is investigated. The turbulent Schmidt number is defined as the ratio between the momentum diffusivity and the mass diffusivity in a turbulent flow. Since it is a property of the turbulent flow, no universal value can be assumed. Table 4-12 reports the simulations set-up.

TEST	C1	C2
Sc_t	0.78	0.68

Table 4-12 . Simulations set-up for testing the effect of turbulent Schmidt number.

Figure 4-28 shows the effect of the turbulent Schmidt number in terms of in-cylinder pressure. The pressure curve ramps up earlier for lower turbulent Schmidt number, reaching a higher pressure peak. In fact, the lower turbulent Schmidt number the higher turbulent mixing inside the combustion chamber and this leads to a faster combustion process.

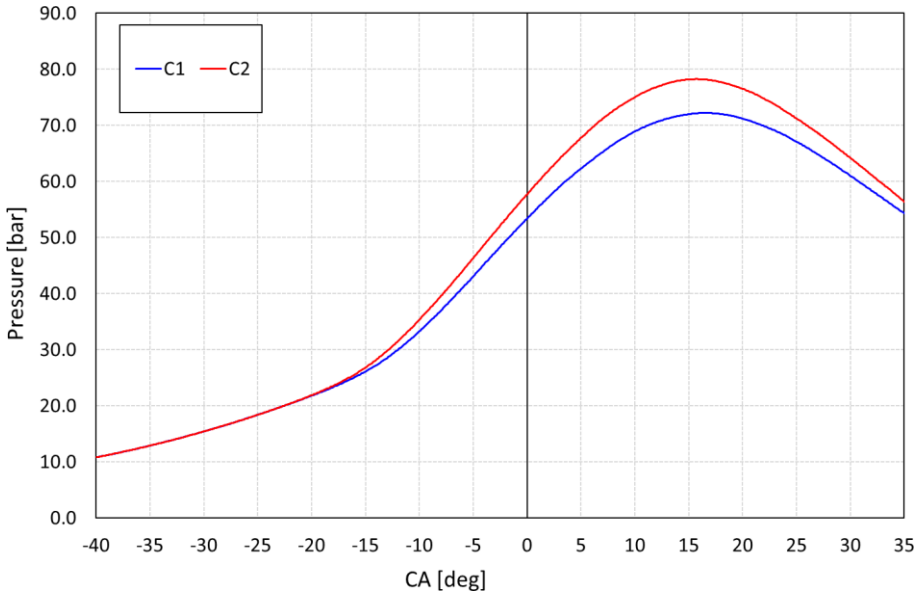

Figure 4-28. Effect of the turbulent Schmidt number on the in-cylinder pressure during the combustion.

Table 4-13 reports the simulations set-up for verifying the effect of the reaction multiplier on the combustion process. The reaction multiplier is a scaling factor of reaction rates in the combustion model. Since the chemical mechanism file is a reduced one, some simplifications are done by not considering several species and reactions which occur in the actual oxidation process. Thus, an investigation on the effect of the reaction multiplier on combustion is needed in order to tune the numerical model.

TEST	C3	C4
R_m	1	1.1

Table 4-13. Simulations set-up for testing the effect of reaction multiplier.

Figure 4-29 shows the effect of reaction multiplier in terms of in-cylinder pressure. As explained before, the reaction multiplier is a combustion model parameter and it acts a scale factor on the reaction rates of the mechanism. Since the lack of information on the actual composition of the mixture, this scaling allows to tune the energy released by the CFD model during the combustion process. Thus, higher the reaction multiplier higher the in-cylinder pressure and higher the energy released during combustion, as shown in Figure 4-29.

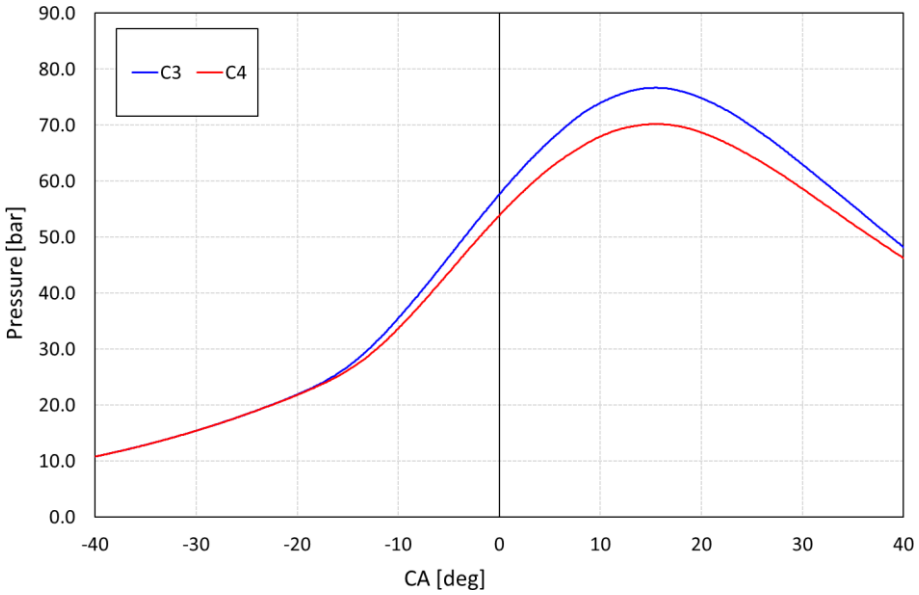

Figure 4-29. Effect of reaction multiplier on the in-cylinder pressure during combustion.

Table 4-14 reports the simulations set-up for verifying the effect of the duration of the sources on the combustion process. T1 refers to the first source applied by the ignition modelling, while T2 refers to the second one.

TEST	C5	C6
T1 [CA]	0.5	0.5
T2 [CA]	20	25

Table 4-14. Simulations set-up for testing the effect of the duration of the sources.

Figure 4-30 shows the evolution of the pressure inside the combustion chamber varying the duration of the energy sources. It can be noted that, increasing the crank angle degrees in which the sources are active leads to a higher pressure inside the cylinder. In fact, higher the duration higher the power released by the ignition modelling and, thus, faster the combustion process. It is worth noting that a further investigation is carried out by varying the duration of the first source applied by the ignition model. The effect of varying the first source duration on combustion process is the same: increasing the duration means increasing the power introduced in the fluid domain, producing a faster combustion process and higher in-cylinder pressure.

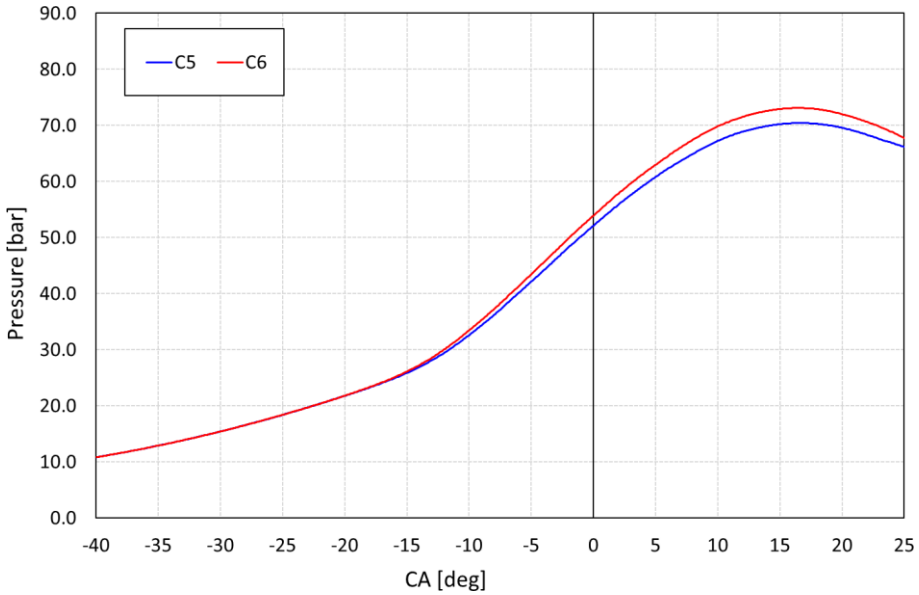

Figure 4-30. Effect of sources duration on in-cylinder pressure during combustion.

Finally, the effects of the energy released by the sources is investigated. Table 4-15 reports the simulations set-up. E1 value refers to the energy released by the first source, while E2 refers to the second one.

TEST	C7	C8
E1 [J]	0.020	0.025
E2 [J]	0.020	0.025

Table 4-15. Simulations set-up for testing the effect of energy sources on combustion process.

Figure 4-31 shows the effect of the energy sources on the pressure inside the cylinder. Similar to the effect of the duration of the sources, increasing the energy released ensures a faster combustion process, since the power introduced into the domain is greater. This is responsible for the higher calculated pressure inside the combustion chamber. A further analysis is carried out by varying the energy of the first sources acting during the ignition phase. Since its duration is very short, the effect of the energy released is much less evident than the effect produced by the second source.

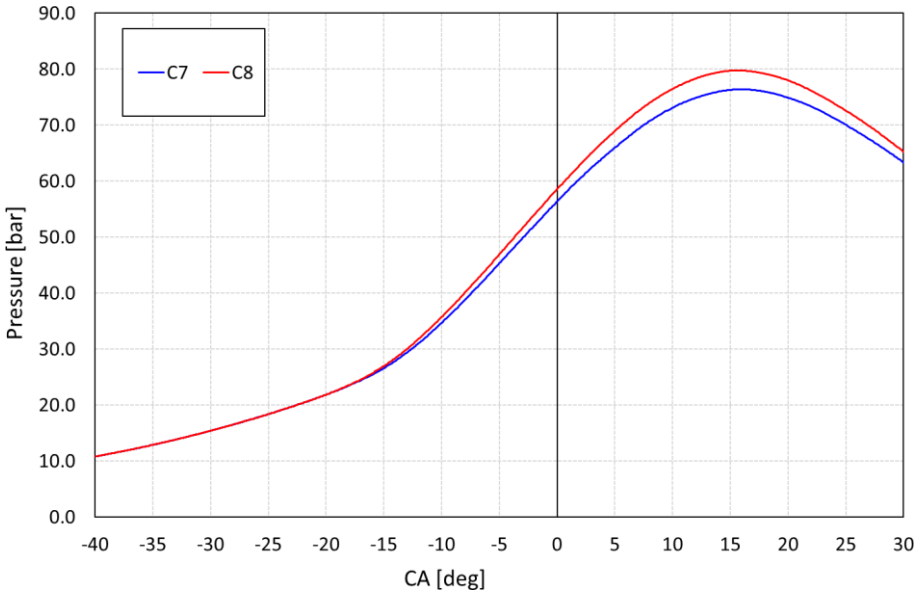

Figure 4-31. Effect of energy sources on in-cylinder pressure during combustion.

After investigated the ignition model and combustion model parameters and their effects on the combustion process, these numerical characteristics are changed for reproducing the experimental data provided by the manufacturer. Figure 4-32 shows the in-cylinder pressure during combustion for the calibrated model, compared to the experimental data. A very good agreement is achieved, especially during the ignition phase and turbulent phase. A slightly overprediction of the CFD peak pressure can be noted: the difference between the numerical data and experimental measurement is less than 1% and the position of the peak is computed at same crank angle of the experimental one. CFD model tends to overestimate the pressure value during the last phase of the combustion. In this phase, the flame front has already reached the walls and the flame goes towards the quenching. During this last part of the combustion process, wall temperatures values and fuel LHV may affect the CFD results, as well as some differences in the geometrical model due to the defeaturing operation. Nevertheless, the in-cylinder pressure is well represented and the numerical set-up is suitable to analyse the combustion process of the engine.

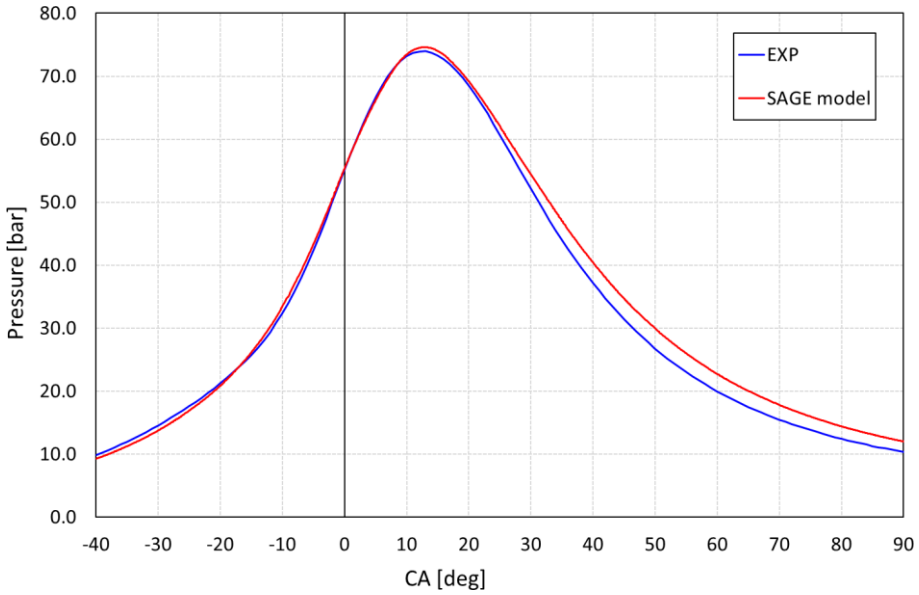

Figure 4-32. Evolution of the in-cylinder pressure for the calibrated model at maximum power (CONVERGE CFD), compared to the experimental data.

Figure 4-33 shows the evolution of the burned mass fraction for the calibrated model, compared to the experimental data. A good accuracy is achieved, especially during the turbulent combustion phase, which is represented by the middle of the curve, from 10% to 70% of burned air/fuel mixture.

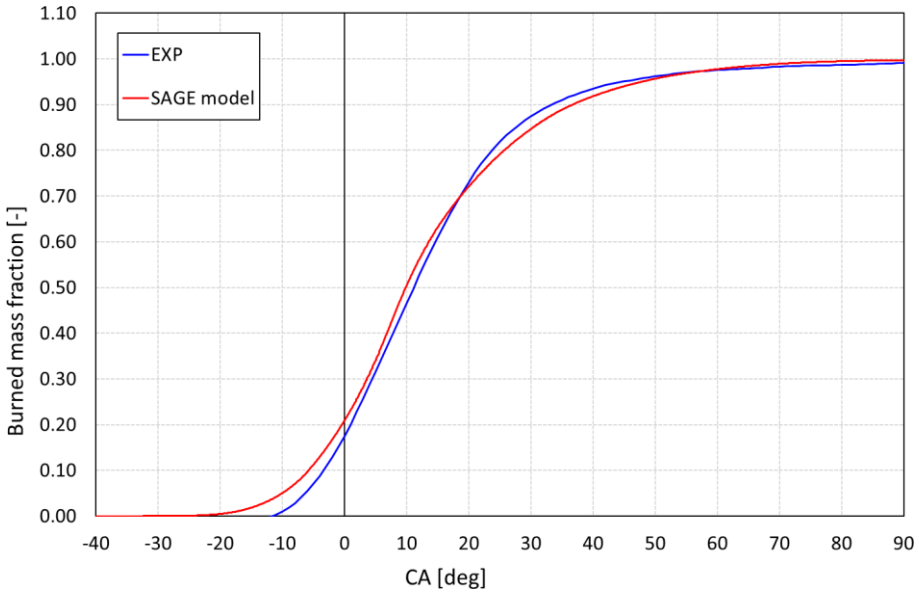

Figure 4-33. Evolution of the burned mass fraction for the calibrated combustion model (CONVERGE CFD) at maximum power, compared to the experimental one.

It is worth noting the interaction between flow field, turbulence and flame. Figure 4-34 shows the TKE and flow field inside the cylinder before the spark time. As observed during the compression phase (Figure 4-27), the flow field inside the cylinder establishes a clockwise recirculation, from the intake valves towards to the exhaust side. Furthermore, a high TKE zone is present on the intake side of the combustion chamber.

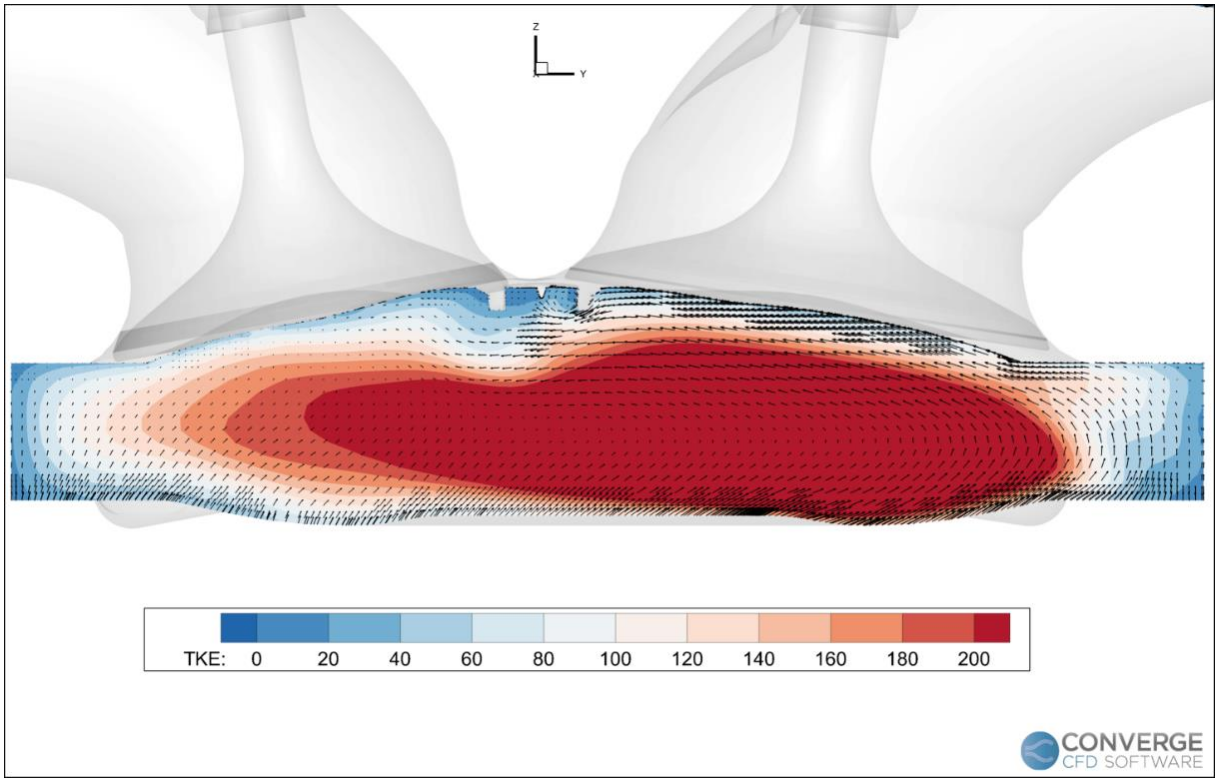

Figure 4-34. Contour of TKE and velocity vectors inside the cylinder at -40°CA on a section passing through the spark plug.

These two phenomena both affect the combustion process, but in sequence, depending on the phase it is. Figure 4-35 shows the contour of TKE inside the cylinder and the contour of temperature during at different piston positions, during the combustion process. It can be noted that, during the ignition phase, the flame kernel is mainly affected by the tumble motion inside the cylinder and it is stretched towards the exhaust valves. As the flame kernel grows and the turbulent combustion phase becomes, the flame front is mainly affected by the turbulent kinetic energy in the combustion chamber and it tends to propagate where the TKE is higher.

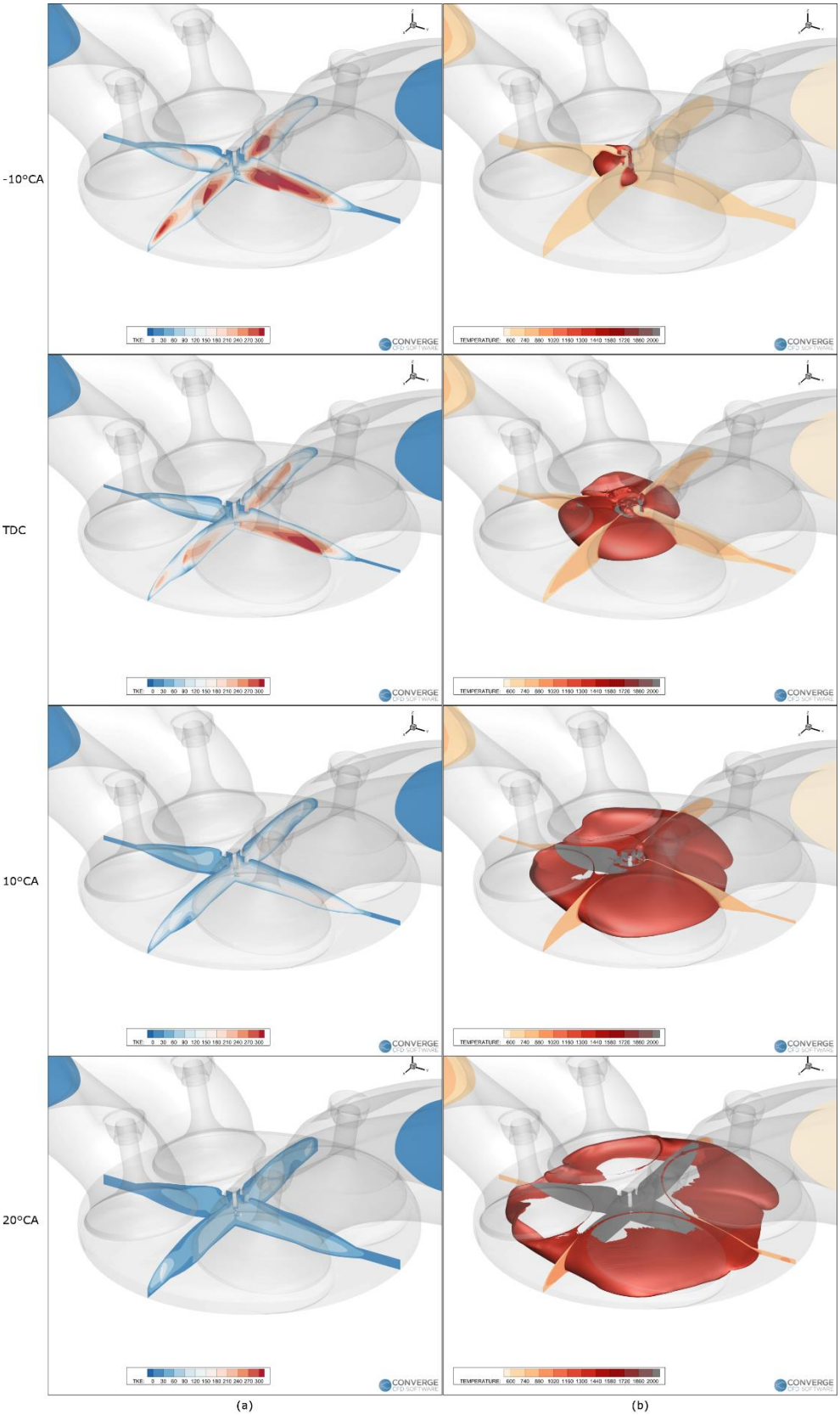

Figure 4-35. Evolution of TKE (a) and flame front (b) inside the cylinder during the combustion process for different crank angle degrees.

Combustion model validation

After the combustion model validation at maximum power, a different rotational speed is tested in order to verify the predictivity of the calibrated CFD model. A regime at 4000 rpm and full load is chosen and the boundary conditions for this operational point are set into the CFD model. Thus, the wall temperatures values are set according to the 1D model and the equivalence ratio is replaced, according to the experimental data. The finest mesh is used for this simulation and the minimum time-step is set to 10^{-8} s, as well as used for calibrating the model at maximum power. Table 4-16 summarizes the numerical set-up and boundary conditions used for the simulation at 4000 rpm and full load.

Operation point	4000 rpm @full load
Fuel	iso-octane (IC_8H_{18})
Equivalence ratio	1.16
Mesh	finest
Minimum time-step [s]	10^{-8}
Maximum time-step [s]	10^{-6}
Liner temperature [K]	388
Head temperature [K]	416
Piston temperature [K]	490
Intake port temperature [K]	359
Exhaust port temperature [K]	377
Intake valves steam temperature [K]	462
Exhaust valves steam temperature [K]	521
Intake valves plate temperature [K]	483
Exhaust valves plate temperature [K]	526

Table 4-16. Boundary conditions and numerical set-up for CFD simulation at 4000rpm and full load (CONVERGE CFD).

The numerical procedure is the same followed for the calibration model at maximum power. Thus, two revolutions of the engine are run to wash out the test case from the initial conditions and to ensure a sufficient resolution of the turbulent structures inside the cylinder. The following results refer to the third revolution of the CFD simulation. Figure 4-36 shows the evolution the in-cylinder pressure during the cold flow simulation. Comparing the results with the experimental pressure, a very good agreement is achieved during the whole scavenging process. The CFD tends to underestimate the in-cylinder pressure during the exhaust phase, while minimum differences are noticeable during the overlap phase and intake and compression phases. At the end of the compression stroke, the difference between the pressure computed by CFD and experimental measurements is roughly 4%.

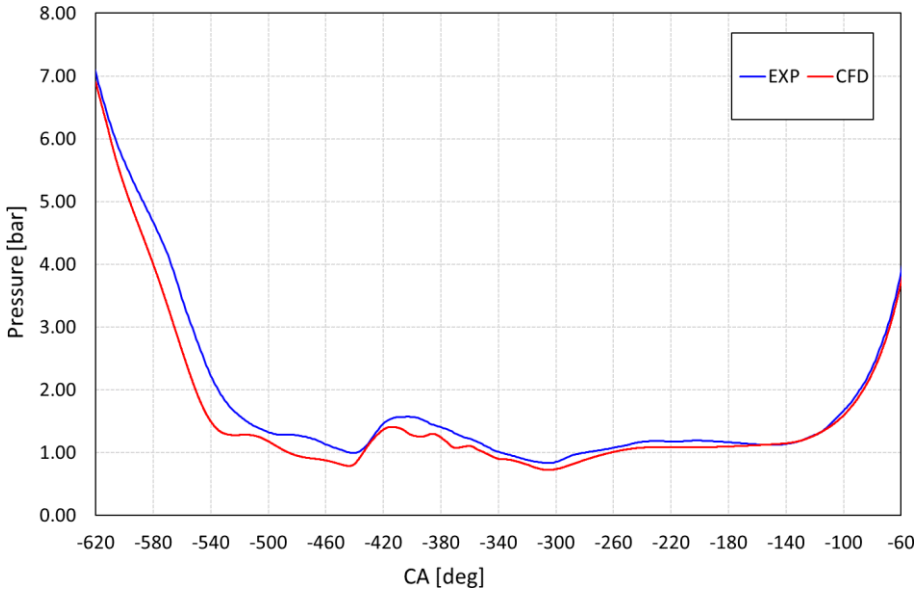

Figure 4-36. Evolution of in-cylinder pressure during the cold flow simulation at 4000rpm, compared to experimental measurements.

Figure 4-37 show the comparison of the in-cylinder temperature between the CFD and 1D model results. It can be noted that the two models are in agreement, especially during the intake and compression phases, where the differences are very small.

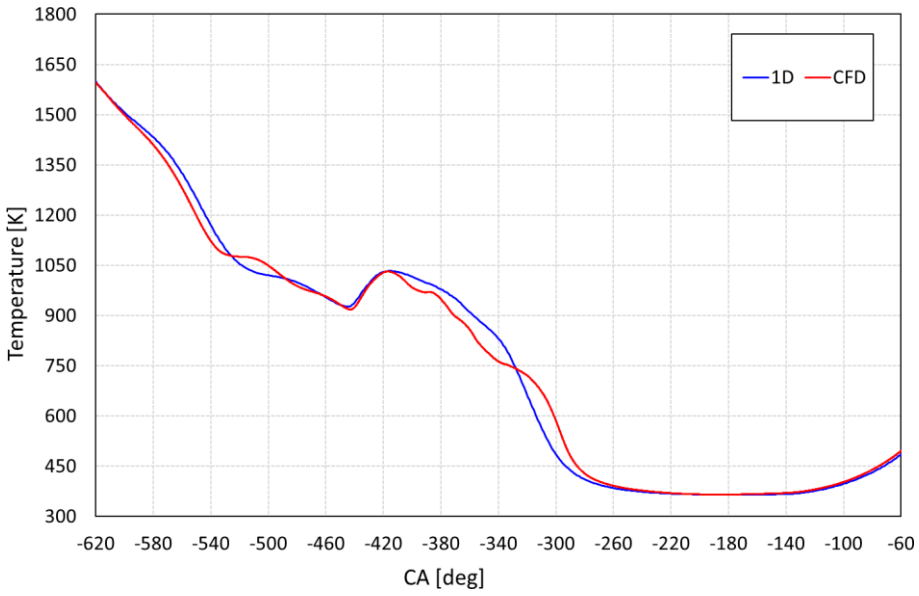

Figure 4-37. Evolution of in-cylinder temperature during the cold flow simulation at 4000 rpm, compared to the 1D model results.

Figure 4-38 shows the comparison of the turbulent kinetic energy inside the cylinder between the two operational points tested. It can be noted that during the overlap phase and while the intake valves are opening, the TKE at 4000 rpm is higher than the one computed at maximum power, since the dynamic effects coming from the intake port are not perfectly tuned. Conversely, during the intake and compression phases, the TKE at maximum power is much higher, due to the higher turbulence generated by the high

rotational speed of the engine. It is important to highlight how the turbulent flow field varies at different engine conditions, since turbulence has a great influence on the flame front propagation.

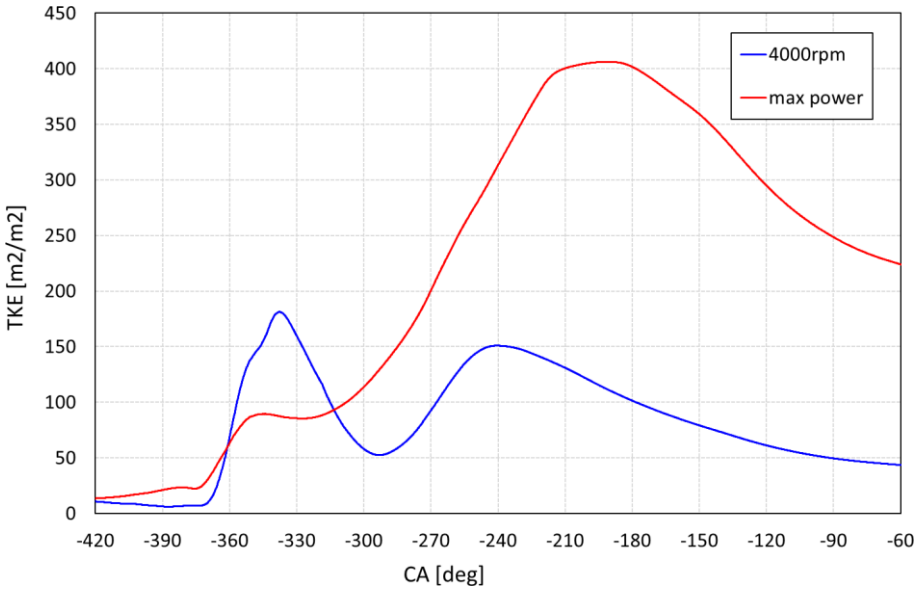

Figure 4-38. Evolution of TKE inside the cylinder: comparison between 4000 rpm and maximum power results.

Figure 4-39 reports the comparison of the turbulent kinetic energy inside the cylinder between the two different rotational speeds simulated, for three different crank angle degrees. It can be noted that at 4000 rpm, during the overlap phase, the flow coming from the exhaust port generates a recirculation zone near the exhaust valves plates while, at maximum power, the flow coming from the intake port enters with higher velocity and it tend to go towards the exhaust port. This dynamic behaviour generates a higher TKE zone inside the cylinder, which gradually decays during the intake phase, since at 4000 rpm the fresh mixture entering in the combustion chamber has less inertia than the one entering at maximum power.

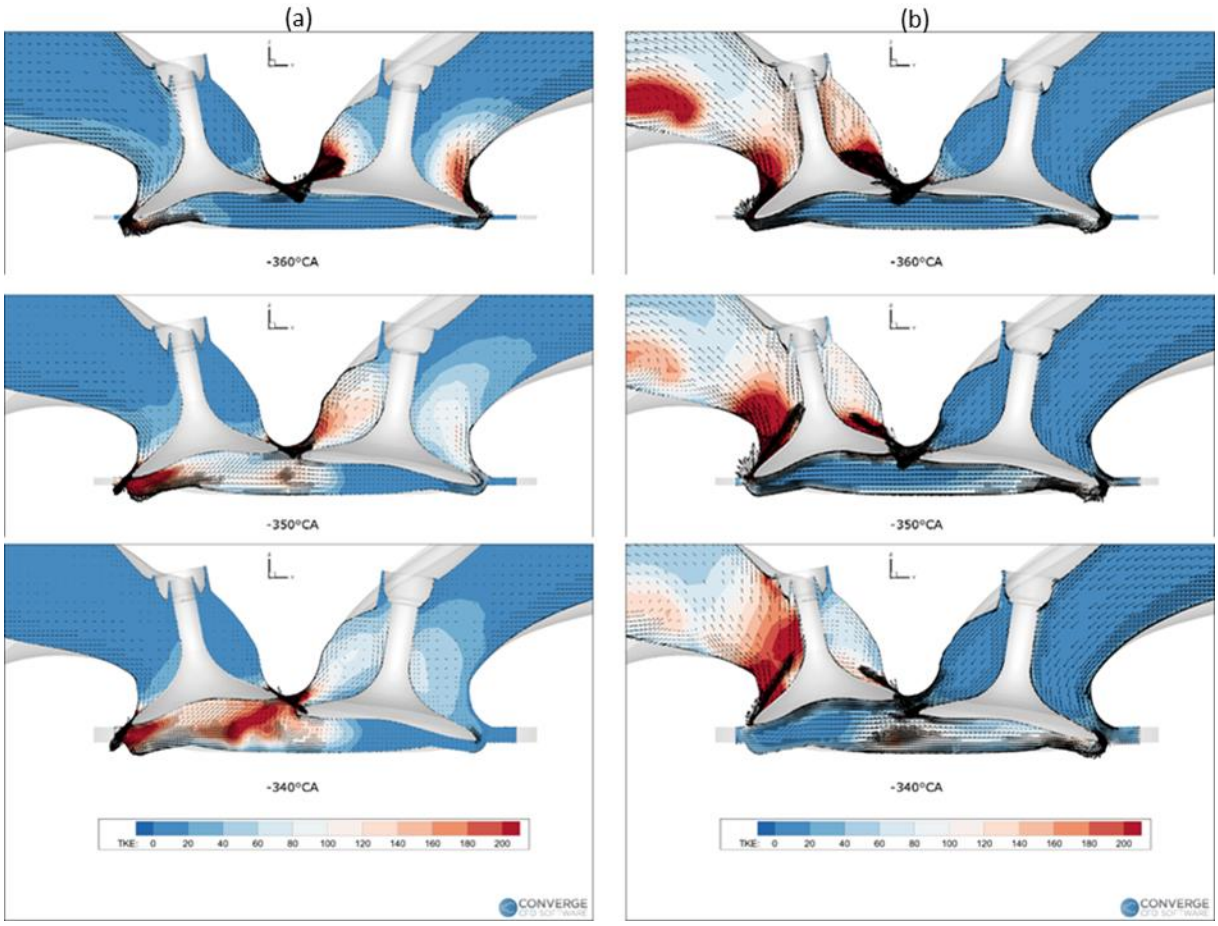

Figure 4-39. Contour of TKE and vector velocity during the overlap phase: comparison between 4000rpm (a) and maximum power (b) simulations.

The numerical set-up for combustion modelling at 4000 rpm is the same used for the calibration at maximum power. Thus, the cylinder region is refined and two different embedding are activated in the spark zone, in order to simulate properly the ignition phase. The ignition modelling is the one used for the case at maximum power, except for the crank angle durations of the energy sources, which are changed according to the rotational speed of the engine. Figure 4-40 shows the pressure inside the cylinder during the combustion process. A good accuracy is achieved during the whole process, with a slightly overestimate of the in-cylinder pressure during the exhaust phase by the CFD. As explained before, this may be caused by several factors, such as the simplified reaction mechanism used for the combustion model, which introduces differences in thermodynamic properties between the CFD and actual mixture, and the wall temperatures values, which derived from the 1D model. Nevertheless, the comparison between the CFD results and experimental measurements confirms the robustness of the numerical set-up and the predictivity of the combustion model, which is able to predict very well the pressure at different rotational speed.

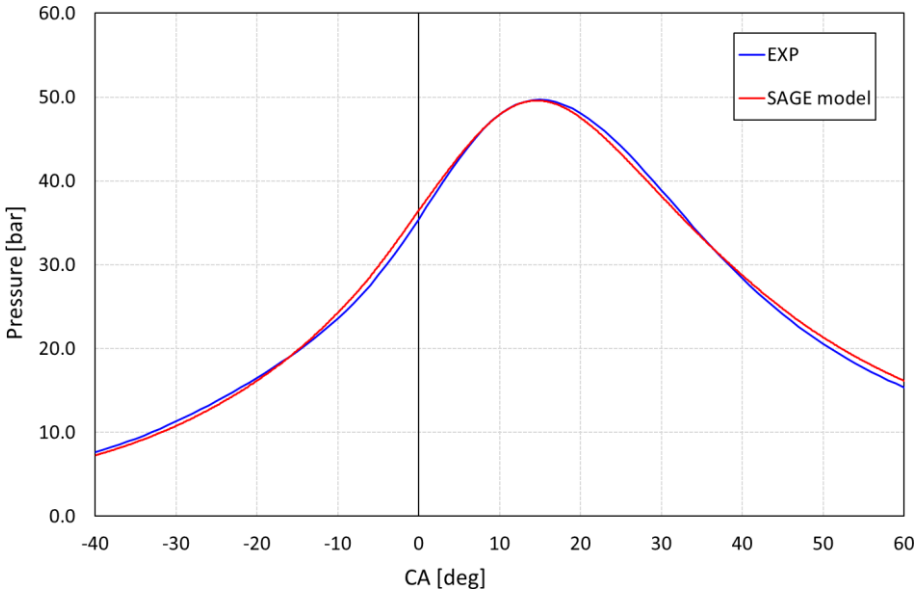

Figure 4-40. Evolution of in-cylinder pressure during combustion at 4000 rpm, compared to the experimental measurements.

Figure 4-41 shows the evolution of the flame front inside the cylinder for both 4000 rpm and maximum power CFD simulations, at different crank angles degrees. It can be noted that, during the ignition phase, the flame front at 4000 rpm is much less stretched than the one at maximum power and the flame tends to grow like a spherical shape. This behaviour is caused to the turbulent structures and fluid motion inside the cylinder: in fact, lower the rotational speed lower the turbulent kinetic energy, as reported in Figure 4-42. Thus, the flow field has less influence on the flame front propagation at 4000 rpm and turbulent motions tend to not modify the flame growth.

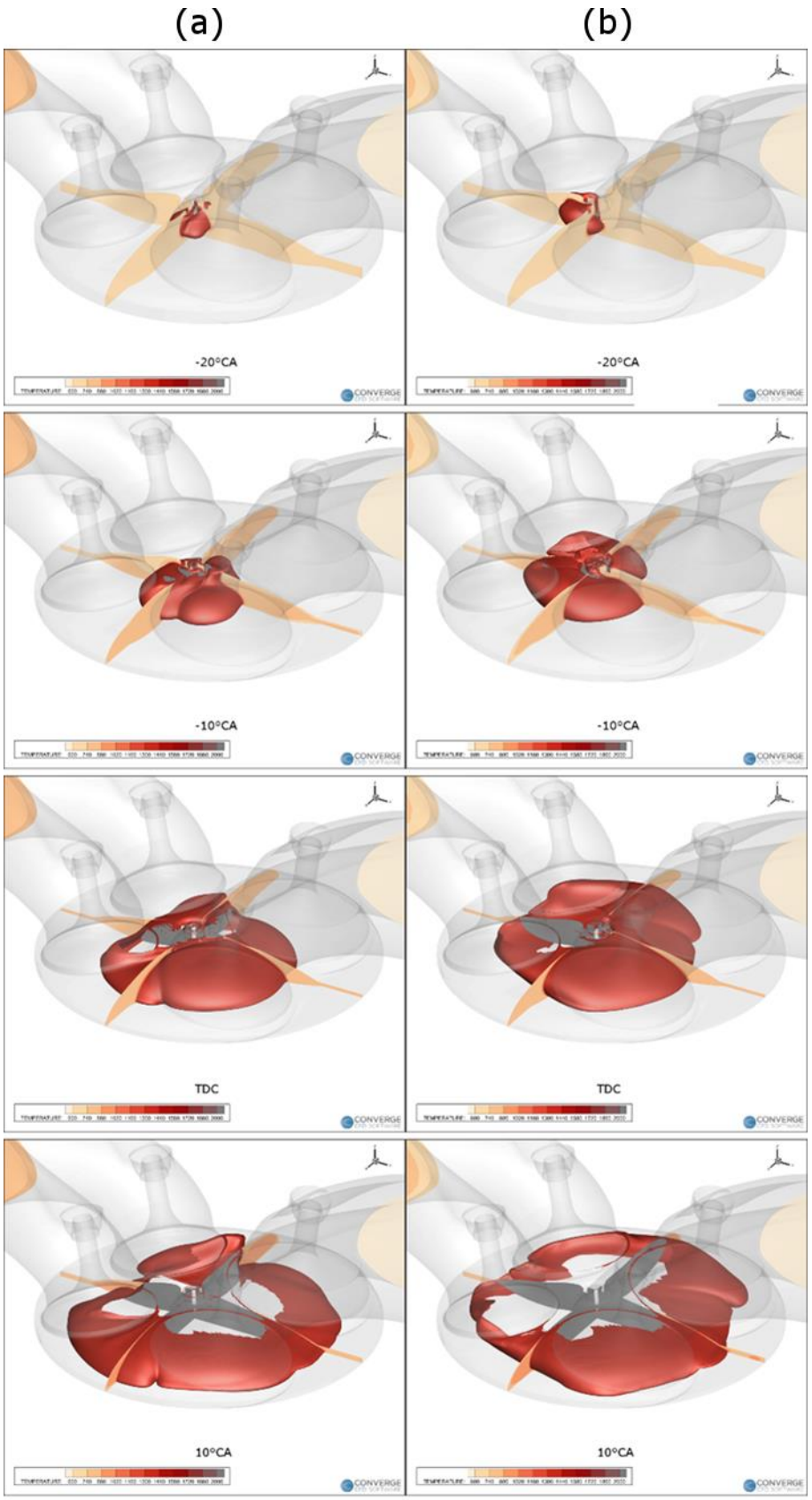

Figure 4-41. Evolution of the flame front inside the cylinder: comparison between 4000 rpm (a) and maximum power (b) combustion process.

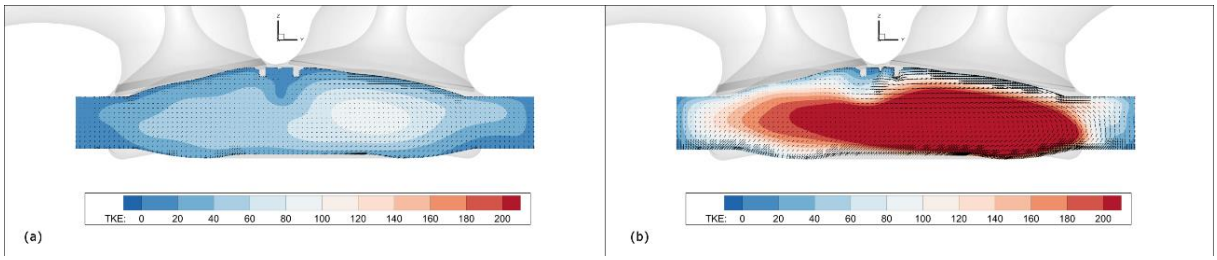

Figure 4-42. Contours of TKE inside the cylinder at 680°CA: (a) 4000 rpm and (b) maximum power.

4.4.3 - Flame surface density model: numerical set-up

As explained before, the ECFM-3Z combustion model is also used to verify the potential of a simplified model in simulating the engine performance with prechamber. This simplified approach is used with a commercial software, in which the aforementioned model is implemented. The software used for simulation with ECFM-3Z is different from the one used with the detailed chemistry model. For competition and licensing reasons between competitors, the software used for simulation with ECFM-3Z will not be declared. Figure 4-43 shows the fluid domain used for the CFD simulations with the software for modelling with ECFM-3Z, with the piston at the top dead centre.

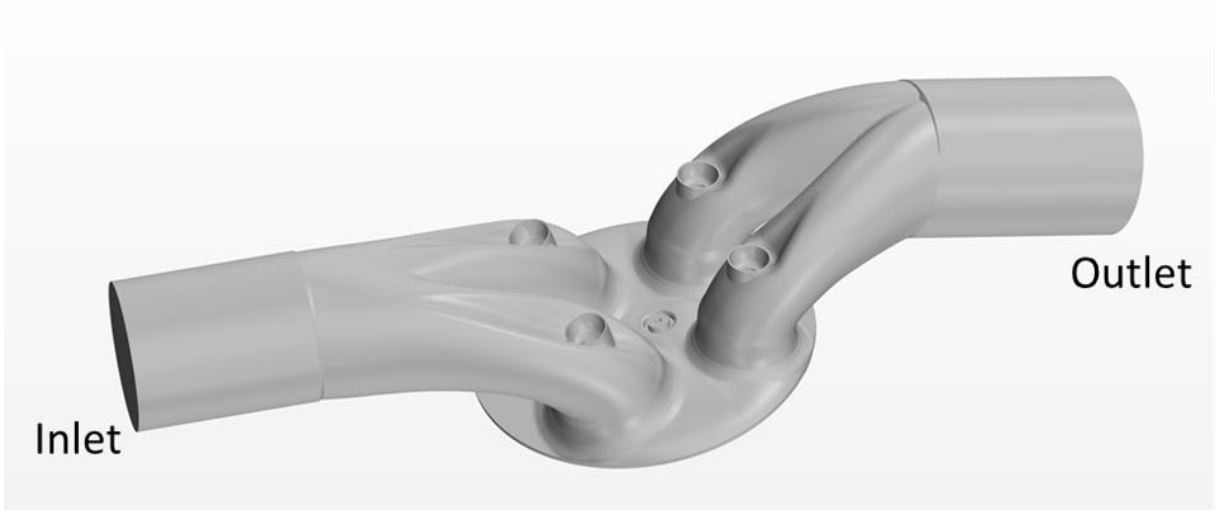

Figure 4-43. Fluid domain for 3D CFD simulations with usual software (piston at TDC).

Meshing

The internal combustion engines functioning is inherently unsteady, since the motion of the piston causes volume variations: the piston squeezes the fluid while moving from the bottom dead centre (BDC) to the top dead centre (TDC) during the compression phase, and expands it after the combustion phase, transferring energy to the crank shaft. Due to the piston motion, the shape of the fluid domain changes; thus, a dynamic

mesh is required, which allows the motion and deformation of its elements. The computational grid inside the cylinder is generated by an add-on pack that can handle the dynamic mesh during the unsteady analysis of internal combustion engines simulations. The mesh generated is built using the trimming method. This technique requires a 2D mesh that is extruded to build the 3D non-structured mesh. The base grid size of cells is set to 0.75 mm for the engine simulations, with a minimum cell size of 0.3 mm in zones where the mesh is refined, like in the spark-plug zone and near the valves. The growth rate, i.e. the parameter that handles the change dimension between adjacent cells, is set to 1.1. After defining the 2D mesh properties, the computational two-dimensional template is extruded by 0.57 mm to obtain the 3D mesh for the cylinder and valves zone (Figure 4-44).

Figure 4-44. 3D computational grid inside the cylinder for CFD simulation with flame surface density model.

The computational grid inside the intake and exhaust ports is then coupled to the one generated for the cylinder region. The fluid domain referring to ports is shown in Figure 4-45 and the base grid size in the ports is set to 1 mm.

Figure 4-45. Fluid domain for meshing intake and exhaust ports for CFD simulation with flame surface density model.

The different grids are coupled through an interface, called stub, which ensures the continuity between the ports and the cylinder during the CFD simulations. After coupling the ports mesh with the cylinder one, the computational grid for the whole fluid domain is obtained. Figure 4-46 shows the mesh of the engine with piston at the TDC on two different sections, one passing through the spark plug (a) and one passing through the valves (b).

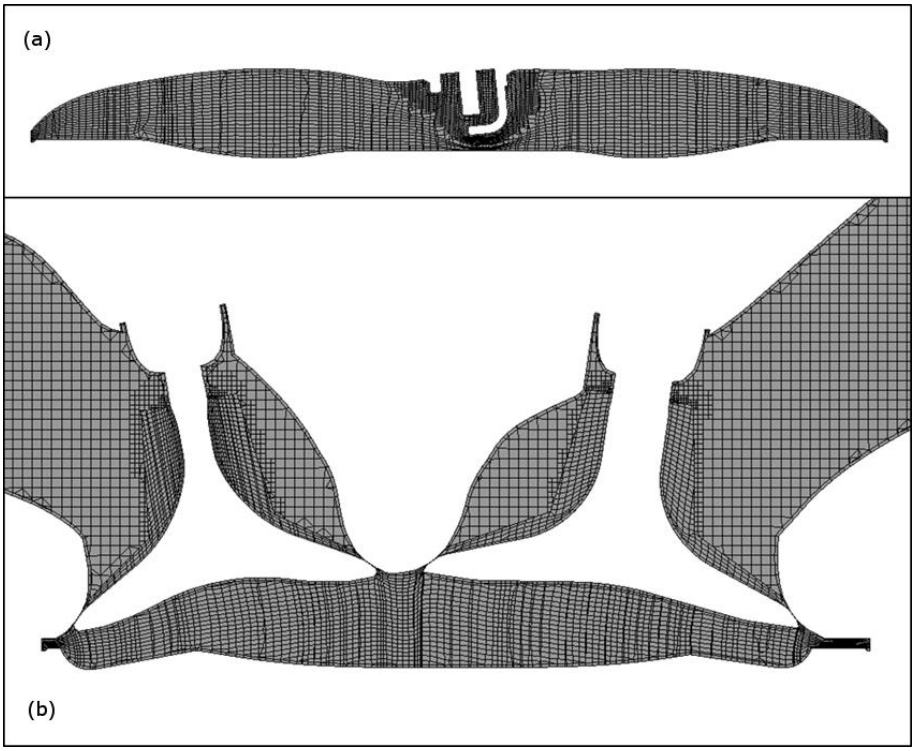

Figure 4-46. Computational grid for CFD simulations with flame surface density model: (a) section passing through spark plug; (b) section passing through the valves.

Table 4-17 summarizes the number of cells during CFD simulations.

Total cells number	2229083
Cells number @BDC	1814352
Cells number @TDC	913963

Table 4-17. Mesh properties for CFD simulations with flame surface density model.

Numerical models

Unsteady RANS (U-RANS) simulations are carried out to analyse the combustion process of the tested engine and the RNG $k-\varepsilon$ model is used for turbulence modelling. The pressure velocity coupling is handled by PISO algorithm. The time step is set to 0.1° for the whole simulation, except for combustion phase and opening/closing valves, during which the time step is set to 0.05°. The second order central difference numerical scheme is used for the spatial discretization of the continuity equation, while the MARS (Monotone Advection and Reconstruction Scheme) is used for all the other equations. The GruMO-UniMORE model is used for wall heat transfer modelling inside the cylinder during the CFD simulations. In this approach, the Prandtl number is considered as a constant in space but not in time [62]. Thus, in the internal zone of the boundary layer, it is recomputed every time step for each near wall cell according to the thermodynamic values of the fluid, i.e. specific heat, thermal conductivity and dynamic viscosity. As explained in previous chapter, the ECFM-3Z is used as combustion model. The Imposed Stretch Spark Ignition Model (ISSIM) is used for modelling the ignition phase [63]. It is a Eulerian spark-ignition model for 3D RANS simulations of internal combustion engine applications, in which a simplified inductive electrical scheme is used to simulate the spark plug and model the flame kernel growth. The model provides an amount of energy to the fluid, which leads to an increase of temperature and laminar flame speed. Thus, the laminar flame speed is modified to take into account the effect of the energy released by the spark plug to the gas. Table 4-18 summarizes the ignition parameters of ISSIM model used to simulate the ignition phase.

X-spark plug [mm]	-5.30
Y-spark plug [mm]	1.392
Z-spark plug [mm]	1.125
Energy [J]	0.05
Inductance [H]	10
Resistance [Ω]	5000

Table 4-18. Characteristic of ISSIM model.

Materials

Since the test case is a port fuel injection engine, the air/fuel mixture is considered homogeneous: thus, the injection phase is not modelled and the combustion is considered purely premixed. The fuel is modelled as gasoline and the equivalence ratio of the mixture is set from experimental data. Since the lack of data on actual fuel used for experimental tests, the thermodynamic properties of the mixture are set based on previous experiences with the commercial software. Table 4-19 summarizes the mixture properties used with for the simplified approach.

Fuel chemical composition	$C_{7.4}H_{13.2}$

Fuel LHV [kJ/kg]	43277.8
Equivalence ratio	1.213
Density	Ideal gas
Molecular weight [kg/kmol]	28.96
Specific heat at constant pressure [J/kg/K]	Polynomial
Thermal conductivity [W/m/K]	Polynomial
Molecular viscosity [Pa*s]	Sutherland

Table 4-19. Air/fuel mixture properties for the simplified approach.

4.4.4 - Flame surface density model: combustion model calibration

With the presented setup, the 3D CFD simulation of the engine is carried out in order to calibrate the combustion model. At first, the results of the cold-flow are presented, in order to analyse the flow field before the combustion starts. Contours of velocity, together with velocity vectors, are presented during the scavenging process and the results are compared to the experimental data and 1D model. The tumble motion inside the cylinder is also described, in order to provide a larger comprehension of the flow field inside the engine. Finally, the reacting-flow simulations results are presented, together with the combustion model calibration. The CFD in-cylinder pressure is compared to the experimental results and the contours of progress variable and turbulent kinetic energy are shown for a visualization and understanding of the combustion process.

Non-reacting flow results

The simulations start before the opening of the exhaust valves, in order to model the entire exhaust phase properly. Figure 4-47 shows the evolution of the pressure inside the cylinder during the cold-flow. The results of the CFD simulation are quite accurate, especially during the exhaust and compression phases. It can be noted that the CFD in-cylinder pressure is under predict during the overlap phase respect to the experimental data, with calculated values differing from the experimental ones by 15% at most. Furthermore, a slightly under predict of in-cylinder pressure can be observed at the end of the compression phase, with a difference between the CFD data and experimental one of 7%. Nonetheless, concluding that CFD results are inaccurate would be inappropriate, since CFD calculations are based on some assumptions that simplify the flow modelling such as the ideal gas assumption for the air/fuel mixture. Lastly, the experimental values are obtained through a sensor that measures the in-cylinder pressure relative to a reference value, which corresponds to the absolute pressure inside the cylinder at the valve overlap and which is assumed equal to the atmospheric pressure.

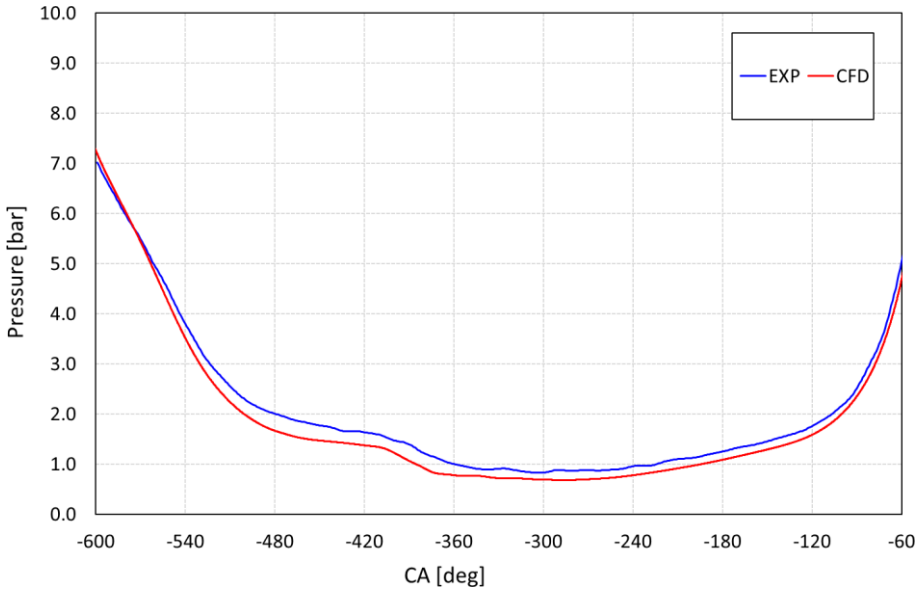

Figure 4-47. Evolution of the in-cylinder pressure for the cold-flow simulation, compared to the experimental data.

Figure 4-48 shows the exhaust gas recirculation (EGR) contour and the flow field on a section passing through the valves, during the overlap phase. Since the CFD analysis is performed at the maximum power, the thermodynamic effects are not tuned: as the intake valve opens, the in-cylinder pressure is greater than the pressure in the intake port and a small amount of burnt gases is pushed towards to the inlet. Furthermore, after the exhaust valves closing, a small amount of burnt gases is still remained inside the cylinder, due to the not perfect tuning of the exhaust dynamic effects. Nevertheless, the amount of burnt gases trapped in the cylinder after the exhaust phase is 1.17%, testifying the well scavenging process despite the high rotational speed.

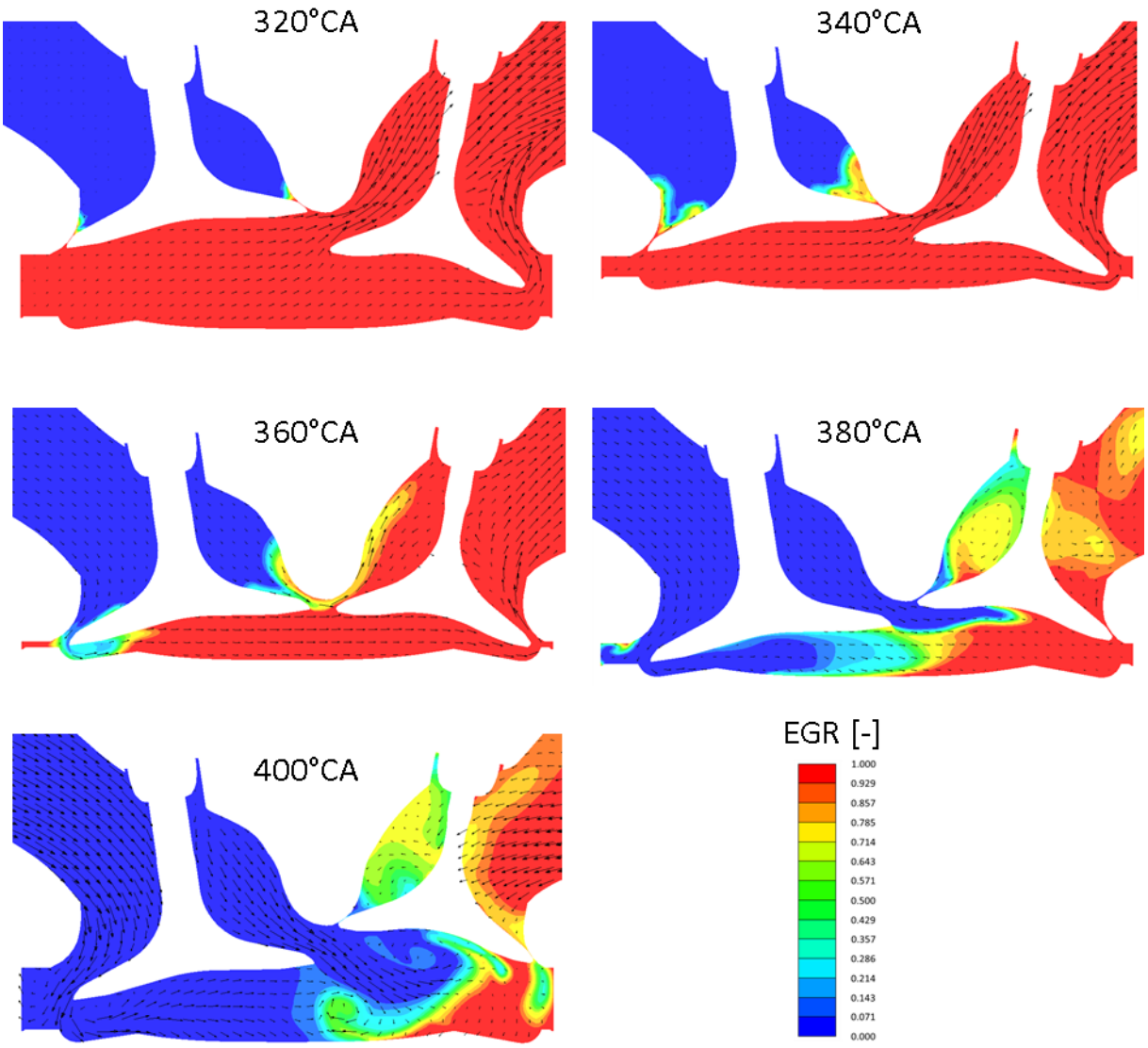

Figure 4-48. EGR contour and flow field during the overlap phase.

The flow field inside the cylinder during the compression phase is shown in Figure 4-49. The contours of velocity and vectors are shown on a section passing through the spark plug. The intake valves are on the left, while the exhaust valves are on the right. While the piston is moving towards the TDC, the tumble motion is clearly noticeable. This recirculation is caused by the interaction between the fresh mixture entering from the intake valves and the piston motion.

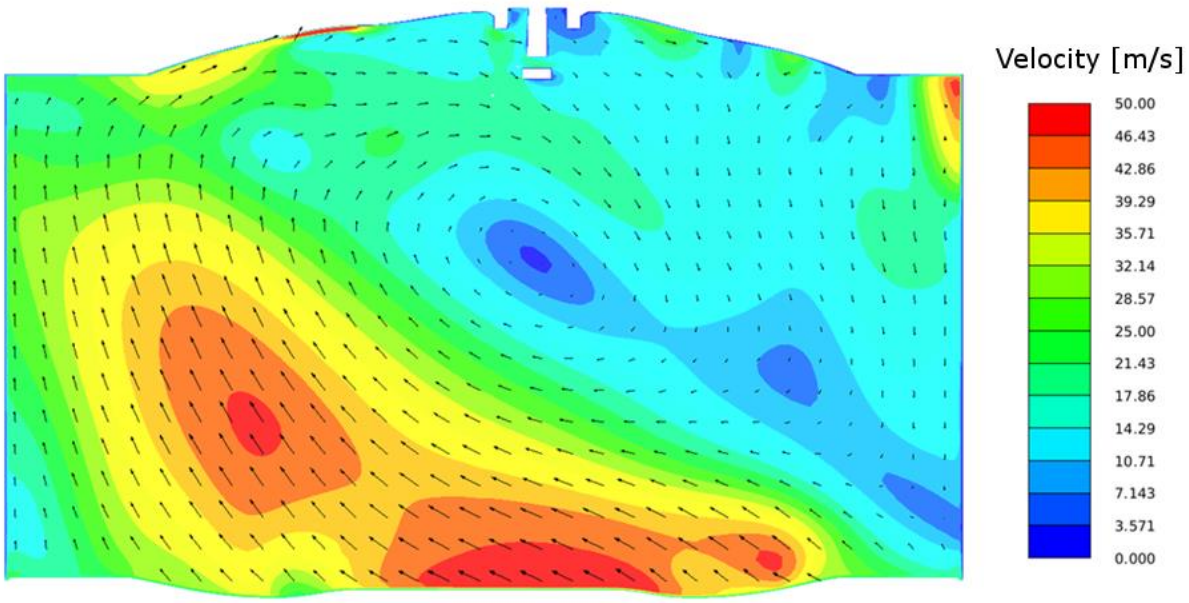

Figure 4-49. Velocity contours and vectors at 600°CA (section passing through the spark plug).

Tumble motion can be evaluated by means of tumble ratio, i.e. the ratio of the flow angular velocity (relative to the axis perpendicular to the piston one) to the crankshaft rotational speed. It is a dimensionless quantity and it is used to compare the flow motion inside the different engines, in order to quantify the differences due to geometrical features or working parameters. Figure 4-50 shows the evolution of tumble ratio inside the cylinder. Two different peaks can be noted: the first, during the overlap phase, during which the intake and exhaust valves are both opened and the fresh mixture starts to enter the cylinder; the second, where the piston is almost at the BDC, due to the wave coming from the intake port. As the piston moves upwards to the TDC, the tumble motion gradually decays.

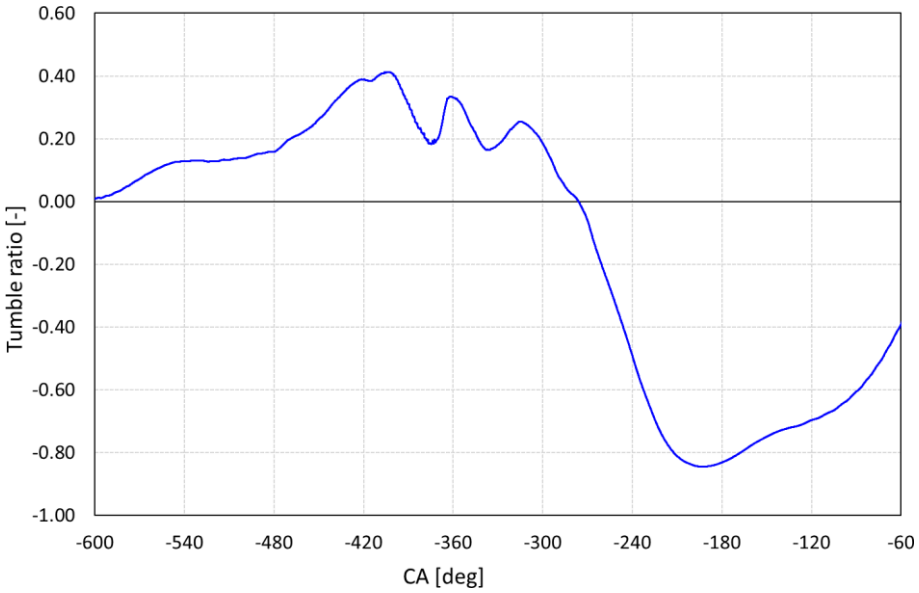

Figure 4-50. Evolution of tumble ratio during the cold flow.

Figure 4-51 reports the evolution of the mass trapped in the cylinder, comparing the 1D model and CFD results. The CFD results slightly overpredicted the in-cylinder mass at the end of the intake phase, respect to the 1D model. Nevertheless, a good agreement is achieved with the 1D model results, confirming the accuracy of the numerical set-up.

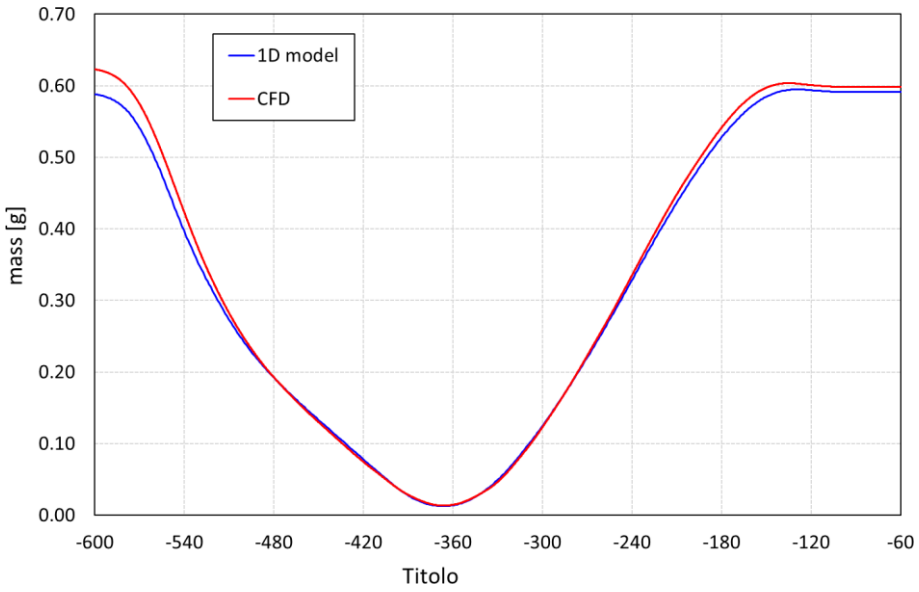

Figure 4-51. In-cylinder mass during cold flow: comparison between 1D model (blue line) and CFD (red line).

Reacting flow results

After the cold flow analysis, the combustion results of the engine are presented. As explained before, the combustion model used to analyse the engine with the usual software is the ECFM-3Z, which is based on

the progress variable and flame surface density definition. The flame propagation is thus modelled using semi-empirical correlations, based on local values of pressure, temperature and equivalence ratio. Since the chemical reactions are not accounted for in the simplified model, its calibration is carried out by varying the spark advance. It is worth noting that a simplified approach based on the progress variable is not able to correctly model the ignition delay, since the model uses semi-empirical correlations to simulate the flame kernel growth and flame propagation. Thus, a sensitivity to the spark advance is needed. Figure 4-52 shows the pressure inside the cylinder varying the spark advance. As we can see, earlier the spark time higher the pressure peak inside the cylinder and earlier the combustion starts.

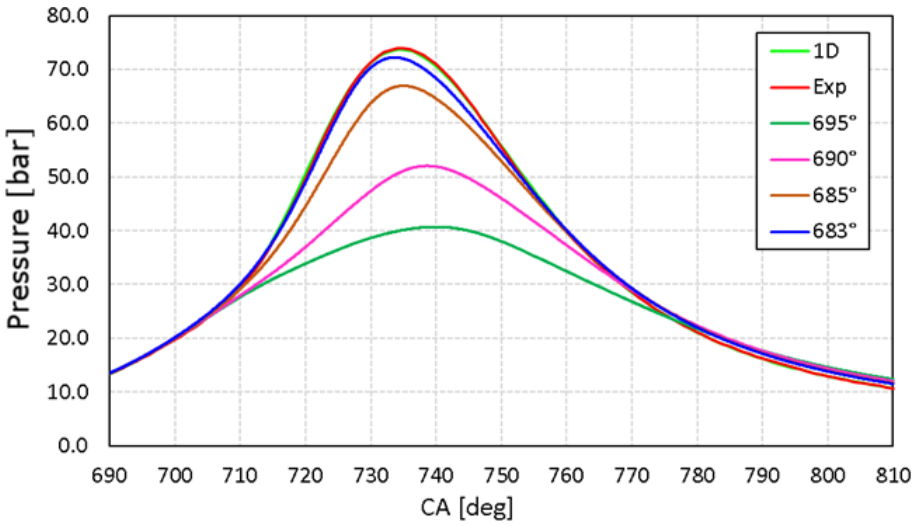

Figure 4-52. In-cylinder pressure during combustion: spark advance sensitivity (flame surface density model).

The spark advance adopted at the test bench is 687° (-33° before the top dead centre). The ECFM-3Z combustion model is calibrated for a spark advance equal to 683°. The evolution of the in-cylinder pressure during the combustion for the calibrated model is shown in Figure 4-53. The CFD calculations tend to underestimate the pressure values during the first phase of the combustion process, with a pressure peak 2.3% lower than the experimental one. The CFD results show a higher in-cylinder pressure during the expansion phase. These differences may be caused by many factors: as explained before, the assumption of ideal gas may affect the compression ratio, as well as assumptions regarding the fresh mixture. Furthermore, the wall temperatures and thermodynamic properties of the mixture may influence the expansion regime too. In particular, the lower heating value has a strong influence on the energy release and expansion phase. Nevertheless, CFD results are satisfactory and a good agreement is achieved with the experimental data.

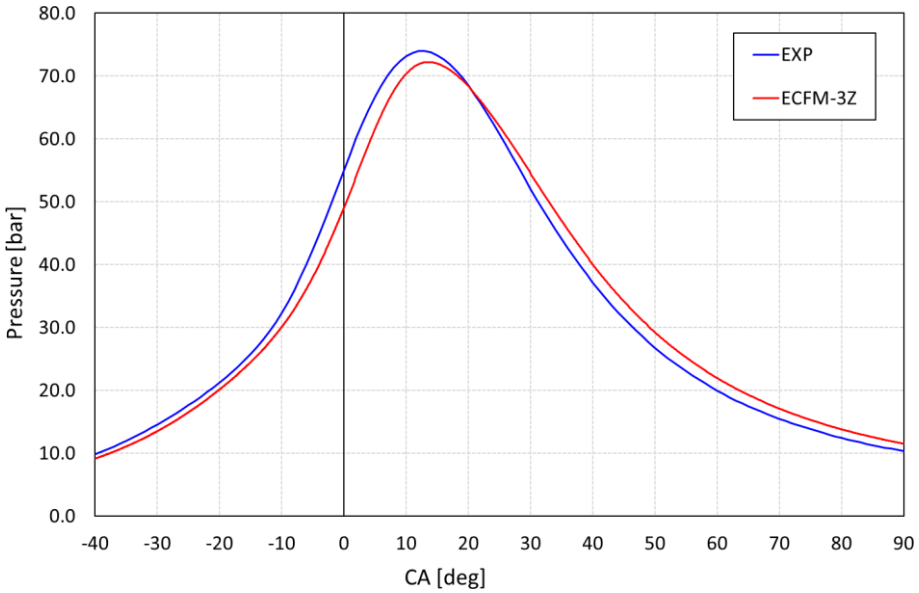

Figure 4-53. Evolution of the in-cylinder pressure for the calibrated combustion model (ECFM-3Z), compared to the experimental data.

Figure 4-54 shows the comparison between CFD and experimental data of the burned mass fraction. A very good accuracy is achieved, especially in the middle of the curve, from 10% to 60% of burned gas mixture. CFD calculations tend to model a slower process, as previously observed from the in-cylinder pressure trend (Figure 4-53). Notwithstanding some differences, the combustion process is well represented, especially during the turbulent combustion phase, which is predicted with very good accuracy.

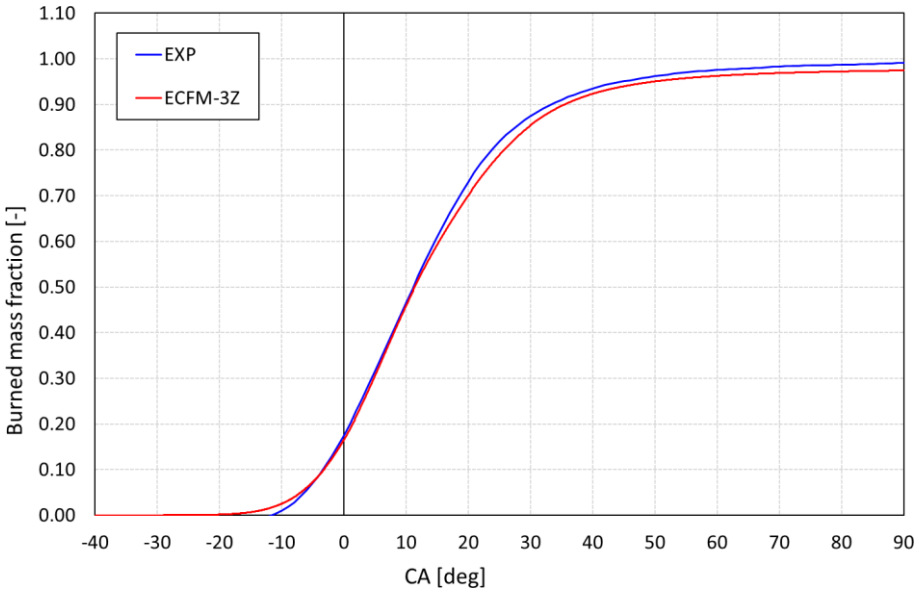

Figure 4-54. Evolution of the burned mass fraction for the calibrated combustion model (ECFM-3Z), compared to the experimental data.

Figure 4-55 reports the durations of the combustion process in terms of 10%-50% and 10%-90% of burned mass fraction. It can be noted that this simplified approach models a combustion slightly slower than the

experimental one: the CFD combustion process is roughly 8% longer (10-90% duration) than the experimental one.

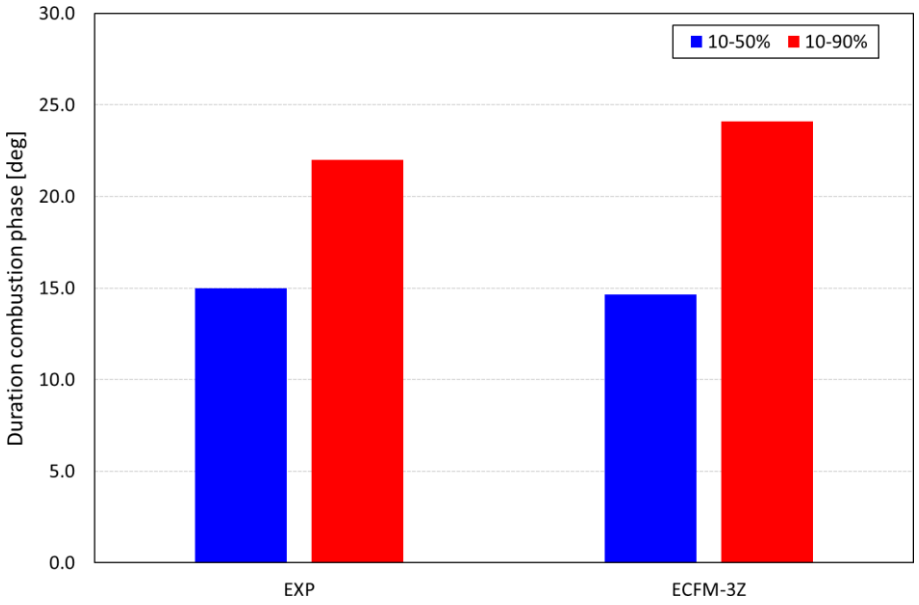

Figure 4-55. Duration of combustion process: comparison between ECFM-3Z and experimental results.

Figure 4-56 shows the evolution of turbulent kinetic energy and vector velocity (a) for different crank angle degrees during the combustion process, together with the contour of progress variable (b). In Figure 4-56 (b), the grey area represents the burned gases and the unburned air/fuel mixture, while the red and yellow areas identify the zones where the combustion is taking place. It is clearly noticeable how the combustion process is influenced by the flow field and how turbulent motions affects the flame front propagation. Since the ignition phase, the flame kernel is stretched by the flow field inside the combustion chamber. Once the flame kernel grown and the turbulent combustion phase begins, the flame front is faster towards the intake valves side, since the turbulent kinetic energy is greater than the other side, confirming that combustion process is enhanced by turbulence.

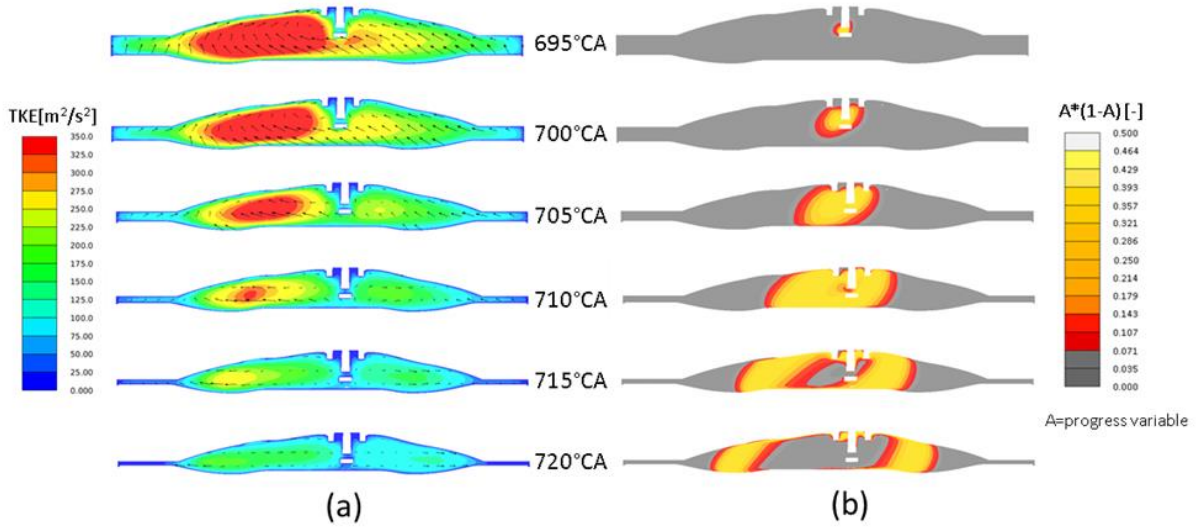

Figure 4-56. Evolution of combustion process on a section passing through the spark plug (flame surface density model): contours of TKE (a) and progress variable (b).

5 - Prechamber CFD results

After the calibration and validation of the combustion model, the same numerical set-up is used for CFD simulations of the engine with prechamber. This part of the thesis is conducted in collaboration with HPE COXA, an industrial partnership based in Modena. At first, several geometries of prechamber are generated with different shape and orifices diameters. The dimensions of the prechambers tested are not provided for confidentiality reasons. Later, the numerical set-up of the CFD simulations with prechamber will be briefly explained. Finally, the results of CFD simulations of the engine equipped with prechamber will be presented. At the beginning, the CFD results of the first geometry tested will be shown, comparing the numerical solutions of the SAGE model with the flame surface density model, in order to evaluate the advantages and drawbacks of the two different methods. Then, the CFD results of the remaining geometries will be presented, using the detailed chemistry solver only, and the effects of shape and nozzles variations will be analysed. Since the use of the prechamber allows to ignite a lean air/fuel mixture in order to reduce the fuel consumption and increase the engine efficiency, a further investigation on the engine equipped with prechambers will be shown. This analysis is carried out by varying the air-to-fuel ratio of the mixture. The CFD results of the engine with prechamber are compared to the ones with baseline configuration.

5.1 - Test case

The prechamber combustion consists of a small volume mounted above the head of the engine, in which the spark plug is located. During the scavenging process, the burned gases exit the prechamber during the exhaust phase and the fresh mixture enters during the intake and compression phases through small orifices, which connect the prechamber with the main combustion chamber in the cylinder. The fresh mixture consists of oxidant and oxidizer in case of passive prechamber: the fuel is injected in the intake port and it is already pre-mixed with the air when it enters the combustion chamber. The objective of this thesis is to evaluate the man advantages of a passive prechamber on the 4-stroke engine and to analyse how the main geometrical parameters may affect the combustion process. Thus, different geometries are designed, according to the literature information and based on previous experience of the industrial partnership. Figure 5-1 shows a schematic design of the prechamber used in this thesis. All the geometries simulated are characterized by six cylindrical orifices, in order to encourage the scavenging process of the prechamber. The orifices are inclined at 75° respect to the cylinder axis to facilitate the fresh mixture filling inside the prechamber. Concerning the prechamber volume, high values of the prechamber volume means higher amount of fuel inside the prechamber. It is worth noting that the fuel burning inside the prechamber is affected by energy losses when the flame enters in the main chamber. Thus, the combustion in the prechamber provides a less contribution to work than the one occurs in the main chamber. Therefore, high values of prechamber volume may generate faster combustion process at the cost of a less increase in in-cylinder pressure curve. Conversely, small values of the prechamber volume may generate flame jets with low inertia, since the amount of fuel burnt is very low, frustrating the advantages of the prechamber itself. Thus, based on literature review (see 1.2.1 -), the volume is chosen equal to 2% of the volume of the combustion chamber.

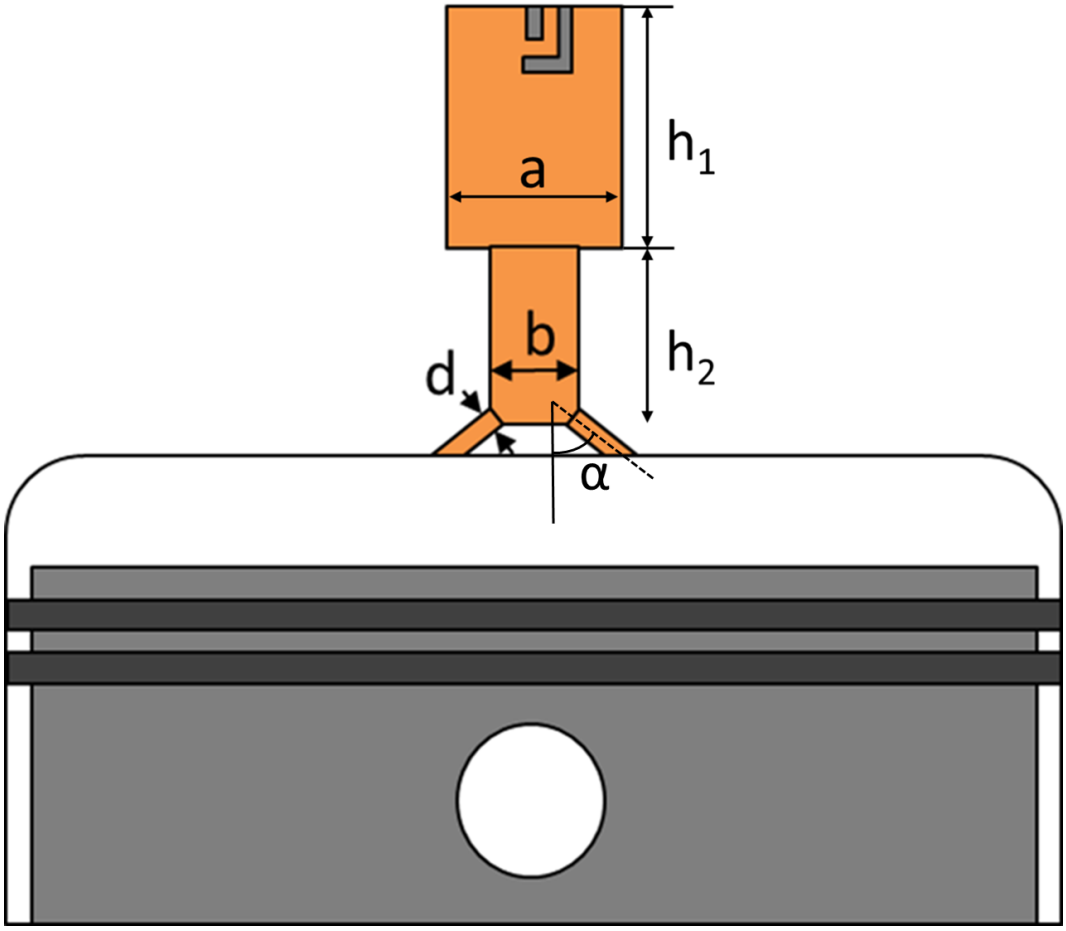

Figure 5-1. Prechamber scheme.

At first, two different prechambers are designed, namely PC1 and PC1_S. The geometrical characteristics in terms of volume, number of orifices and nozzles diameters are identical. They differ from each other in the shape of the prechamber and in the aspect ratio, i.e. the ratio between the height of the prechamber and the radial dimensions. The geometrical characteristics of the prechamber simulated are summarized in Table 5-1. The actual dimensions of the tested prechambers are not provided for confidentiality reasons, therefore each parameter is reported in a dimensionless form, with respect to a reference value. As explained before, the PC1_S geometry differs from the others in the shape. In fact, it has a more shaped profile, with sharp edges, while the others have a fillet radius between the rod and the upper part of the prechamber, i.e. where the spark plug is located. Considering the thermal effects and the high temperatures on the walls of the prechamber, the rounded shape is to be preferred. The orifices diameter is probably the most uncertain and pivotal feature in the prechamber design. It affects the scavenging process of the prechamber, together with the fresh mixture filling: large diameters lead to a better scavenging process since the pressure drop is lower. Furthermore, it affects the combustion process and flame front propagation too: high value of the diameters may lead to a worse combustion process, since the passage area is too large for generating fast flame turbulent jets. Thus, in order to investigate the effect of the orifice diameter on the engine and to verify the optimum in terms of ratio between the overall flow passage area and volume (A_t/V_{pc}), two additional geometries are designed, starting from the PC1 one, by varying the orifices diameters (Table 5-1).

Prechamber	PC1_S	PC1	PC2	PC3
Volume (%V_{cc})	2	2	2	2
Number of orifices	6	6	6	6
A	a	1.1*a	1.1*a	1.1*a
b	b	b	b	b
d	d	d	1.1*d	1.2*d
h_1	h	1.1*h	1.1*h	1.1*h
h_2	s	1.2*s	1.2*s	1.2*s
α [°]	75	75	75	75
AR	1.70	1.85	1.85	1.85
A_t/V_{pc} [1/m]	6.00	6.00	7.26	8.64

Table 5-1. Geometrical properties of prechambers tested.

The prechamber is placed where the spark plug is located in the baseline configuration. The spark plug mounted in the prechamber is the same of the baseline configuration. It is worth noting that the prechambers PC1 and PC2 are actually manufactured for experimental testing, since, as explained in next paragraphs, according to the CFD results, they are found to be the best configuration for the engine. At the time of writing this thesis, the engine prototype is being modified for carrying out the experimental activity at the test bench. Thus, no measurements are available for the engine with prechamber.

5.2 - Numerical set-up

The same numerical set-up used for calibrating the combustion model is used for the CFD simulations of prechamber. Thus, U-RANS simulations are carried out to analyse the combustion process of the tested engine and the RNG $k-\varepsilon$ model is used for turbulence modelling. The pressure velocity coupling is handled by PISO algorithm and the second-order upwind numerical scheme is used for the spatial discretization of the governing equations. The convergence residuals are set to 10^{-5} for all the solved quantities. The numerical set-up of the combustion model is the same obtained after the calibration and validation analysis. The set-up of the mesh inside the cylinder is equal to the simulation of the baseline configuration. In addition, a refinement in the prechamber volume is added in order to resolve properly the flow field and turbulent structures. Thus, an embedding with scale 4 is used inside the prechamber, during the cold flow simulation, while a scale 5 is set during the combustion process in the whole prechamber domain. It is worth noting that the AMR is still active, thus a minimum size of 0.125 mm is obtained inside the cylinder too during the combustion simulation. The boundary conditions are the same extracted from the 1D model, which are used for the baseline configuration. Concerning the wall temperature, an increase of roughly 30% is assumed for the wall temperature of the prechamber respect to the head one. This hypothesis seems to be reasonable, since the prechamber volume is more difficult to cool and the scavenging process is less efficient than the in-cylinder one: thus, residuals gases trapped in the prechamber may be produce a higher wall temperature.

A maximum cells number of five million is set for combustion simulations to limit the required computational effort of CFD tests. Table 5-2 reports the numerical set-up used for simulations with prechamber.

Numerical simulation	U-RANS
Solver	CONVERGE CFD
Turbulence model	RNG $k-\varepsilon$
Combustion model	SAGE
Algorithm	PISO
Numerical scheme	Second-order upwind
Convergence residuals	10^{-5}
Mesh	Finest
Minimum time-step [s]	10^{-8}
CFL [-]	1
Cell size in prechamber during cold flow [m]	0.250
Cell size in prechamber during combustion [m]	0.125
Maximum cells number during cold flow	2601580
Maximum cells number during combustion	5078493
Prechamber wall temperature [K]	580

Table 5-2. Numerical set-up for CFD simulations with prechamber.

Figure 5-2 shows the refinement of the fluid domain inside the cylinder and prechamber during the combustion simulation.

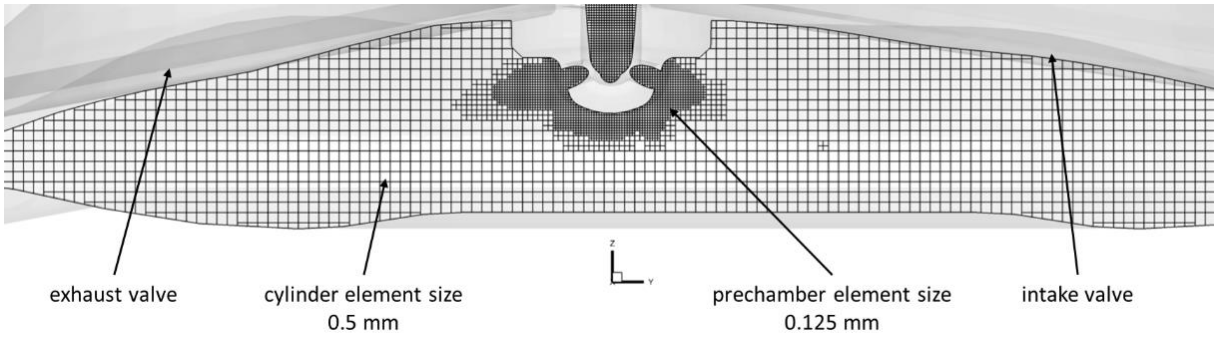

Figure 5-2. Example of mesh with prechamber during combustion simulation.

As explained in previous chapter, when using a detailed chemistry solver, it is crucial to model the interaction between the turbulent structures and chemical reactions. Thus, it is fundamental to resolve properly the flow field, which has a strong influence on the flame growth and propagation. Therefore, as already done during the calibration of the combustion model, two revolutions are run before to simulate the combustion process. The results of the combustion simulations with prechamber will be shown in next paragraphs, together with the flow field analysis during the scavenging process of both cylinder and prechamber. As explained before, the CFD results in next paragraphs refer to the third revolution of the engine.

5.3 - Prechamber results at maximum power

With the presented numerical set-up, the 3D CFD analysis of the engine equipped with prechamber is carried out. At first, the results of the cold-flow are presented, together with the contours of velocity during the scavenging process for both main chamber and prechamber. In the beginning, the results of the simulation of the prechamber PC1_S will be presented in terms of in-cylinder pressure, pressure inside the prechamber and contour flame front propagation. The CFD results between the SAGE model and the ECFM-3Z model will be compared, analysing the flame front propagation and the pressure inside the engine during combustion. The comparison of the CFD results of the engine with prechamber and the baseline configuration will be presented too, in order to evaluate the benefits by using the prechamber. Since the simplified combustion model is not able to predict the combustion process in the prechamber accurately, only the SAGE model is used for modelling the combustion process with the remaining prechambers geometries. Finally, the reacting-flow simulations results carried out with the detailed chemistry solver are shown, analysing the combustion process inside the prechamber and the main chamber and comparing the pressure curves, flame front propagation and combustion duration with the baseline results. In order to investigate the accuracy of the simulations, the results of the detailed chemistry solver with the first prechamber geometry are compared with the ones obtained using the simplified approach. Finally, the CFD results with the remaining prechamber geometries are analysed in order to identify the best configuration for the engine.

Figure 5-3 shows the comparison in terms of pressure, during the cold flow simulation, between the baseline configuration and the engine with prechamber. The pressure inside the prechamber is the dashed red line. It can be noted that the differences between the in-cylinder pressures are minimum, sign that the prechamber does not affect the pressure inside the main prechamber during the scavenging process. It can be observed that, during the compression phase, a pressure drop between the main chamber and prechamber is established, due to the narrow orifices. At the end of the compression phase, the pressure difference between the main chamber and prechamber is roughly 1.5 bar.

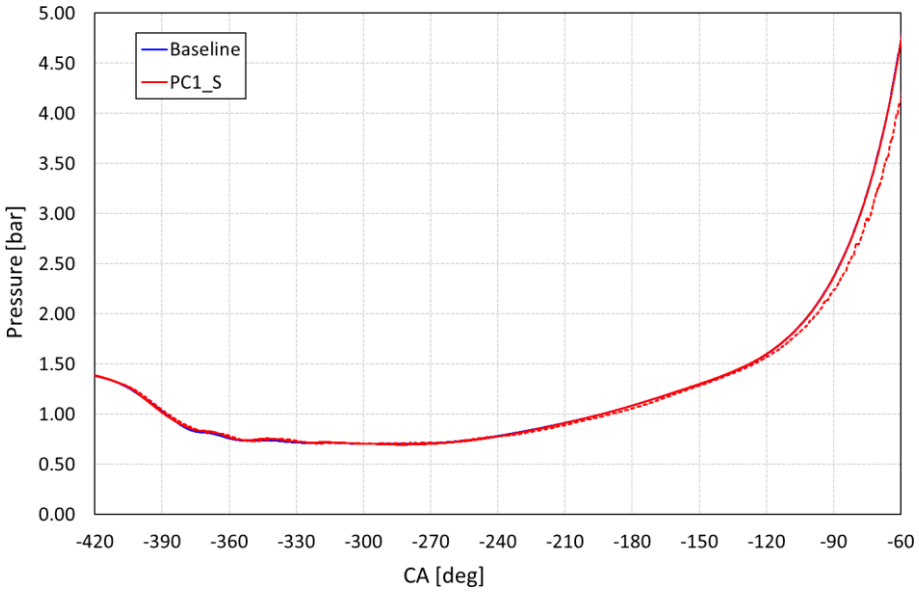

Figure 5-3. Evolution of pressure during the overlap, intake and compression phases: comparison between baseline (blue line) and prechamber (red line) configuration.

It is worth noting that the residuals mass of burnt gases trapped in the prechamber at the end of the compression phase is less than 2%, to reflect the goodness of the scavenging process. This is very important in prechamber applications, since a high amount of burnt gases around the spark plug may inhibit the chemical reactions, slowing the combustion process and suppressing part of the heat release. Figure 5-4 shows the contour of turbulent kinetic energy inside the cylinder during the compression phase on a section passing through the spark plug, for the baseline configuration and PC1_S test case. A high TKE zone is well established on the intake side of the main chamber, for both simulations, but a wider area can be observed with prechamber. In fact, the narrow orifices introduce turbulent structures inside the cylinder and they cause higher values of turbulent kinetic energy. Observing the vector velocity magnitude, it can be noted the recirculation of the fresh mixture inside the cylinder and how the air and fuel is pushed inside the prechamber.

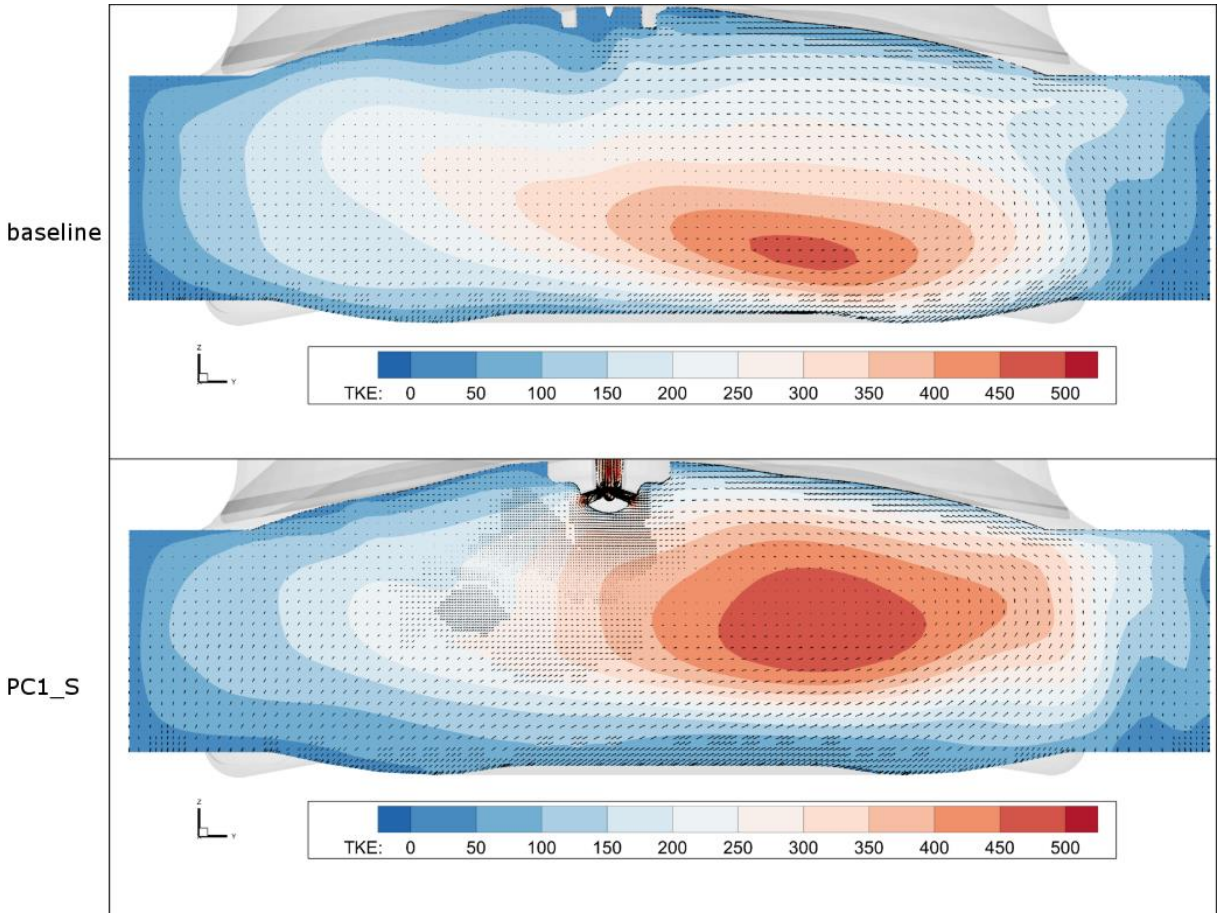

Figure 5-4. Contours of TKE and vectors velocity inside the cylinder at 660°CA: comparison between baseline and PC1_S simulations.

Figure 5-5 shows the evolution of the tumble ratio inside the cylinder during the cold flow, for both baseline and prechamber simulations. Minimum differences can be noted in the tumble ratio during the exhaust and overlap phases between the two configurations. Conversely, as the intake valves are closing, it can be noted that the tumble ratio is higher for PC1_S than the baseline configuration. This means that, even if the prechamber does not affect the in-cylinder pressure, the turbulent structures coming from the prechamber generate higher tumble motion and higher turbulent kinetic energy (Figure 5-4), modifying the local flow field inside the combustion chamber.

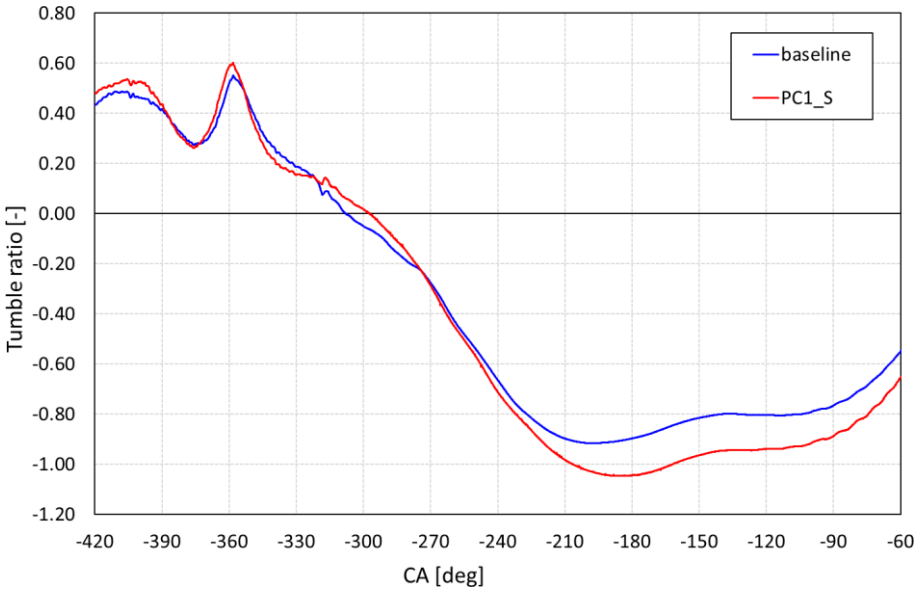

Figure 5-5. Evolution of tumble ratio during the cold flow simulation: comparison between baseline and prechamber.

After analysing the cold flow results and the flow field inside the cylinder, the combustion results are here presented. Figure 5-6 shows the evolution of the pressure during combustion, comparing the baseline results with the PC1_S ones. The red solid line refers to the in-cylinder pressure, while the dashed line refers to the pressure inside the prechamber. The simulation with prechamber is carried out with equal spark time of baseline, which is 33°CA before the TDC, deriving from the experimental data. The fresh mixture ignites inside the prechamber and entering in the main chamber in the form of hot flame jets. From the graph, two different peaks of pressure inside the prechamber can be noted: the first occurs when the fresh mixture is completely burnt and the flame is passing through the orifices; the second is due to the combustion inside the main chamber and the pressure rise inside the cylinder. Comparing the pressure curves, the engine with prechamber is subjected to a very high pressure: the maximum with prechamber is roughly 20 bar higher than the baseline configuration and it occurs 5 degrees earlier. This means that using the prechamber to ignite the mixture inside the cylinder produce a combustion process faster and more efficient.

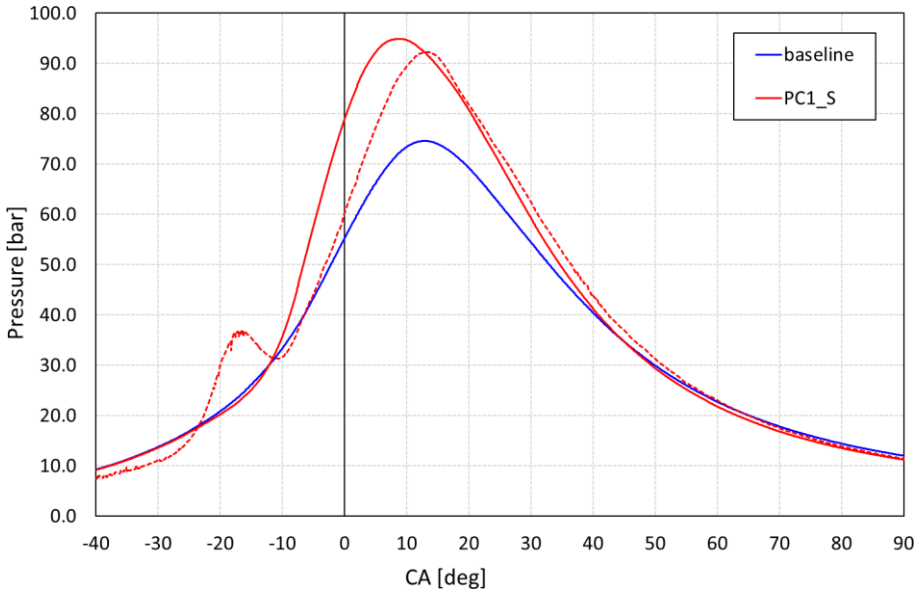

Figure 5-6. Evolution of pressure during combustion: comparison between baseline configuration (blue line) and PC1_S (red line: the dashed line refers to the prechamber pressure and the solid line to the cylinder pressure).

Figure 5-7 shows the specific fuel mass burnt inside the cylinder for both baseline and PC1_S simulations. It can be noted that, as previous explained, the combustion with prechamber is faster, especially during the ignition phase of the mixture inside the main chamber. In fact, as the hot flame jets enter in the cylinder (roughly 15 crank angle degrees before the TDC), the mixture inside the main chamber immediately ignites. Thus, the combustion process inside the cylinder can be considered already in the turbulent phase and the flame front moves forward in the main chamber, burning the remaining fresh mixture quickly. In Figure 5-8 can be noted the gain of using the prechamber in terms of combustion duration. The two phases are calculated respect to the spark time and they refer to the process inside the main chamber, which is the phenomenon that does work on the piston surface. In PC1_S test case, even if the mixture inside the main chamber ignites later than the baseline configuration, the first phase of the combustion lasts less of roughly crank angle degrees and the speed up of the process results in a gain of roughly 20 crank angle degrees.

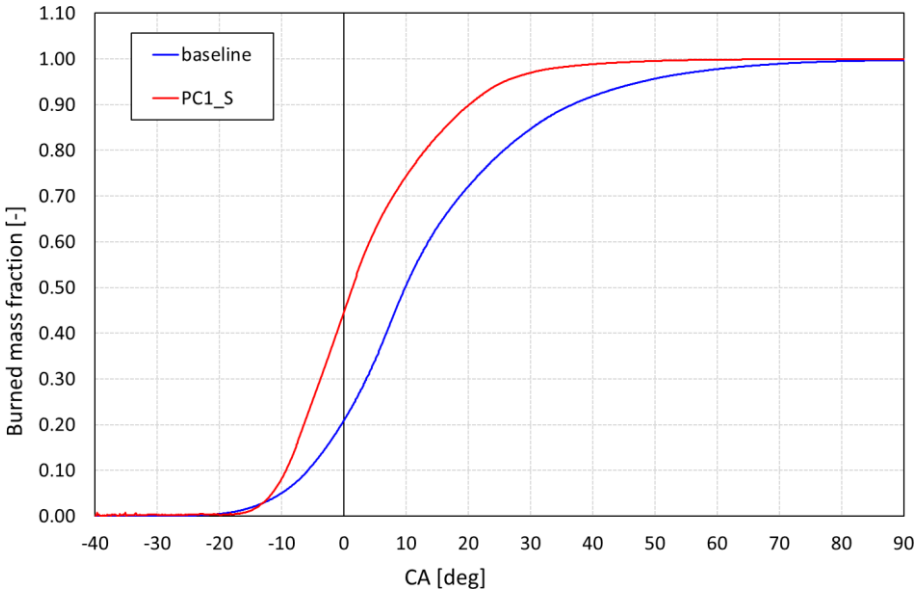

Figure 5-7. Specific fuel mass burnt inside the cylinder: comparison between baseline and PC1_S simulations.

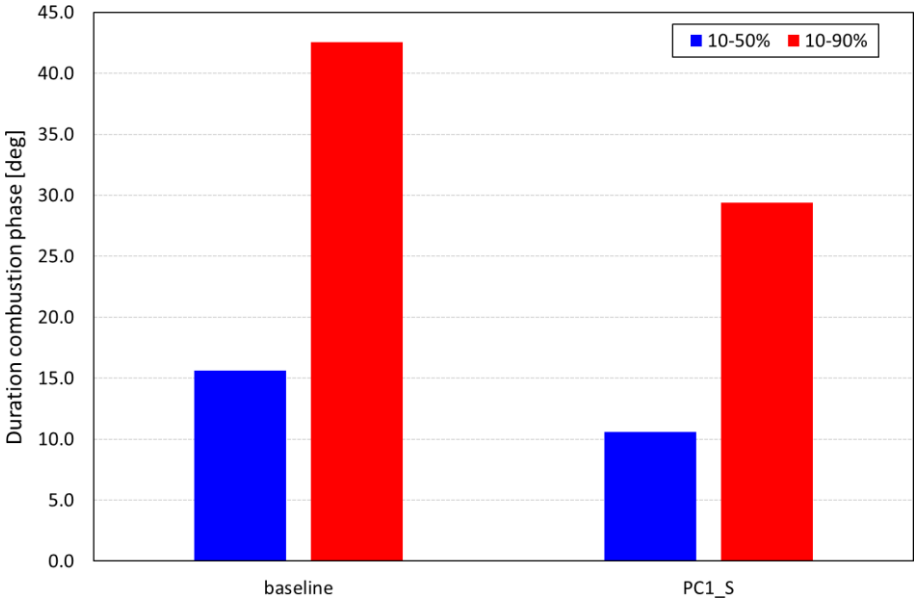

Figure 5-8. Duration of combustion phase inside the cylinder: comparison between the baseline and PC1_S simulations.

Figure 5-9 shows the contour of temperature inside the cylinder during combustion, for baseline and PC1_S, at different crank angle degrees. At 20 degrees before the TDC, the hot jets are entering into the main chamber, while the process in the baseline configuration is still in the laminar phase and the fuel mass burnt is not yet at 10%. At 10 degrees before the TDC, the flame jets impinge on the piston surface and they ignite the fresh mixture in the main chamber. When the piston is at the TDC, the flame front in PC1_S affects 2/3 of the combustion chamber and roughly the 50% of the fuel trapped in the cylinder has already burnt. Then, the flame front propagates through the squish area of the engine faster than the baseline configuration, due to the flame jets that enhance the turbulent flame speed.

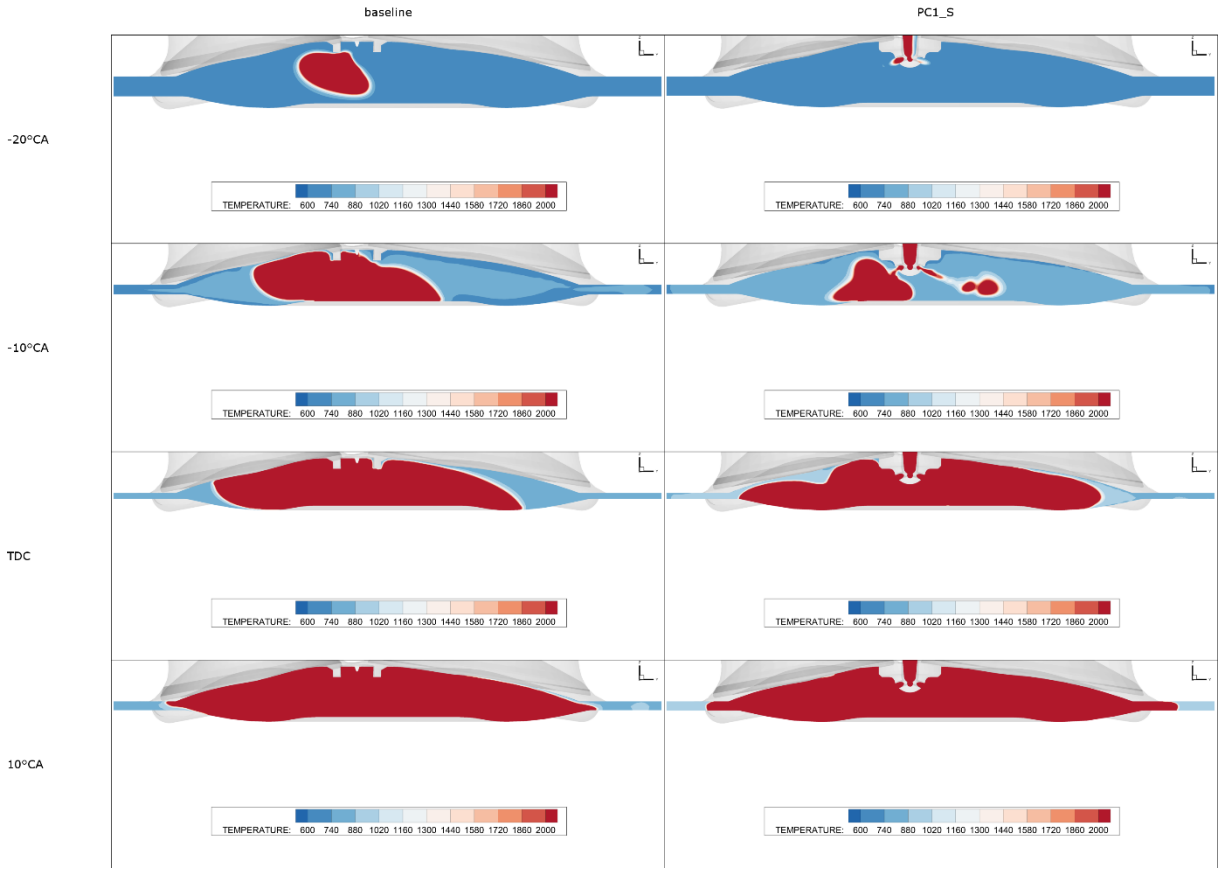

Figure 5-9. Evolution of the flame front inside the cylinder on a section passing through the spark plug: comparison between the baseline and PC1_S simulations.

It is worth noting that the flow field inside the main chamber affects the behaviour of the flame exiting from the prechamber (Figure 5-10). The hot jets coming out from the orifices on the exhaust side are pushed towards the piston surface because they are co-flow respect to the flow field, which enhances the flame front propagation. Conversely, the hot jets on the intake side are counter-flow respect to the flow field and their advance is hindered by the recirculation zone below the intake valves. Thus, while the hot jets on the exhaust side are wider and more stretched towards the piston surface, the flame jets on the intake side seems thinner and delayed. Nevertheless, once the fresh mixture in the main chamber is ignited by the hot flame jets coming from the prechamber, the higher turbulent kinetic energy on the intake side of the cylinder enhances the flame propagation. Thus, the flame front reaches the liner earlier on the intake side than the exhaust side, confirming that the prechamber allows to speed up the ignition and laminar phase of combustion and the flow field inside the main chamber has still a great influence on the flame front propagation.

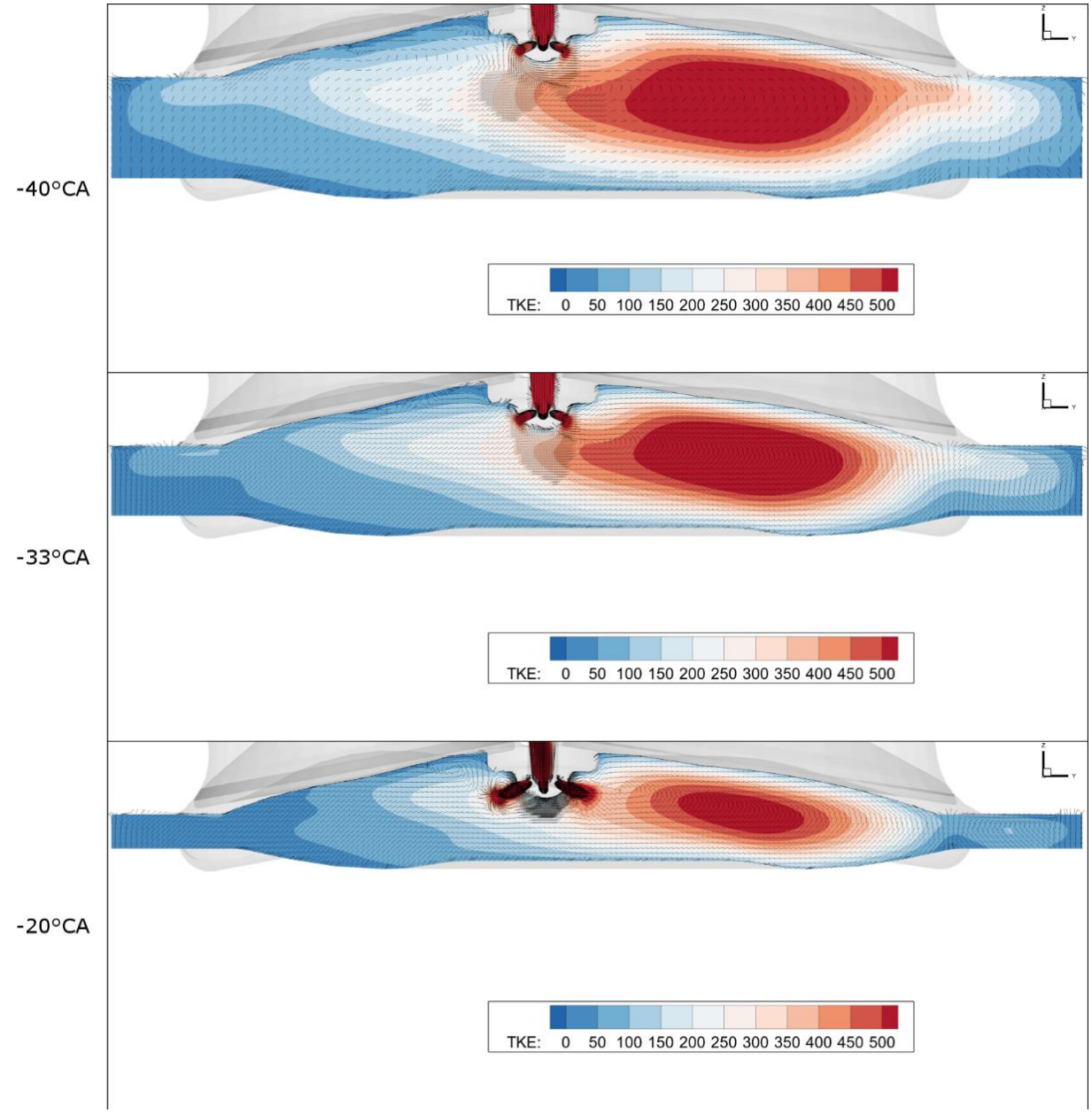

Figure 5-10. Contours of TKE and velocity vectors inside the cylinder for PC1_S (section passing through the spark plug inside the prechamber).

Comparison between detailed chemistry solver and flame surface density model

After the CFD simulation of PC1_S test case with the detailed chemistry solver, the same prechamber geometry is tested using the flame surface density model. As explained in previous chapter, the ECFM-3Z is a simplified approach, based on the definition of the progress variable and flame surface density for tracking the rate of the burnt gases and the evolution of the flame front propagation. The closure of the reaction rate is based on empirical correlations and two transport equations, one for the progress variable and one for the flame surface density. Since the chemical reactions are not considered, the computational effort for combustion simulation is much less than the one requested with SAGE model, against a significant reduction of the level of detail of the CFD analysis. As already seen for the engine in baseline configuration, not major

differences are notable for cold flow simulations. As explained before, the numerical setup for simulation with prechamber is unchanged respect to the baseline test and the combustion model is set using the parameters found during the calibration. Figure 5-11 shows the comparison between the SAGE model and flame surface density model, in terms of pressure inside the cylinder (solid line) and prechamber (dashed line). It can be noted that SAGE model computed a higher pressure than the one simulated with flame surface density model, in both cylinder and prechamber. With the flame density model, combustion in prechamber occurs earlier: thus, the pressure arises in advance respect to the SAGE model. As the flame passing through the narrows passages and entering in the main chamber, the in-cylinder pressure computed by the detailed chemistry solver increases rapidly, while the one derived from the flame density model has a lower slope, resulting in a slower combustion process inside the main chamber (Figure 5-12).

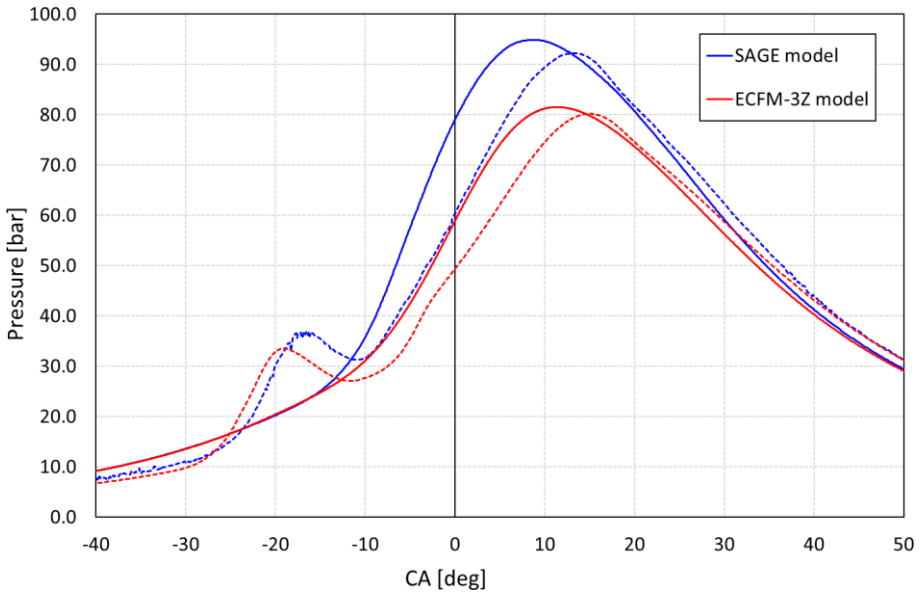

Figure 5-11. Evolution of pressure during combustion for PC1_S test case: comparison between SAGE model and ECFM-3Z model.

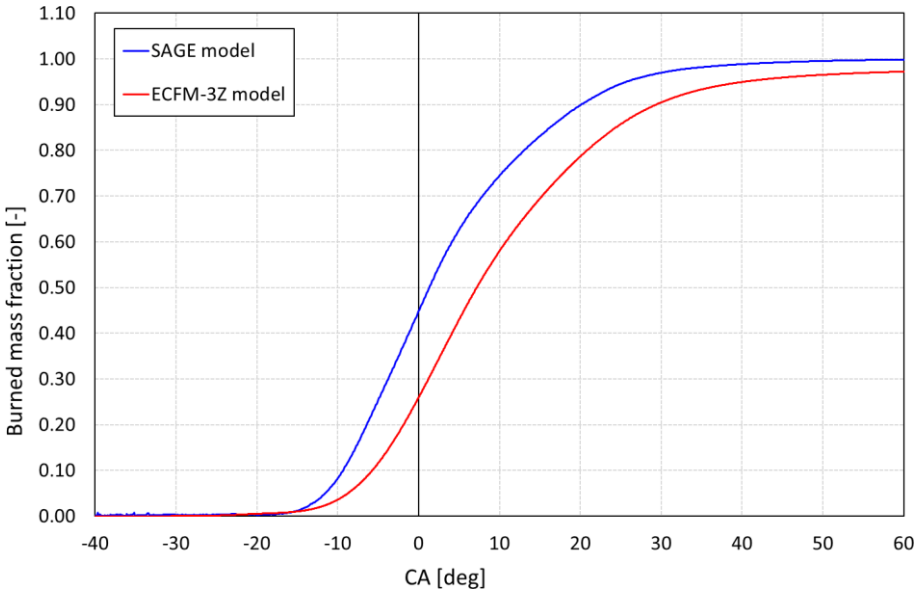

Figure 5-12. Burned mass fraction inside cylinder for PC1_S test case: comparison between SAGE model and ECFM-3Z model.

This behaviour can be caused by the model itself. As explained in previous chapter, the flame surface density model does not take into account the chemical reactions during the oxidation of the fuel. This simplified approach does not consider the intermediate species that are formed during the combustion process. In real flames and in all computations using detailed chemistry model, many radicals are found within the flame front. These intermediate species have high chemical reactivity and allow to sustain the combustion process. This particular aspect is crucial in prechamber applications. The hot flame jest coming from the prechamber flow through narrow orifices and enter in the main chamber, mixing with a low temperature fresh mixture. The high gradient of temperature lead to a partially quenching of the flame, but several chemical radicals still remain in the mixture. A simplified model based on the definition of the progress variable and flame surface density model can not model this particular feature of the process. In this simplified approach, the reaction rate is computed through empirical correlation, based on local pressure, temperature and equivalence ratio of the mixture. Thus, it does not take into account for the high chemical reactivity of the intermediate species. Conversely, a detailed chemistry solver computes the reaction rates of every species specified in the chemical mechanism, taking into account for the radicals too. Thus, the SAGE model is able to model the effect of the low temperature of the mixture inside the main chamber on the hot flame jets exiting from the orifices. Consequently, the detailed chemistry model computes a faster combustion process than the one simulated with ECFM-3Z (Figure 5-11 and Figure 5-12). Therefore, the detailed chemistry solver is used for further analyses of the combustion process of the engine equipped with prechamber. It is worth remembering that, at the moment of writing this thesis, the bench for experimental test of the engine with prechamber is under construction. Thus, no experimental data are available for prechamber test case.

5.3.1 - Influence of the aspect ratio

After the comparison between the two different combustion models, as explained before, the detailed chemistry solver is used for combustion analysis with prechamber, since it allows a more in-depth analysis of the process, taking into account the chemical mechanism. At first, a comparison between the two different shapes of the prechamber is carried out. Thus, in this paragraph, the PC1_S and PC1 simulations results are shown, comparing the influence of the prechamber on the flow field inside the cylinder and the combustion process, in terms of in-cylinder pressure and duration. As seen in previous paragraph, these two prechambers have the same orifices diameters and rod diameter; they differ from each other for the aspect ratio, which is greater for PC1. Furthermore, the prechamber PC1_S has sharp angles and it is more shaped than the PC1 prechamber, which has instead a greater fillet radius when passing from the rod to the volume where the spark plug is located. No appreciable differences can be noted in the pressure during the cold flow simulation, for both cylinder and prechamber (Figure 5-13).

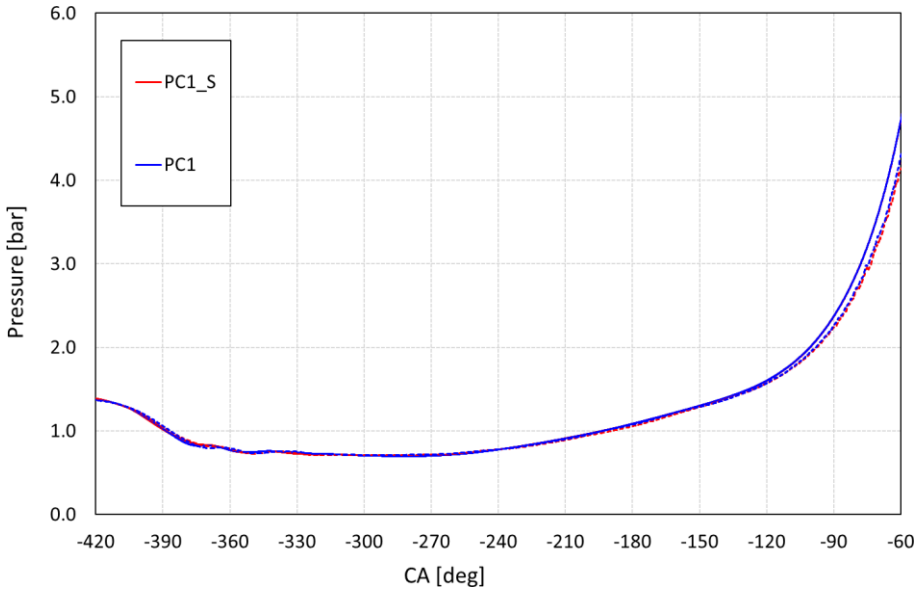

Figure 5-13. Evolution pressure during the cold flow simulation: comparison between PC1_S and PC1.

Observing the evolution of turbulent kinetic energy and tumble ratio inside the cylinder during the cold flow (Figure 5-14 and Figure 5-15), it can be noted that the two prechambers have a similar behaviour, testifying that the shape and the aspect ratio have a minimum influence on the in-cylinder flow field during the scavenging process. Little differences are visible during the compression phase, for both turbulent kinetic energy and tumble ratio: the PC1_S produces lower TKE inside the cylinder during compression but it tends to recover the gap with PC1 before the spark time, while the tumble ratio is greater in PC1_S than PC1 prechamber.

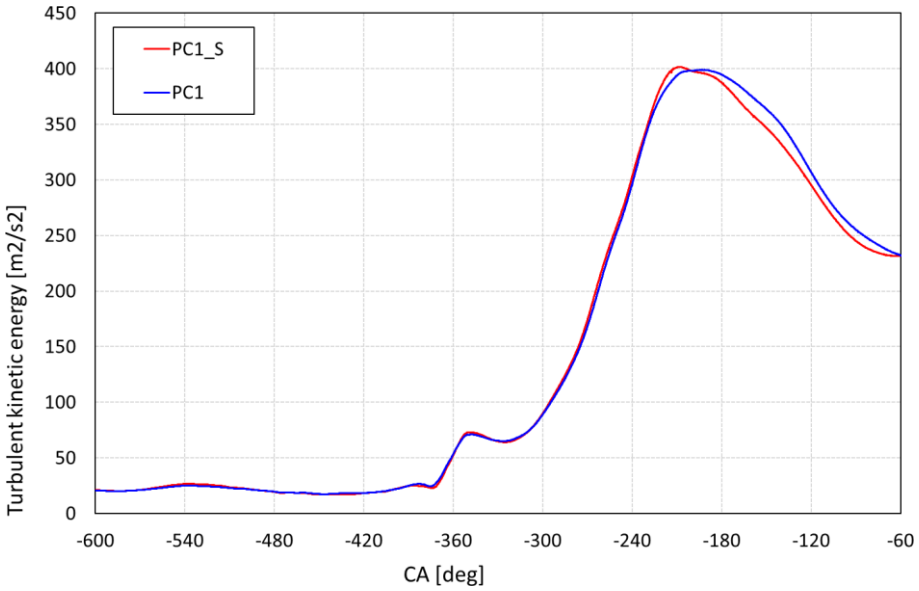

Figure 5-14. Evolution of turbulent kinetic energy inside the cylinder during the cold flow: comparison between PC1_S and PC1.

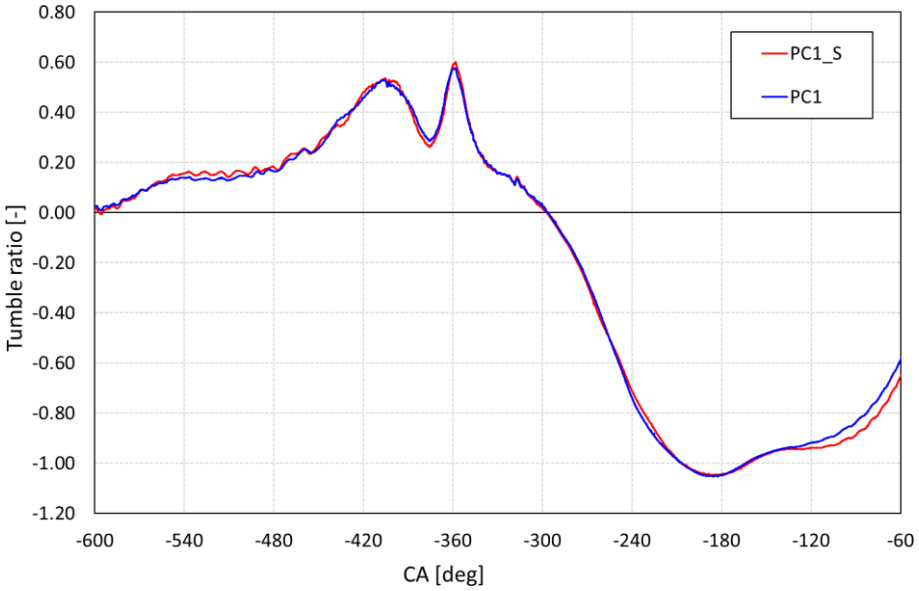

Figure 5-15. Evolution of tumble ratio inside the cylinder during the cold flow: comparison between PC1_S and PC1.

Nevertheless, the flow field inside the cylinder is very similar between the two prechambers, as it can be seen in Figure 5-16, where the comparison between the TKE contours on a section passing through the spark plug is reported. Minimum differences are visible between the two prechambers: while both test cases generate a high TKE zone on the intake side of the combustion chamber, in PC1 simulation the area with high turbulent kinetic energy seems to be more stretched towards the exhaust side too.

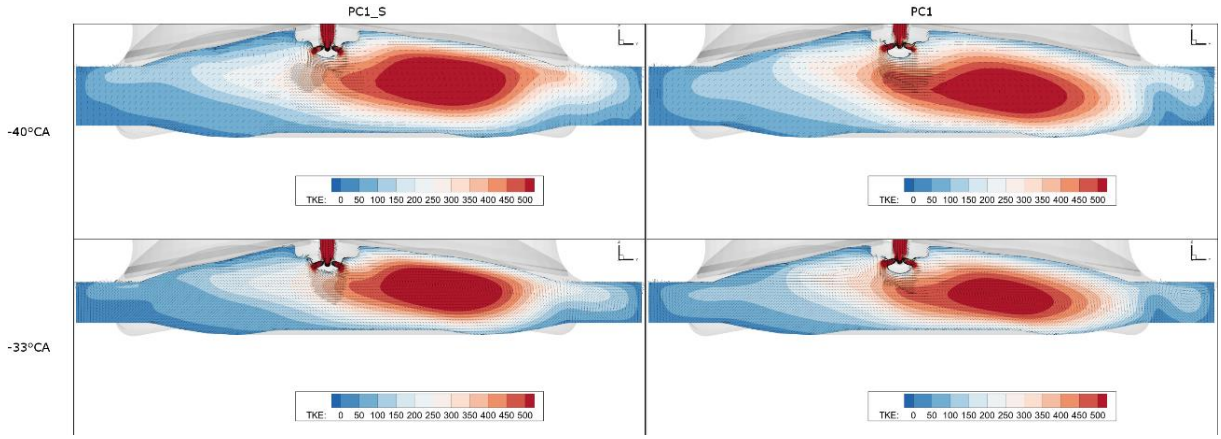

Figure 5-16. Contour of TKE and velocity vector inside the cylinder before the combustion process: comparison between PC1_S and PC1.

It is worth noting that, even if the fuel mass trapped during the intake phase is the same for the two test cases, the fuel trapped inside the prechamber PC1 is slightly greater than the other one (Figure 5-17).

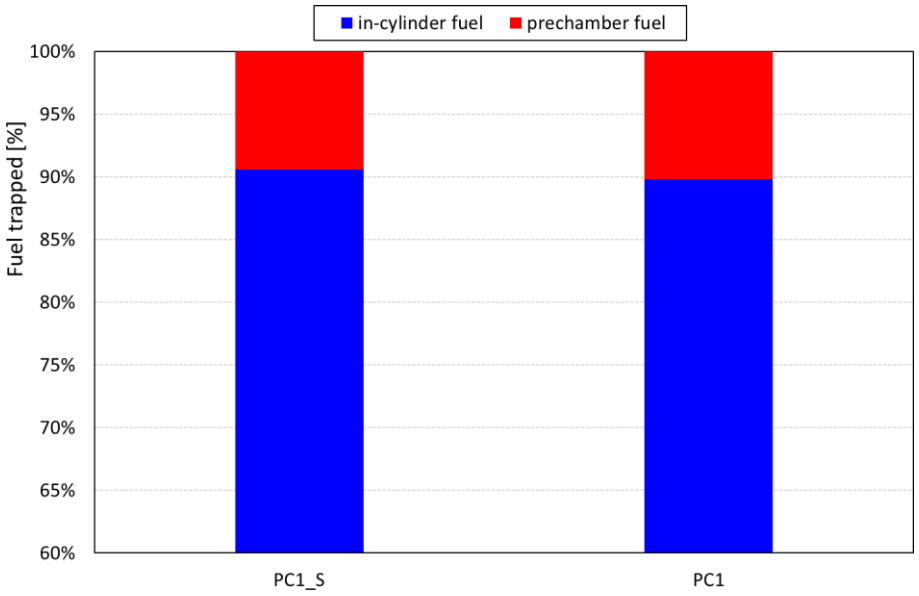

Figure 5-17. Fuel mass trapped at the spark time: comparison between PC1_S and PC1.

Figure 5-18 shows the comparison between PC1_S and PC1 combustion process in terms of pressure. The solid lines refer to in-cylinder pressure, while the dashed ones refer to the pressure inside the prechamber. Since the fuel mass trapped inside the prechamber PC1 is greater, the pressure peak after the spark time (i.e. when the hot jets exit from the orifices) is higher respect to the PC1_S test. Moreover, the combustion in the main chamber occurs early in the PC1_S simulation, since the aspect ratio of the prechamber is lower, and the pressure peak inside the main chamber is slightly greater than PC1, because a greater amount of fuel mass remains in the cylinder during the scavenging process (Figure 5-17). Notwithstanding the hot jets enter later in the main chamber, the combustion process with PC1 is faster than the other prechamber, as it can be seen in Figure 5-19: considering the 10-90% phase, PC1 combustion lasts roughly one crank angle degrees less.

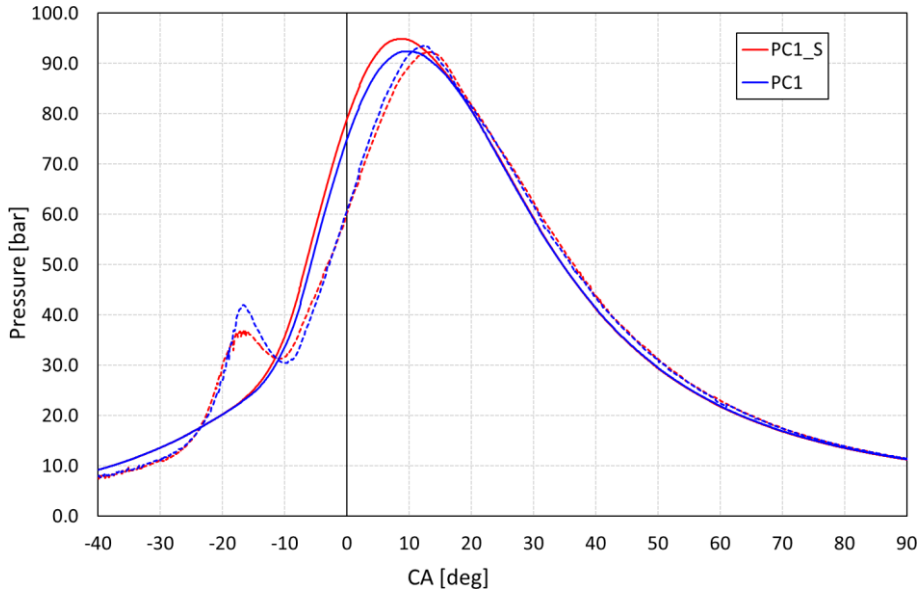

Figure 5-18. Evolution of the pressure during combustion: comparison between PC1_S and PC1 simulations.

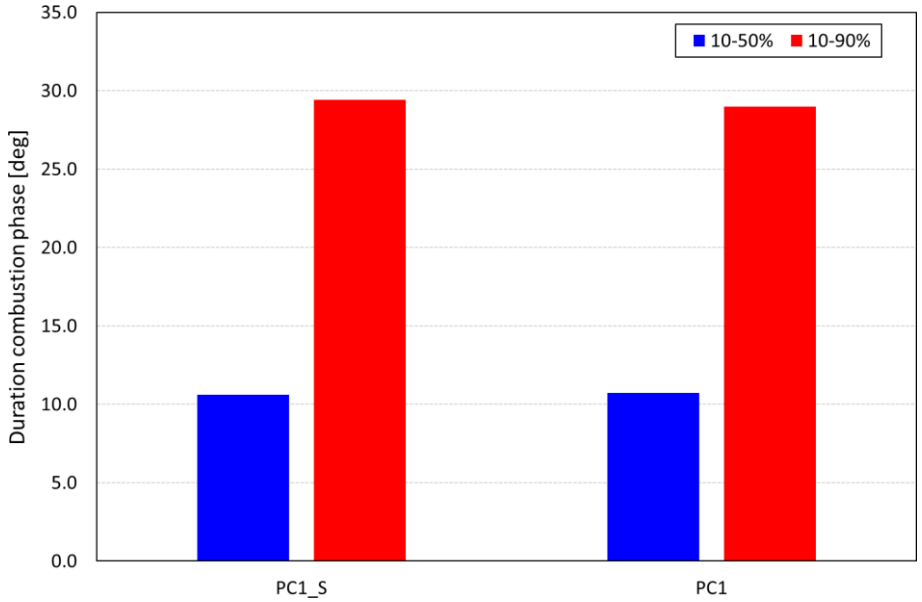

Figure 5-19. Combustion duration: comparison between PC1_S and PC1.

Figure 5-20 shows the contour of temperature during combustion for both PC1_S and PC1 prechambers, on a section passing through the spark plug. As reported before, the flame jets coming from the prechamber PC1_S seems to enter early in the main chamber. From the comparison of the flame propagation between the two prechambers, it can be noted that the flame jets enter into the cylinder in a different way. The TKE field inside the cylinder in the prechamber PC1 enhances the flame propagation on the exhaust side of the cylinder too. Furthermore, it can be noted that, despite the first phase of combustion in PC1 is slower, the fuel mass in the main chamber burns very quickly, due to the greater inertia of the jets, which allows to ignite the mixture shortly. From the comparison of the flame front propagation at 10 crank angle degrees after the TDC, it can be noted that the flame front has reach almost the liner wall for both the test cases.

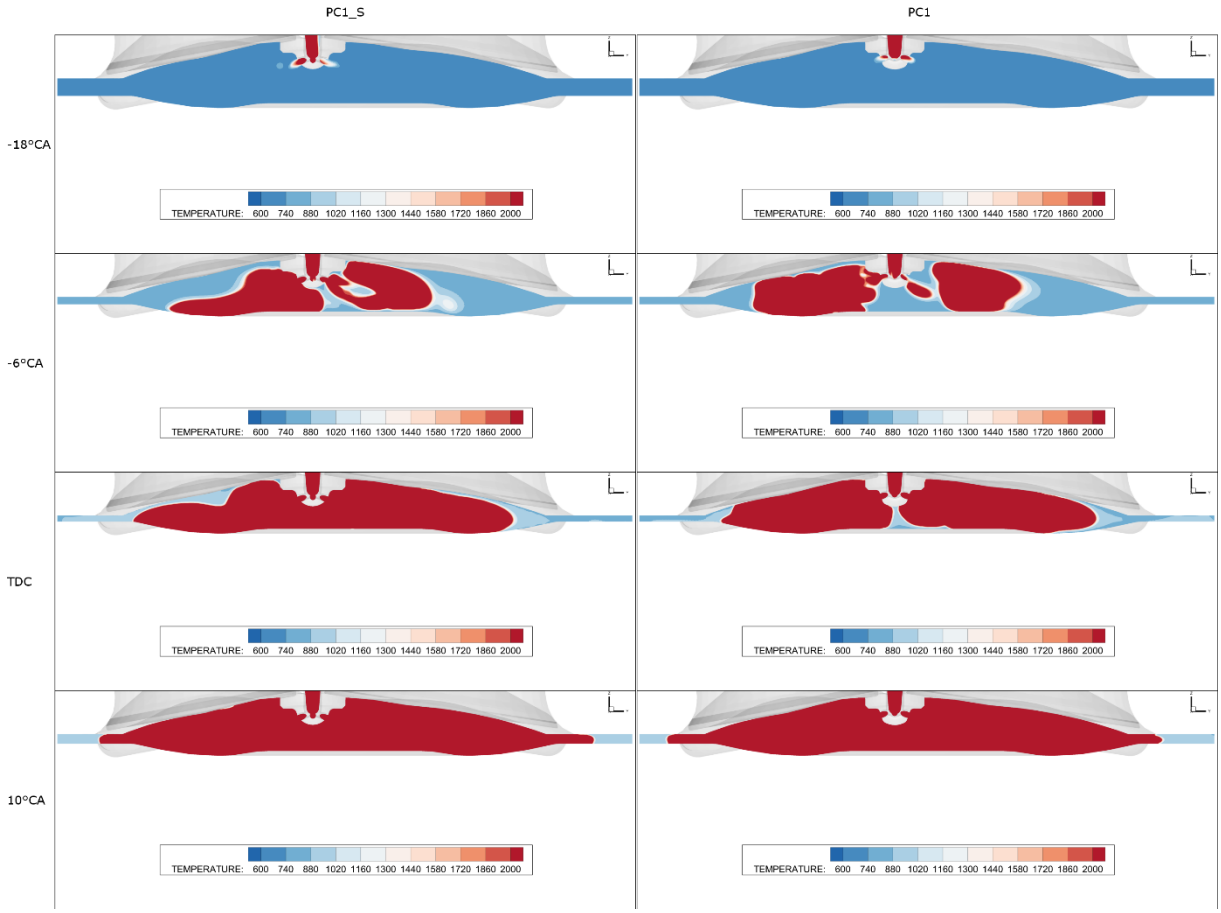

Figure 5-20. Evolution of the flame front during combustion: comparison between PC1_S and PC1.

Notwithstanding the different behaviour of the flame front out of the orifices, the combustion process is very similar between the two prechambers. As reported before, the durations of the combustion are similar too. Some reflections on the feasibility of the prechamber must be done. Considering the shape of the two aforementioned prechambers, since the PC1 has greater fillet radius and a shape less sharped than PC1_S, it can be assumed that the latter is more difficult to cool and some hot spots may arise during operation. This is a detail not to be underestimated, since the prechamber is subjected to higher temperature than the liner. In light of this, the shape of the prechamber PC1 is used to carry out the further analysis on the engine, since the less sharped shape should avoid cooling problem. Thus, the next CFD analysis are carried out with an aspect ratio of 1.85 of the prechamber.

5.3.2 - Influence of wall temperatures

As explained before, the prechamber with aspect ratio 1.85 is chosen for next sensitivity analysis. Before to investigate the effect of the orifices diameters on the combustion process, a sensitivity analysis to the wall temperature of the prechamber is carried out. For the simulations in previous paragraphs, a wall temperature 30% higher than the head one is assumed for the prechamber. This value is adopted based on literature review and previous experience of the industrial partnership. Thus, a sensitivity to the prechamber wall temperature is necessary in order to investigate how this parameter can affect the combustion process and

the engine performance. Three different values are tested, which correspond to a temperature higher 10%, 30% and 50% than the head temperature, as reported in Table 5-3.

Test	T+10%	T+30%	T+50%
Prechamber	PC1	PC1	PC1
Head temperature [K]	446	446	446
Prechamber temperature [K]	490	580	670

Table 5-3. Test matrix for the sensitivity to the prechamber wall temperature.

The wall temperature of prechamber does not affect significantly the pressure inside the engine during the cold flow, as shown in Figure 5-21: there are not any major differences in terms of in-cylinder and prechamber pressure.

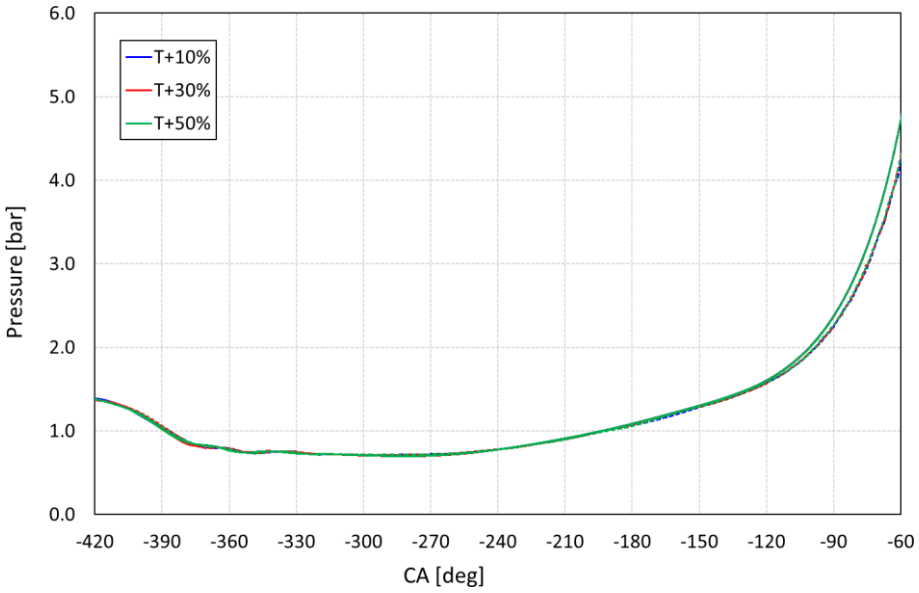

Figure 5-21. Evolution of the pressure during the cold flow simulation for PC1: sensitivity to prechamber wall temperature.

Observing the contour of TKE (Figure 5-22) at the end of the compression phase on a section passing through the spark plug, it can be noted that the flow field are very similar between the three test cases, testifying that the temperature of the prechamber does not affect the in-cylinder conditions.

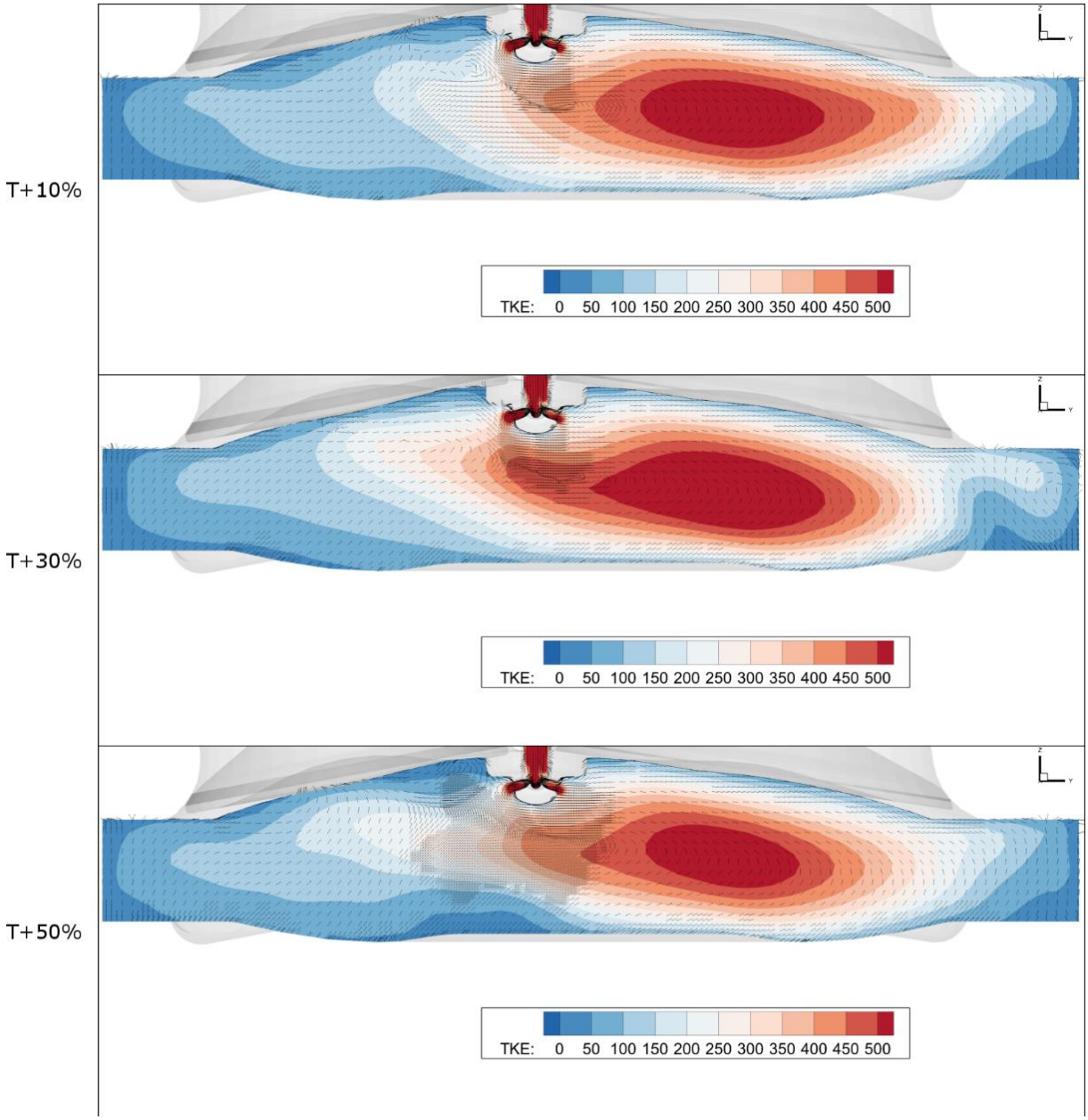

Figure 5-22. Contour of TKE and velocity vector at -40°CA: prechamber wall temperature sensitivity.

Figure 5-23 shows the evolution of pressure inside cylinder (solid lines) and prechamber (dashed lines) during combustion for different prechamber wall temperatures. Higher the wall temperature, higher the pressure peak inside the cylinder and faster the combustion occurs. In fact, while the in-cylinder thermodynamic conditions not seem to be sensitive to the prechamber wall temperature during the scavenging process, the higher wall temperature causes an increase in the mixture temperature inside the prechamber (Figure 5-24). Thus, the combustion occurs early since the higher thermal agitation of molecules.

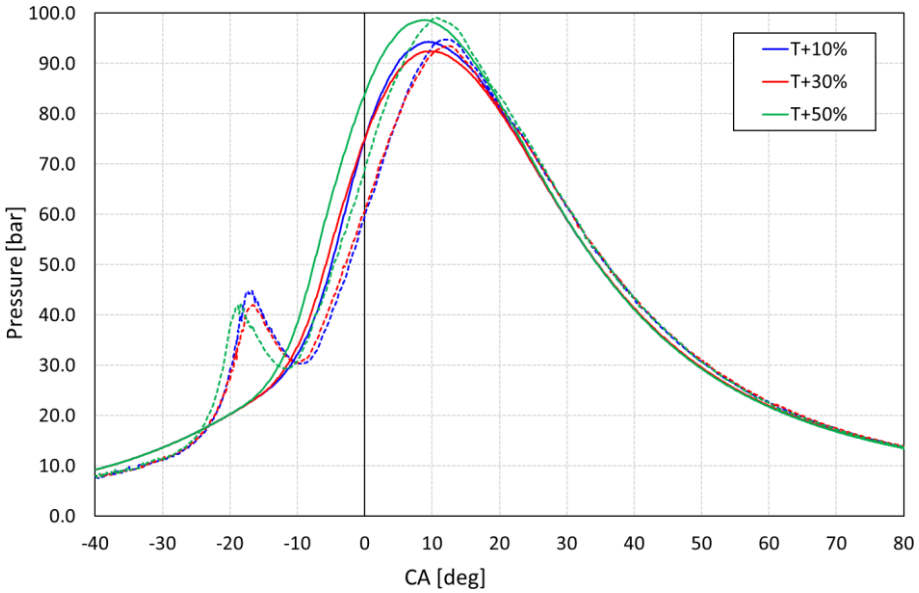

Figure 5-23. Evolution of pressure during combustion for PC1: prechamber wall temperature sensitivity.

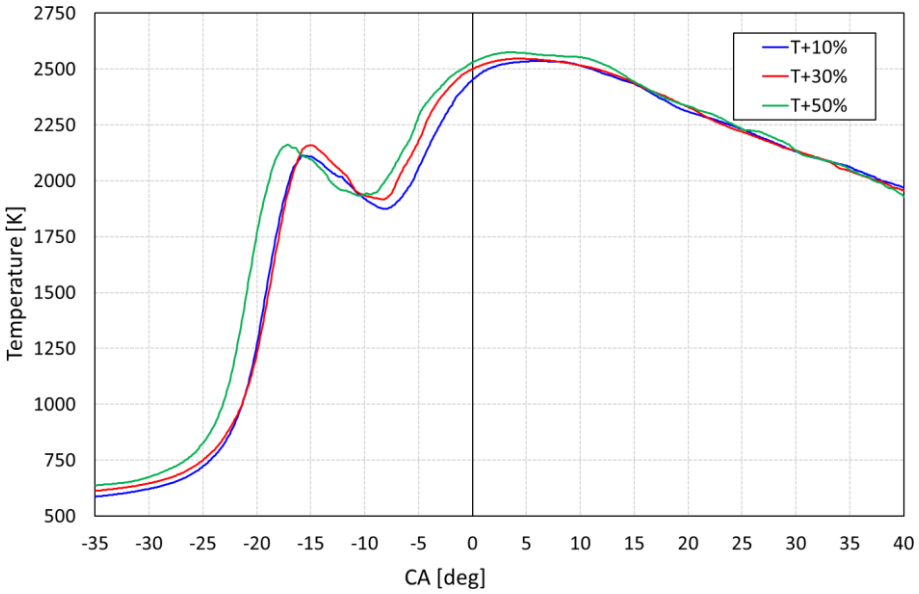

Figure 5-24. Evolution of temperature inside the prechamber PC1 during combustion: prechamber wall temperature sensitivity.

It is worth noting that the pressure peak inside the prechamber for test T+10% is higher than the one computed in T+30% test. In fact, the lower temperature of the mixture the higher fuel mass trapped inside the prechamber. With a wall temperature of 490 K, the fuel mass trapped in the prechamber is roughly 15% higher than the test case with temperature of 580 K. The higher amount of fuel inside the prechamber produces hot flame jets with greater inertia. Thus, even if the combustion in T+10% starts later than T+30%, as the flame enters in the cylinder, the mixture in the main chamber burns faster (Figure 5-25), compensating for the lower temperature of the mixture inside the prechamber during the ignition phase.

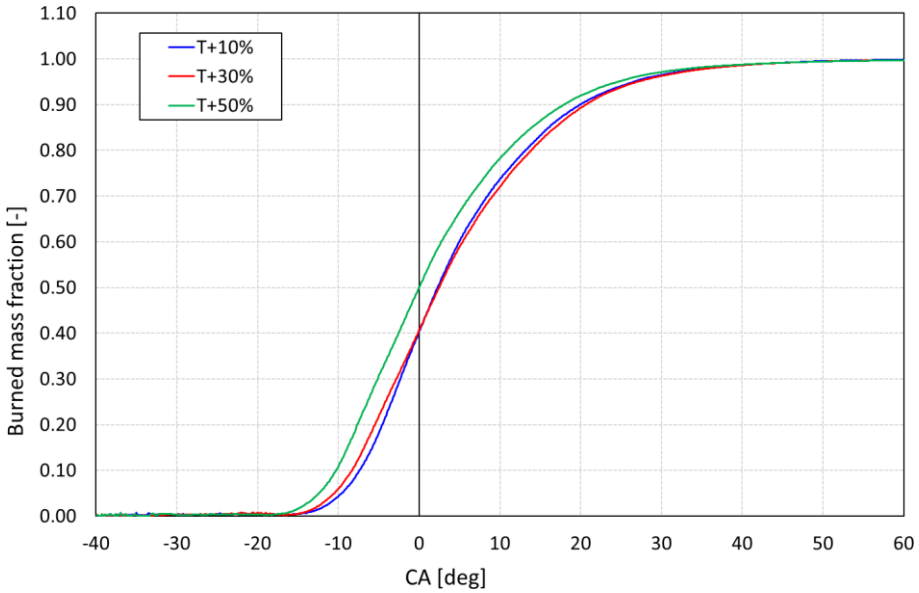

Figure 5-25. Burned mass fraction inside the cylinder during combustion for PC1: sensitivity to the wall prechamber temperature.

While not any major differences are visible in the flow field inside the cylinder during the scavenging process, during combustion it can be noted that higher the temperature higher the TKE inside the cylinder (Figure 5-26). The piston in Figure 5-26 is 20 crank angle degrees before the TDC, shortly before the hot jets exit from the orifices.

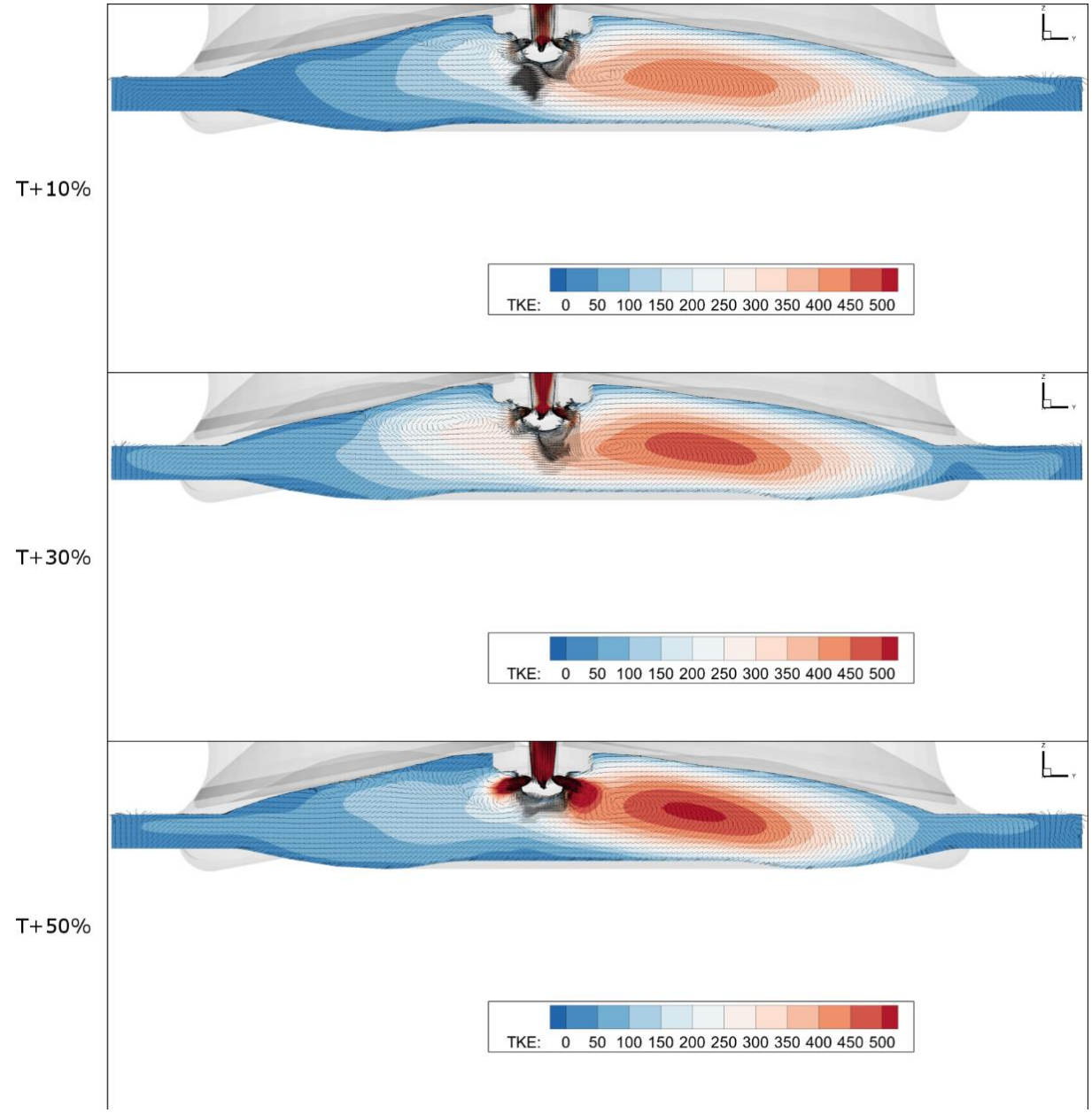

Figure 5-26. Contour of TKE and vector velocity at -20°CA: prechamber wall temperature sensitivity.

Figure 5-27 shows the flame front propagation inside the cylinder for two different crank angle degrees, for the three wall temperatures simulated. It can be noted that, at -18°CA, the flame jets are entering in the combustion chamber if the wall temperature is 670 K, while the flame front is still propagating through the rod of the prechamber if the wall temperature is 490 K. In fact, as explained before, the low temperature tends to inhibit the ignition phase of combustion; this results in a slower ignition of the mixture. When the piston is at the TDC, the flame front of T+30% test is more stretched towards the exhaust side than the others did, since the turbulent kinetic energy is greater. It is worth noting that the flame front propagation of test case with the highest wall temperature seems to be hindered towards the exhaust side, confirming the crucial role of the turbulent kinetic energy in the flame propagation. In test T+10%, the flame jets balance the lowest TKE with the highest inertia of the flame jets: thus, when the piston is at the TDC, the flame front

seems to propagate more easily through the main chamber than the test case T+50%. The differences between the simulations tend to disappear when over the 70% of the fuel is burnt.

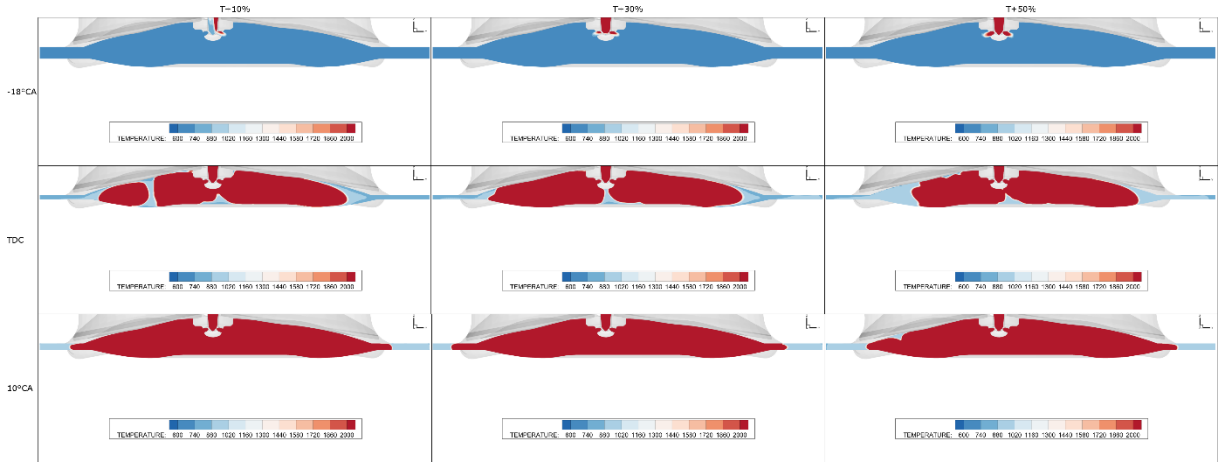

Figure 5-27. Contour of temperature during combustion for two different crank angle degrees: prechamber wall temperature sensitivity.

After the sensitivity on the temperature of prechamber wall, a value of 580 K is set for further simulations, since a temperature 30% higher than the head one is a reasonable hypothesis.

5.3.3 - Influence of orifices diameter

In this paragraph, the results to the orifices diameter sensitivity are shown. The temperature of the prechamber wall is set equal to 580 K for the all simulations run. As explained in previous chapters, the orifices diameters may affect not only the cold flow simulation, but the combustion process too. On the one hand, small diameters can obstruct the scavenging process of the prechamber, making difficult the fuel filling. On the other hand, small diameters may enhance the combustion performance, accelerating the flame jets and increasing the flame front propagation. Thus, a sensitivity to this parameter is necessary in order to find out the best configuration for the engine. As reported in Table 5-1, three different diameters are tested. At first, the results of the cold flow are presented, in order to evaluate how the orifices diameters may affect the scavenging process of the engine. Finally, the combustion results are compared, in terms of pressure curves, duration and flame front propagation.

Figure 5-28 shows the evolution of pressure during the overlap, intake and compression phases, for the three different aforementioned prechambers. It can be noted that the orifices diameter does not affect the in-cylinder pressure (solid lines). Slightly differences can be noted in the prechamber pressure: higher the diameter lower the pressure drop through the orifices and higher the pressure inside the prechamber at the end of the compression phase.

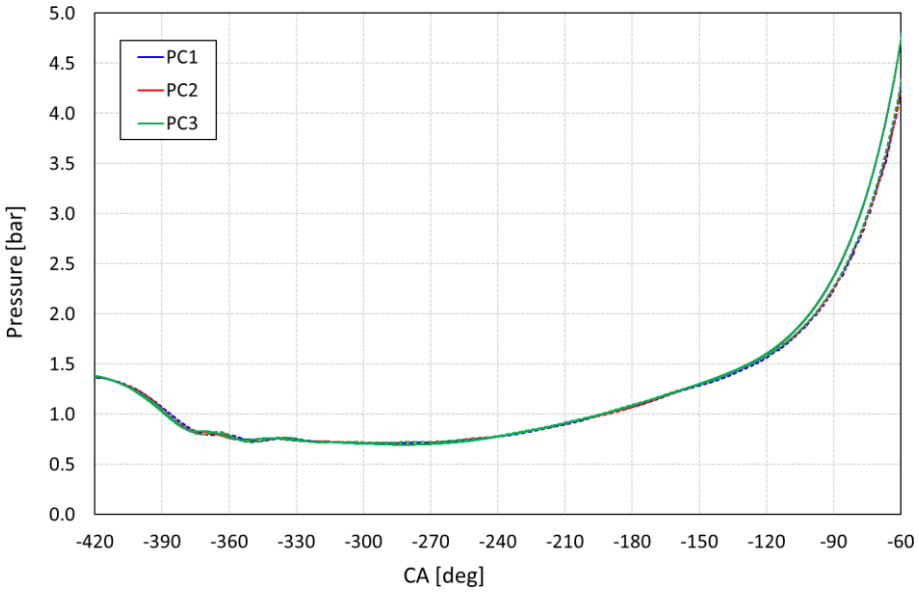

Figure 5-28. Evolution of pressure during cold flow: comparison between prechambers with different orifices diameters.

The orifices diameters do not affect the behaviour of the engine during the cold flow simulation, except for the compression phase. As can be seen from Figure 5-29, higher the diameters lower the tumble ratio during compression phase.

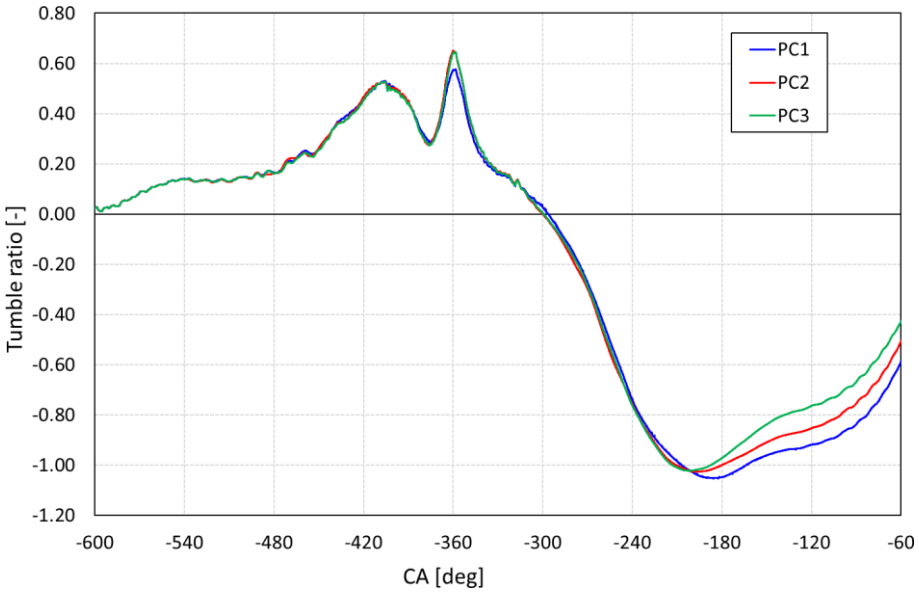

Figure 5-29. Tumble ratio inside the cylinder during the cold flow: comparison between prechambers with different orifices diameters.

Figure 5-30 shows the contour of turbulent kinetic energy for the three different prechambers. It can be noted that a high TKE zone still remain, increasing the orifices diameters, but the area is different between the prechambers: in particular, the region is greater with the lowest diameter. Furthermore, it can be noted that the turbulent kinetic energy inside the rod of the prechamber decreases increasing the orifices diameter.

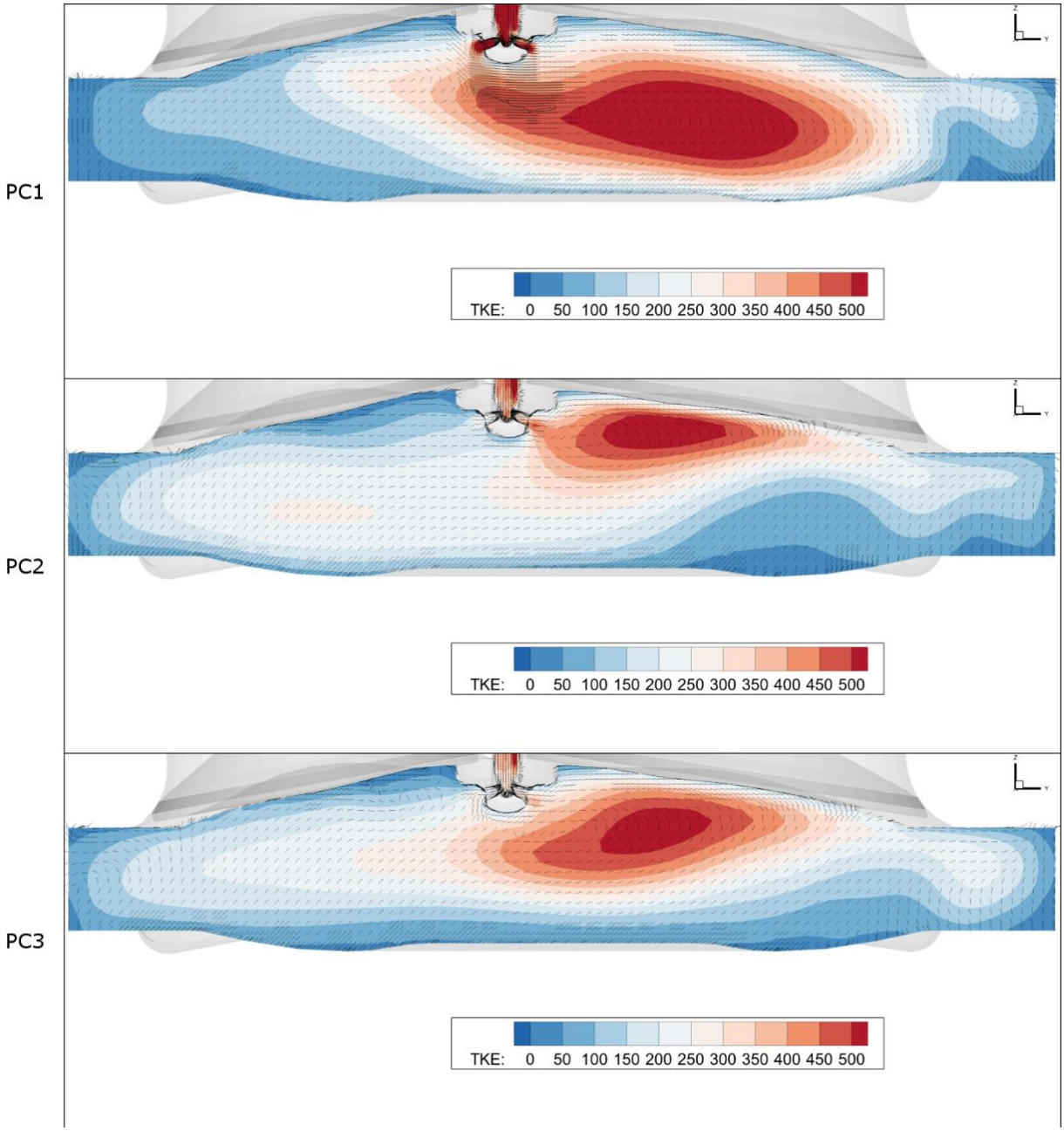

Figure 5-30. Contour of TKE and velocity vector at -40°CA: comparison between prechambers with different orifices diameters.

Figure 5-31 shows the evolution of pressure during combustion for the three different prechambers. It can be noted that higher the orifices diameters early the combustion occurs in the prechamber. It is worth noting that, in PC3, the pressure peak inside the prechamber during the ignition phase is lower than the other prechambers due to the highest diameter. This produces hot flame jets with lower inertia exiting from the prechamber, resulting in a combustion process in the main chamber slightly slower than the other prechambers, as can be seen from Figure 5-32. Minimum differences can be seen between PC1 and PC2 results: the latter prechamber has a faster ignition phase and the highest pressure difference between the main chamber and prechamber when the hot jets exit from the orifices; the combustion process in the former prechamber is faster when the mixture ignites in the cylinder due to the highest turbulent kinetic energy.

Thus, the combustion process of PC1 and PC2 are similar in terms of both pressure evolution and burned mass fraction.

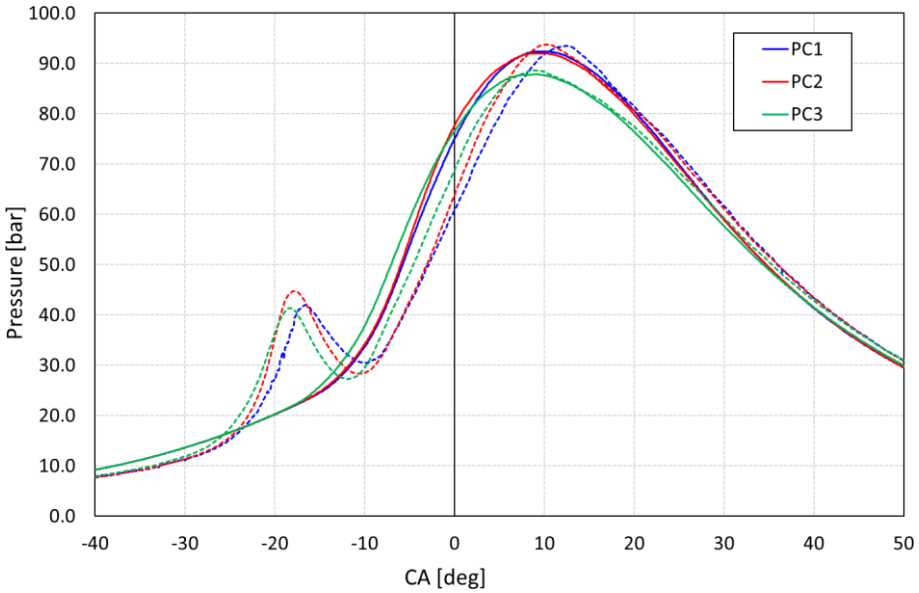

Figure 5-31. Evolution of pressure during combustion for three different orifices diameters.

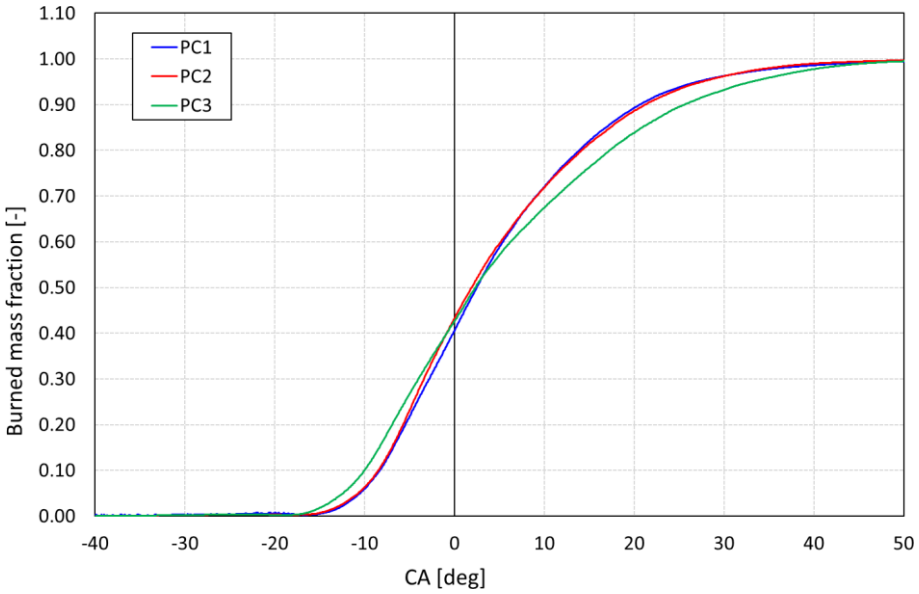

Figure 5-32. Burned mass fraction during combustion for three different orifices diameters.

Figure 5-33 shows the contour of temperature during combustion for the three prechambers. As can be seen, the flame jets from the PC3 prechamber 20 crank angle degrees before the TDC, while in the other test cases the flame front is still in the prechamber. As explained before, the flame coming from prechamber PC2 is able to penetrate the cylinder mixture with higher inertia, resulting in faster combustion process, even if the ignition phase is slower.

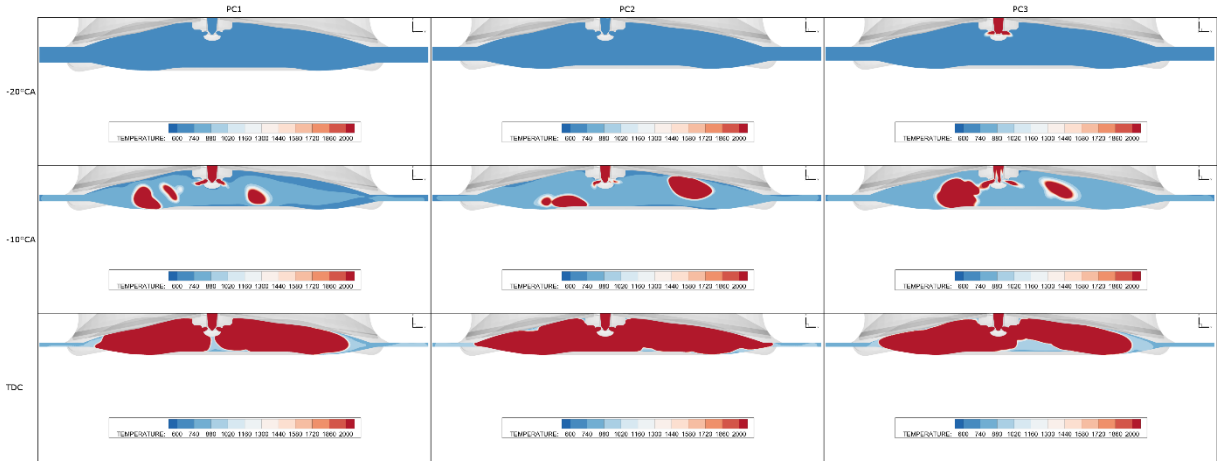

Figure 5-33. Contour of temperature during combustion on a section passing through the spark plug: comparison between three different orifices diameters.

Figure 5-34 shows a top view of the evolution of the flame front during the combustion. Contours are computed on a section perpendicular to the cylinder axis, located in the main chamber. The intake valves are located on the right side, while the exhaust valves on the left one. As explained before, smaller the diameters, thinner the shape of the flame jets.

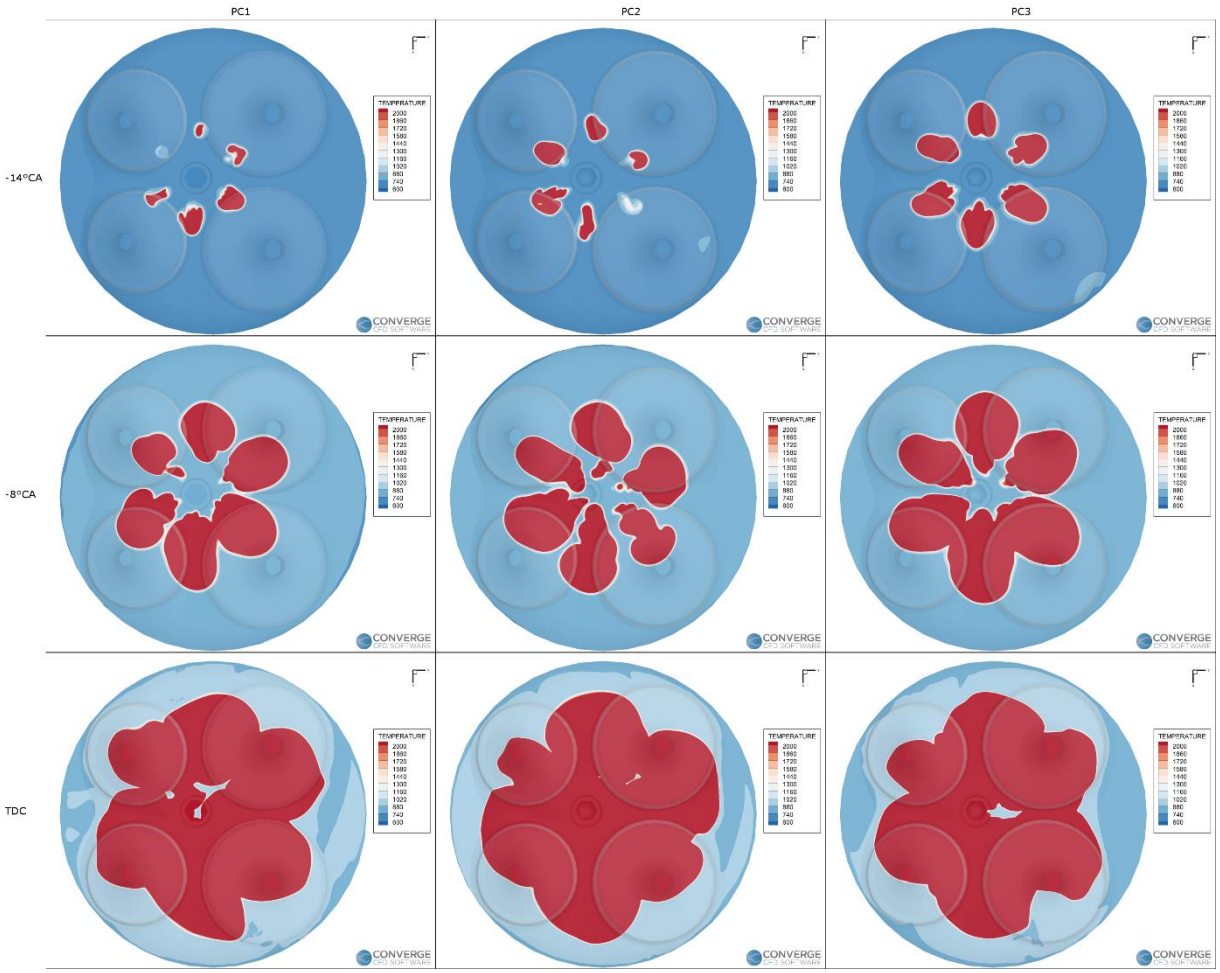

Figure 5-34. Contour of temperature during combustion on a section XY in the main chamber: comparison between three different orifices diameters.

Comparing the in-cylinder pressure of the prechambers during combustion with baseline configuration (Figure 5-35), it is remarkable the increase of pressure inside the main chamber for the whole test cases and how the prechamber can speed up the combustion process (Figure 5-36). In fact, when the 50% of fuel is burnt in the baseline configuration, the amount of gasoline burnt with prechambers is roughly 80%.

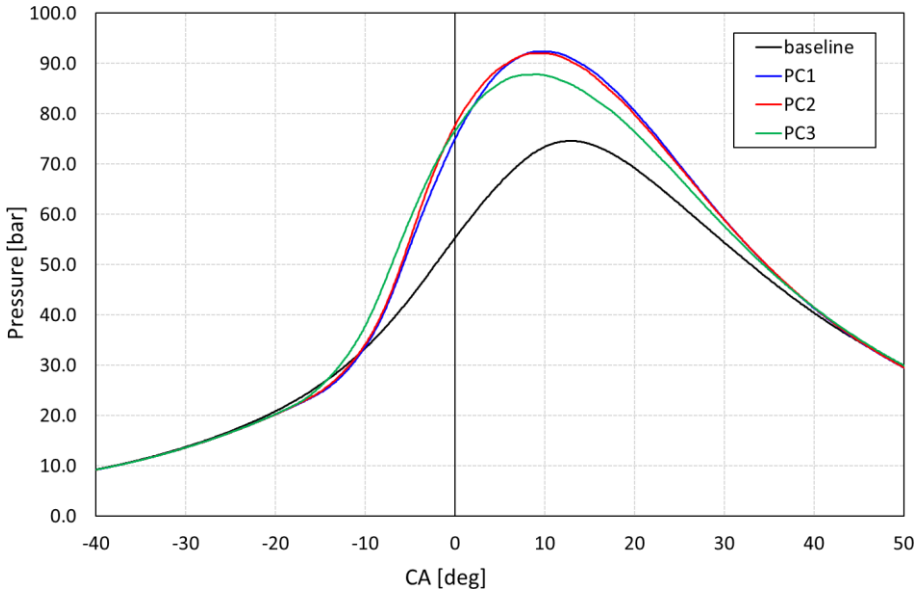

Figure 5-35. Evolution of in-cylinder pressure during combustion: comparison between prechambers and baseline simulations.

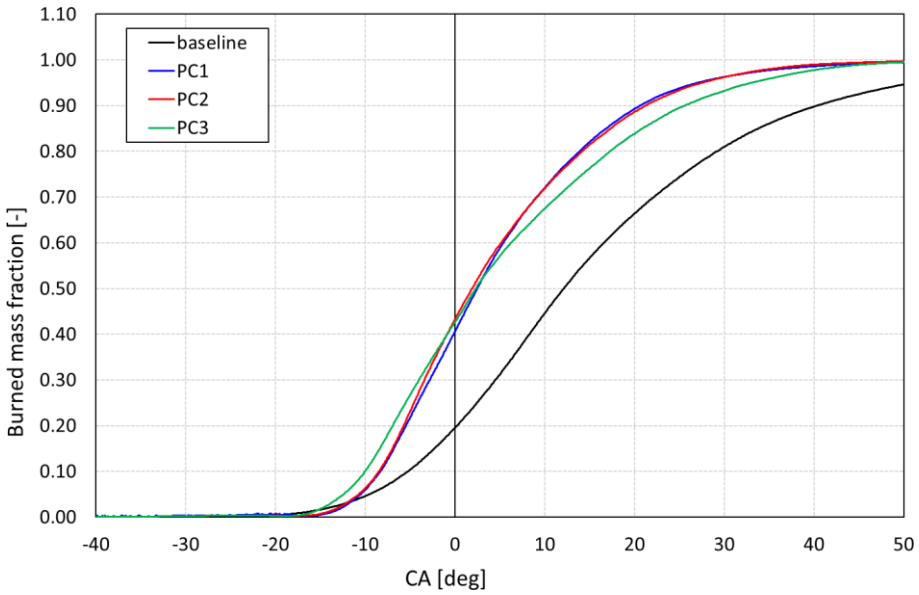

Figure 5-36. Burned mass fraction inside the cylinder: comparison between prechambers and baseline simulations.

It is interesting to compare the test cases in terms of indicated work. Pressure data for the gas in the cylinder can be used to calculate the work transfer from the gas to the piston. The indicated work per cycle $W_{i,c}$ can be obtained as follows:

$$W_{i,c} = \oint pdV$$

Since the high computational effort required for the CFD simulations, the performance of the prechambers are evaluated by calculating the indicated work limited to the combustion frame. In fact, the computational

cost of the CFD simulations with a detailed chemistry model is particularly high, since the solver has to take into account for several 41 chemical species. For this reason, the indicated work is not defined on the entire engine cycle but it is computed as follows:

$$W_{i,flame} = \int_{-40°}^{50°} pdV$$

The flame indicated work is defined considering the crank angles in which the combustion occurs. Figure 5-37 reports the indicated work of the prechambers with different diameters. The W_i is scaled on the $W_{i,baseline}$ obtained with the baseline configuration. Thus, a unity value means that the test case produces the same indicated work of the engine without prechamber. It can be noted that the whole test cases produce greater indicated work, especially PC1 and PC2 prechambers, which produce over 12% than the baseline engine.

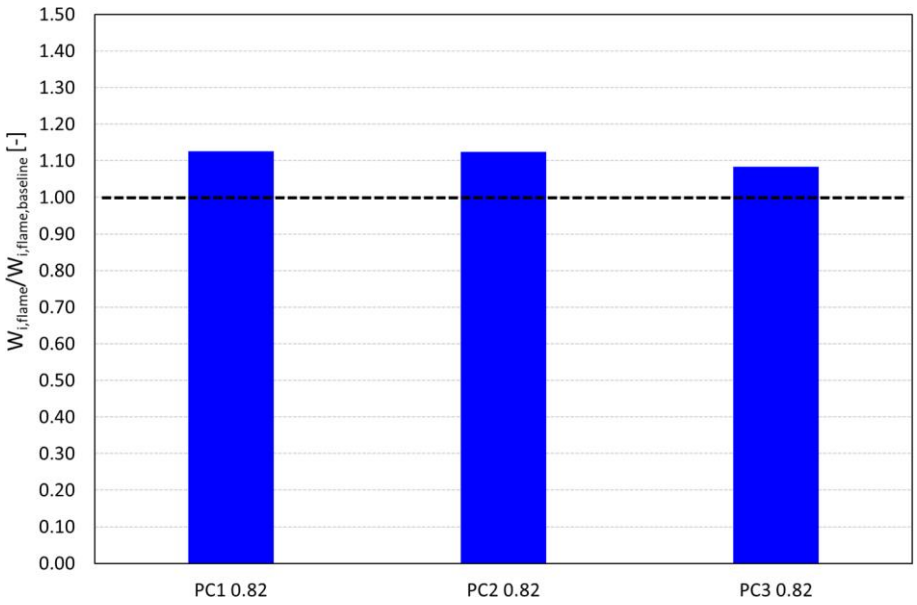

Figure 5-37. Indicated work of prechambers with different orifices diameter.

It is worth remembering that the simulations are carried out with the same spark time. Since the spark time derives from the test bench on the engine without prechamber, it can be assumed that this value is optimized for the baseline configuration in order to provide the maximum in terms of Indicated Mean Effective Pressure (IMEP). Figure 5-38 shows the maximum pressure inside the main chamber during combustion for the whole test cases, including the baseline engine. The tags in the figure indicate the crank angle when the maximum is computed. As seen before, the whole test cases with prechamber produce roughly a 17% rise of the maximum pressure (up to 23% with PC1 and PC2), and roughly 4 crank angle degrees in advance.

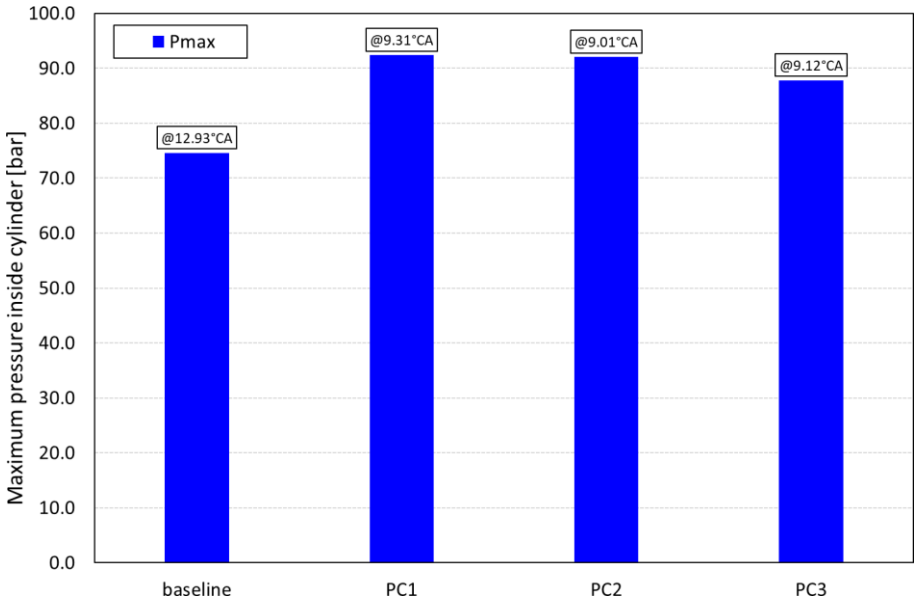

Figure 5-38. In-cylinder maximum pressure during combustion: comparison between prechambers and baseline simulations.

Thus, a sensitivity analysis to the spark time of the engine with prechamber is necessary in order to calibrate the combustion process and trying to obtain a maximum in-cylinder pressure occurring at same piston position of the baseline configuration. Furthermore, it is worth noting that roughly the 40% of the fuel burns during the compression phase causing an increase in the compression work. Figure 5-39 shows the evolution of pressure inside the cylinder (solid line) and prechamber (dashed line) for the PC1 test case with different spark advance. In particular, the PC1 test has a spark time equal to 33 crank angle degrees before the TDC, while the other test case has a spark time equal to 25 crank angle degrees before the TDC. Delaying the spark time, the fuel mass trapped in the prechamber rises, resulting in a higher pressure peak during the ignition phase. Consequently, the pressure peak in the main chamber decreases and it occurs later than the original spark time, since the flame front enter in the combustion chamber later. Accordingly, the whole combustion process occurs later respect to the base spark time (Figure 5-40).

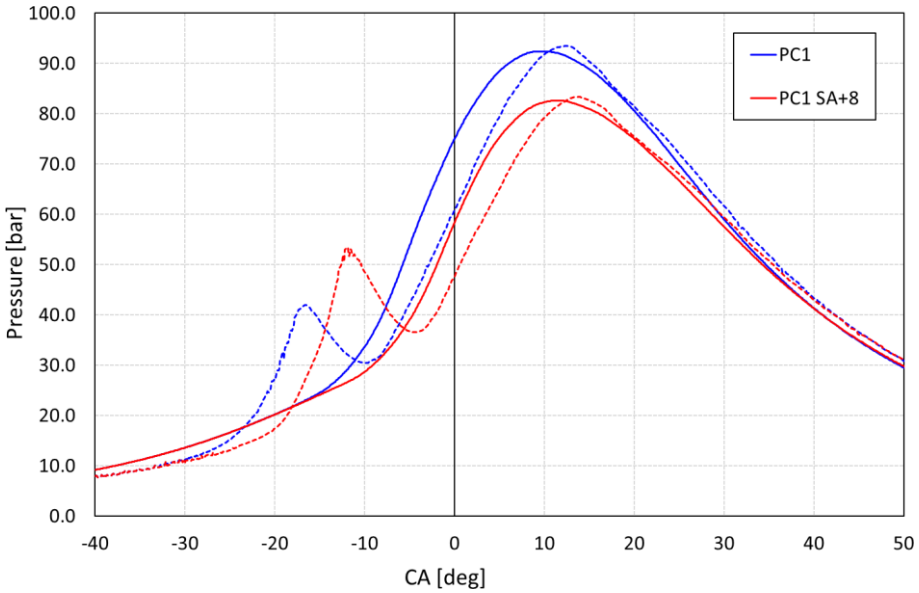

Figure 5-39. Evolution of pressure during combustion for PC1 prechamber: spark advance sensitivity.

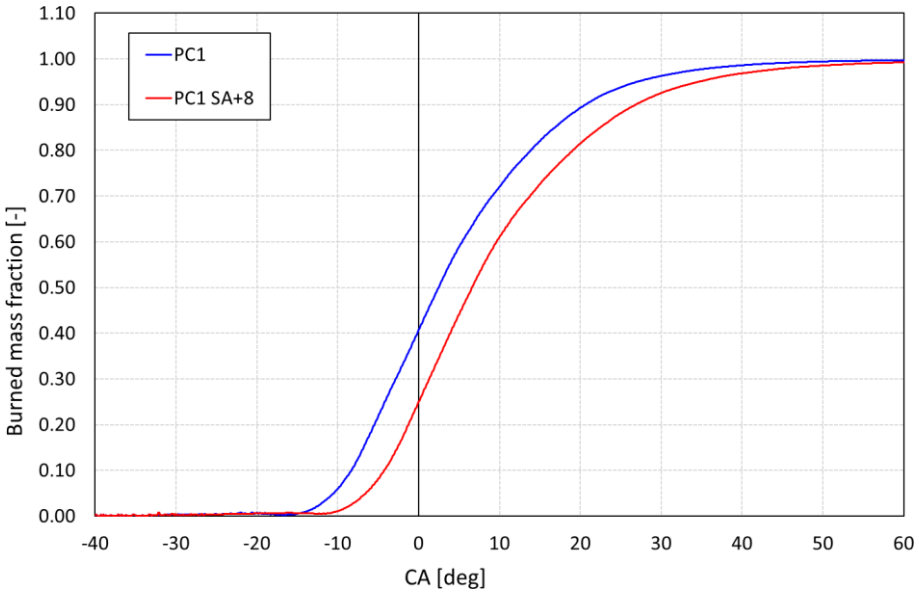

Figure 5-40. Burned mass fraction for PC1 prechamber: spark advance sensitivity.

Figure 5-41 shows the comparison of the flame front propagation on a section perpendicular to the axis of the engine and passing through the main chamber between the two spark advances simulated. It can be noted how the flame front is delayed with a later spark time.

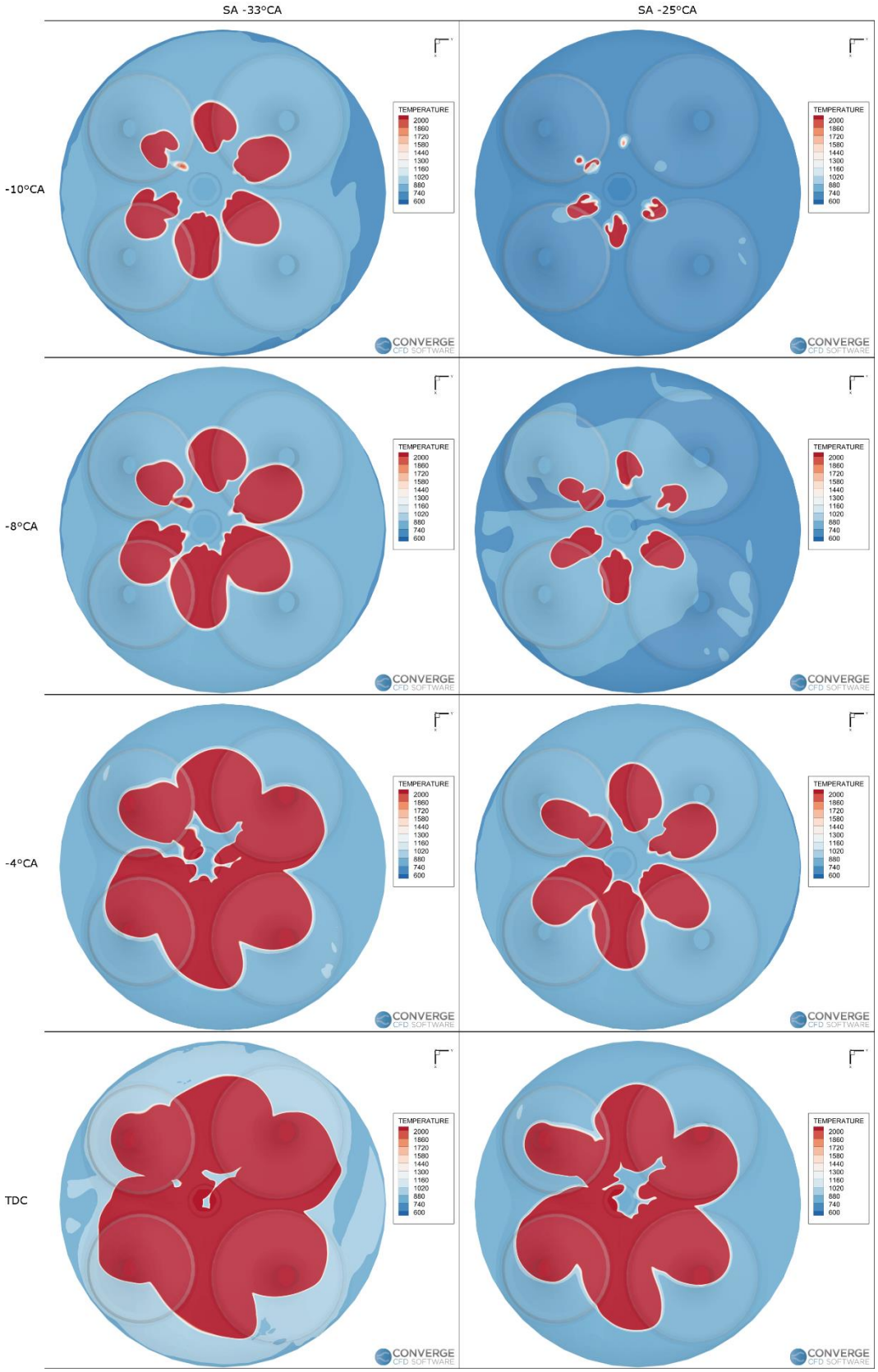

Figure 5-41. Contour of temperature on a section xy in the cylinder for PC1: comparison between two different spark advances.

All the prechambers with different diameters show the same behaviour when varying the spark advance, with a pressure curve and burned mass fraction shift towards the TDC and a higher pressure peak inside the prechamber during the ignition phase than the simulation with the experimental spark time.

Thus, the prechambers analysed above are simulated varying the spark advance. In the whole test cases, the spark advance is delayed of 8 crank angle degrees (Table 5-4).

Test case	PC1 SA+8	PC2 SA+8	PC3 SA+8
Prechamber	PC1	PC2	PC3
Spark advance	-25°CA	-25°CA	-25°CA

Table 5-4. Test matrix for spark advance sensitivity.

Figure 5-42 shows the in-cylinder pressure during combustion for the test cases reported in Table 5-4 and the baseline configuration, which has the experimental spark time, i.e. -33 crank angle before the TDC. It can be noted that the maximum in-cylinder pressure roughly occurs at the same crank angle of the baseline simulation, as shown in Figure 5-43 too. Even if the spark time is delayed by 8°CA, the maximum pressure during combustion inside the main chamber is greater than the one computed in the baseline configuration (by roughly 6% with PC3 up to 12% with PC2).

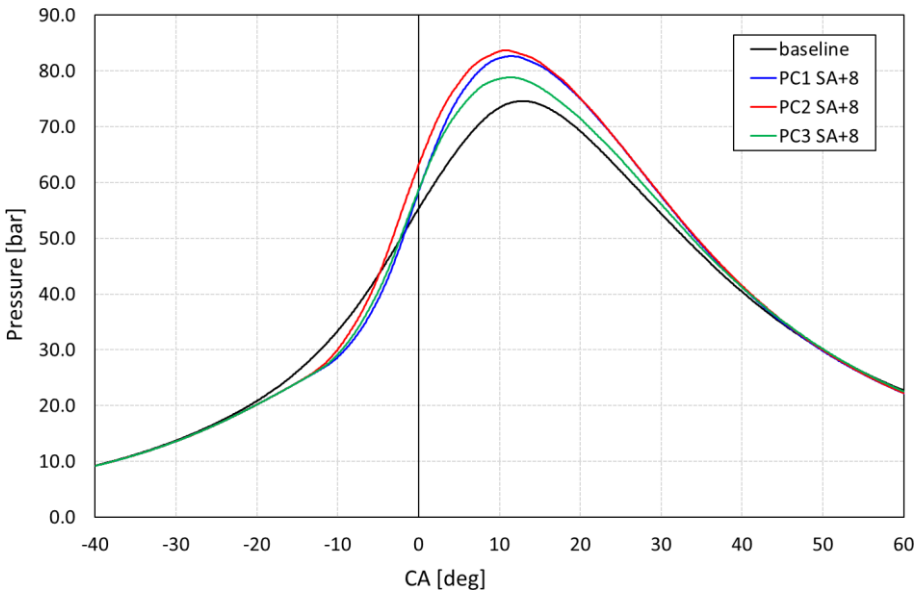

Figure 5-42. Evolution of in-cylinder pressure during combustion: comparison between the baseline and prechambers configuration with different spark advance.

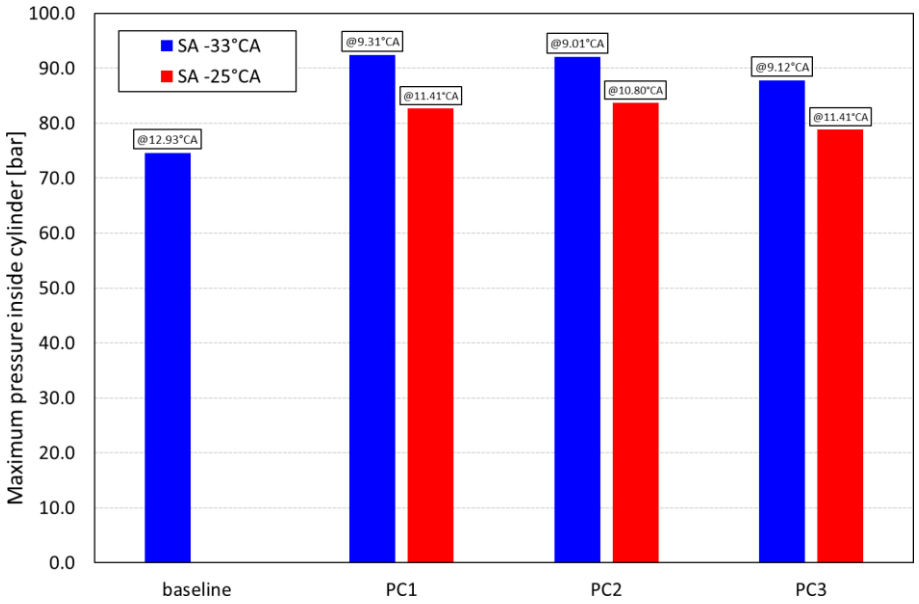

Figure 5-43. Maximum pressure inside the cylinder during combustion: spark advance sensitivity.

Although the spark advance delayed, the combustion inside the main chamber results faster than the one simulated in the baseline engine, as reported in Figure 5-44. The process inside the cylinder starts later than the baseline configuration but, as the hot jets exit from the orifices, the flame front allows to burn the fresh mixture quickly, confirming the advantages in using the prechamber. It is worth noting that the combustion inside the main chamber starts before in PC2, which has the diameters equal to 1.1d. The test case with the highest diameters generates a process slower in the last phase of the combustion. This behaviour is a combination of the low inertia of the hot jets coming from the prechamber and less the turbulent kinetic energy inside the main chamber.

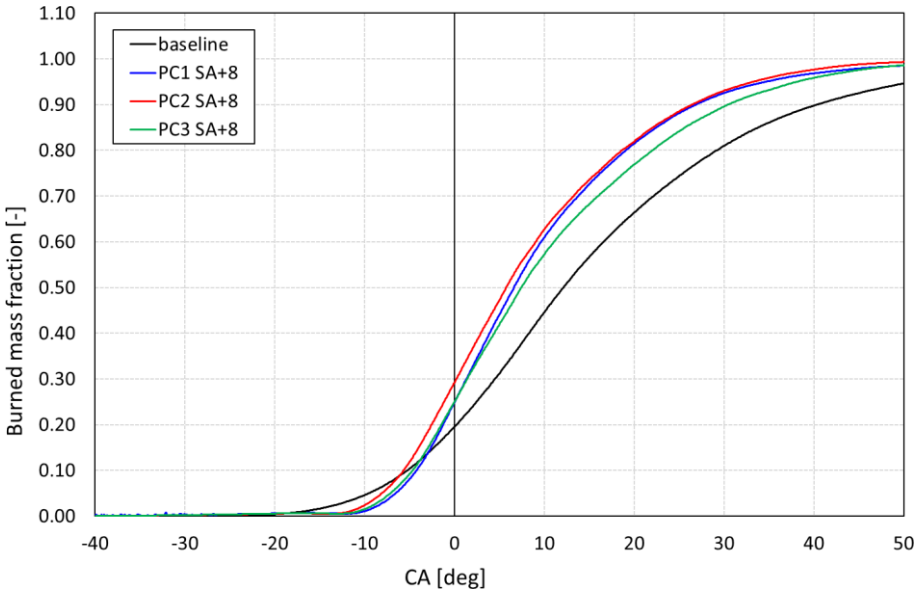

Figure 5-44. Burned mass fraction inside the cylinder: comparison between the baseline and prechambers configuration with different spark advance.

Figure 5-45 shows the evolution of the flame front inside the main chamber on a section perpendicular to the axis of the engine. The hot jets coming from the prechamber PC2 enter in the main chamber before the other two test cases, while the flame front with PC1 is able to speed up the process when the mixture is ignited in the main chamber due to the highest turbulent kinetic energy. Furthermore, it is evident that the combustion process in PC3 is the most delayed, since the flame front has filled the less volume of the combustion chamber.

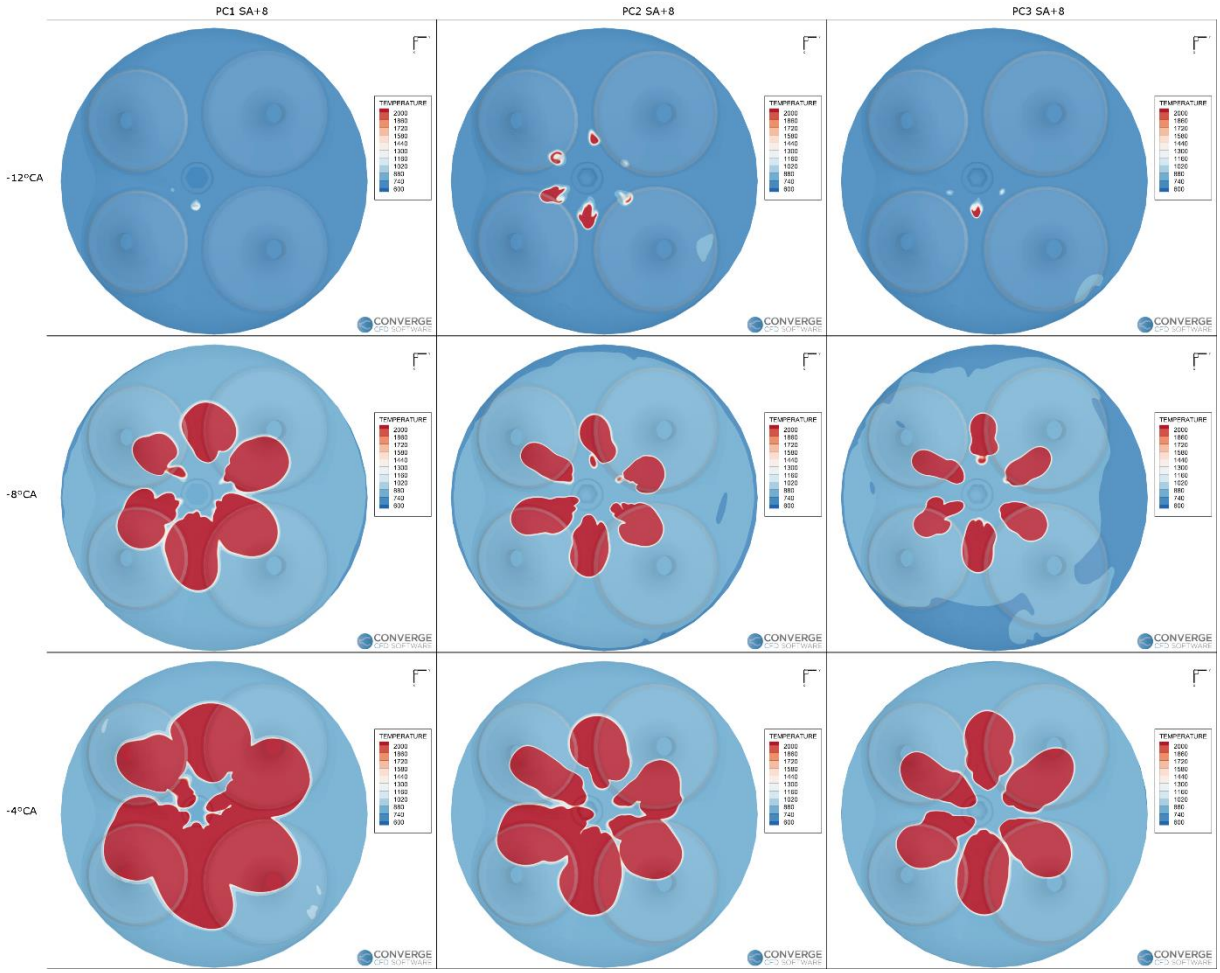

Figure 5-45. Contour of temperature inside the cylinder on a section xy: comparison between different prechambers with spark advance -25°CA.

5.4 - Prechamber results: sensitivity to the air-to-fuel ratio

According to the theory and to the literature, the prechamber in internal combustion engine allows to speed up the combustion of the fresh mixture inside the cylinder, resulting in a faster and more efficient process. As seen in previous paragraphs, all the test cases simulated show a reduction in terms of crank angle degrees necessary to complete the oxidation of the fuel. Respect to the baseline configuration, the hot flame jets exiting from the orifices are able to start the ignition process in the main chamber and to speed up the laminar phase of combustion, during which the chemical reactions are activated and the flame kernel grows slowly. In practice, the prechamber plays the role of a more powerful and more efficient ignition system and the flame jets play the role of multiple spark plug. Thus, the prechamber is able to extend the ignition limit of the fresh mixture through the hot jets, compensating for the lack of turbulent kinetic energy and air-to-fuel ratio. In particular, the composition of the mixture has a major influence on the combustion process, since the equivalence ratio affects the flame front propagation through the laminar flame speed. Furthermore, internal combustion engines suffer from the cycle-to-cycle variation: there are fluctuations in the flow field, which alter the local composition of the mixture and may lead to instabilities during the

combustion process, since the local air-to-fuel ratio differs from the optimal operation conditions. The prechamber may overcome this drawback. Thus, a sensitivity to the air-to-fuel ratio is carried out for all the prechambers with different diameters tested above. The equivalence ratio of the fresh mixture is varied by reducing the amount of fuel. In order to evaluate the potential of the prechamber when the engine operates with lean mixture and have a benchmark of the engine performance for comparison, the baseline configuration is simulated too with different equivalence ratio. At first, the results of air-to-fuel ratio sensitivity of the engine in the baseline configuration are presented, comparing the in-cylinder pressure with the one at maximum power, derived from the calibration analysis. Finally, the results of the sensitivity to the equivalence ratio of the mixture are shown, comparing the evolution of the combustion process with the baseline results. The simulations carried out by varying the equivalence ratio are summarized in Table 5-5.

Air-to-fuel ratio [-]	0.82	1.05	1.10	1.2	1.4
Test case	Baseline, PC1, PC2, PC3	PC2	PC2	Baseline, PC1, PC2, PC3	Baseline, PC1, PC2, PC3

Table 5-5. Test matrix for air-to-fuel ratio sensitivity.

At first, the CFD simulations with high air-to-fuel ratio (i.e. 1.2 and 1.4) are carried out, in order to evaluate the combustion performance and in-cylinder pressure when the engine is operating close to the flammable limit. The comparison of the CFD results showed that the PC2 geometry allows to obtain the best performance in terms of flame propagation, combustion duration and in-cylinder pressure. Thus, the prechamber PC2 is tested with air-to-fuel ratio close to the stoichiometric value, in order to evaluate the engine performance and the fuel saving.

Figure 5-46 shows the comparison of the air-to-fuel ratio sensitivity for the baseline configuration, in terms of in-cylinder pressure during combustion. It can be noted that, as the mixture gets lean, the combustion process tends to slow down (Figure 5-47), since the laminar flame speed decrease due to the low amount of fuel. Consequently, the pressure peak inside the cylinder decreases and it is shifted towards the TDC. When the air-to-fuel ratio is equal to 1.4, the combustion starts with difficulty and the in-cylinder pressure is similar to a motored curve (i.e. without combustion).

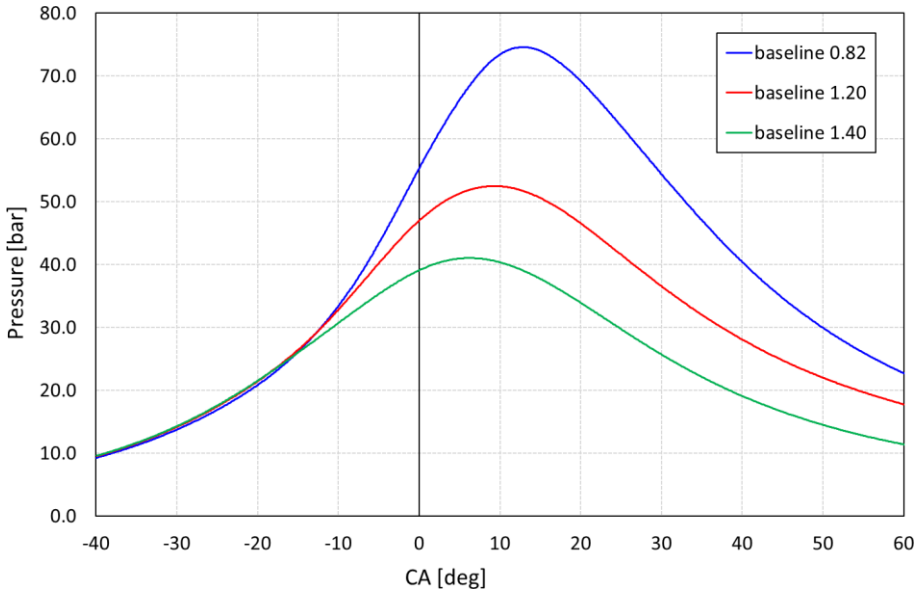

Figure 5-46. Evolution of the in-cylinder pressure during combustion of baseline configuration: air-to-fuel ratio sensitivity.

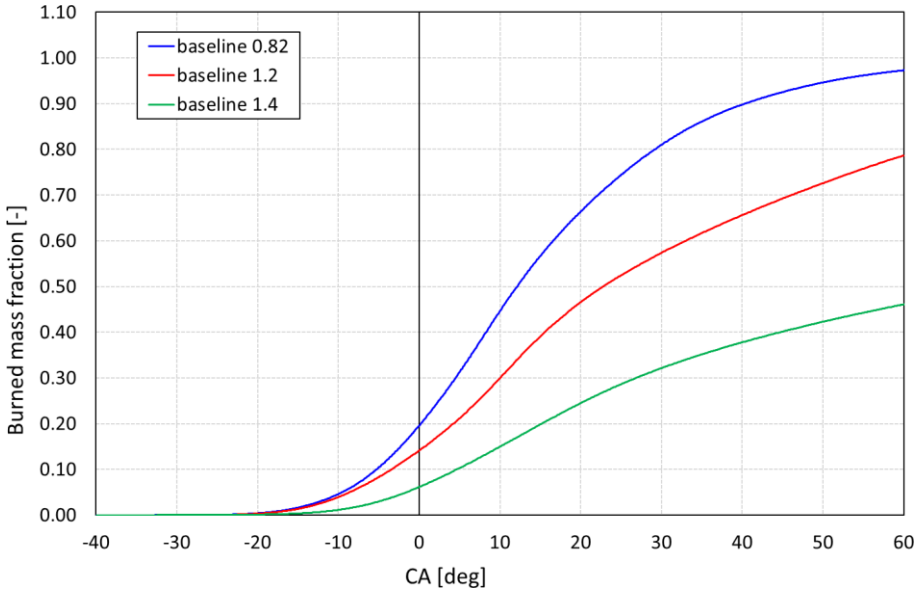

Figure 5-47. Burned mass fraction during combustion of baseline configuration: air-to-fuel ratio sensitivity.

Figure 5-48 shows the evolution of the flame front inside the cylinder between the different equivalence ratios tested for the baseline configuration. It can be noted how the flame front propagation is very different, depending on the fresh mixture composition. For the whole test cases, the flame front tends to propagate where the turbulent kinetic energy is higher, resulting a flame stretched towards the intake valves. As the amount of fuel reduces, the flame speed decrease and it is not able to propagate where the turbulent structures are missing (as can be seen in Figure 5-49).

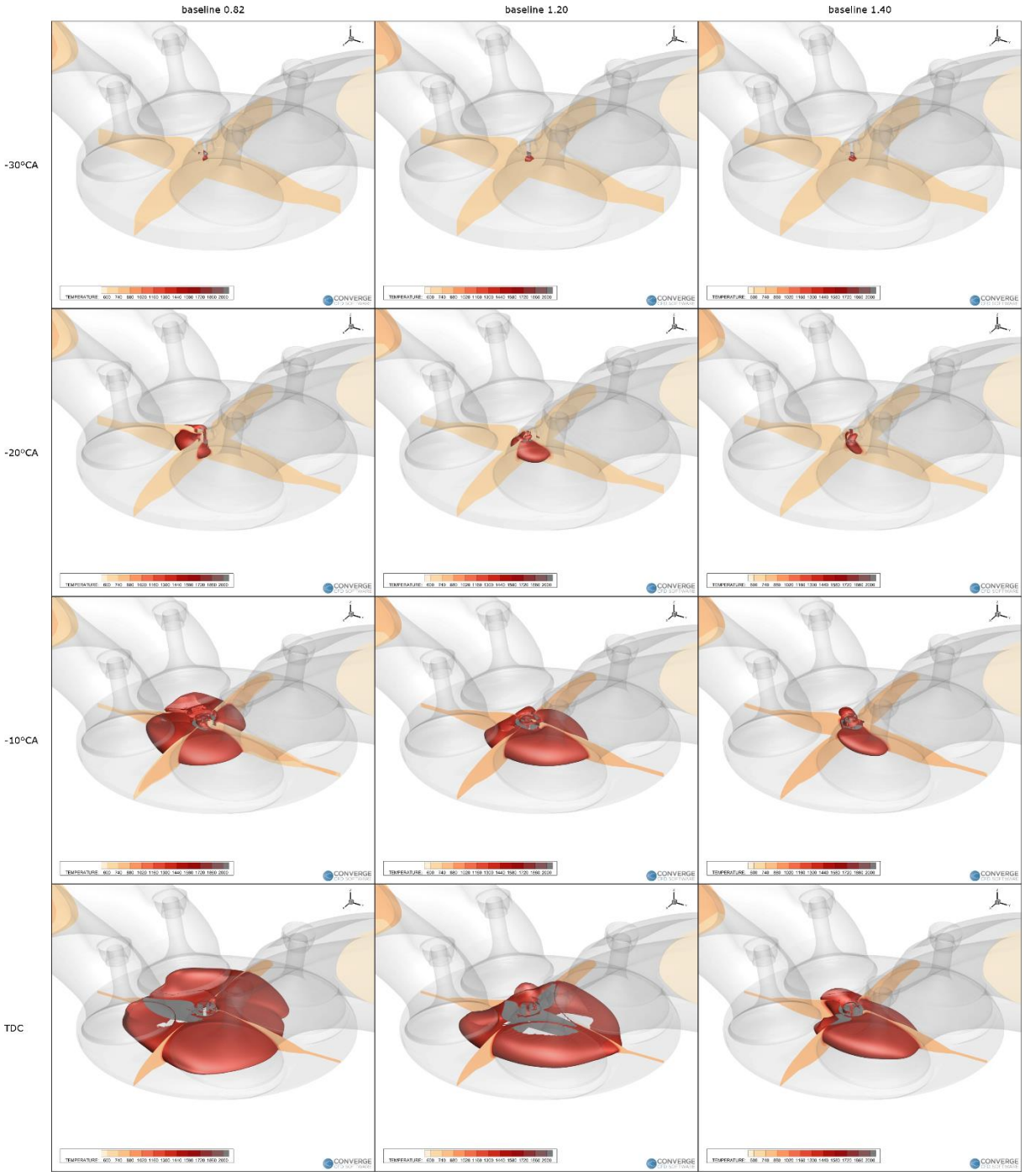

Figure 5-48. Flame front propagation during combustion in baseline configuration: comparison between different air-to-fuel ratios.

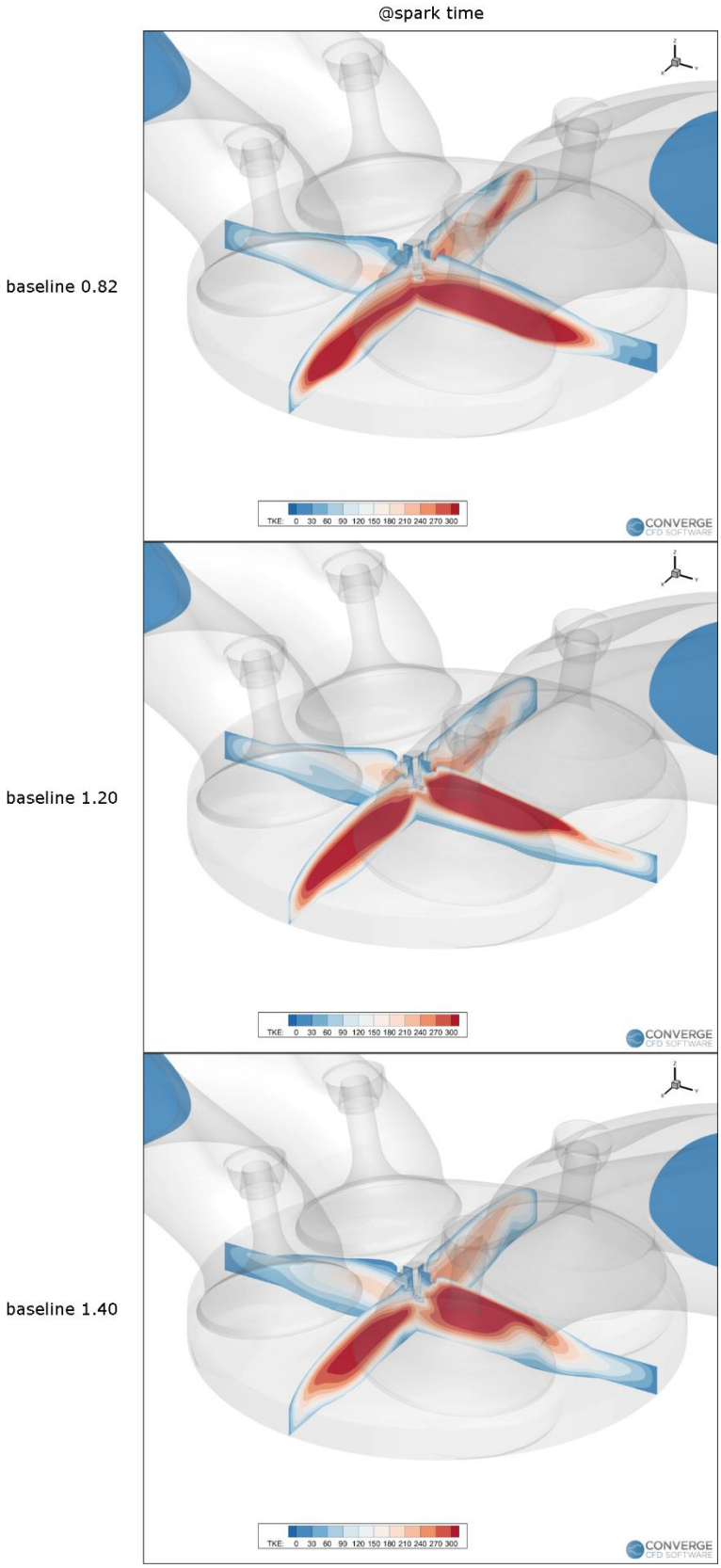

Figure 5-49. Contour of TKE inside the cylinder at the spark time for the baseline configuration: comparison between different air-to-fuel ratios.

After the sensitivity of the equivalence ratio on the baseline configuration, the CFD analysis on the prechamber is carried out by varying the amount of fuel in the fresh mixture. At first, the results of the sensitivity on the prechamber PC1 are presented, in order to evaluate how the mixture composition affects the combustion process. Finally, the comparison between the different prechambers and baseline configuration are shown, in order to evaluate the best configuration for the engine. Since the lack of experimental information on the operating point simulated, the spark time is set equal to the one measured at maximum power, in the baseline configuration.

Figure 5-50 shows the pressure inside the cylinder (solid lines) and prechamber (dashed lines) during combustion for the prechamber PC1, with different equivalence ratios. As the mixture gets lean, the ignition phase in the prechamber takes longer: lower the fuel, later the pressure peak inside the prechamber. The pressure peak inside the cylinder decreases with increasing the air-to-fuel ratio, since the amount of fuel is lower. It is worth noting that the equivalence ratio of the mixture does not affect notable the position of the maximum pressure inside the cylinder. While in baseline configuration the pressure peak inside the cylinder gets close to the TDC reducing the fuel in the fresh gases, with prechamber the maximum pressure remains roughly in the same position. This means that the hot jets coming from the prechamber that are able to ignite the fresh gases and to generate a fast combustion process in the main chamber, even if the mixture is very lean.

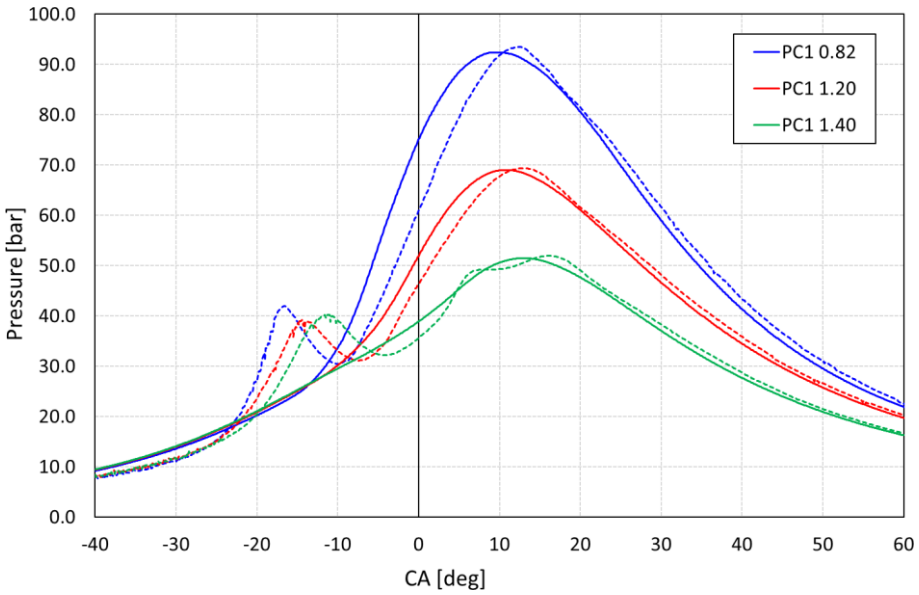

Figure 5-50. Evolution of pressure during combustion for prechamber PC1: air-to-fuel ratio sensitivity.

Even if the prechamber allows to ignite the fresh gases in the cylinder, the combustion process slows decreasing the equivalence ratio of the mixture, as shown in Figure 5-51 and Figure 5-52.

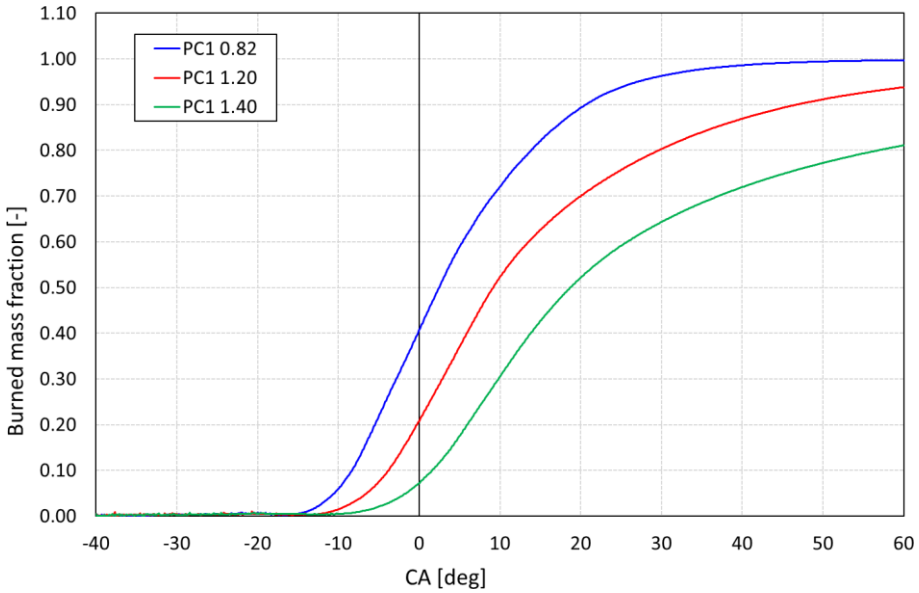

Figure 5-51. Burned mass fraction of PC1: air-to-fuel ratio sensitivity.

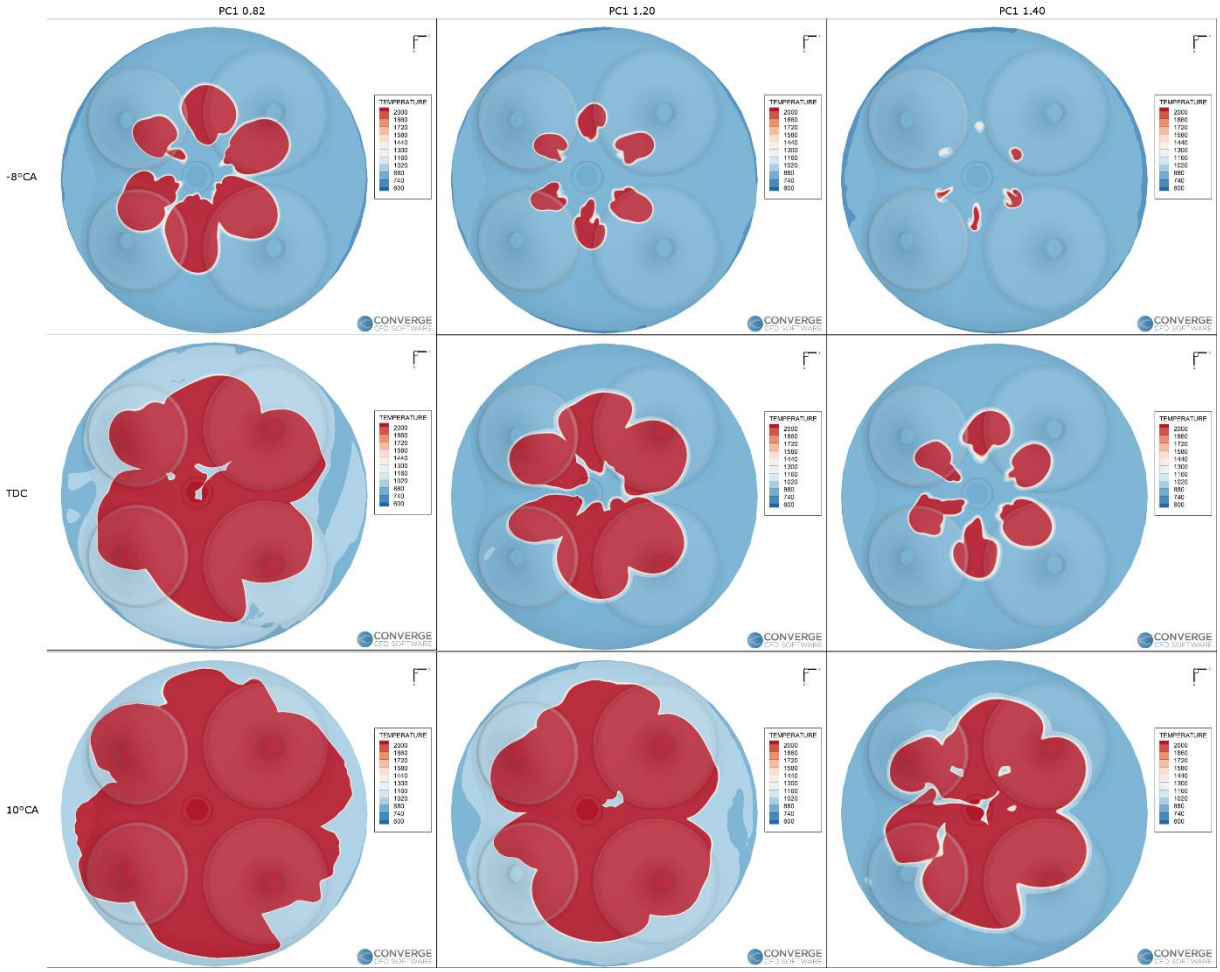

Figure 5-52. Evolution of the flame front in the cylinder for PC1 prechamber: air-to-fuel ratio sensitivity.

In order to understand the capability of the prechamber operating with lean mixture, it is necessary to compare the prechamber results with the baseline ones, at the same equivalence ratio. Considering an air-

to-fuel ratio equal to 1.20 (Figure 5-53), it can be noted that the prechamber allows to decrease the compression work, since the combustion is not yet occurred in the main chamber. As the hot jets enters into the cylinder, the fresh gases ignite quickly, even if the mixture is lean, increasing the pressure inside the combustion chamber. As seen before, the maximum pressure occurs roughly in the same position of the baseline one at maximum power. It is worth noting that, during the expansion phase the pressure curve with prechamber remains above the one computed in baseline configuration.

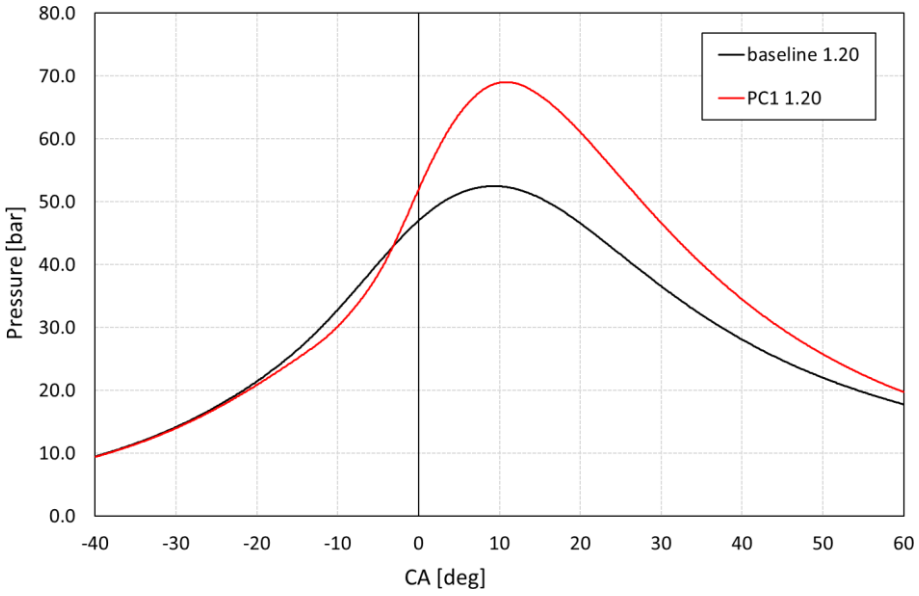

Figure 5-53. Comparison of in-cylinder pressure between baseline and PC1 with air-to-fuel ratio 1.20.

The advantages of the prechamber with a lean mixture are more evident observing the burned mass fraction of fuel inside the main chamber (Figure 5-54). It can be noted that the process in the cylinder start later with prechamber, since the flame is still in the prechamber. Even if the two test cases burn the 10% of fresh gases at the same crank angle degrees, the rate of burn of PC1 is much greater than the baseline configuration. At 60°CA, while the piston is moving towards the BDC, the PC1 test case has already burnt over than 90% of the fresh gases, while the baseline test case under the 80%.

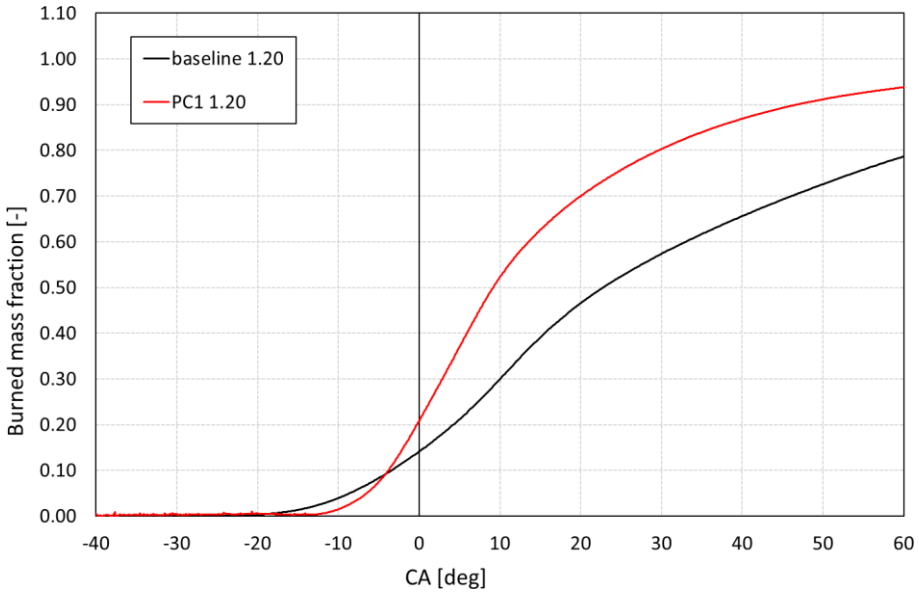

Figure 5-54. Burned mass fraction inside the cylinder for air-to-fuel ratio 1.20: comparison between baseline and PC1.

Figure 5-55 compares the flame front propagation of the baseline and PC1 test case, with an air-to-fuel ratio 1.20. It can be noted how the hot jets coming from the prechamber are able to ignite the lean mixture inside the main chamber, which burns faster even the low amount of fuel in the fresh gases. Comparing the evolution of the process, as explained before, it can be noted that with lean mixture, the flame front in baseline test case is not able to propagate where the turbulent kinetic energy is missing: thus, the flame results strongly stretched towards the intake valves. Conversely, with prechamber, the hot jets allow to ignite the mixture even if the turbulent structures are weak, resulting in a more homogeneous propagation inside the main chamber.

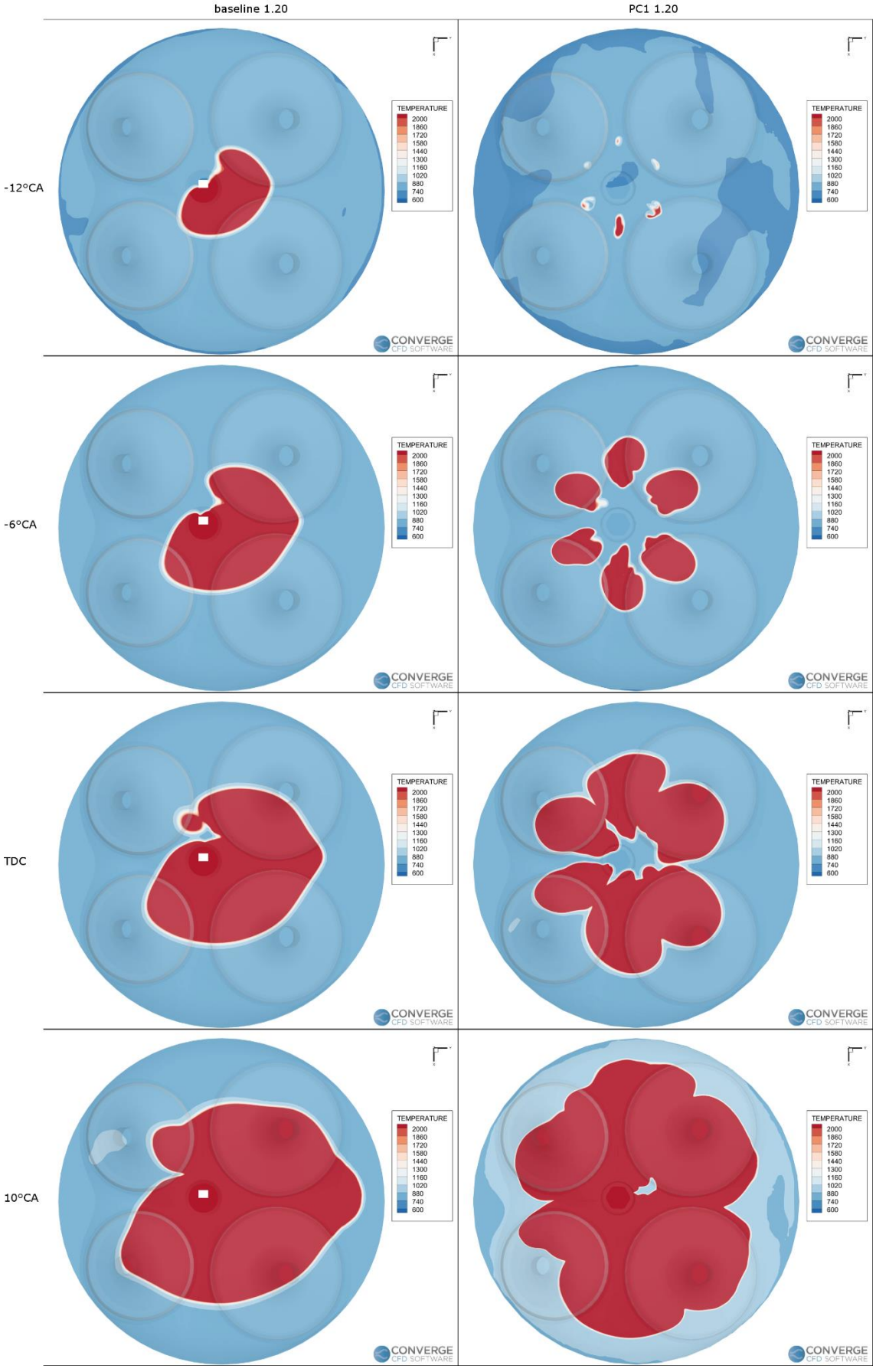

Figure 5-55. Contour of temperature with air-to-fuel ratio 1.20: comparison between baseline and PC1.

Observing the comparison in terms of in-cylinder pressure between baseline and PC1 results with the leanest mixture tested (i.e. 1.40), it can be noted that without prechamber the combustion almost does not occur, with a pressure peak close to the TDC (Figure 5-56). Conversely, using the prechamber allows increase the pressure peak over 50 bar, greater than 30% respect to the baseline one.

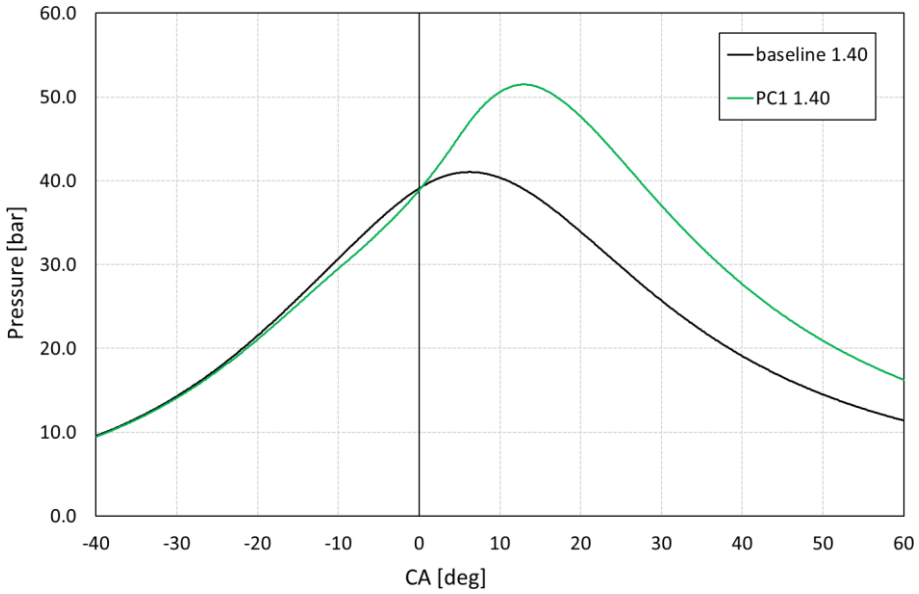

Figure 5-56. Evolution of in-cylinder pressure for air-to-fuel ratio 1.40: comparison between baseline and PC1.

Comparing the burned mass fraction (Figure 5-57), it can be seen that the prechamber produces a faster combustion process, allowing to extend the ignitable limit of the mixture.

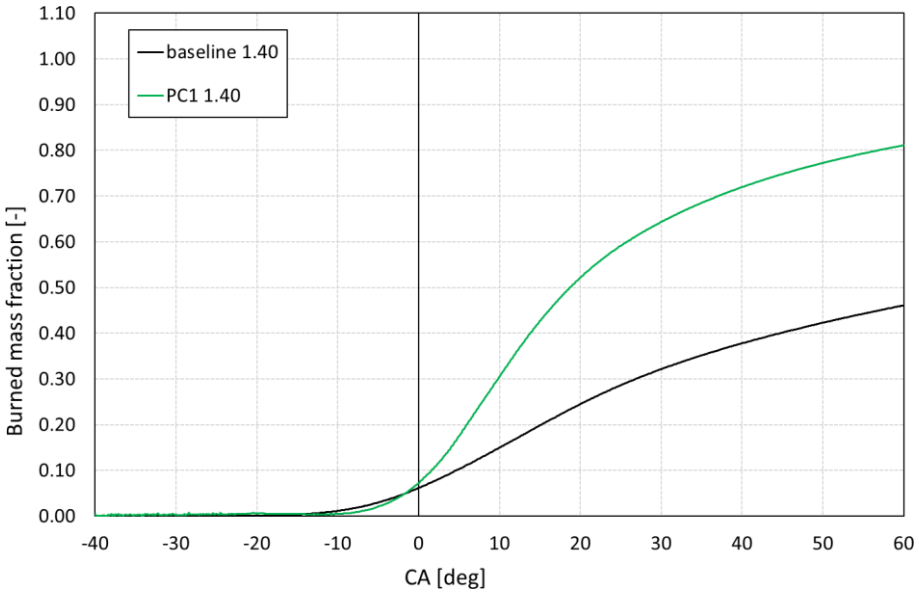

Figure 5-57. Burned mass fraction inside cylinder for air-to-fuel ratio 1.40: comparison between baseline and PC1.

Figure 5-58 shows the evolution of the flame front when the air-to-fuel ratio is equal to 1.40. From the comparison between the baseline configuration and prechamber PC1, it can be noted that without prechamber the process is very slow: even if the spark advance is -33 crank angle degrees, at the TDC the flame front is limited to a spark plug zone. Conversely, in PC1 test case, the hot jets are able to ignite the fresh gases in the cylinder as they exit from the orifices.

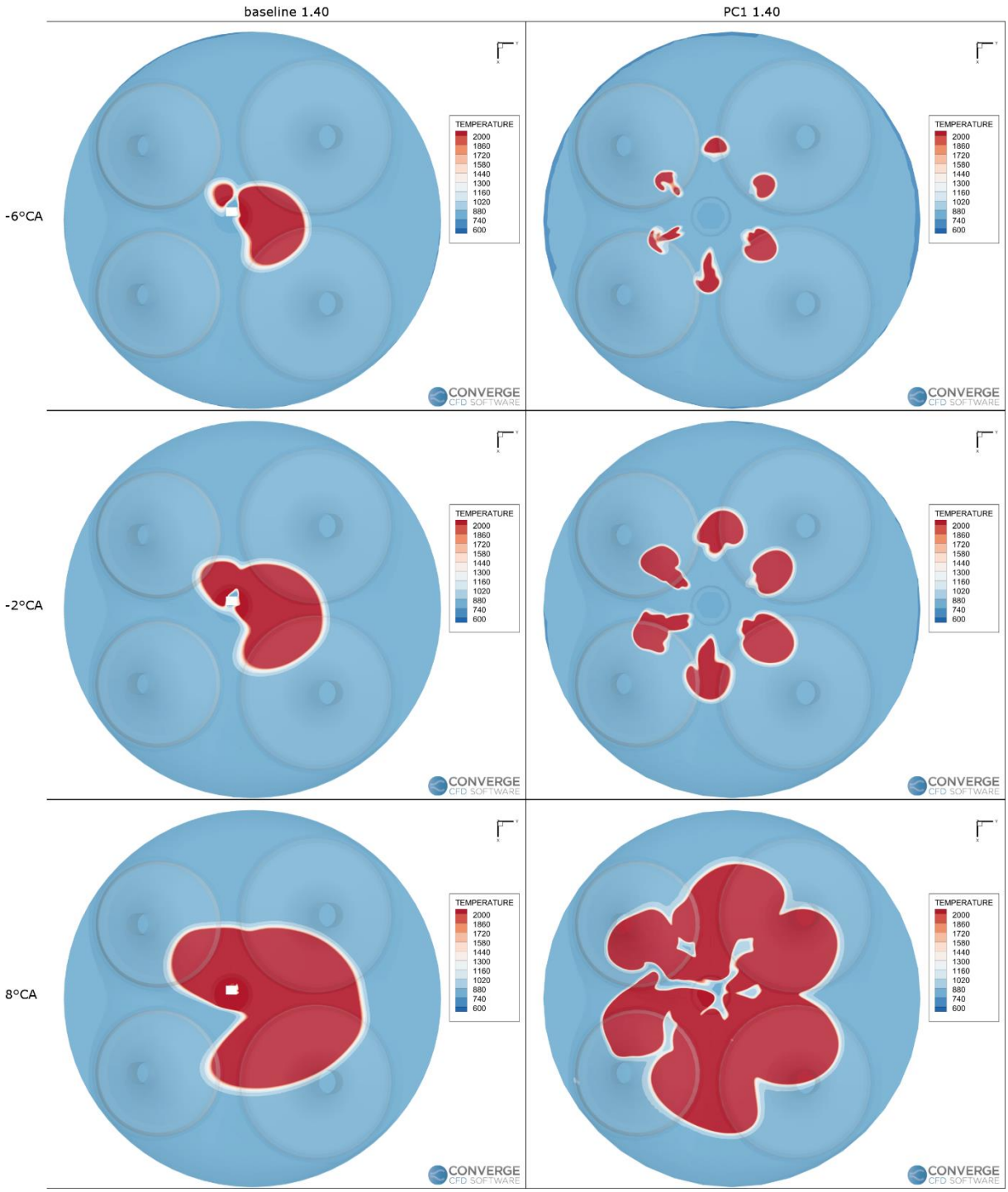

Figure 5-58. Flame front propagation inside the cylinder for air-to-fuel ratio 1.40: comparison between baseline and PC1.

After the analysis of air-to-fuel ratio sensitivity on prechamber PC1, it is obvious that the prechamber allows to speed up the combustion process at lean condition and it allows to extend the ignitable limit of the mixture. Thus, a comparison between the prechamber tested in previous paragraph is necessary. Figure 5-59 shows the evolution of pressure inside cylinder (solid lines) and prechamber (dashed lines) for simulations with air-to-fuel ratio equal to 1.20. With a lean mixture, increasing the orifices diameters leads to an increase of pressure inside the cylinder. In fact, since the amount of fuel is low, higher the diameters lower the pressure

drop through the orifices and higher the amount of fresh mixture trapped in the prechamber. Thus, the prechamber with the smallest diameter seems to be the worst between the three test cases simulated. Even then, the prechamber PC2 produces the highest peak inside the prechamber after the spark time, due to the best ratio between the total passage area and volume, resulting in a faster ignition phase (Figure 5-60). As the flame jets enter in the main chamber, the PC3 produces the fastest combustion process and the highest pressure in the main chamber (Figure 5-61).

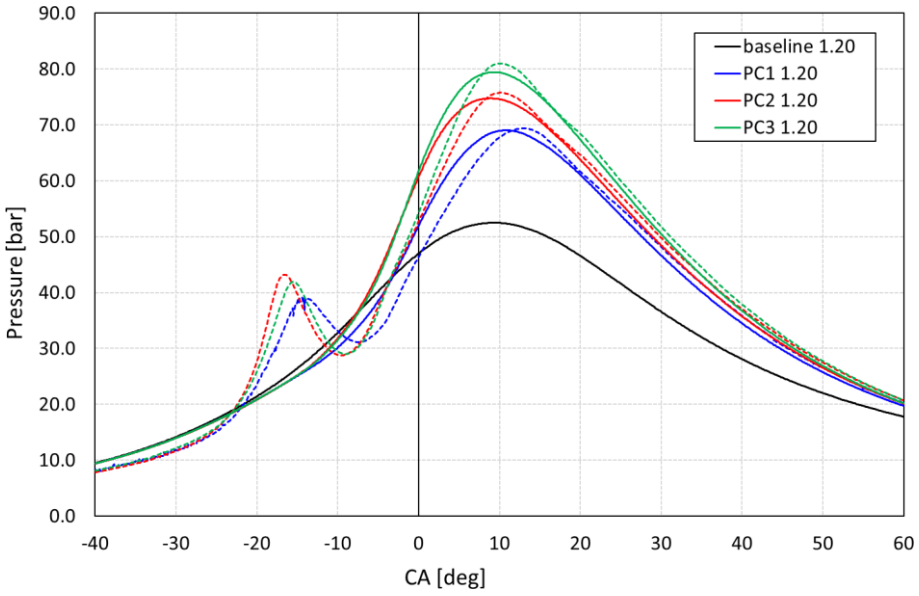

Figure 5-59. Evolution of pressure inside cylinder for air-to-fuel ratio 1.20: comparison between baseline and prechambers.

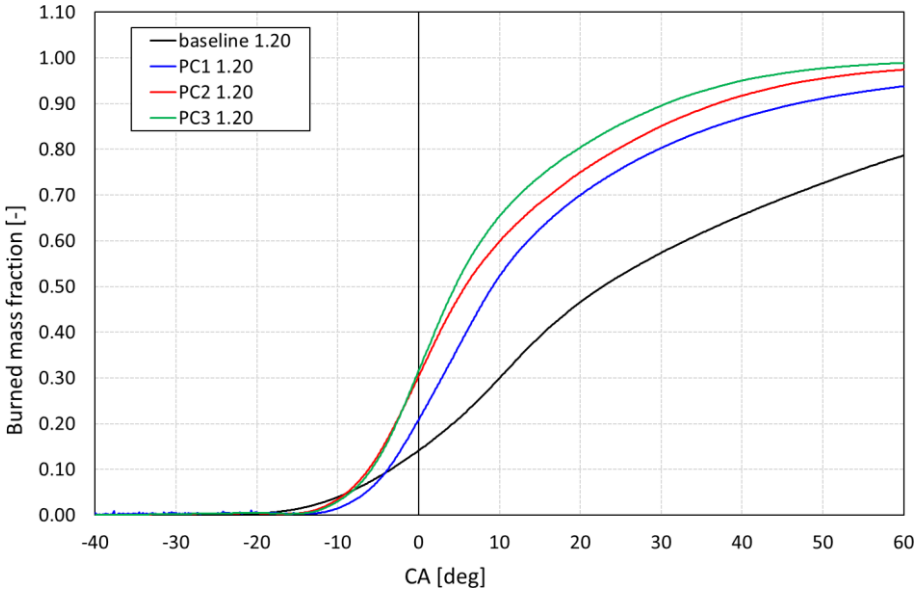

Figure 5-60. Burned mass fraction inside the cylinder with air-to-fuel ratio equal to 1.20: comparison between baseline and prechambers.

With an air-to-fuel ratio equal to 1.20 the combustion process with prechamber results much faster than the baseline one, with a reduction of 10-50% of burned mass fraction roughly 55% with PC2 and 60% with PC3.

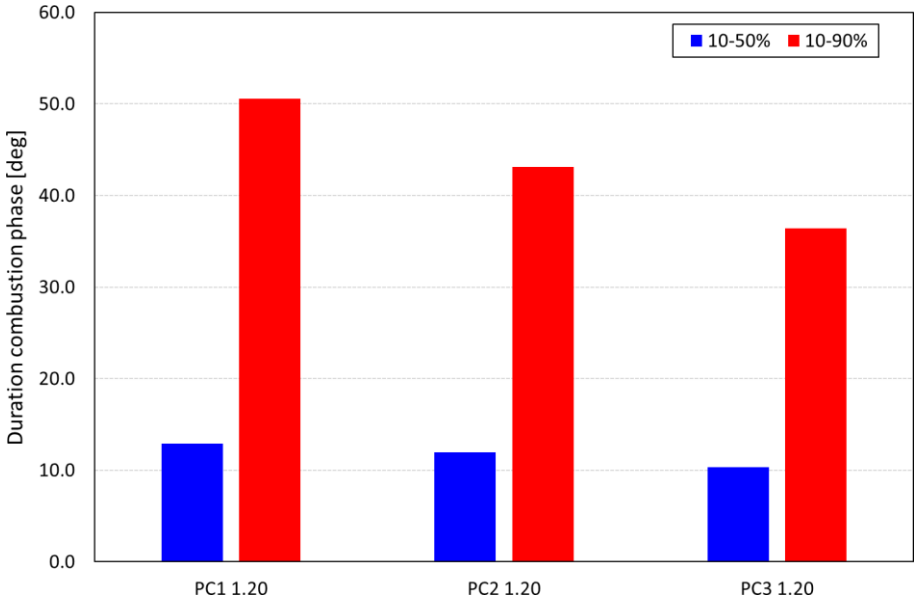

Figure 5-61. Combustion phase with air-to-fuel ratio 1.20: comparison between different prechambers.

As can be seen in Figure 5-62, the flame generated in PC1 is delayed respect to the other two prechambers. PC2 and PC3 are able to produce the faster ignition phase: thus, the jets coming from the prechamber enter in the main chamber earlier respect to PC1. There are not major differences in flame front propagation between PC2 and PC3 before the TDC.

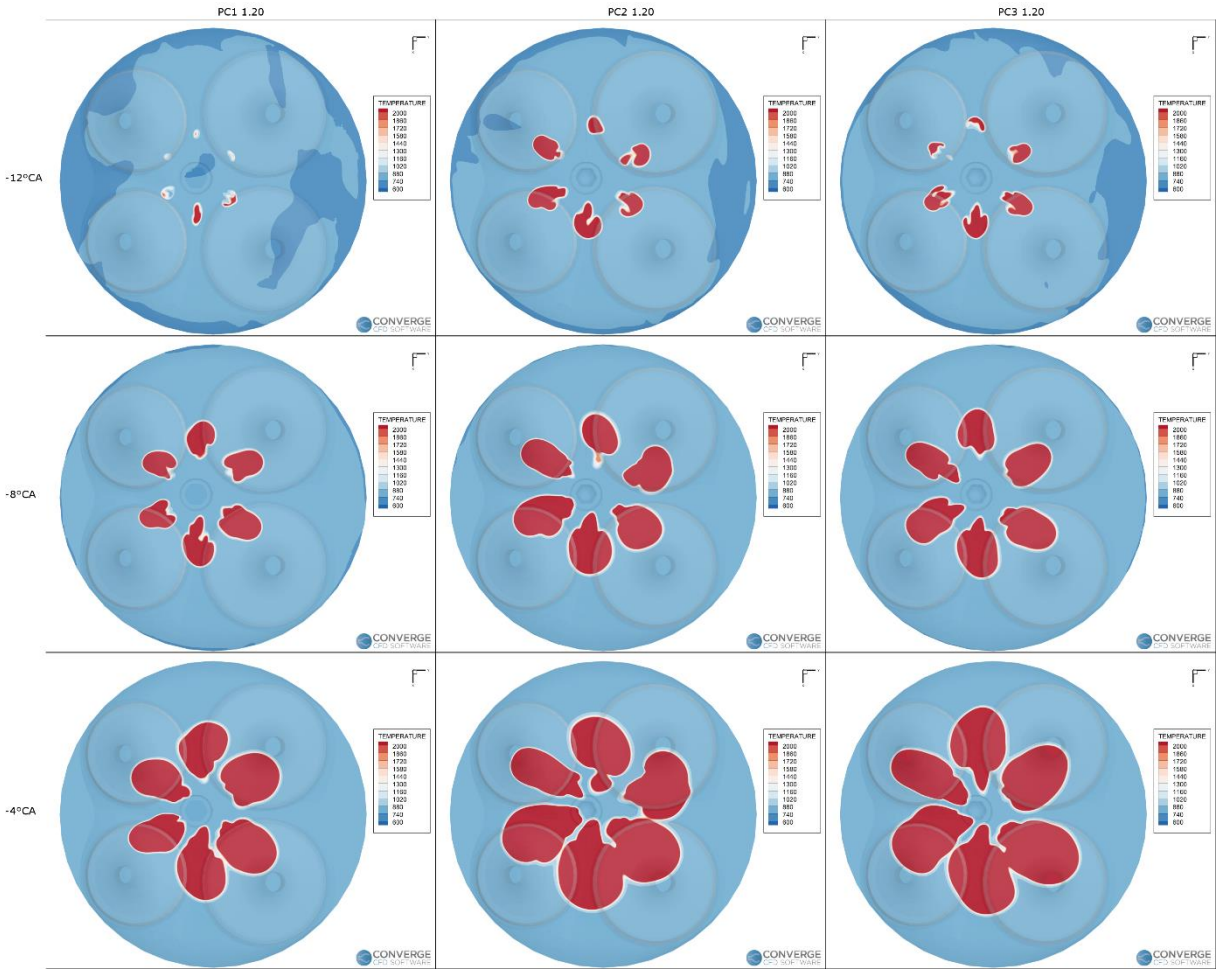

Figure 5-62. Evolution of the flame front inside the cylinder for air-to-fuel ratio 1.20: comparison between different prechambers.

Some differences arise after the TDC, as can be seen in Figure 5-63. It can be noted that the flame with PC3 is slightly further than PC2 flame front. This is due to the higher turbulent kinetic energy inside the cylinder before the entering of the flame jets (Figure 5-64). The greater turbulence enhances the flame front propagation, resulting in a faster combustion process for the prechamber PC3. Nevertheless, the differences between the two prechambers are minimal.

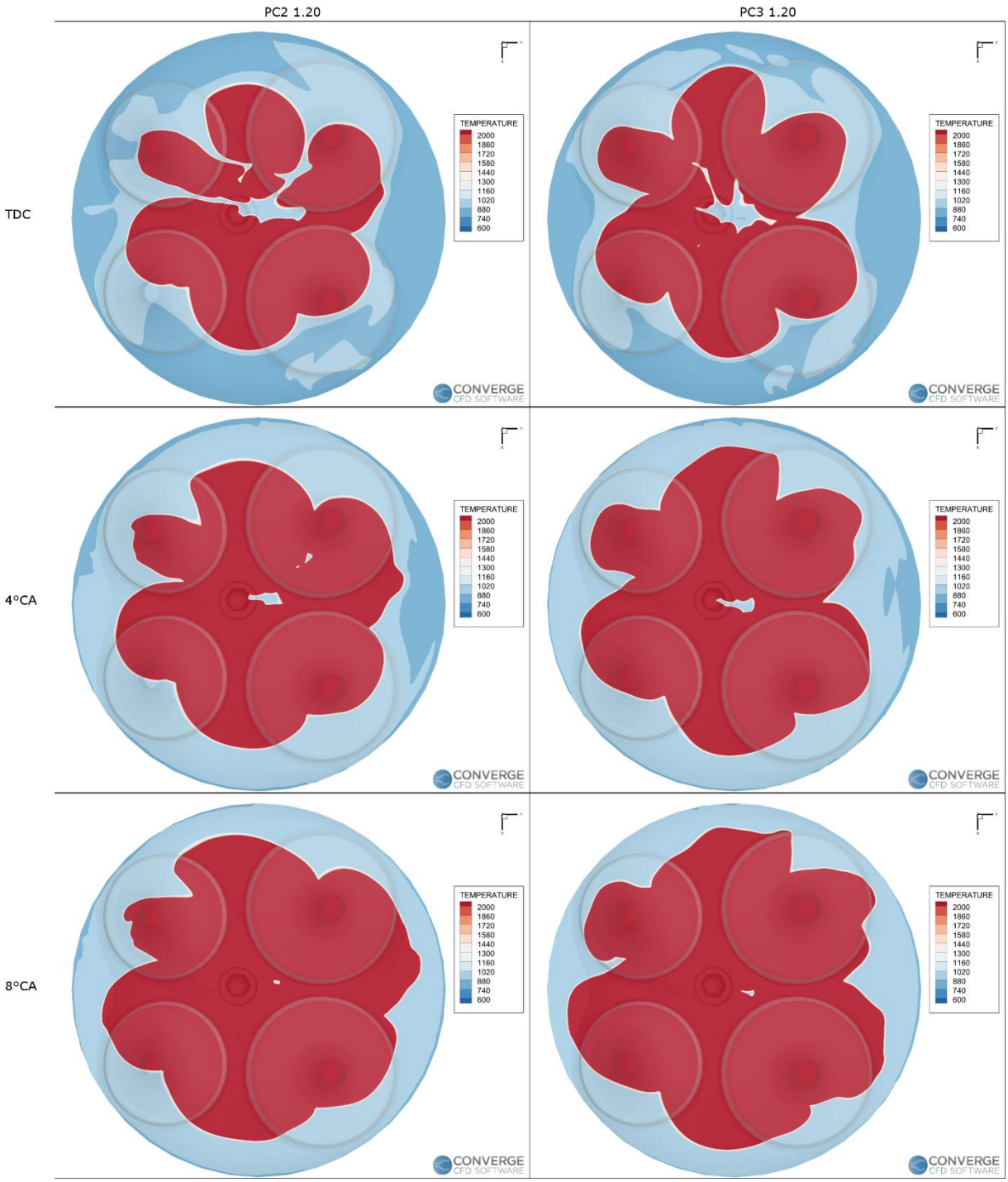

Figure 5-63. Flame front evolution inside the cylinder with air-to-fuel ratio 1.20: comparison between PC2 and PC3.

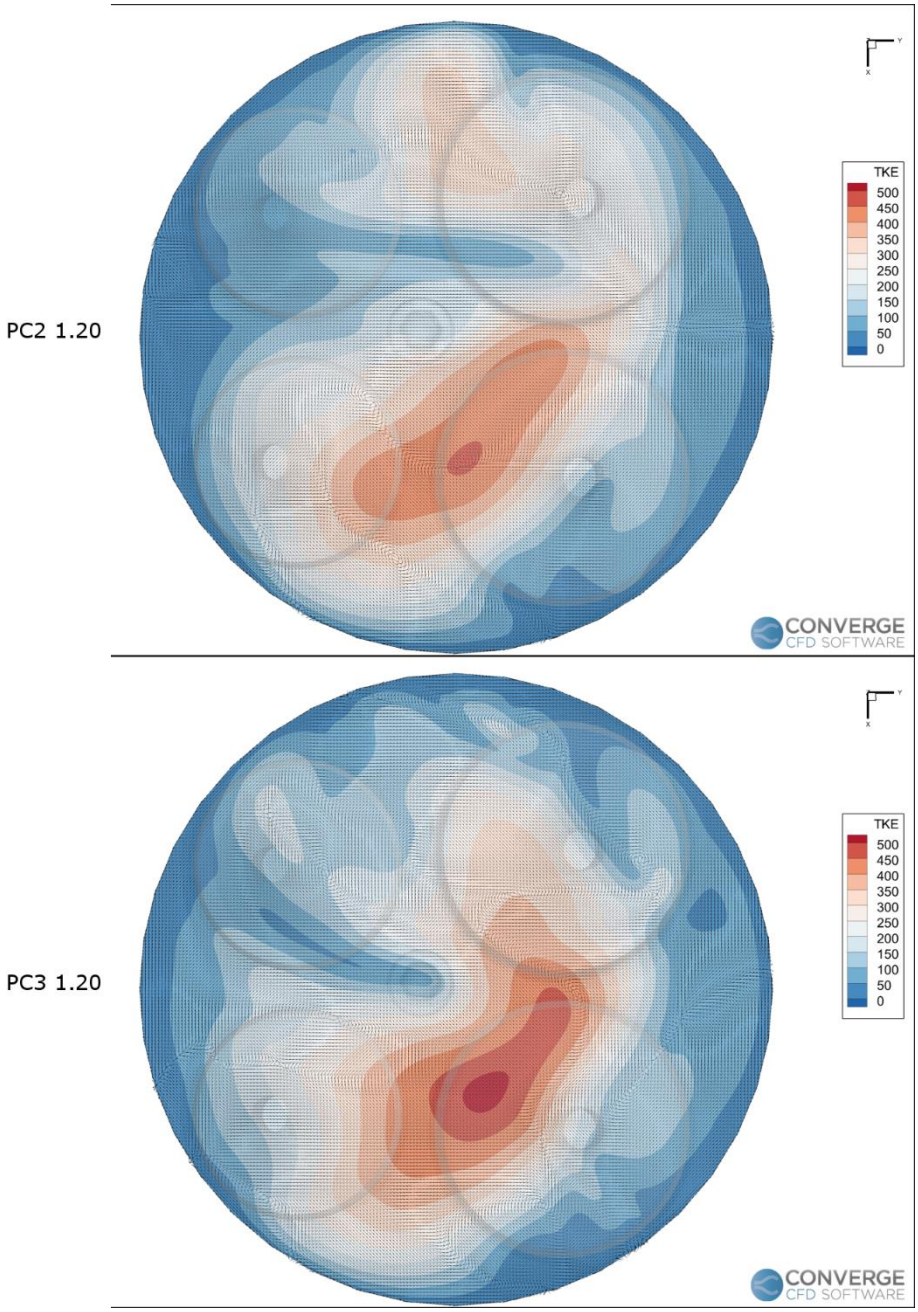

Figure 5-64. TKE contour and velocity vectors inside the cylinder at -18°CA: comparison between PC2 and PC3.

It is worth noting that the use of prechamber increases the indicated work by 40% with respect to the baseline configuration (Figure 5-65).

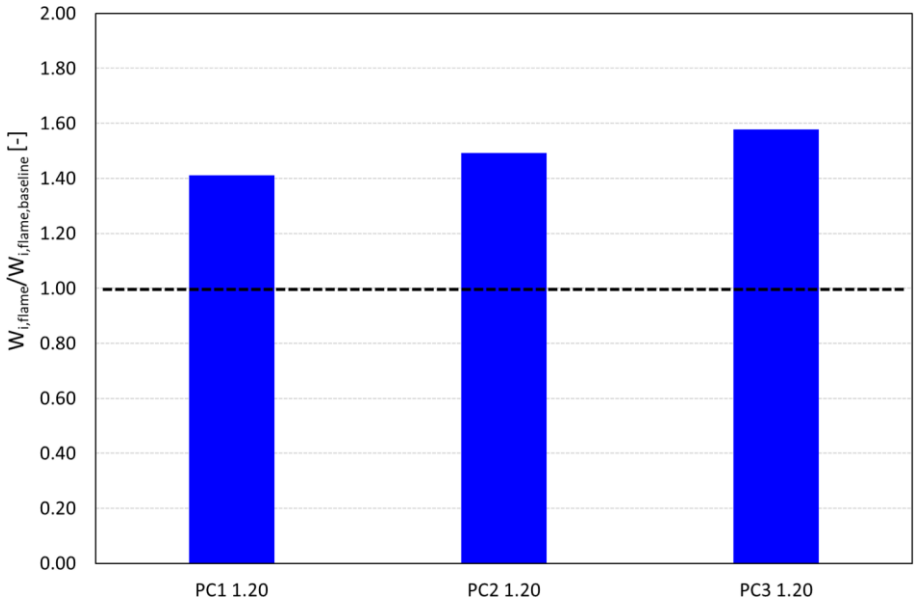

Figure 5-65. Indicated work with air-to-fuel ratio 1.20 for prechambers with different orifices diameters.

Figure 5-66 shows the comparison in terms of in-cylinder pressure for air-to-fuel ratio equal to 1.40. In this case, the differences between the prechambers are less notable than the previous case, since the lean condition of the mixture tend to level the behaviour of the engine. Nevertheless, all the prechambers shows a remarkable improvement in the combustion process respect to the baseline configuration, in terms of in-cylinder pressure and burned mass fraction (Figure 5-67). It is worth noting that with the leanest conditions tested, the prechamber PC2 produces the highest pressure inside the main chamber, with the highest maximum value.

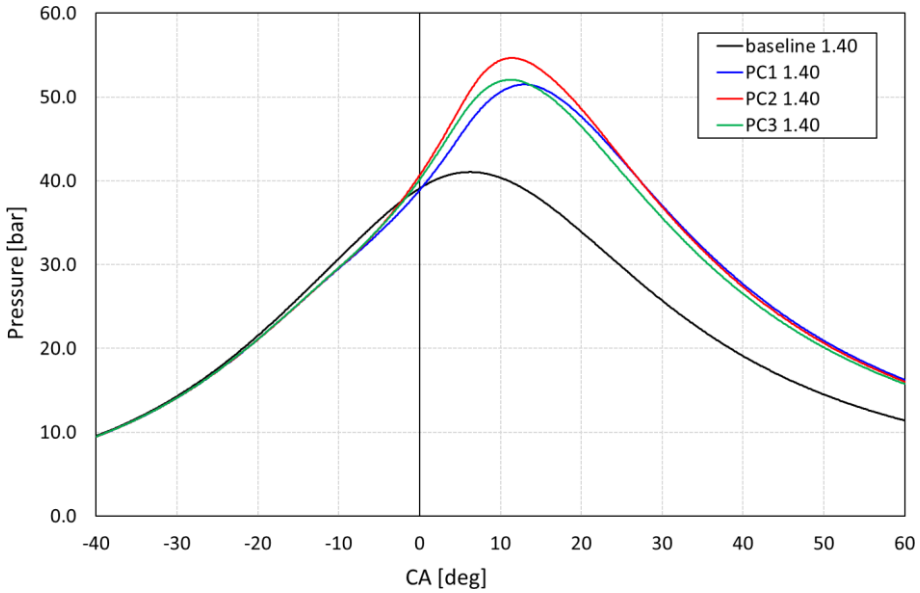

Figure 5-66. In-cylinder pressure with air-to-fuel ratio 1.40: comparison between baseline and prechambers.

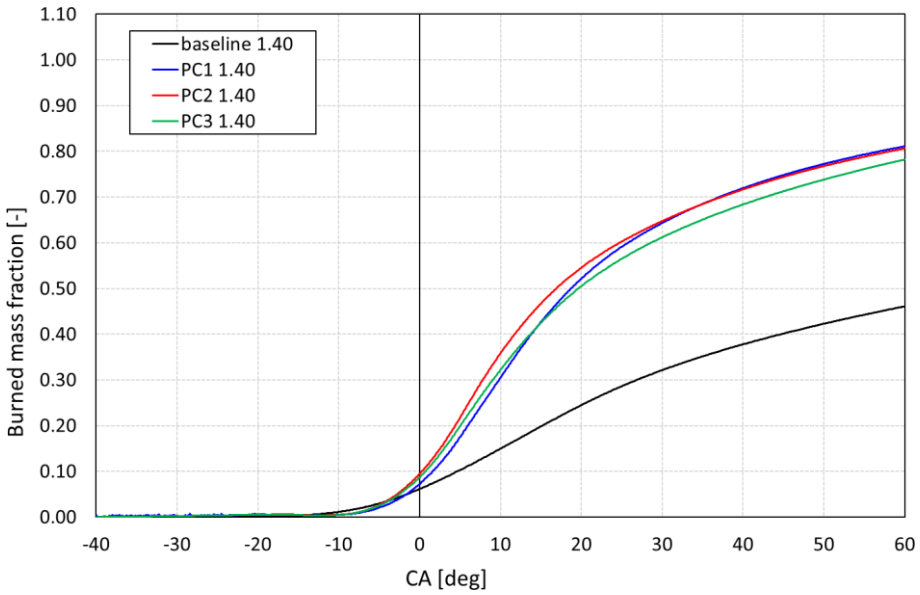

Figure 5-67. Burned mass fraction inside cylinder with air-to-fuel ratio 1.40: comparison between baseline and prechambers.

It is worth noting that, as the mixture gets lean, the flame front inside the prechamber tend to propagate like a spherical shape. Observing Figure 5-68, the flame results much less stretched than the one observed in rich condition. Furthermore, it can be noted that, with the leanest mixture condition, the differences in flame front propagation are less evident between the different prechambers.

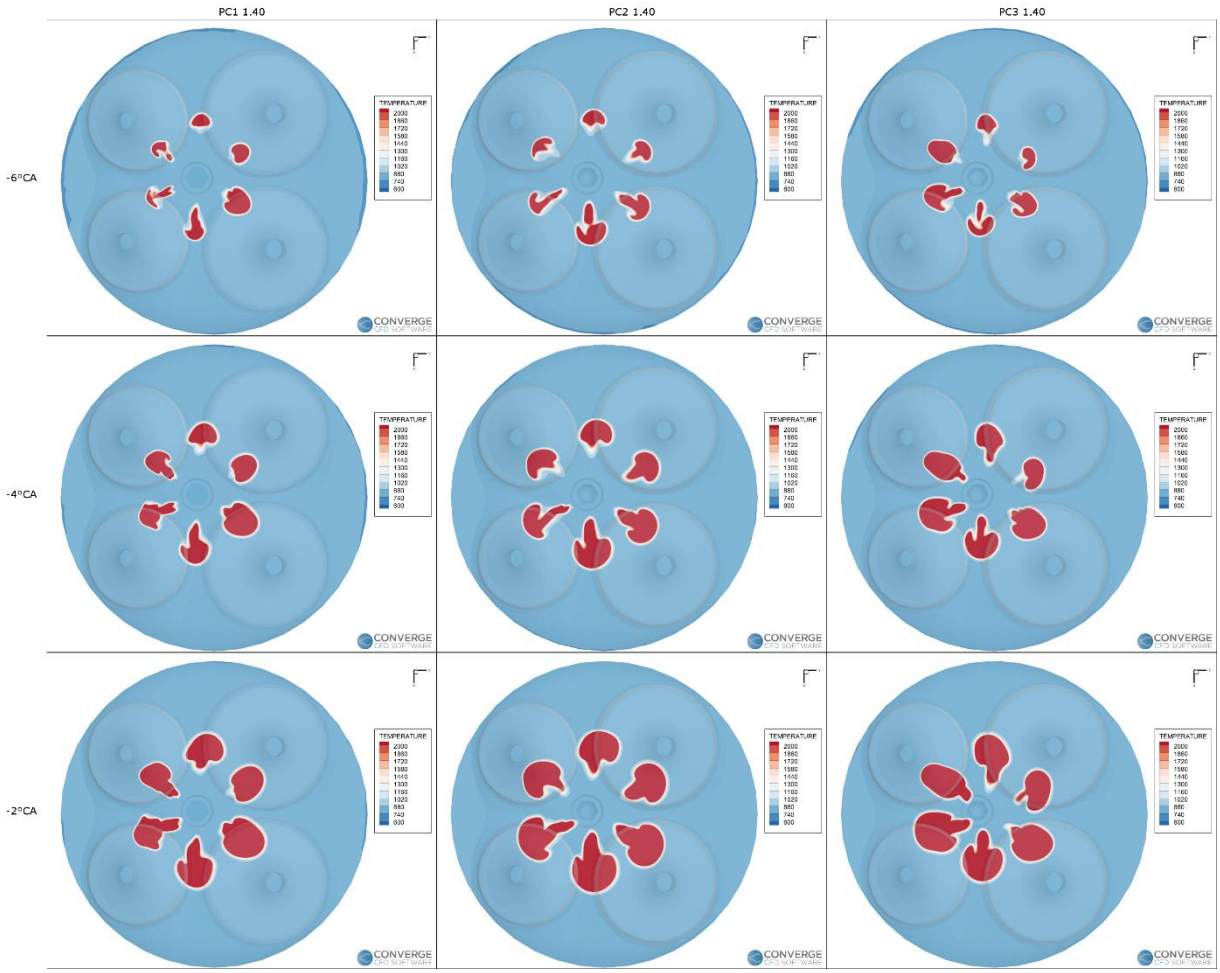

Figure 5-68. Flame front propagation inside cylinder with air-to-fuel ratio 1.40: comparison between different prechambers.

It is worth noting that the use of prechamber increases the indicated work by 80% with respect to the baseline configuration (Figure 5-69).

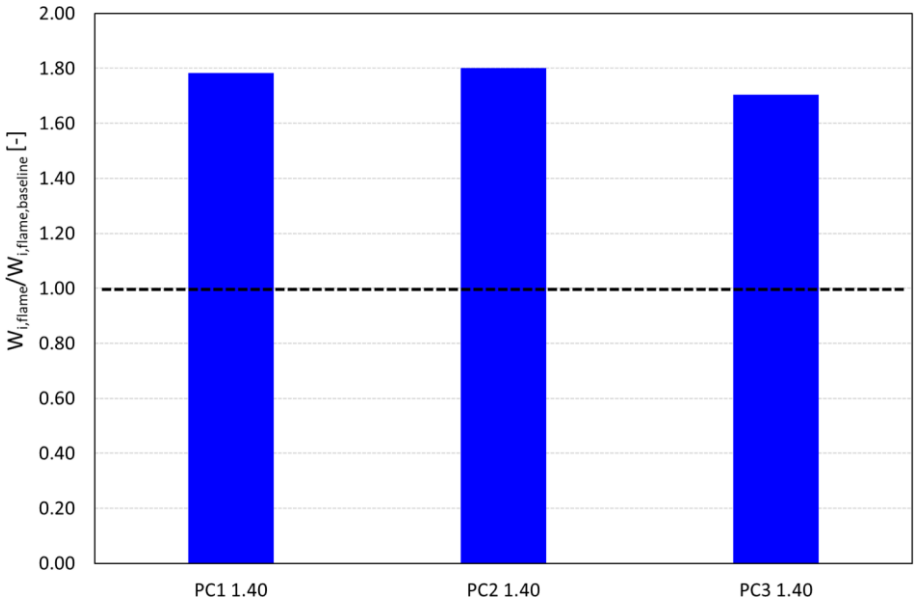

Figure 5-69. Indicated work for air-to-fuel ratio 1.40 for prechambers with different orifices diameters.

Considering the air-to-fuel ratio 1.20, the results of the engine with prechamber are very promising. Comparing the in-cylinder pressure with the baseline configuration in rich condition (Figure 5-70), it can be noted that the performance in terms of in-cylinder pressure are comparable with the one at maximum power.

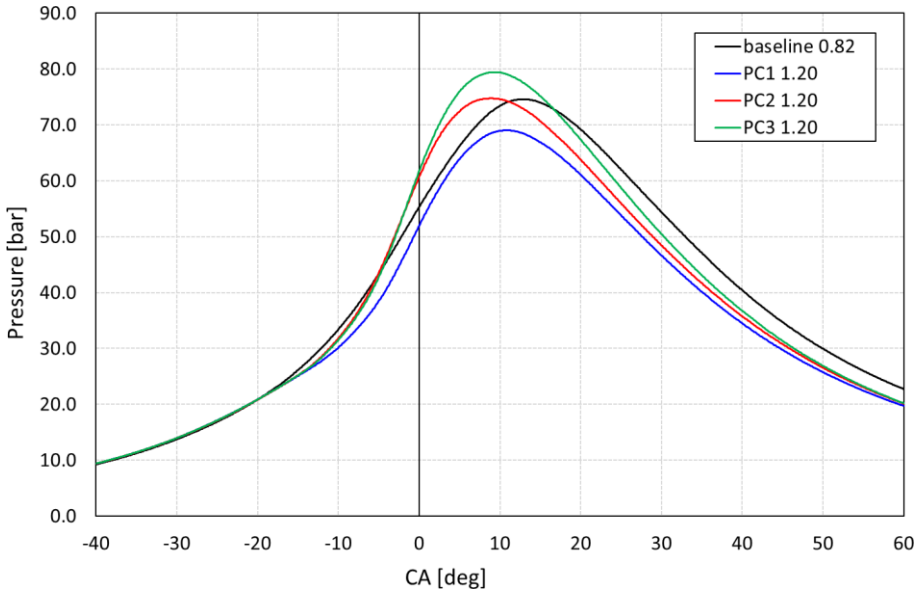

Figure 5-70. In-cylinder pressure during combustion: comparison between baseline at maximum power and prechambers with air-to-fuel ratio 1.20.

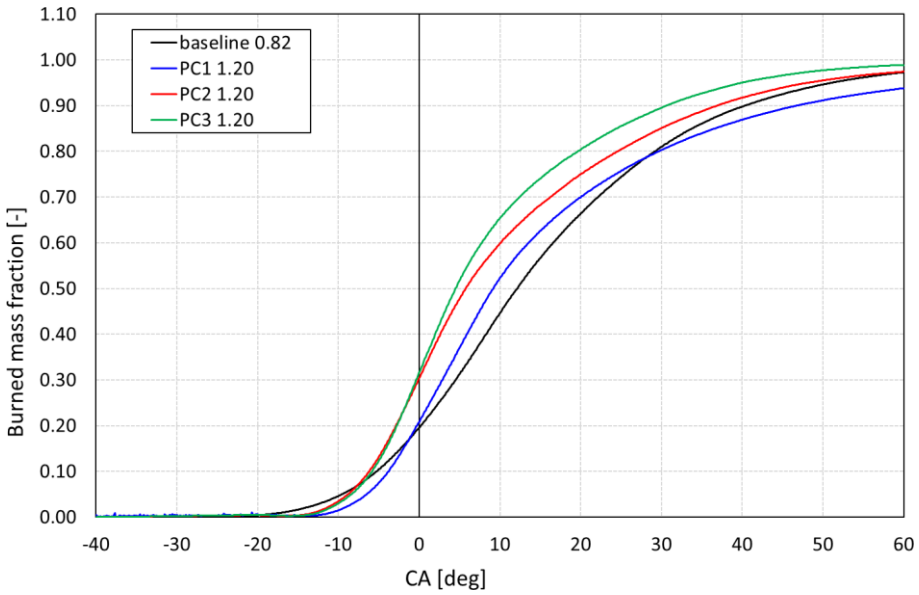

Figure 5-71. Burned mass fraction inside cylinder: comparison between baseline and maximum power and prechambers with air-to-fuel ratio 1.20.

Observing the graphs in Figure 5-70 and Figure 5-71, the combustion process with prechambers PC2 and PC3 with lean mixture appears not centered: both cases computed a maximum in-cylinder pressure earlier than the baseline at maximum power and the 50% of combustion phase occurs too early respect to the baseline one in rich condition. Thus, a further sensitivity analysis on the spark advance is carried out for the prechambers PC2 and PC3 operating with air-to-fuel ratio equal to 1.20. The spark time is delayed in order to shift the pressure and burned mass fraction curves and to obtain a combustion process similar to the one at maximum power. It is worth remembering that the baseline at maximum power represents the actual engine, since the model is calibrated against the experimental data. Thus, the spark time in this case is chosen

for obtaining the maximum indicated mean effective pressure. The simulations carried out are summarized in Table 5-6. The spark timing of this sensitivity are chosen based on the results seen in previous paragraphs.

Test case	PC2 1.20 SA+4	PC3 1.20 SA+5
Air-to-fuel ratio [-]	1.20	1.20
Spark advance [deg]	-29	-28

Table 5-6. Test matrix for spark advance sensitivity on PC2 and PC3 with air-to-fuel ratio 1.20.

Figure 5-72 and Figure 5-73 show the comparison between the baseline at maximum power and PC2 and PC3 results, in lean condition and with spark delayed. Delaying the spark timing produces a decrease of the in-cylinder pressure for both prechambers tested, since the flame jets enter in the main chamber later: thus, the mixture in the cylinder burns later. Even if the spark time is delayed of 4°CA and 5°CA, the combustion process occurs earlier than the baseline one, for both prechambers PC2 and PC3.

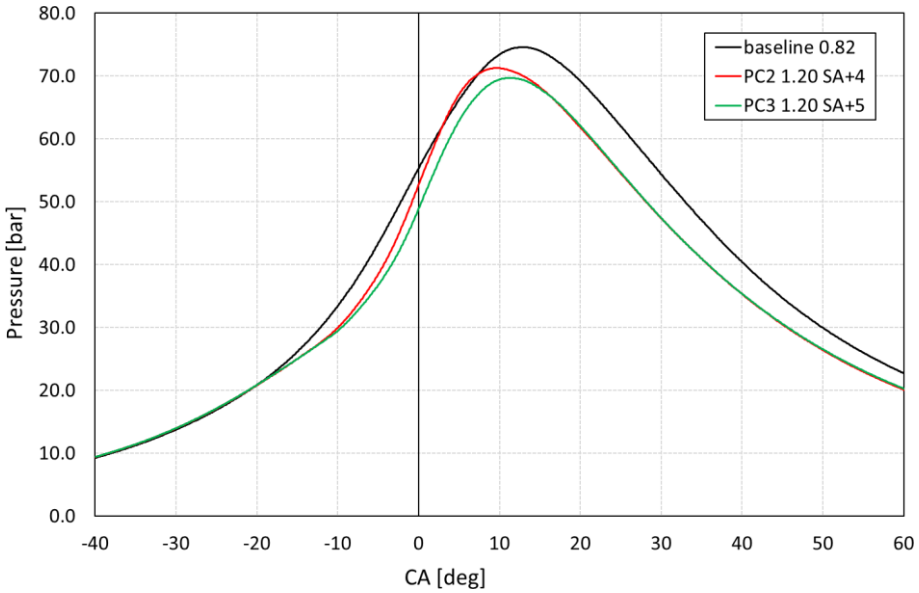

Figure 5-72. Comparison of in-cylinder pressure between baseline at maximum power and prechambers at lean condition and spark delayed.

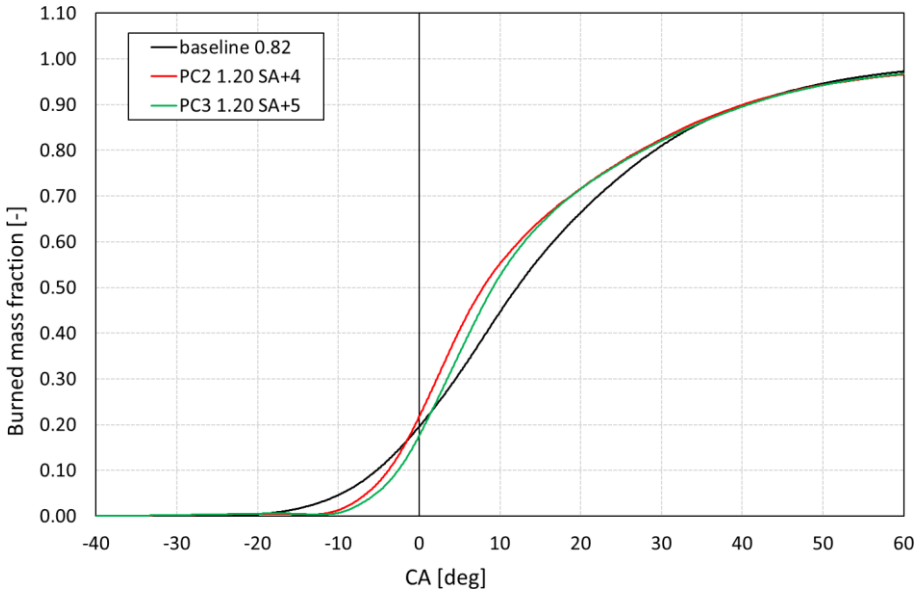

Figure 5-73. Comparison of burned mass fraction between baseline at maximum power and prechambers at lean condition and spark delayed.

From Figure 5-72 it can be noted that the pressure inside the cylinder for test cases PC2 and PC3 during the expansion phase is still lower than the one computed with baseline at maximum power. Thus, no further analysis is carried out by varying the spark advance.

From the sensitivity on the air-to-fuel ratio of the mixture, and considering the results come out from the sensitivity on orifices diameters, all the prechambers allow to obtain a consistent increment during the combustion process, in terms of both in-cylinder pressure and combustion duration. Comparing the all sensitivities carried out, the prechamber PC2 seems to be the best compromise for increasing the engine performance. In fact, PC2 has shown very good results for both rich and lean conditions and it has shown fast combustion process with different spark time too. Thus, a further air-to-fuel ratio value is simulated in order to obtain a combustion process faster than the baseline configuration and, in the meantime, to obtain a pressure inside the main chamber above the one computed at maximum power, especially during the expansion phase. Thus, as reported in Table 5-5, two additions air-to-fuel ratios equal are simulated with prechamber PC2: 1.05 and 1.10. Figure 5-74 and Figure 5-75 show the results of the air-to-fuel ratio sensitivity on PC2, compared with the baseline at maximum power, in terms of both in-cylinder pressure and burned mass fraction inside the main chamber. The results with air-to-fuel ratios of 1.05 and 1.10 are similar, in terms of in-cylinder pressure and burned mass fraction. Nevertheless, the test case at 1.05 computes a pressure during the expansion phase very close to the one obtained at maximum power without prechamber. It is interesting to note that with an air-to-fuel ratio equal to 1.05, the performance of the prechamber are similar to the ones obtained in rich conditions. In fact, even if the in-cylinder maximum pressure is higher with the richest mixture, during the expansion phase the curves tend to converge one on the other. Furthermore, the in-cylinder pressure at 1.05 is still higher than the one computed for baseline at maximum power. In addition, the whole air-to-fuel ratios simulated with PC2 produce a faster combustion process than the one computed at maximum power, except for the one at 1.40, which corresponds to a very lean condition. However, it is worth remembering that an air-to-fuel ratio of 1.40 represents the flammable limit of the mixture in the

baseline configuration: the use of prechamber allows to obtain a stable process even if the amount of fuel in the fresh gases is very low.

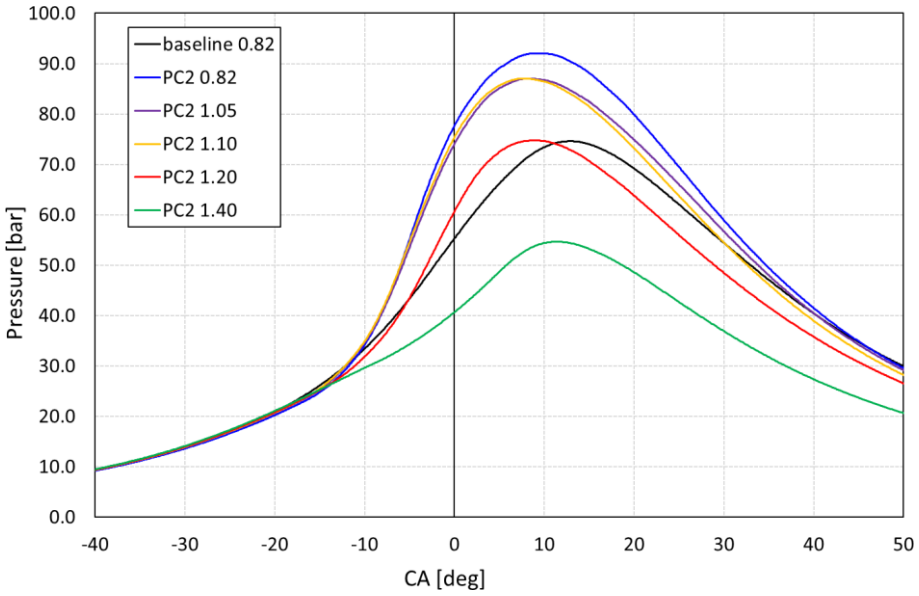

Figure 5-74. Comparison of in-cylinder pressure between baseline at maximum power and air-to-fuel ratio sensitivity on PC2.

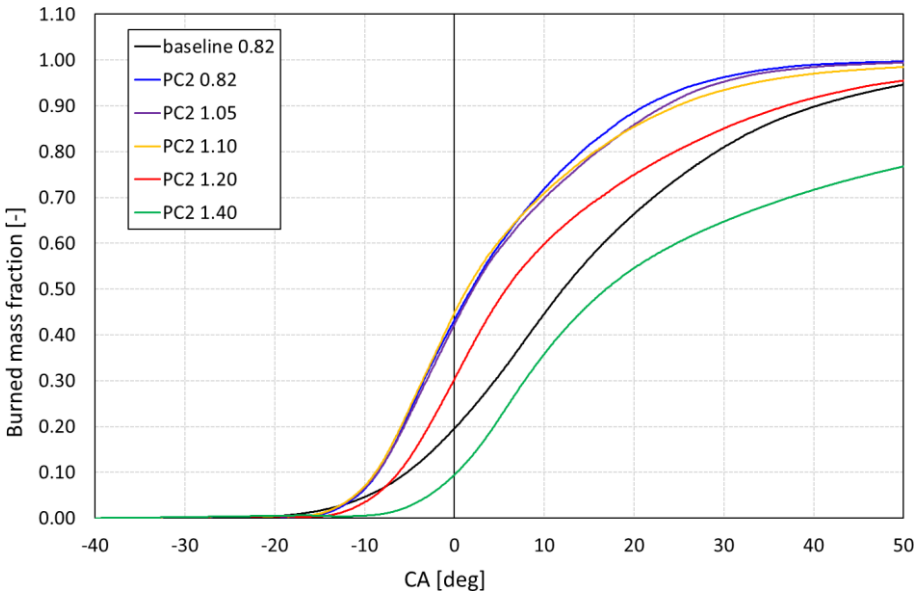

Figure 5-75. Comparison of burned mass fraction between baseline at maximum power and air-to-fuel ratio sensitivity on PC2.

It is worth noting that the performance with PC2 at 1.05 of air-to-fuel ratio are obtained with a reduction of fuel of 22% less than the baseline configuration at maximum power, as reported in Figure 5-76.

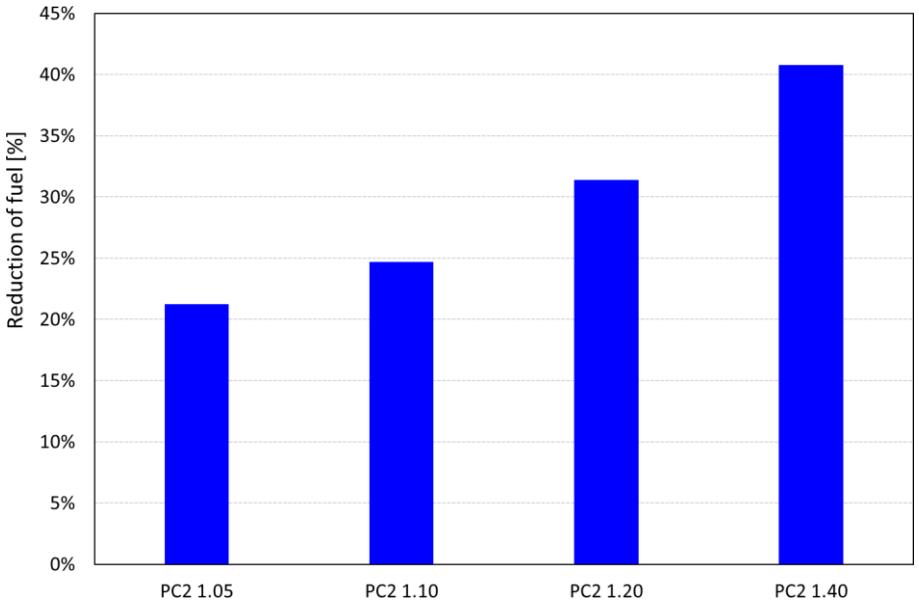

Figure 5-76. Reduction of fuel respect to the maximum power for PC2.

Furthermore, from Figure 5-77 it can be noted that, considering the combustion frame (from -40°CA to 50°CA), the indicated work in PC2 with air-to-fuel ratio equal to 1.05 and 1.10 is higher than the one computed with the engine without prechamber at maximum power, even the low amount of fuel.

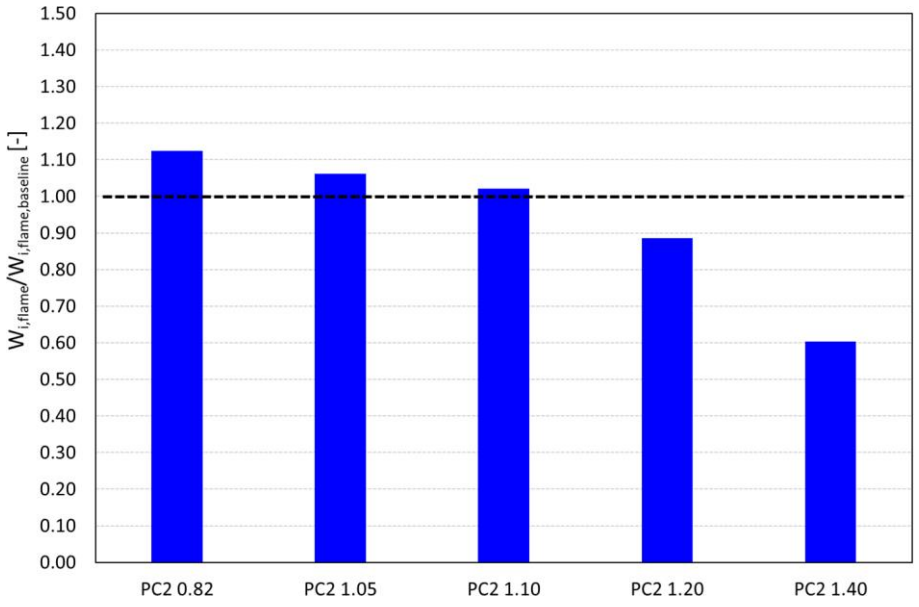

Figure 5-77. Indicated work for PC2 with different air-to-fuel ratios.

5.5 - Prechamber results at 4000 rpm

Since the PC2 prechamber represents the best test case for increasing the combustion performance of the engine, in terms of both in-cylinder pressure and flame speed, this geometry is used for simulating the combustion performance at 4000 rpm. The numerical procedure is the same used for the analyses of the

maximum power conditions. Thus, two revolutions of the engine are necessary to wash out the fluid domain from the initial conditions. During these first two revs, a user defined function is used to model the combustion process and accelerate the computational time required by the simulations. Then, the CFD simulation of the cold flow and the reacting flow is carried out. Figure 5-78 shows the evolution of pressure inside the cylinder (solid lines) and prechamber (dashed line). The use of prechamber produces a significantly improvement of the combustion process. The ignition occurs after few crank angles of the spark time. As the flame jets enter in the main chamber, the mixture ignites quickly, generating a pressure peak over the 100 bar. As can be seen in Figure 5-79, when the piston is at the TDC, over the 70% of fuel is burned, confirming the significantly increase of the speed of combustion. The increase in combustion performance at 4000 rpm are greater than the ones analysed at maximum power. In fact, the lower rotational speed means larger time for the flame growth. Thus, the prechamber is able to generate an in-cylinder pressure 110% higher than the baseline configuration, and a combustion process 50% faster (Figure 5-80). It is worth noting that the spark time set for the CFD simulations with prechamber is not optimized for working with prechamber (as happened for the maximum power condition). In fact, roughly 70% of the amount of fuel burns during the compression stroke (Figure 5-79). Nevertheless, the CFD results show the benefits of the prechamber on a 4-stroke engine, increasing the performance even if the rotational speed is low.

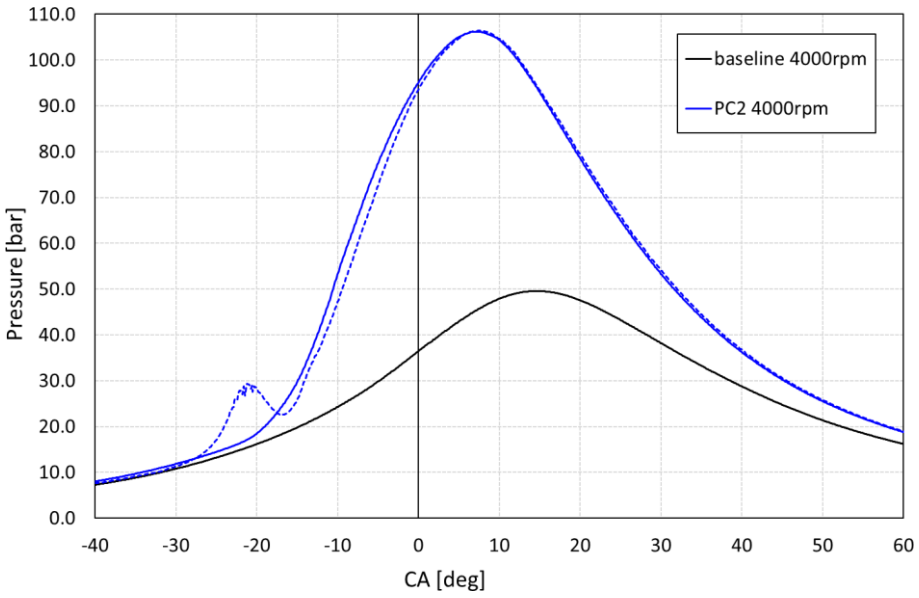

Figure 5-78. Evolution of pressure during combustion fat 4000 rpm: comparison between PC2 and baseline configuration.

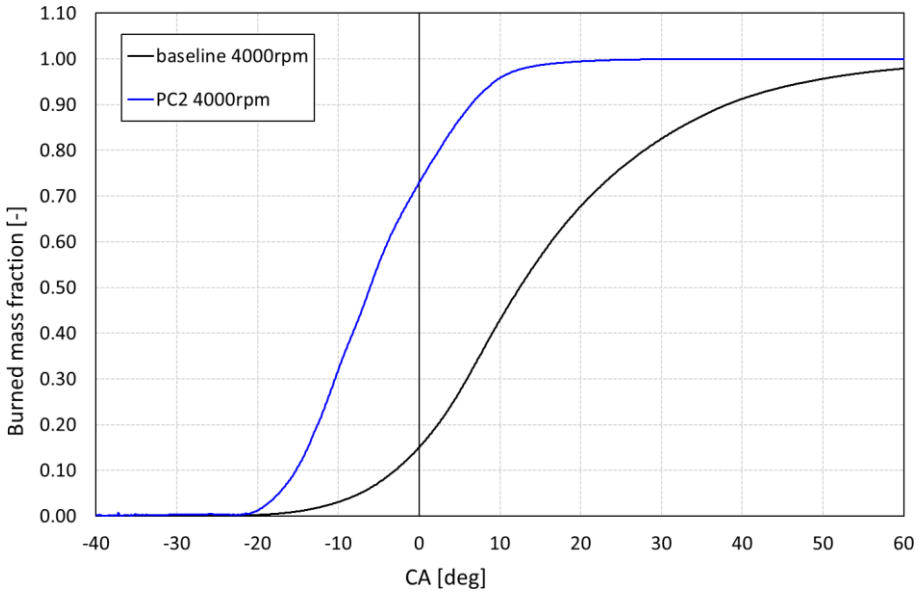

Figure 5-79. Evolution of burned mass fraction inside the cylinder at 4000 rpm: comparison between PC2 and baseline configuration.

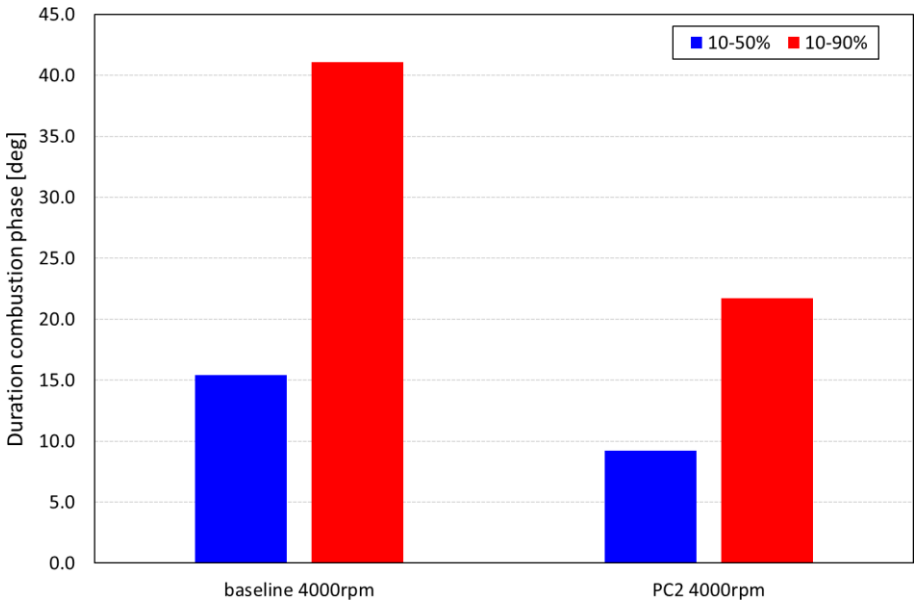

Figure 5-80. Combustion duration phase at 4000 rpm: comparison between PC2 and baseline configuration.

Conclusions

The main objectives of this thesis were the development of a predictive and accurate numerical setup for the three-dimensional simulation of the combustion process in SI engines and the analysis of the advantages and potential of the prechambers in terms of increasing the combustion speed, enhancing the combustion quality and extending the flammable limit. To accomplish that, two different combustion models were set up, based on a detailed chemistry model and a flame surface density model, respectively, with the goal of finding the best trade-off between the accuracy and complexity of the numerical approach and computational. The test case investigated in this study is a Betamotor 430 cm^3 4-stroke, four valves, PFI spark ignition engine. Since the test case was a PFI engine, the air/fuel mixture was considered homogeneous: therefore, the fuel injection was not simulated.

At first, unsteady RANS simulations of the engine without prechamber were carried out. Concerning the detailed chemistry solver, the simulation required three subsequent engine cycles in order to properly initialize the fluid domain and accurately model the combustion process. The first two engine cycles were simulated through non-reacting flow calculations, in order to simulate the cold-flow part of the cycle, while the combustion phase was imposed through a specific User Defined Function (UDF). Then, the final (third) cycle was performed by activating the SAGE combustion model involving 41 chemical species and 124 reaction mechanisms.

An in-depth analysis on the numerical parameters of the detailed chemistry solver was carried out, in order to investigate the settings of the combustion model. The calibration of the SAGE model at maximum power condition was performed against the experimental data. A very good agreement was achieved in terms of in-cylinder pressure and burned mass fraction: the difference between CFD and experimental peak pressure values is less than 1%. Then, the prediction capability of the calibrated SAGE model was verified at a different engine operating point. A very good agreement was achieved with experimental data for 4000 rpm, for the whole combustion process. Regarding the flame surface density model, the CFD cold flow computed an in-cylinder pressure during the compression phase less than 7% respect to the experimental one. Nevertheless, the non-reacting simulation was in agreement with the experimental data. Thus, the ECFM-3Z was calibrated for the maximum power engine condition. A good agreement was achieved in terms of in-cylinder pressure and flame front propagation, with a difference in terms of peak pressure between the CFD results and experimental value less than 2.5%.

After CFD simulations on the engine in baseline configuration, four different prechambers were designed, by varying the shape, the aspect ratio and the dimensions of the orifices, since these parameters were found to be the main variables that affect the combustion process. The whole test cases simulated showed a combustion process with prechamber faster than the baseline configuration, with a significantly improvement in terms of in-cylinder pressure and flame speed propagation.

A comparison between the two combustion models on the first geometry generated was carried out. The results showed the superior capability and reliability of the detailed chemistry model against the flame surface density model. The former was able to model properly the jet ignition and the flame propagation through the narrow orifices thanks to the chemical mechanism file. In fact, the SAGE model was able to take into account for radicals and intermediate species that sustain the combustion when the flame jets enter into the main chamber. The SAGE model computed a peak pressure values 14% higher than the one simulated with ECFM-3Z and combustion process faster than the one performed with the flame surface density model. It was observed that, since the flame density model did not take into account for species intermediate and radicals during the oxidation of the fuel, the ECFM-3Z was not able to model properly the interaction between the hot jets and the fresh gases in the cylinder. Thus, the detailed chemistry solver was used for further analyses on combustion process with prechamber.

Two different shape of prechambers were tested, PC1_S and PC1, in order to investigate the effect of the aspect ratio on the combustion process. The CFD results showed that the combustion process is not significantly affected by the aspect ratio. The combustion was found to be similar between the two prechambers, in terms of in-cylinder pressure and flame front propagation. Since the prechamber PC1 was designed with larger fillet radius, this shape was chosen for further analyses. The presence of sharper edges could have led to hot spots and thus, anomalies during the combustion process.

A sensitivity to the wall temperature of the prechamber was also carried out, in order to evaluate the effect of wall temperature on the reaction rates of the mixture and on the combustion process. In addition, since the lack of information on the value to assign, this sensitivity was necessary in order to provide information for future design and manufacturing. The results showed that increasing the wall temperature lead to a faster combustion process, due to the higher chemical reactivity of the mixture. A 15% increase of the wall temperature of the prechamber led to a 6% higher peak pressure inside the cylinder.

Concerning the dimension of the orifices, three different diameters were tested. The whole test cases showed an improvement of the combustion performance in terms of both in-cylinder pressure and flame speed. The peak pressure inside the cylinder was roughly 23% higher than the one computed for the baseline configuration, considering the same spark advance. The flame front propagation was enhanced by the hot flame jets, resulting in a combustion process 30% faster. Furthermore, the sensitivity to the orifices diameters showed that the highest dimension tested generated hot flame jets with low momentum, since the pressure drop between the main chamber and the prechamber was lower. Thus, the combustion process with the highest diameters was 20% slower than the process simulated with the others two prechambers, and the in-cylinder pressure was 5% lower.

Finally, since the use of the prechamber allows to ignite a lean mixture, a further sensitivity to the air-to-fuel ratio was carried out, in order to evaluate the advantages and capability of prechamber system. The results showed an improvement in the combustion performance for the whole test cases. The hot flame exiting from the orifices were able to ignite the fresh gases inside the main chamber even if the amount of fuel was very low, extending the flammable limit of the mixture and still guaranteeing a fast combustion process. With

an air-to-fuel ratio equal to 1.20 the pressure peak inside the cylinder with prechamber was 42% higher than the one computed in the baseline configuration and the combustion duration was more than halved.

Considering the outcome of the whole set of CFD sensitivity analyses, the best results were obtained with the prechamber PC2, which was then simulated at 4000 rpm, in order to evaluate its performance at low rotational speed. The comparison of the CFD results between the PC2 and baseline configuration showed a significant improvement of the combustion process at low rotational speed. The pressure peak inside the main chamber with prechamber was 110% higher and the combustion process was 50% faster than the baseline engine one.

List of references

[1] G. Ferrari. Internal combustion engines. Società editrice ESCULAPIO, 2014.

[2] John B. Heywood. Internal combustion engines fundamentals. McGraw-Hill Inc, 1988.

[3] The rise of cfd in building internal combustion engines of tomorrow. URL http://www.hitechcfd.com/cfd-knowledgebase/the-rise-of-CFD-inbuilding- internal-combustion-engines-of-tomorrow.html .

[4] T. Lucchini, M. Fiocco, A. Onorati, A. Montanaro, L. Allocca, P. Sementa, B. M. Vaglieco, and F. Catapano. Full-cycle cfd modelling of air/fuel mixing process in an optically accessible gdi engine. SAE International Journal of Engiens, 6(2013-24-0024):1610-1625, 2013/9/8.

[5] Sjeric, Momir & Kozarac, Darko & Schuemie, Henrik & Tatschl, Reinhard. (2018). A new quasi-dimensional flame tracking combustion model for spark ignition engines. Energy Conversion and Management. 165. 263-275. 10.1016/j.enconman.2018.03.008.

[6] Forte, Claudio & Bianchi, Gian Marco & Corti, Enrico & Fantoni, Stefano. (2015). Evaluation of the Effects of a Twin Spark Ignition System on Combustion Stability of a High Performance PFI Engine. Energy Procedia. 81. 897-906. 10.1016/j.egypro.2015.12.143.

[7] Forte, Claudio & Bianchi, Gian Marco & Corti, Enrico & Fantoni, Stefano & Costa, Marco. (2014). CFD Methodology for the Evaluation of Knock of a PFI Twin Spark Engine. Energy Procedia. 45. 859-868. 10.1016/j.egypro.2014.01.091.

[8] Emanuele, Fanelli & Viggiano, Annarita & Braccio, Giacobbe & Magi, Vinicio. (2014). On laminar flame speed correlations for H2/CO combustion in premixed spark ignition engines. Applied Energy. 130. 166–180. 10.1016/j.apenergy.2014.05.012.

[9] Miyagawa, Hiroshi & Nomura, Yoshihiro & Koike, Makoto & Tomoda, Terutoshi. (2003). CFD Simulation of Stratified Combustion Process in a Direct Injection Spark Ignition Engine. Jsme International Journal Series B-fluids and Thermal Engineering - JSME INT J SER B. 46. 332-339. 10.1299/jsmeb.46.332.

[10] Boccardi, Simone & Catapano, Francesco & Costa, Michela & Sementa, P & Sorge, Ugo & Vaglieco, B.M.. (2016). Optimization of a GDI engine operation in the absence of knocking through numerical 1D and 3D modeling. Advances in Engineering Software. 95. 38-50. 10.1016/j.advengsoft.2016.01.023.

[11] Sjeric, Momir & Kozarac, D & Ormuz, Krunoslav. (2016). Cycle-simulation turbulence modelling of IC engines. International Journal of Automotive Technology. 17. 51-61. 10.1007/s12239-016-0004-2.

[12] Corti, Enrico & Forte, Claudio & Cazzoli, Giulio & Moro, Davide & Falfari, Stefania & Ravaglioli, Vittorio. (2016). Comparison of Knock Indexes Based on CFD Analysis. Energy Procedia. 101. 917-924. 10.1016/j.egypro.2016.11.116.

[13] Gaseous emissions from light-duty vehicles: moving from NEDC to the new WLTP test procedure. Marotta, A, et al. 14, 2015, Environmental Science & Technology, Vol. 49, pp. 8315–8322.

[14] A perspective on the range of gasoline compression ignition combustion strategies for high engine efficiency and low NOx and soot emissions: Effects of in-cylinder fuel stratification. Dempsey, A B, Curran, S J and Wagner, R M. 8, 2016, International Journal of Engine Research, Vol. 17, pp. 897–917.

[15] Basic research needs for clean and efficient combustion of 21st century transportation fuels. [book auth.] F Cebulski, T R Garcia and D Strong. Report of the basic energy sciences workshop on basic research needs for clean and efficient combustion of 21st century transportation fuels. s.l. : U.S. Department of Energy, 2006, p. 19.

[16] Mixed-mode diesel HCCI/DI with external mixture preparation. Midlam-Mohler, S, et al. s.l. : SAE International, 2004, SAE Technical Paper 2004-05-0446.

[17] Evolution, challenges and path forward for low temperature combustion engines. Agarwal, A K, Singh, A P and Maurya, R K. 2017, Progress in Energy and Combustion Science 61, Vol. 61, pp. 1-56.

[18] Compression ratio influence on maximum load of a natural gas fueled HCCI engine. Olsson, J, et al. 2002, SAE Technical Paper 2002-01-0111.

[19] Expanding the operating range of homogeneous charge compression ignition–spark ignition dual-mode engines in the homogeneous charge compression ignition mode. Yang, J. 2015, International Journal of Engine Research 6 (4), pp. 279-288.

[20] A study of the influence of orifice diameter on a turbulent jet ignition system through combustion visualization and performance characterization in a rapid compression machine. Gentz, G, et al. 2015, Applied Thermal Engineering, Vol. 81.

[21] Development of an innovative combustion process: spark-assisted compression ignition. Chiodi, M, et al. s.l. : SAE International, 2017, SAE International Journal of Engines 10(5):2486-2499.

[22] Ignition and burning process in a divided chamber bomb. Yamaguchi, S, Ohiwa, N and Hasegawa, T. 2, s.l. : Elsevier, 1985, Combustion and flame, Vol. 59, pp. 177-187.

[23] Prechamber hot jet ignition of ultra-lean H2/air mixtures: effect of supersonic jets and combustion instability. Biswas, S and Qiao, L. 3, s.l. : SAE International, 2016, SAE Int. J. Engines, Vol. 9, pp. 1584-1592. doi:10.4271/2016-01-0795.

[24] Theory and evaluation of auxiliary combustion (torch) chambers. Adams, T G. s.l. : SAE International, 1978, SAE Transactions, Vol. 87, pp. 2328-2339.

[25] Numerical analysis of a torch-ignition system for an internal combustion engine. Radicchi, F, et al. s.l. : Trans Tech Publications, 2015, Applied Mechanics and Materials, Vol. 798, pp. 234-238.

[26] Baptista. Desenvolvimento de um sistema de ignicao por lanca-chamas para motor do ciclo otto. Universitade Federal de Minas Gerais. Belo Horizonte : s.n., 2007. Programa de pos-graduacao.

[27] Research on the ignition-chamber GDI engine combustion system. Fu, L, et al. 1, 2009, Journal of Thermal Science and Technology, Vol. 4. DOI: 10.1299/jtst.4.53.

[28] Looking into the prechamber of a lean-burn gas engine. Wolff, D, et al. 2, 1997, JSME Int. J. Series B, Vol. 40, pp. 320-327. https://doi.org/10.1299/jsmeb.40.320.

[29] Project and adaptation of torch-ignition system in an otto cycle engine. Gomes, J R C, et al. Ouro Preto : s.n., 2005. Proceedings of COBEM 2005 18th Int. Congress of Mechanical Engineering Nov 6-11.

[30] Torch ignition: ideal for lean burn premixed-charge engines. Mavinahally, N S, et al. 4, 1994, J. Eng. Gas Turbines Power, Vol. 116, pp. 793-798. doi:10.1115/1.2906887.

[31] Combustion process in a divided chamber spark ignition engine. Kataoka, K and Hirako, Y. 210, 1982, Bullettin of JSME, Vol. 25, pp. 1945-1952.

[32] Moreira, A. Analise e caracterizacao de um sistema de ignicao por lanca chamas operando com carga homogenea. Belo Horizonte: s.n., 2014. Programa de pos-graduacao.

[33] Sá, D C C. Análise de um sistema de ignição por lança-chamas adaptado a um motor do ciclo Otto. Escola de Engenharia, Universidade Federal de Minas Gerais. Belo Horizonte: s.n., 2001. Dissertação de Mestrado.

[34] Investigation of the prechamber geometrical configuration of a natural gas spark ignition engine for cogeneration: part II. Experimentation. Roethlisberger, R P and Favrat, D. s.l.: Elsevier, 2003, Int. J. Thermal Sciences, Vol. 42, pp. 239-253. doi:10.1016/S1290-0729(02)00024-8.

[35] Investigation of the prechamber geometrical configuration of a natural gas spark ignition engine for cogeneration: part I. Numerical simulation. Roethlisberger, R P and Favrat, D. s.l.: Elsevier, 2003, Int. J. Thermal Sciences, Vol. 42, pp. 223-237. doi:10.1016/S1290-0729(02)00023-6.

[36] Torch Ignition for Combustion Control of Lean Mixtures. Adams, T G. 1979, SAE Technical Paper 790440. https://doi.org/10.4271/790440.

[37] Combustion analysis with gas temperature diagrams measured in a prechamber spark ignition engine. Ryu, H and Asanuma, T. 1, s.l.: Elsevier, 1985, Twentieth Symposium (International) on Combustion, Vol. 20, pp. 195-200.

[38] Stephen B. Pope, Turbulent Flows, Cambridge University Press, 2000.

[39] C. Hirsch, Numerical computation of internal and external flows, Volume 1, Elsevier, 2007.

[40] C. Hirsch, Numerical computation of internal and external flows, Volume 2, Elsevier, 2007.

[41] David C. Wilcox, Turbulence modelling for CFD, DCW Industries, 1994.

[42] Yakhot, V., et al., "Development of Turbulence Models for Shear Flows by a Double Expansion technique", 1992, Physics of Fluids A: Fluid Dynamics 4, 1510.

[43] F. A. Williams. Combustion theory. The Benjamin/Cummings Publishing Company, Inc, 1985.

[44] Thierry Poinsot, Denis Veynante. Theoretical and Numerical Combustion. R.T. Edwards, Inc., 2005.

[45] K. K. Kuo. Principles of Combustion. John Wiley, New York, 1986.

[46] Tarek Echekki, Epaminondas Mastorakos, Turbulent Combustion Modelling, Springer, 2011.

[47] Lartigue, G. 2004 Simulation aux grandes échelles de la combustion turbulente PhD Thesis, INP Toulouse.

[48] Abdel-Gayed, R.G., Bradley, D. Hamid, M.N. & Lawes, M. 1984 Lewis number effects on turbulent burning velocity. Proc. Of the Combustion Institute 20, 505-512.

[49] Gulder, O. 1990 Turbulent premixed flame propagation model for different combustion regimes. 23rd Symp. (Int.) on Comb., The Combustion Institute, Pittsburgh, 743-835.

[50] Peters, N. 1999, The turbulent burning velocity for large-scale and small-scale turbulence. J. Fluid Mech. 384, 107-132.

[51] Roland Borghi. "Réactions chimiques en milieu turbulent". PhD thesis. 1978.

[52] CONVERGE v3.0 Manual, Richards, K. J. Senecal, P. K., Pomraning, E., Convergent Science, Inc., Madison, WI.

[53] Senecal, P.K., Pomraning, E., and Richards, K.J., "Multi-Dimensional Modeling of Direct-Injection Diesel Spray Liquid Length and Flame Lift-off Length using CFD and Parallel Detailed Chemistry," SAE Paper 2003-01-1043, 2003. DOI: 10.4271/2003-01-1043.

[54] Turns, S.R., An Introduction to Combustion, McGraw-Hill, Inc., 1996.

[55] Colin, O., and Benkenida, A., "The 3-Zones Extended Coherent Flame Model (ECFM3Z) for Computing Premixed/Diffusion Combustion", 2004, Oil & Gas Science and Technology – Rev. IFP, Vol. 59, No. 6, pp. 593-609.

[56] Bedford, K.W. and Yeo, W.K., "Conjunctive Filtering Procedures in Surface Water Flow and Transport," Large Eddy Simulation of Complex Engineering and Geophysical Flows, eds. Galperin, B., and Orszag, S., Cambridge University Press, 1993.

[57] Pomraning, E., "Development of Large Eddy Simulation Turbulence Models," Ph.D. Thesis, University of Wisconsin-Madison, Madison, WI, 2000.

[58] B. Dempsey, Adam & Reitz, Rolf. (2011). Computational Optimization of Reactivity Controlled Compression Ignition in a Heavy-Duty Engine with Ultra Low Compression Ratio. SAE International Journal of Engines. 4. 2222-2239. 10.4271/2011-24-0015.

[59] Contino, Francesco & Foucher, F & Dagaut, Philippe & Lucchini, Tommaso & D'Errico, Gianluca & Mounaïm-Rousselle, Christine. (2013). Experimental and numerical analysis of nitric oxide effect on the ignition of iso-octane in a single cylinder HCCI engine. Combustion and Flame. 160. 1476-1483. 10.1016/j.combustflame.2013.02.028.

[60] Kosmadakis, George & Rakopoulos, C.D. & Demuynck, Joachim & De Paepe, Michel & Verhelst, Sebastian. (2012). CFD modeling and experimental study of combustion and nitric oxide emissions in hydrogen-fueled spark-ignition engine operating in a very wide range of EGR rates. International Journal of Hydrogen Energy. 37. 10917–10934. 10.1016/j.ijhydene.2012.04.067.

[61] Yao-Dong Liu, Ming Jia, Mao-Zhao Xie, and Bin Pang, Enhancement on a Skeletal Kinetic Model for Primary Reference Fuel Oxidation by Using a Semidecoupling Methodology, Energy Fuels 2012, 26, 7069– 7083 doi.org/10.1021/ef301242b.

[62] Sideri, M., Berton, A., and D'Orrico, F., "Assessment of the wall heat transfer in 3D-CFD in cylinder simulations of high performance diesel engines", 2017, Energy Procedia, Vol. 126, pp. 963-970.

[63] M. Zellat, G. Desoutter,D. Abouri, A. Desportes, J.Hira, A new spark model for SI engine in STAR-CD: The Imposed Stretch Spark Ignition Model-Concept and preliminary validations to SI-GDI combustion, 2018.